APPLICATION OF GENETICALLY ENCODED INDICATORS TO MAMMALIAN CENTRAL NERVOUS SYSTEM

EDITED BY: Yoshiyuki Yamada and Katsuhiko Mikoshiba

PUBLISHED IN: Frontiers in Molecular Neuroscience

frontiers Research Topics

ISSN 1664-8714
ISBN 978-2-88919-804-7
DOI 10.3389/978-2-88919-804-7

About Frontiers

Frontiers is more than just an open-access publisher of scholarly articles: it is a pioneering approach to the world of academia, radically improving the way scholarly research is managed. The grand vision of Frontiers is a world where all people have an equal opportunity to seek, share and generate knowledge. Frontiers provides immediate and permanent online open access to all its publications, but this alone is not enough to realize our grand goals.

Frontiers Journal Series

The Frontiers Journal Series is a multi-tier and interdisciplinary set of open-access, online journals, promising a paradigm shift from the current review, selection and dissemination processes in academic publishing. All Frontiers journals are driven by researchers for researchers; therefore, they constitute a service to the scholarly community. At the same time, the Frontiers Journal Series operates on a revolutionary invention, the tiered publishing system, initially addressing specific communities of scholars, and gradually climbing up to broader public understanding, thus serving the interests of the lay society, too.

Dedication to Quality

Each Frontiers article is a landmark of the highest quality, thanks to genuinely collaborative interactions between authors and review editors, who include some of the world's best academicians. Research must be certified by peers before entering a stream of knowledge that may eventually reach the public - and shape society; therefore, Frontiers only applies the most rigorous and unbiased reviews.
Frontiers revolutionizes research publishing by freely delivering the most outstanding research, evaluated with no bias from both the academic and social point of view.
By applying the most advanced information technologies, Frontiers is catapulting scholarly publishing into a new generation.

What are Frontiers Research Topics?

Frontiers Research Topics are very popular trademarks of the Frontiers Journals Series: they are collections of at least ten articles, all centered on a particular subject. With their unique mix of varied contributions from Original Research to Review Articles, Frontiers Research Topics unify the most influential researchers, the latest key findings and historical advances in a hot research area! Find out more on how to host your own Frontiers Research Topic or contribute to one as an author by contacting the Frontiers Editorial Office: **researchtopics@frontiersin.org**

APPLICATION OF GENETICALLY ENCODED INDICATORS TO MAMMALIAN CENTRAL NERVOUS SYSTEM

Topic Editors:
Yoshiyuki Yamada, Brain Science Institute, RIKEN and Central Institute for Experimental Animals, Japan; University of Geneva, Switzerland
Katsuhiko Mikoshiba, Brain Science Institute, RIKEN and Central Institute for Experimental Animals, Japan

Genetically encoded indicators emerged as promising tools for cell type-specific and chronic recording of neuronal population activity. Since publication of the first prototypical genetically encoded Ca^{2+} indicators (Cameleons) in 1997, we have witnessed remarkable evolution of the field, with rapid improvement of indicator performance as well as expanded application to many model organisms in the neuroscience community. Challenges still remain, however, concerning the mammalian central nervous system: limited sensitivity of indicators to subtle changes in activity, slow signal kinetics, cytotoxicity after a long-term and high-level expression of indicators, and variable performance across cell types. In addition to improvement of the indicators per se, development of strategies that allow combined use of the indicators and optogenetic tools is also desired.

In this Research Topic, we recruited top researchers in the field and their young colleagues to present their cutting-edge research as well as insightful opinions on the following subtopics:

1. Latest breakthroughs on development of genetically encoded indicators
2. Novel scientific findings obtained with genetically encoded indicators
3. Wishlist for the next-generation genetically encoded indicators
4. Guideline for selecting an appropriate indicator
5. Optimal methodology for indicator delivery to mammalian CNS

Citation: Yamada, Y., Mikoshiba, K., eds. (2016). Application of Genetically Encoded Indicators to Mammalian Central Nervous System. Lausanne: Frontiers Media.
doi: 10.3389/978-2-88919-804-7

Table of Contents

frontiers in Molecular Neuroscience

EDITORIAL
published: 22 December 2015
doi: 10.3389/fnmol.2015.00076

Editorial: Application of Genetically Encoded Indicators to Mammalian Central Nervous System

Yoshiyuki Yamada[1,2*†] *and Katsuhiko Mikoshiba*[1,2*]

[1] *Laboratory for Developmental Neurobiology, Brain Science Institute, RIKEN, Wako-shi, Japan,* [2] *Central Institute for Experimental Animals, Kawasaki-shi, Japan*

Keywords: genetically encoded sensors, fluorescent protein sensors, genetically encoded calcium indicators (GECIs), *in vivo* imaging, genetically encoded voltage sensor

The Editorial on the Research Topic

Application of genetically encoded indicators to mammalian central nervous system

Genetically encoded indicators are fluorescent proteins engineered to change their optical properties and report the dynamics of intracellular molecules or voltage. Encoded in a relatively compact size of DNA (typically 2–3 kilobase pairs), they are readily compatible with standard gene delivery techniques, including viral vectors and transgenesis. They can be thus expressed in specific types of cells with the use of cell type-specific promoters and/or Cre-loxP recombination system, which makes them beneficial for disentangling the complex mammalian neural circuitry. Another unique advantage of genetically encoded indicators is that they can be stably expressed for a long period, which allows chronic tracking of the same neuronal ensemble by longitudinal imaging, and offers unprecedented opportunities to investigate the neural basis of development, learning, and disease.

Since the prototypical genetically encoded Ca^{2+} indicators (GECIs) were reported for the first time (Miyawaki et al., 1997), genetically encoded indicators have drastically evolved in terms of signal to noise ratio, response kinetics, and spectral variety. In this Research Topic, Tian and colleagues provide a review on genetically encoded indicators of neuronal activity in general, including GECIs, with a special focus on the GCaMP family (GECIs composed of a circularly permutated GFP, the Ca^{2+}-binding protein calmodulin, and the calmodulin-binding peptide M13), as well as genetically encoded indicators of voltage and synaptic activity (Broussard et al.). Griesbeck and colleagues present an overall review of GECIs, covering from the basics of Ca^{2+} imaging in neurons to the description of latest variants, and also discuss recent studies where GECIs were applied to neuronal population imaging in awake head-restrained mice (Rose et al.). The article by Nagai and colleagues focuses on affinity variants, color variants and photoactivatable variants of GECIs, the last two of which are of considerable importance for simultaneous use with optogenetic tools (Nagai et al.). Lin and colleagues then provide a review, for the first time to our knowledge, on a rapidly growing subfamily of optogenetic tools—a group of photoactivatable effector proteins that control the dynamics of intracellular molecules, rather than the membrane voltage (Zhou et al.).

It is also noteworthy that an important update of red GECI, R-CaMP2 was recently published (Inoue et al., 2015), reflecting the highly active nature of this field. R-CaMP2 was shown to have fast kinetics, high linearity, and remarkable sensitivity to detect single action potentials, making it even competitive with the state-of-art green GECIs; the proof of principle experiments show that it can be simultaneously used with GCaMP and/or channelrhodopsin, paving the way to multicolor

OPEN ACCESS

Edited by:
Robert J. Harvey, University College London, UK

Reviewed by:
Joe Lynch, University of Queensland, Australia

****Correspondence:***
Yoshiyuki Yamada
yy@brain.riken.jp;
Katsuhiko Mikoshiba
mikosiba@brain.riken.jp

†Present Address:
Yoshiyuki Yamada, Department of Basic Neurosciences, University of Geneva, Geneva, Switzerland

Received: *29 October 2015*
Accepted: *23 November 2015*
Published: *22 December 2015*

Citation:
Yamada Y and Mikoshiba K (2015) Editorial: Application of Genetically Encoded Indicators to Mammalian Central Nervous System. Front. Mol. Neurosci. 8:76. doi: 10.3389/fnmol.2015.00076

longitudinal imaging and all-optical manipulation/recording of neural activity. Another group is also developing different variants of red GECIs independently (Dana et al., 2014), and it would be interesting to see side-to-side comparison in the future.

More specific technical advances are also reported in this Research Topic. Knöpfel and colleagues characterize a new series of genetically encoded voltage indicators, with a chimeric voltage sensing-domain (fragments from the Ci-VSP and the Kv3.1 potassium channel) sandwiched by a FRET donor and acceptor ("butterfly" design; Mishina et al.). Tsutsui and colleagues present their attempts to turn a GFP variant into a genetically encoded chromophore optimized for second harmonic generation microscopy, which can be used for voltage imaging (Jinno et al.). White and colleagues describe a set of *in utero* electroporation vectors carrying genetically encoded Ca^{2+} indicators (GCaMP), and investigate Ca^{2+} dyanamics of astrocytes in rat organotypic slice culture (Gee et al.).

The improved performance and rich repertoire of genetically encoded indicators have stimulated their widespread application to biologically relevant questions. Tvrdik and colleagues demonstrate 2-photon Ca^{2+} imaging in transgenic mice expressing GCaMP in microglia, and study Ca^{2+} dynamics induced by lipopolysaccharide and focal laser injury (Pozner et al.). Ohki and colleagues perform wide-field Ca^{2+} imaging in transgenic mice expressing GCaMP broadly across the cortex, and identify two visual association areas that respond to drifting gratings, where they further examine the cellular responses by 2-photon imaging (Murakami et al.). Fletcher and colleagues also perform wide-field Ca^{2+} imaging in transgenic mice expressing GCaMP in excitatory output neurons in the olfactory bulb, and examine the circuit element responsible for olfactory habituation (Ogg et al.).

We thank all the authors and reviewers for their valuable contributions to our Research Topic, and sincerely hope that it will provide readers with useful information and inspiration for further innovation in the field.

AUTHOR CONTRIBUTIONS

YY and KM conceived the overall plan of Research Topic, recruited contributors, and wrote the manuscript.

ACKNOWLEDGMENTS

This work was supported by JST International Cooperative Research Project–Solution Oriented Research for Science and Technology (KM); JSPS Grants-in-Aid for Scientific Research S (20220007, 25221002, to KM), JSPS Grant-in-Aid for Young Scientists (B) (24700401, to YY), RIKEN BSI Grant (KM), and the Special Postdoctoral Researchers Program in RIKEN (YY).

REFERENCES

Dana, H., Sun, Y., Hasseman, J.-P., Tsegaye, G., Holt, G.-T., Fosque, B.-F., et al. (2014). "Improved red protein indicators for *in vivo* calcium imaging," in *Program#/Poster#: 566.06/VV68, Society for Neuroscience* (Washington, DC).

Inoue, M., Takeuchi, A., Horigane, S.-I., Ohkura, M., Gengyo-Ando, K., Fujii, H., et al. (2015). Rational design of a high-affinity, fast, red calcium indicator R-CaMP2. *Nat. Meth.* 12, 64–70. doi: 10.1038/nmeth.3185

Miyawaki, A., Llopis, J., Heim, R., McCaffery, J. M., Adams, J. A., Ikura, M., et al. (1997). Fluorescent indicators for Ca^{2+} based on green fluorescent proteins and calmodulin. *Nature* 388, 882–887. doi: 10.1038/42264

Conflict of Interest Statement: The authors declare that the research was conducted in the absence of any commercial or financial relationships that could be construed as a potential conflict of interest.

frontiers in
MOLECULAR NEUROSCIENCE

REVIEW ARTICLE
published: 05 December 2014
doi: 10.3389/fnmol.2014.00097

Monitoring activity in neural circuits with genetically encoded indicators

Gerard J. Broussard*[1,2]*, Ruqiang Liang*[1] *and Lin Tian*[1,2] *

[1] *Department of Biochemistry and Molecular Medicine, University of California Davis, Davis, CA, USA*
[2] *Neuroscience Graduate Group, University of California Davis, Davis, CA, USA*

Edited by:
Katsuhiko Mikoshiba, RIKEN Brain Science Institute, Japan

Reviewed by:
Mazahir T. Hasan, Charité-Universitätsmedizin-Berlin, Germany
Bernd Kuhn, Okinawa Institute of Science and Technology Graduate University, Japan

***Correspondence:**
Lin Tian, Department of Biochemistry and Molecular Medicine, University of California Davis, Davis, CA 95817, USA
e-mail: lintian@ucdavis.edu

Recent developments in genetically encoded indicators of neural activity (GINAs) have greatly advanced the field of systems neuroscience. As they are encoded by DNA, GINAs can be targeted to genetically defined cellular populations. Combined with fluorescence microscopy, most notably multi-photon imaging, GINAs allow chronic simultaneous optical recordings from large populations of neurons or glial cells in awake, behaving mammals, particularly rodents. This large-scale recording of neural activity at multiple temporal and spatial scales has greatly advanced our understanding of the dynamics of neural circuitry underlying behavior—a critical first step toward understanding the complexities of brain function, such as sensorimotor integration and learning. Here, we summarize the recent development and applications of the major classes of GINAs. In particular, we take an in-depth look at the design of available GINA families with a particular focus on genetically encoded calcium indicators (GCaMPs), sensors probing synaptic activity, and genetically encoded voltage indicators. Using the family of the GCaMP as an example, we review established sensor optimization pipelines. We also discuss practical considerations for end users of GINAs about experimental methods including approaches for gene delivery, imaging system requirements, and data analysis techniques. With the growing toolbox of GINAs and with new microscopy techniques pushing beyond their current limits, the age of light can finally achieve the goal of broad and dense sampling of neuronal activity across time and brain structures to obtain a dynamic picture of brain function.

Keywords: *in vivo* imaging, mammalian and rodent brain, neural activity, genetically encoded sensors, calcium sensor, voltage sensor, synaptic activity reporter

INTRODUCTION

Within the mammalian brain, neuronal and glial cells communicate at spatial and temporal scales spanning orders of magnitude. One of the fundamental challenges with which modern neuroscience is currently grappling is the development of tools that can record this communication as it occurs at the relevant scales. Furthermore, it is desirable that these tools should be deployable in living animal models. Such probes will aid the study of neural communication within the context of phenomena such as experience dependent plasticity, sensorimotor integration, learning, and memory.

An extensive set of tools for studying brain function *in vivo* currently exists, and each of these possesses its own set of strengths and weaknesses. For example, recordings of intracellular voltage or transmembrane current can be made using patch clamp (Liu et al., 2009; Crochet et al., 2011) or extracellular potential recordings can be achieved with fine-tipped metallic electrodes (Hubel and Wiesel, 1959; Reid et al., 1997; Mante et al., 2013). These methods provide an exquisitely detailed temporal signal, but are limited by the number of cells that can be recorded simultaneously. Simultaneous neural recordings with near-cellular resolution can be achieved using multiple electrode arrays (Buzsaki, 2004). However, this technique cannot precisely localize cell position and yields limited information about cell types. Optical imaging of bolus loaded AM ester dyes allows recordings at high spatial resolution from many cells simultaneously (Stosiek et al., 2003; Helmchen and Denk, 2005). But this technique results in high background due to residual fluorescence in the extracellular space as well as the lack of genetic control (Stosiek et al., 2003). A lack of genetic control can in particular lead to increased fluorescent background due to unspecific staining of non-neuronal cells as well as neurons not pertinent to a given study. In addition, small molecule-based dyes are not compatible with chronic imaging (Aramuni and Griesbeck, 2013). Both small-molecule dyes and electrode methods are highly invasive and can negatively impact the health of recorded cells (Polikov et al., 2005; Dombeck et al., 2010) making chronic recordings from the same cell population difficult.

Genetically encoded indicators combined with modern microscopy (such as multi-photon microscopy), can potentially overcome these challenges to allow non-invasive, ultrasensitive and chronic measurement at specific synapses and within or across circuit elements in behaving animals. A large array of protein based indicators has been created to monitor neurotransmission, synaptic spillover, excitable membrane potential, calcium dynamics, vesicle trafficking, receptor mobilization and other essential biochemical events related to neural activity. A subset of these—detecting changes in intracellular calcium concentration, synaptic signaling events, and changes in membrane

potential—have been successfully deployed for the imaging of action potentials (APs) *in vivo*. Here, we refer to this group of probes as genetically encoded indicators of neural activity (GINAs). For a more exhaustive review of available fluorescent sensors of cellular activity, please see VanEngelenburg and Palmer (2008), Ibraheem and Campbell (2010). Application of GINAs have facilitated large-scale recording of neural activity in genetically identified populations over multiple spatial and time scales in living neurons *in vitro*, *ex vivo*, and *in vivo*.

Here we review advances in design and engineering of GINAs. We discuss various properties of genetically encoded calcium indicators (GECIs) and their optimization for improved detection of single and multiple APs in *in vivo* imaging. In particular, as a case study, we present protein engineering efforts to incrementally improve intrinsic properties of the GCaMP family to match with challenging signal to noise ratio (SNR) in *in vivo* imaging. We further discuss technologies developed to aid *in vivo* imaging in the rodent brain. Finally, we briefly summarize recent findings based on the strength of GINAs as a toolbox for analyzing neural circuit function.

DESIGN OF GENETICALLY ENCODED INDICATORS OF NEURAL ACTIVITY

The first protein used to detect functionally relevant changes within a cell was an aequorin protein which was purified from jellyfish (Shimomura et al., 1962) and introduced exogenously to muscle fibers of a barnacle to sense changes to intracellular calcium that occur during fiber contraction (Ashley and Ridgway, 1968). The era of the modern GINAs, however, began in earnest with the introduction of biosensors based on fluorescent proteins (FPs) which were able to detect changes to intracellular calcium levels (Miyawaki et al., 1997; Romoser et al., 1997), membrane voltage (Siegel and Isacoff, 1997) and synaptic vesicle secretion (Miesenbock et al., 1998). A guide to the general design of several GINA families is presented in **Figure 1**.

Genetically encoded indicators of neural activity typically consist of an analyte-binding or sensing domain and a reporter element which is based on either a single FP or two FPs. In the case of single FP GINAs, changes in the cellular environment detected by the analyte-binding or sensing domain result in changes in the chromophore environment of the FP leading to an increment or decrement of fluorescence intensity (Siegel and Isacoff, 1997; Baird et al., 1999; Nakai et al., 2001). For example, as illustrated diagrammatically in **Figure 1A**, in the scaffold of GCaMPs, calmodulin (CaM) binds the M13 peptide from myosin light chain kinase in the presence of calcium; this coupling reverses when calcium is absent (Nakai et al., 2001). The sensor domain transduces conformational changes of analyte binding to a change in the fluorescence intensity through its coupling with the reporter FP(s). Additionally, some single FP-based GINAs contain FPs in which fluorescence intensity is environmentally sensitive (e.g., pH sensitive FPs; **Figure 1D**; Miesenbock et al., 1998). In the case of two FP based sensors, the conformational changes in the analyte-binding or sensing domain lead to Förster resonance energy transfer (FRET) between two FPs with overlapping excitation and emission spectra. For example, the Cameleon family contains both M13 and CaM in between a blue/green or cyan/yellow FP pairs as shown for Yellow Cameleon-Nano (YC-Nano; **Figure 1B**). Upon calcium binding, the relative distance and orientation of the FPs are altered, resulting in a change in the non-radiative transfer of energy between the donor and acceptor chromophores.

Single-FP based GINAs are prone to motion artifacts, which can be corrected by algorithms (e.g., Dombeck et al., 2007) and using a reference fluorophore. On the other hand, the FRET based GINAs, by virtue of ratiometric imaging can cancel the motion-related artifacts (Wallace et al., 2008; Lütcke et al., 2010) and are thus highly suitable for imaging neuronal activity in freely moving animals. However, the SNR of FRET-based probes are lower than their single FP counterparts in probing higher numbers of APs (see, e.g., Tian et al., 2009). Single-FP based probes also preserve spectral bandwidth for applications in multiplex imaging and optogenetics. Although the currently used FRET sensors can be coupled with red-shifted FPs and optogenetic tools, the broad emission and excitation spectra of FRET sensors reduce some flexibility.

Relative to other methods for recording neural signals, GINAs possess several advantages. First, they can be targeted to genetically defined cell populations of interest. As such, they can be introduced via minimally invasive interventions such as viral mediated gene delivery or transgenesis (permanent genomic modification). Genetic control also reduces background signal from sources not under scrutiny, increasing SNR (Stosiek et al., 2003), and can permit targeting to a population that is anatomically or functionally related. For example, GINAs allow for specific labeling of direct and indirect pathway neurons in the striatum (Cui et al., 2013) as well as excitatory (Bozza et al., 2004; Ziv et al., 2013) and inhibitory (Kaifosh et al., 2013) neurons which co-localize within the same local neural circuit. Second, GINAs make it possible to record from a large population of cells simultaneously with better spatial resolution than the best electrophysiological techniques (Knöpfel, 2012). Studies exploiting this strength have demonstrated neural network characteristics that were not previously apparent from single cell recordings (Dombeck et al., 2010; Harvey et al., 2012). Finally, GINAs allow for chronic interrogation of the same cells for long periods of time (Mank et al., 2008; Tian et al., 2009; Kuhn et al., 2012; Margolis et al., 2012). As a result, studies which track dynamics of neural circuitry such as learning and memory induced changes to neural ensembles have been made possible (Huber et al., 2012; Petreanu et al., 2012).

Used in conjunction with modern microscopic techniques—most notably two photon (2P) imaging—GINAs are now routinely employed in the interrogation of neural activity under a wide variety of contexts in awake, behaving mammals (Helmchen and Denk, 2005; Bovetti et al., 2014).

GENETICALLY ENCODED CALCIUM INDICATORS

Calcium dynamics are a proxy to monitor APs in neurons (Tank et al., 1988; Miyawaki et al., 1997) and represent excitable states in astrocytes (Perea and Araque, 2005). In neurons, APs lead to calcium transients in the cytosol through voltage-gated calcium channels (Hille, 2001). This rise is reversed as calcium is buffered, extruded, and pumped back into internal stores

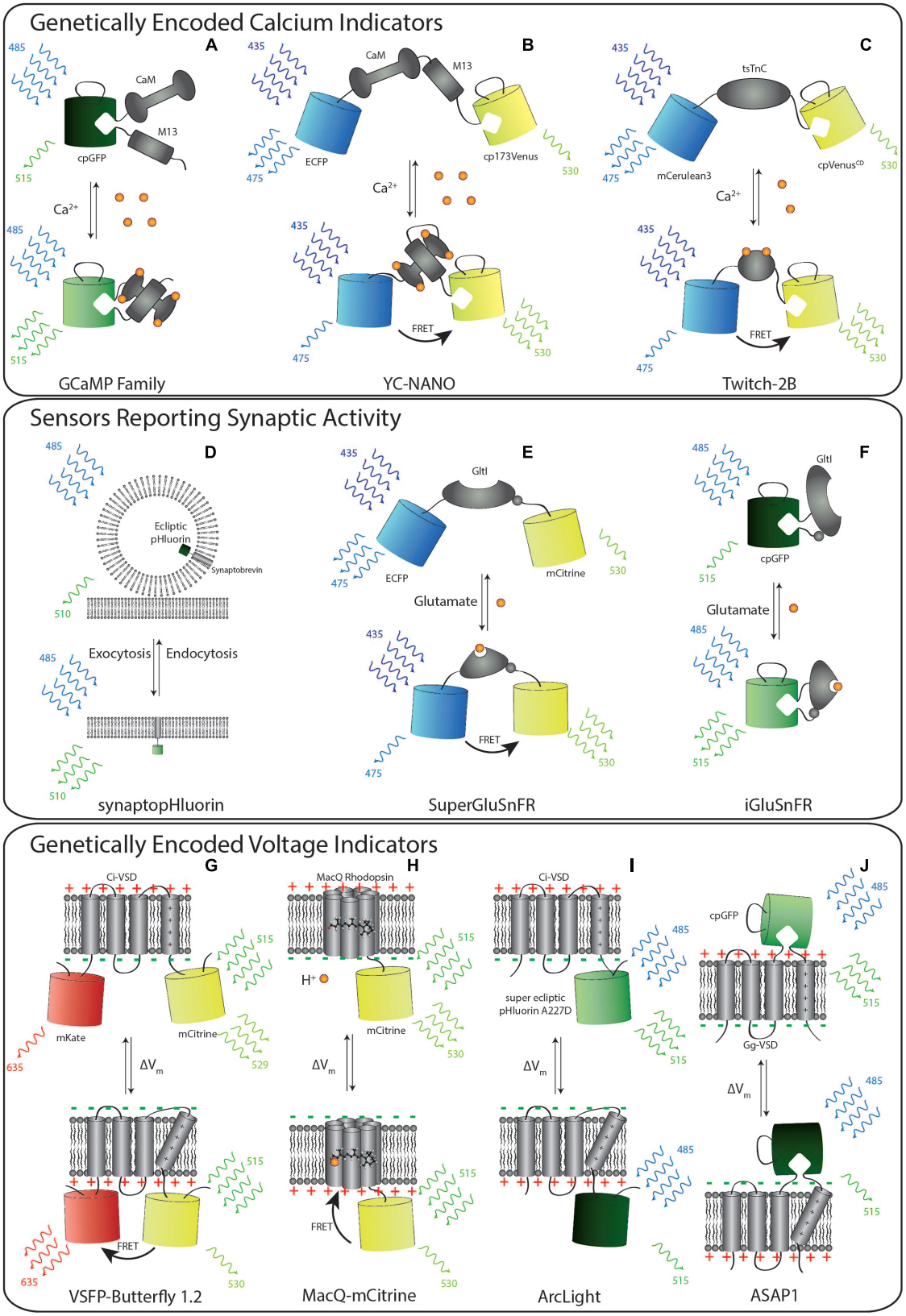

FIGURE 1 | Continued

FIGURE 1 | Continued
Schematic representation of selected members of genetically encoded indicators of neural activity (GINA). (A–C) Calcium indicators. **(A)** GCaMP6 consists of circularly permuted green fluorescent protein (cpGFP) inserted between calmodulin (CaM) and an M13 peptide. Upon calcium binding, conformational changes in the CaM–M13 complex induce fluorescence changes in the circularly permuted enhanced green fluorescent protein (cpEGFP). **(B)** YC-Nano contains CaM–M13 complex sandwiched between the donor FP (ECFP) to the acceptor FP (cp173Venus). Upon calcium binding, conformational changes of CaM–M13 complex increases Förster resonance energy transfer (FRET) between the FP pair. The result is an increase in the ratio of the fluorescence in the yellow to blue channels. **(C)** Likewise, Twitch-2B increases FRET upon calcium being bound by its calcium sensitive domain, tsTnC. **(D–F)** GINAs reporting synaptic activity. **(D)** SynaptopHluorin consists of a ecliptic pHluorin FP fused to the C-terminus of the vesicular protein. Vesicular release places the FP in the low pH environment of the extracellular space, which leads to the deprotonation of the fluorophore and increases pHluorin fluorescence. **(E)** SuperGluSnFR is a linear fusion of CFP, the *Escherichia coli* glutamate binding domain, GltI, and mCitrine. Upon glutamate binding, the conformational changes of GltI result in FRET between CFP to mCitrine. **(F)** iGluSnFR contains a cpGFP fused to the glutamate binding domain. The conformation changes of GltI induced upon glutamate binding results in deprotonation and increased fluorescence of cpGFP. **(G–J)** Genetically encoded voltage indicators. **(G)** Upon membrane depolarization, the voltage-sensing domain of Ci-VSP enters its activated state. The FPs of voltage sensitive fluorescent protein (VSFP)-Butterfly 1.2 are thus drawn into close proximity to one another, increasing FRET. **(H)** The opsin-based MacQ-mCitrine reduces fluorescence output upon membrane depolarization. This effect is driven by enhanced FRET from the mCitrine FP to the weakly fluorescent retinal caused by a shift in the cofactor absorption spectrum upon protonation of the Schiff base. **(I)** ArcLight consists of Ci-VSD and super ecliptic pHluorin carrying the point mutation A227D. Depolarization of the membrane results in a decrease in the fluorescence output of the pHluorin, but the mechanism of this change remains elusive. **(J)** ASAP-1 contains cpGFP fused into an extracellular linker (S3–S4 linker) of the Gag-VSP voltage sensitive domain. Depolarization quenches the fluorescence of the cpGFP.

in a process which generally lasts on the order of 100 ms (Helmchen et al., 1996; Koester and Sakmann, 2000). Astrocytes, a prevalent type of glial cell in the brain implicated to play important roles in synaptic plasticity, also propagate intracellular signals by means of calcium transients. The source of these calcium events in astrocytes largely overlaps those found in neurons, but due to differential expression levels—particularly a dearth of voltage-dependent calcium channels—and relative cellular location of these sources, calcium events in these cells are longer (generally seconds in duration) and in some cases more highly localized (Ben Achour et al., 2010; Ding, 2013) or show waves of activity in other cases (Hoogland et al., 2009).

Of all GINA classes, GECIs are currently the most widely utilized for *in vivo* imaging in model systems including worm (Kerr et al., 2000; Boulin and Hobert, 2012), zebrafish (Higashijima et al., 2003), fly (Wang et al., 2003), rodent (Hasan et al., 2004; Tian et al., 2009), and recently non-human primate (Heider et al., 2010; Yin et al., 2014). In large part, the success of GECIs has been due to their high SNR (Mank et al., 2008; Chen et al., 2013b) via extensive protein engineering efforts to significantly improve their intrinsic properties, such as brightness (Tian et al., 2009), pH insensitivity (Miyawaki et al., 1999), stable folding (Tallini et al., 2006), photostability (Tian et al., 2009), large dynamic range (Chen et al., 2013b), fast kinetics (Sun et al., 2013) and appropriate expression level (Miyawaki et al., 1999), to match with extrinsic parameters of calcium dynamics in neurons. A summary of GECI design is shown in **Figures 1A–C**.

The first GECIs to gain wide usage were the FRET-based Cameleons which contain M13 and CaM in between a blue/green or cyan/yellow FP pair, conceptually similar to YC-Nano as pictured in **Figure 1B**. Several incrementally improved variants of Cameleon have since been engineered, e.g., the YCs series (for review, see Miyawaki, 2011; Palmer et al., 2011), the computationally redesigned variants D1cpv, D2cpv, D3cpv, and D4cpv to reduce impact on endogenous calcium handling and interaction with endogenous proteins (Palmer et al., 2006), and the high-affinity YC-Nano series (Horikawa et al., 2010). Additionally, a family of GECIs has been developed based on the muscle-specific Ca^{2++} -binding protein Troponin C: TN-L15, TN-XL (Mank et al., 2006), TN-XXL (Mank et al., 2008), and the recent Twitch sensor (Thestrup et al., 2014). The troponin family in theory has the lowest probability of having interaction with endogenous proteins in cells. In addition, FP pairs have been optimized or replaced as newer, more advantageous FPs became available (Ai et al., 2014).

Meanwhile, a proliferation of single wavelength calcium probes (Camgaroo, Pericam, Case, and GCaMP family) based on enhanced yellow fluorescent protein (EYFP) or circular permutated green fluorescent protein (GFP) have been engineered (Baird et al., 1999; Nagai et al., 2001; Nakai et al., 2001; Souslova et al., 2007). Since then, several papers have been published on the iterative improvement of the GCaMP scaffold, which include GCaMP1.6 (Ohkura et al., 2005), GCaMP2 (Tallini et al., 2006), GCaMP3, and recently developed highly sensitive GCaMPs such as GCaMP-HS (Muto et al., 2011), Fast-GCaMPs (Sun et al., 2013) and GCaMP5 and GCaMP6 series (i.e., GCaMP6s, GCaMPm, and GCaMPf; Chen et al., 2013b). It is noted that a different group uses a distinct numbering system for GCaMP variants which include GCaMP6 (Ohkura et al., 2012), GCaMP7a (Muto et al., 2013), and GCaMP8 (Ohkura et al., 2012). However, these GCaMPs are not incremental improvements upon the GCaMP6 series (Chen et al., 2013b).

With the demonstration that a YC (D3cpv) can readily detect a single AP in mammalian neurons, both *in vitro* and *in vivo* (Wallace et al., 2008), various members of the YC [especially YC3.60 (Nagai et al., 2004)], TN-L [especially TN-XXL (Mank et al., 2008)], and GCaMP [especially GCaMP3 (Tian et al., 2009) and GCaMP5 (Akerboom et al., 2012)] lineages have seen extensive use in *in vivo* preparations. Recent additions to the YC [YC-Nano (Horikawa et al., 2010)], TN-L [Twitch (Thestrup et al., 2014)], and GCaMP families [GCaMP6(s,m,f) (Chen et al., 2013b)] have achieved the long-standing goal of single spike detection in pyramidal neurons on par with or surpassing synthetic dyes in the neurons of living rodents. A summary of performance of GECIs for spike detection in *in vivo* mammalian preparations is presented in **Table 1**.

Another exciting advance in GECI development in the past few years has been the expansion of new color-palette variants, such as the red-shifted variant R-GECO (Zhao et al., 2011) based on mApple and RCaMP based on mRuby (Akerboom et al., 2013). Extending the color-spectrum has greatly increased the potential

Table 1 | Selected examples of modern genetically encoded indicators and their degree of utility in *in vivo* imaging in the mammalian brain.

Genetically encoded indicator lineage/member	Mammalian system *in vivo*	Spontaneous activity detection	Single spike detection	No population or trial averaging	Example reference
Genetically encoded calcium indicators					
GCaMP					
GCaMP3	Yes	Yes	No	Yes	Tian et al. (2009)
GCamP5	Yes	Yes	Yes	Yes	Akerboom et al. (2012)
Fast-GCaMPs	No	Yes	Yes	Yes	Sun et al. (2013)
GCaMP6(s,m,f)	Yes	Yes	Yes	Yes	Chen et al. (2013b)
Yellow Cameleon					
YC2.60	Yes	No	Yes	Yes	Yamada et al. (2011)
YC3.60	Yes	No	Yes	Yes	Lütcke et al. (2010)
D3cpV	Yes	Yes	Yes	Yes	Wallace et al. (2008)
YC-Nano	Yes	Yes	Yes	Yes	Horikawa et al. (2010)
TropininC-based					
TN-XXL	Yes	ND	ND	ND	Mank et al. (2008)
Twitch	Yes	Yes	Yes	Yes	Thestrup et al. (2014)
Reporters of synaptic activity					
pHluorin-based					
synaptopHluorin	Yes	Yes	ND	No	Bozza et al. (2004)
GluSnFR					
SuperGluSnFR	No	ND	ND	ND	Hires et al. (2008)
iGluSnFR	Yes	Yes	ND	Yes	Marvin et al. (2013)
Genetically encoded voltage indicators					
FlaSh					
Flare	Yes	Yes	ND	No	Ahrens et al. (2012)
VSFP					
VSFP2.3	Yes	Yes	No	Yes	Akemann et al. (2010)
VSFP-Butterfly 1.2	Yes	Yes	ND	No	Akemann et al. (2013)
ArcLight					
ArcLight	No	Yes	Yes	Yes	Cao et al. (2013)
Rhodopsin-based					
MacQ	Yes	Yes	Yes*	Yes	Gong et al. (2014)
ASAP					
ASAP1	No	ND	ND	ND	St-Pierre et al. (2014)

**Detected long-lasting Ca^{2+} spikes only. Shorter duration Na^{+} spikes were not resolved.*
ND, not determined.

of GECIs in multiplex imaging. Multi-color imaging allows simultaneous assay of diverse cell types. For example, different color probes will aid in the elucidation of the interplay between neurons and astrocytes in shaping the neural circuitry. Red-shifted indicators will additionally reduce tissue scattering (for both excitation and emission), phototoxicity, and background fluorescence, facilitating deep imaging. Finally, color-shifted indicators will seamlessly integrate into imaging experiments with other types of indicators and optogenetic tools (for review, see Akerboom et al., 2013).

For the past years, GECIs have driven the expansion of knowledge about the dynamics of neural circuitry gained through *in vivo* imaging of the intact brain (For details, see Recent Findings through GINA Technologies). GECI variants continue to open up new applications in neuroscience. Transgenic expression of inverse pericam and camgaroo-2 allowed the first detection of calcium signals evoked via sensory manipulation in a single trial in mouse (Hasan et al., 2004). D3cpv produced the first recordings of single spikes from mouse cortical cells *in vivo* (Wallace et al., 2008). Several GINAs have been deployed under a glial

fibrillary acidic protein (GFAP) promoter in mice to allow readout of astrocytic activity in acute slice (Haustein et al., 2014) and in the intact, anesthetized animal (Atkin et al., 2009; Hoogland et al., 2009). Members of the TN-L (TN-XXL; Heider et al., 2010) and GCaMP (GCaMP5; Yin et al., 2014) lineages have recently been deployed for imaging studies in non-human primates. Future work within this model organism will produce results more pertinent to the human nervous system. GCaMP6 was used to report calcium transients from dendritic spines of excitatory and the dendrites of inhibitory interneurons located in primary visual cortex (Chen et al., 2013b). All of these milestones continue to demonstrate that GECIs have been a useful tool for breaking down barriers to advance our understanding of the dynamics of neural circuitry.

Despite the fact that calcium transients are an indirect measure of systems level circuit function, their superior SNR values relative to other GINA classes have assured their continued dominance in this arena for the near future. Though the advance of monitoring circuitry function depends on the improvement of genetically encoded voltage indicators (GEVIs) and other sensors probing all kinds of neural activity—for example transient changes to neuromodulator concentration in the extracellular space—GECIs will continue to find utility in the study of electrically silent cells which interact with brain circuitry, such as astrocytes.

SENSORS REPORTING SYNAPTIC ACTIVITY

Rapid information flow in the brain is mediated by anatomical connections at synapses between cells. During the course of an AP, membrane depolarization invades the presynaptic terminal. As noted above, this results in intracellular calcium transients, which in turn drive the fusion of neurotransmitter containing vesicles with the presynaptic cell membrane. This fusion event results in an immediate increase in the vesicular pH, which is maintained at an acidic level, as the lumenal volume is expelled into the extracellular space. The contents of the vesicle are also released into the synaptic cleft, leading to a local increase in the concentration of neurotransmitter (Hille, 2001).

To better access synaptic transmission with optical tools, a variety of GINA classes have been developed. The first of these, synaptopHluorin, is derived from the fusion of a pH sensitive, ecliptic GFP variant at the c-terminus of the vesicular protein, synaptobrevin [also known as vesicular associated membrane protein-2 (VAMP2)], which localizes the FP to the vesicular lumen. The fluorescence of the ecliptic pHluorin is quenched by the acidic environment of synaptic vesicles (pH 5.6). During neurotransmitter release, vesicles fuse with the plasma membrane, exposing the lumen to the neutral pH of the extracellular environment (pH 7.4), causing a dramatic increase in fluorescence intensity. The fluorescence intensity is then quenched once again after reconstitution and reacidification of the vesicle interior (Miesenbock et al., 1998; **Figure 1D**). SynaptopHluorin was one of the first GINAs to be employed for *in vivo* imaging in the mammalian system (Bozza et al., 2004).

Later modifications to these probes included fusions to different proteins which localize with higher specificity to synaptic vesicles such as synaptophysin (Granseth et al., 2006) and the vesicular glutamate transporter (VGLUT-1; Balaji and Ryan, 2007). Red-shifted variants of synaptopHluorin have also been developed for multiplex imaging. These were constructed by exchanging the GFP based pHluorin with relatively red shifted FPs and include VGLUT1-mOrange2 (Li et al., 2011) and sypHTomato (Li and Tsien, 2012). Each of these probes was used concurrently with a GCaMP indicator to simultaneously probe presynaptic calcium signaling and presynaptic release at the same synapses or in distinct pre- and postsynaptic elements. These studies serve as early examples of the future possibilities presented by multiplex imaging.

Genetically encoded indicators of neural activity for probing excitatory neurotransmitter glutamate release and spillover have also been developed. Fluorescent indicator protein for glutamate (FLIPE; Okumoto et al., 2005) and the SuperGluSnFR (Tsien, 2005; Hires et al., 2008) are FRET-based probes which employ the linear fusion of periplasmic glutamate binding protein of *Escherichia coli*, GltI, (also known as ybeJ) with enhanced cyan fluorescent protein (ECFP) and a yellow FP, Citrine or Venus (**Figures 1E,F**). These reporters provide a sensitive optical readout of glutamate concentration *in vitro* by FRET-dependent changes in the CFP/YFP emission ratio. An improved version of GluSnFR, SuperGluSnFR has since been developed. Through linker optimization (Hires et al., 2008), SuperGluSNFR permits efficient optical measurements of the time course of synaptic glutamate release, spillover, and reuptake in cultured hippocampal neurons with centisecond temporal and dendritic spine-sized spatial resolution. Most recently, a single-FP based glutamate sensor, iGluSnFR, was developed. iGluSnFR is based on the fusion of Gltl with circularly permuted enhanced green fluorescent protein (cpEGFP; **Figure 1E**). Due to the superior SNR of this probe, it allows the resolution of glutamate transients at the apical tuft dendrites of layer V neurons in the motor cortex of awake, behaving mice (Marvin et al., 2013).

The development of sensors probing synaptic activity greatly expanded the kinds of neural activity that can be accessed by optical tools. The output activity of a neuron is sometimes thought of as being the voltage transients propagated to synaptic termini during an AP. Calcium transients are currently the most experimentally accessible marker of this phenomenon. However, under some conditions, the relationship between these signals and synaptic release is non-linear (see, e.g., Singer and Diamond, 2006). In this respect, reporters of synaptic activity will sometimes be a better choice of sensor for applications in which vesicle/transmitter release is the primary concern. Furthermore, neurotransmitter sensors allow detection of the presence of extra-synaptic neurotransmitter, which can have important functional consequences when interacting with neuronal receptors expressed distal to synapses (Marvin et al., 2013) and on astrocytes (Haustein et al., 2014).

GENETICALLY ENCODED VOLTAGE INDICATORS

Membrane potential undergoes a rapid change during the course of an AP as well as subthreshold oscillations. These changes can be succeeded by consequent changes to intracellular calcium and evoked synaptic signaling events (Hille, 2001). As such, voltage is considered the primary signal of interest and the most direct

way to monitor neural activity. Despite this fact, imaging voltage is inherently difficult, largely due to the nature of the voltage signal itself. The short duration of the voltage change during APs (1–5 ms) demands faster kinetics and higher sensitivity of fluorescent sensors to yield sufficient photon budget for imaging (Peterka et al., 2011; Looger and Griesbeck, 2012). Additionally, GEVIs are necessarily membrane bound or associated, which reduces imaging volume relative to cytosolic GINAs (Peterka et al., 2011). However, recent advances in the field of protein engineering hold great promise for the development of GEVIs with superior SNR.

As demonstrated in **Figures 1G,I,J**, most GEVIs function as reporter of membrane voltage by tethering one or two FPs to a voltage sensitive protein derived from natural sources. The first genetically encoded voltage indicators—such as FlaSh (Siegel and Isacoff, 1997), sodium channel protein-based activity reporting construct (SPARC; Ataka and Pieribone, 2002), and voltage sensitive fluorescent protein 1 (VSFP 1; Sakai et al., 2001)—were based on intact voltage-gated potassium channels or their "voltage-sensing" domains. However, these probes exhibit low SNR, slow kinetics and localize poorly to the membrane of mammalian cells (Baker et al., 2007).

The next generation of GEVIs was based on the voltage sensitive domain of a phospatase (VSP) derived from the sea squirt, *Ciona intestinalis* (Ci-VSP; Murata et al., 2005; Dimitrov et al., 2007; Akemann et al., 2010; Jin et al., 2012; **Figures 1G,H**). These probes include both FRET-based (Akemann et al., 2010) and single FP-based family (Lundby et al., 2008; Perron et al., 2009), and boasted much improved brightness, kinetics and improved membrane targeting relative to the earlier generation. One of the most advanced probes of this class, VSFP2.3, permitted *in vivo* recording of neural activity in mouse somatosensory cortex, despite poor cellular resolution. Recently, an improved variant, VSFP butterfly 1.2 (**Figure 1G**), showed increased SNR and allowed two-photon imaging of membrane changes produced by layer2/3 neurons of mouse barrel cortex, which represents the first reported use of at depth cellular resolution imaging by a GEVI. However, extensive trial averaging was required in order to resolve the signal (Akemann et al., 2013).

In parallel, protein engineering efforts have also led to single-FP based GEVIs. For example, the ArcLight (**Figure 1H**) fluorescence voltage sensors consist of the fusion of ecliptic pHluorin GFP to Ci-VSP and show significantly improved sensitivity in response to APs compared to other Ci-VSP based probes (Cao et al., 2013). More recently, Accelerated Sensor of Action Potentials 1 (ASAP1) has been developed in which circularly permuted green fluorescent protein (cpGFP) is inserted in an extracellular loop of a voltage-sensing domain of a VSP derived from a chicken (*Gallus gallus*). ASAP-1 showed faster kinetics compatible with the typical 2-ms duration of APs and is capable of probing high-frequency AP trains (St-Pierre et al., 2014), thus permitting detection of subthreshold potential and hyperpolarization waveforms in cultured hippocampal neurons. However, voltage imaging using both ArcLight and ASAP-1 in intact rodent brains remains to be demonstrated.

In addition, another recent class of GEVI including PROPS (Kralj et al., 2011) and VIP1 (Kralj et al., 2012), has been developed based on voltage-induced fluorescence modulation of the retinal cofactor of bacterial and archaeal rhodopsins. In these probes, the rhodopsin itself acts as the sensor domain while the retinal cofactor serves as the fluorescence reporter *via* direct fluorescence (Kralj et al., 2011, 2012; Gong et al., 2013) or acting as FRET acceptor (illustrated in **Figure 1H**; Gong et al., 2014). Relative to the Ci-VSP based sensors, this class of sensor is extremely fast with submillisecond kinetics, sufficient to resolve single AP or subthreshold membrane voltage fluctuations in cultured mammalian neurons. However, because these probes rely on a retinal cofactor as the sole fluorescence source, they exhibit extremely low brightness. The most recent FRET-opsin sensors offer fast kinetics (rise time ∼5 ms) as well as higher brightness, which has allowed for reporting long-lasting complex spikes in the dendritic arbors of Purkinje cells in the cerebellum of a living mouse. These spikes exhibit slower dynamics than typical Na^+ spikes (∼5–10 ms), but nevertheless were apparently detected at sub-cellular resolution with single-trial precision (Gong et al., 2014), a first for this GINA class.

Though current state-of-the art GEVIs have been deployed for *in vivo* imaging, their broad use has remained limited in rodent brain as shown in **Table 1**. As incremental improvements are made to existing and future probes, GEVIs may finally facilitate systems-level, cellular-resolution voltage imaging in living behaving mammals.

Blogs discussing all GINA classes can be found at open websites such as Andrew Hires' Brain Windows[1] and Guillame Dugué's OpenOptogenetics[2].

CASE STUDY: FROM GCaMP3 TO GCaMP6

Extensive protein engineering efforts have improved the properties of GINAs, especially the GCaMP family, to the point that they now rival synthetic alternatives such as Oregon Green Bapta-1 in terms of kinetics and sensitivity. Here we review established sensor design and optimization pipelines (rational design combined with directed evolution) that have proven to be effective to improve the intrinsic properties of GCaMPs, leading to a family of high performing sensors, GCaMP3, GCaMP5, and GCaMP6(s,m,f; **Figures 2A,B**).

Based on GCaMP3 scaffold, an array of GCaMP5 variants was generated by combining improvements from site-directed mutagenesis at cpEGFP/CaM interface and targeted library screening at the two linkers between cpEGFP and M13/CaM (Akerboom et al., 2012). Twelve GCaMP5s were systematically characterized in cultured neurons, astrocytes, and in *Caenorhabditis elegans*, drosophila, zebrafish, and mouse under various conditions. SNR was improved by at least twofold to threefold; all GCaMP5s showed improved dynamic range compared with GCaMP3. Users can choose from different GCaMP5 variants for different applications. Amongst these, GCaMP5A, GCaMP5G, and GCaMP5K exhibit the highest levels of general utility.

Based on the GCaMP5 scaffold, computational design has guided further targeting of 16 amino acid positions on the interface between cpEGFP and CaM at 18 positions including the M13-CaM interface (Chen et al., 2013b). Four hundred and forty seven

[1] https://brainwindows.wordpress.com/

[2] http://www.openoptogenetics.org/

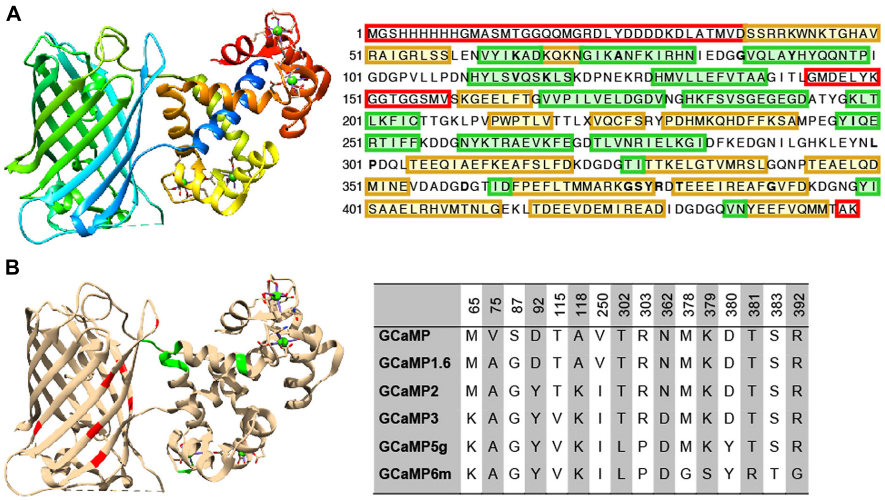

FIGURE 2 | Structure and beneficial mutations of GCaMPs. (A) Crystal structure (Ding et al., 2014) and primary sequence of GCaMP6m. Distinct regions of the crystal structure are indicated by color. The cooler the color, the closer the sequence is to N-terminus. The primary sequence is annotated such that yellow shading corresponds to ß-strands, green shading corresponds to α-helices, and residues in red are those that do not crystallize (i.e., pRSET domain and linkers). **(B)** Beneficial mutations of GCaMPs. Crystal structure of GCaMP6m is annotated with iteratively evolved residues. Red residues are from the cpGFP and green ones are from calmodulin. Note that these residues are typically at the interface between the two domains. Residue matrix shows the evolution of GCaMP lineage with incrementally improved performance. Individual beneficial residues are highlighted in the primary sequence of GCaMP6m in **(A)**.

GCaMP variants in were screened in dissociated neuronal culture resulting in three ultrasensitive GCaMP6 sensors with a variety of kinetics [i.e., GCaMP6s (slow), GCaMP6m (medium; **Figure 2A**), and GCaMP6f (fast)]. Compared to GCaMP5G, these sensors have 1.1- to 1.6-fold increase of dynamic range and threefold higher Ca^{2+} binding affinity. In addition, GCaMP6f shows the fastest kinetics among the entire GCaMP family due to a mutation at the M13-CaM interface (A317E).

Besides protein engineering efforts, the success of GCaMP6 development also depended on the establishment of a highly efficient high-throughput screening platform (Wardill et al., 2013). This system directly employed screening in dissociated rat cortical/hippocampal neuronal culture, bypassing the screening steps in bacterial and mammalian cells (Tian et al., 2009; Zhao et al., 2011). Specifically, lentivirus encoding GCaMP variants driven by human *synapsin-1* promoter were produced to achieve dense and neuron-specific labeling in cultured neurons. To assist automated processing of imaging acquisition and analysis, internal ribosome entrance site (IRES) were introduced downstream of GCaMP to drive the expression of a second FP, nuclear targeted mCherry. The process of screening has been automated from probe development to imaging analysis (Wardill et al., 2013). This screening system can be easily adapted to aid in the optimization of other members of the GINA family.

As new members of the GCaMP family and other GINA classes are developed, their creators will often make them available for the larger research community. Frequently, genetic material encoding the probes can be acquired through Addgene[3], a non-profit plasmid repository. For ready-made application, GINAs packaged into viral vectors can be obtained through viral core facilities of institutions such as the University of Pennsylvania[4] and the University of North Carolina at Chapel Hill[5]. Finally, animals transgenic for several GINAs have been produced and are available for purchase through services such as those provided by the Jackson Laboratory[6] and the Zebrafish International Resource Center[7].

IN VIVO IMAGING WITH GINAs IN LIVING, BEHAVING RODENT BRAIN

Though some classes of GINAs have been optimized to the point that they are compatible for *in vivo* imaging, the noise level *in vivo* greatly challenges the SNR of the sensors, especially in the mammalian brain. To make imaging experiments meaningful and successful, consideration must be taken for proper selection of imaging configuration, expression systems, surgical procedure, imaging depth, and analytical techniques. To provide guidance for the end-users for choosing most suitable experimental settings, here we review a few important intrinsic and extrinsic parameters that are essential to maximize SNR and to achieve best imaging outcomes.

GINA TRANSDUCTION METHODS

The expression level of a GINA influences its SNR in cells and organisms in a complex manner. Low expression level will preclude

[3]http://www.addgene.org

[4]http://www.med.upenn.edu/gtp/vectorcore/

[5]http://www.med.unc.edu/genetherapy/vectorcore

[6]http://jaxmice.jax.org

[7]http://www.zebrafish.org

sensor visualization and decrease SNR. It also demands imaging with higher laser power and longer exposure time, which may lead to phototoxicity, reduced imaging speed, and increased photobleaching. On the other hand, high expression level increases photon budget, but also increases substrate buffering (e.g., calcium by GECIs) and may perturb cell signaling pathways leading to cytotoxicity and cytomorbidity (see, e.g., Kuhn et al., 2012). Variation of expression level from cell to cell also impacts sensor performance, potentially confounding quantitative imaging analysis. To balance all these effects, it is essential to explore multiple promoters and regulatory sequences combined with the most suitable gene delivery methods to maximize the SNR of the sensor. Several methods of gene delivery have been optimized for the expression and subsequent recording of GINAs in the intact mammalian brain. These include introduction via stereotaxic viral injection, *in utero* electroporation, and stable transgenesis.

In the case of viral gene delivery, virus-encoding GINAs are injected directly into the brain region of interest (Wallace et al., 2008). Typically, recombinant adeno-associated virus (rAAV) has been broadly used due to its ability to diffuse easily away from the site of injection and relative simplicity (Grieger and Samulski, 2005). But others, such as adenoviral vector (e.g., Mohamed et al., 2013) and lentiviral vectors (e.g., Akerboom et al., 2012), are also in use (Packer et al., 2013). Combined with tissue specific promoters, such as synapsin-1, viral injection permits labeling of genetically defined local populations of neurons. The efficiency of probe expression can vary as a function of cell type, promoters, brain regions, and AAV serotype (Cearley and Wolfe, 2006; Wallace et al., 2008; Kuhn et al., 2012; Aschauer et al., 2013). For example, rAAV2 drives differential probe expression in cerebellar interneurons (Kuhn et al., 2012). However, when combined with specific promoter system, rAAV can be targeted to Purkinje cells in cerebellum cortex (Kuhn et al., 2012). In addition, rAAV9 is well suited for the transduction of cortical neurons (Cearley and Wolfe, 2006), while rAAV8 is particularly efficient in labeling astrocytes (Aschauer et al., 2013). Hybrid viruses have been developed which increase potential combinations of transduction efficiency and tropism. For example, AAV2/1 encoding GINAs have been widely used because they display a broad tropism within the central nervous system combined with high transduction efficiencies (Burger et al., 2004). Viral labeling results in long-term, relatively stable probe expression over months, during which time imaging experiments can be performed repeatedly (Mank et al., 2008; Tian et al., 2009; Kuhn et al., 2012; Margolis et al., 2012). The popularity of this method of gene transfer is due in large part to its relatively easy adoption with flexibility in choosing tool payload and injection locations.

In utero electroporation is a process in which plasmid is injected, usually to the ventricles of an animal during the prenatal period of its life. The plasmid is driven into cells at the ventricular surface via application of electrical current across the target structure. Due to the temporal pattern of laminar development and spatial pattern of cell lineages present in the cortex, the time and location at which the procedure is performed can restrict probe expression to specific layers (Tabata and Nakajima, 2001) or cell populations (Borrell et al., 2005) within the cortex. However, the expression level of GINAs driven by this method has been reported to cause cytotoxicity as expression begins during a developmentally sensitive period (Tian et al., 2009). Furthermore, the variation of expression level in cells appears more pronounced than that using viral transduction. Still, studies that are based around developmental questions of circuit formation can benefit from the use of this method.

Transgenesis refers to the permanent modification of the genome of an organism by the use of, for example, bacterial artificial chromosomes (Van Keuren et al., 2009), zinc finger nucleases (Urnov et al., 2010), transcription activator-like effector nucleases (Joung and Sander, 2013), or clustered regularly interspaced short palindromic repeats (CRISPR) associated genes (Mali et al., 2013). Transgenic rodent lines that stably express GINAs through multiple generations have been a standard tool in neuroscience. Transgenic lines have been engineered expressing GINAs such as inverse pericam and camgaroo-2 (Hasan et al., 2004), synaptopHluorin (Bozza et al., 2004), GCaMP2 (Díez-García et al., 2005), YC3.60 (Atkin et al., 2009), the hybrid voltage sensor (hVOS; Wang et al., 2012), and GCaMP3 under control of the Thy1 promoter (Zariwala et al., 2012). Gene transfer through transgenesis results in the stable and ubiquitous expression of the genetic construct in target cells throughout the organism, although expression levels tend to vary across lines and tissue regions (Zeng and Madisen, 2012). Studies that require dense sampling from a genetically defined population over the life course of an organism benefit from the use of transgenic organisms.

Targeting GINAs with adequate cell type specificity can be achieved through recombinase systems such as the Cre/loxP and FLP/FRT, especially by pairing recombinase-dependent viruses with recombinase-expressing animal lines. Selective expression of GINAs in subsets of anatomically or functionally related populations is possible by placing the GINA construct into the double-floxed inverted orientation (DIO) configuration (Atasoy et al., 2008) or using recently developed INTRSECT (Intronic recombinase sites enabling combinatorial targeting) strategy in which expression is contingent upon the presence of Boolean subsets of transcription factors (Fenno et al., 2014).

Pharmacological control can be exerted to achieve temporal control of GINA expression. For example, the Tet-On(Off) system causes expression(repression) of GINA expression in the presence of tetracycline or one of its analog (Gossen and Bujard, 1992; Hasan et al., 2004). Such temporal control can be important to prevent perturbation of early developmental processes or animal behavior, which may confound imaging results (Tian et al., 2009).

OPTICAL INSTRUMENTATION

One of the most vital components for successful *in vivo* fluorescence imaging in the mammalian brain is the microscopic system. Brain tissue is highly scattering to light and contains fluorophores, for example flavoproteins, with spectra which can overlap to a high degree with those of current GINAs. At the same time, the neural activity which is tracked by GINAs unfolds on the order of 1s to 100s of milliseconds, limiting the time-window for photon capture. Fluorescence microscopy including systems based on

one photon (1P) or multiple photons have been developed and optimized to facilitate imaging experiments.

In one photon fluorescence microscopy, a fluorophore is initially bombarded with photons from a relatively high energy excitation light source. After absorption, some of the energy of the photon is lost through non-radiative processes. The fluorophore then emits lower energy photons which can be detected. Visible light employed in 1P microscopy scatters more easily in tissue because mean path length of a photon increases shorter wavelength. This effect limits the depth at which 1P systems are capable of imaging unaided to ∼100 μm. However, charge-coupled device and complementary metal oxide semiconductor detectors which can be used in conjunction with this imaging modality are capable of extremely fast (>kHz) full field image acquisition rates. They are also typically relatively inexpensive when compared with comparable multi-photon alternatives (Helmchen and Denk, 2005).

In addition, 1P imaging light paths can be channeled through endoscopes (Flusberg et al., 2008; Barretto et al., 2011) as well as single and multimode fiber optic cable (Ferezou et al., 2006; Flusberg et al., 2008; Lütcke et al., 2010; Gunaydin et al., 2014) to image cells at depth within brain tissue. These systems can be deployed to image the brains of head-immobilized animals (Akemann et al., 2010) or miniaturized and mounted to a freely moving animal (Ghosh et al., 2011). As a note of caution, the introduction of an endoscope to brain tissue is highly invasive, while fiber-optic techniques generally result in data nearly devoid of fine-scale spatial information (although see, e.g., Ferezou et al., 2006), in which a braided fiber optic cable allowed the acquisition of coarse-grained spatial data).

Multi-photon—and in particular 2P—microscopy has been the workhorse for *in vivo* imaging in the field of systems neuroscience (Denk et al., 1990). This is due primarily to two attractive, intrinsic features of these systems to reduce out of focus emission, light scattering, and phototoxicity. First, in multi-photon microscopy photon absorption varies non-linearly with excitation photon density. For example, this relationship is quadratic in the case of 2P microscopy. As a result, only fluorophores within the focal volume of the excitation light cone are activated. Second, the energy of multiple photons must combine to excite the fluorophore, meaning that lower energy (and thus, less scattering) excitation photons may be used (Denk et al., 1990).

Traditional 2P systems are limited in acquisition speed by the galvanometer mirrors, which give rise to low frame rate (up to 15 Hz at 512 × 512 frame size), but full flexibility of arbitrary scan geometries within a two-dimensional plane. Such geometric patterns can be extended into three dimensions by controlling axial motion with a piezoelectric focusing element, allowing fast, single line scans within this space (Göbel et al., 2007). Alternatively, resonant laser scan mirrors enable very fast scanning of high resolution full field frames (512 × 512 pixels) at 30 fps or higher with 8 kHz scanners (Denk et al., 1990; Helmchen and Denk, 2005; Kerr and Denk, 2008). However, arbitrary scan patterns cannot be accommodated with a resonant mirror.

Imaging depths of ∼500 μm using GINAs have been achieved routinely in 2P imaging while maintaining excellent spatial resolution in intact mammalian preparations (Helmchen and Denk, 2005). This depth has been increased through the use of adaptive optics, regenerative amplifiers (Theer et al., 2003; Mittmann et al., 2011) and three photon microscopy (Ouzounov et al., 2014) to ∼1000 μm, though the imaging depth can be increased up to ∼1600 μm using small molecule dyes (Kobat et al., 2011). Greater depths can be achieved by using a fiber optic light path in conjunction with a piezoelectric driven actuator for raster scanning through the fiber (Helmchen et al., 2001; Flusberg et al., 2005; Sawinski et al., 2009). The relatively slow speed of image acquisition can be addressed through random access scanning of small regions of the volume of a cell or field of cells using acousto-optic devices to control the excitation scan path (Grewe et al., 2010; Katona et al., 2012; Fernández-Alfonso et al., 2014). Alternatively, multiple excitation beams can be multiplexed for near- simultaneous imaging of different spatial patterns (Cheng et al., 2011).

Widefield illumination with multi-photon techniques can be achieved through the use of spatial light patterning techniques such as spatial light modulation (Nikolenko et al., 2008) and the generalized phase contrast method (Palima and Gluckstad, 2008) as well temporal focusing (Oron and Silberberg, 2005; Papagiakoumou et al., 2010). When employed in conjunction, such techniques allow simultaneous excitation of large, 3D volumes. The resultant emission patterns can then be interrogated through a typical widefield microscopic detection apparatus (Papagiakoumou et al., 2010).

As imaging technologies such as these become more developed and widespread, GINAs will become ever more useful. Microscopes which are mountable to an unrestrained animal will allow recordings from animals in more ethologically relevant states. Technologies that produce faster frame rates in 2P imaging will allow denser sampling of neurons within a single recording epoch with current GECIs. These technologies will further be indispensable for constructing accurate recordings of future GEVIs expressed in mammalian systems.

ACQUISITION OF MICROSCOPIC IMAGES

Due to its propensity to scatter light, the skull presents a significant barrier to imaging an intact brain. However, it also serves to dampen pulsations arising from the movement of blood and cerebrospinal fluid through cerebral tissue. As a result, simply removing the cranium above the imaged region is not a common practice in modern GINA imaging. Typically, the skull's impact on image quality is reduced by either thinning the skull above the imaged region(s) (Grutzendler et al., 2002) or by inserting a glass cover slip above a craniotomy (Holtmaat et al., 2009). Both methods stabilize cellular position within brain tissue while allowing high-quality optical access.

Motion artifacts can further complicate imaging acquisition in living animals. Multiple approaches have been devised to reduce motion artifacts, including mechanical changes to the imaged tissue, animal restraint, and online and *post hoc* computational processing for maintaining image stability.

For 2P imaging, head fixation techniques to maintain the animal's position have been used in monkeys (Wurtz, 1968), flies (Dahmen, 1980), and rodents (Komisaruk, 1970). Head

and body restraint allow stable imaging while both stimulus and behavioral response parameters can be tightly controlled. This, in turn, eases the task of quantifying neural activity with respect to these variables (Akemann et al., 2010; Andermann et al., 2010; Huber et al., 2012; Petreanu et al., 2012). Head restraint can be used in conjunction with a spherical (Dombeck et al., 2007) or linear (Marvin et al., 2013) treadmill, which allows the addition of assays which require locomotion on the part of the animal. Animals restrained in this manner can then be presented with passive stimuli (Niell and Stryker, 2010) or virtual sensory environments in which they can exert control over the stimulus via movement of the treadmill (Dombeck et al., 2010).

The microscope objective itself can also be stabilized relative to the imaged specimen via closed-loop designs whereby movement of the animal results in registered movement of the relevant optics. These systems function by detecting and correcting for motion in the axial direction based on general movement of tissue (e.g., Laffray et al., 2011) or by modeling and avoiding (Paukert and Bergles, 2012) or counteracting (Chen et al., 2013a) movement due to specific motion artifacts relevant to the experimental settings.

In addition, a number of algorithms have been developed for motion correction. These algorithms function by appropriately reshaping images in a time series such that consecutive frames are aligned. Algorithms developed for this purpose are based on Hidden Markov Models (Dombeck et al., 2010), cross-correlation based registration (Guizar-Sicairos et al., 2008), or gradient-descent based minimization of image differences (Greenberg and Kerr, 2009). Besides computational approaches, FRET sensors or single FP sensors expressed along with a reference FP can be used to cancel the effects of motion artifact.

IMAGE PROCESSING

Image processing is a necessary step, as signals must be assigned to specific cells or subcellular compartments and described according to their content. A large array of approaches for analyzing and visualizing GINA data has been developed. One of the first questions addressed using such methods was image segmentation (i.e., what parts of the imaged field contain responsive elements) and spike or event detection (i.e., when does the fluorescence contained within these elements change significantly from baseline). Such approaches reduce variability and bias introduced to analysis by methods such as hand drawing of regions of interest (ROIs). Early algorithms developed for spike detection were based on simple thresholding of the $\Delta F/F$ signal [i.e., $(F - F_0)/F_0$ where F is the moment by moment spatially averaged fluorescence data and F_0 is typically defined as a time-averaged, background subtracted baseline fluorescence value] where event detection was triggered by this signal passing above the threshold (e.g., Mao et al., 2001). Later efforts have employed linear deconvolution (Yaksi and Friedrich, 2006; Holekamp, 2008; Vogelstein et al., 2010) or subtraction (Seelig et al., 2010) to detect occurrence of spiking events. These algorithms perform well in systems in which probe response is linear to the input signal. Other methods have used pixel-wise correlation in the fluorescence signal (Ozden et al., 2008), principle components analysis followed by independent components analysis (Mukamel et al., 2009), Monte Carlo spike detection (Vogelstein et al., 2009), and supervised learning algorithms (Valmianski et al., 2010).

As the size of imaging datasets grows ever larger, it becomes increasingly critical to extract salient features within and across populations of cells expressing GINAs, especially correlating the activity of cells to the behavioral output of an animal. Such approaches can correlate the activity of single cells to behavioral data by simple coincidence (Seelig et al., 2010), regression (Miri et al., 2011), or machine-learning based classification schemes (Huber et al., 2012; Petreanu et al., 2012). Additionally, dynamics of entire cell populations can be visualized in low dimensional space by methods based on factor analysis of the dataset (Harvey et al., 2012). Recently, many of the most successful approaches examined above have been integrated into a suite of open source tools optimized for the analysis of large datasets termed "THUNDER" (Freeman et al., 2014) which can be accessed at http://thefreemanlab.com/thunder/. Taken together, the computational approaches for imaging analysis and visualization represent an indispensable set of tools for interpreting the vast quantities of data acquired in the course of GINA-enabled experiments.

RECENT FINDINGS THROUGH GINA TECHNOLOGIES

Genetically encoded indicators of neural activity attributes—particularly genetic specificity and long-term expression—make them excellent tools for circuit interrogation at multiple spatial and temporal scales. They have thus been used in recent years to make fundamental contributions to our understanding of brain function. In addition, several GINA classes have made important strides toward becoming standard tools for various applications in the study of mammalian neural circuitry *in vivo*.

TOPOGRAPHICAL REPRESENTATIONS

Topographical maps are systematic variations in the spatial layout of the response properties of a brain region which reflects the organization of a stimulus space (Hubel and Wiesel, 1959; Felleman and Van Essen, 1991). While electrophysiological techniques have generally been used to develop mesoscopic-scale [order of 100 μm (Knöpfel, 2012)] mappings of brain regions, the application of GINAs in topographic mapping provides single cell spatial resolution. In addition, GINAs make it straightforward to rapidly transition between spatial scales, acquiring data from the cellular or population level or anywhere in between by simply changing image magnification.

The activity of genetically specified elements of a neural circuit can be recorded using GINAs. Topographical mapping of odorant to region of the rodent olfactory bulb has been described using GINAs transgenic animals (e.g., Hasan et al., 2004) or by intrinsic optical signals. Indeed, both techniques report a systematic olfactory map of homologous aliphatic compounds of increasing length (Johnson et al., 1999; Meister and Bonhoeffer, 2001; Fletcher et al., 2009). Only imaging studies with GINA, however, were able to leveraged the genetic specificity of GINAs to discern that the aliphatic odorant map is formed *de novo* within the

postsynaptic circuitry of the olfactory bulb (Bozza et al., 2004; Fletcher et al., 2009).

One of the most powerful aspects of GINAs in studying topographical maps is the ability to allow for imaging cellular activity at spatial scales ranging from subcellular to millimeter, providing researcher to inspect the proverbial forest, individual trees, or both, all while maintaining awareness of current location. For example, a conspicuous lack of correlation between CA1 place cell location and the space they encoded has been demonstrated through cellular resolution imaging of virally driven GCaMP3 (Dombeck et al., 2010). In another recent study, optical recording auditory cortex at different spatial scales has resolved coarse and then cellular scale cortical activity in response to different tones. These results support the existence of a tonotopic axis along primary auditory cortex whose strength had been called into questions by previous studies (Issa et al., 2014).

FUNCTIONAL ORGANIZATION OF NEURAL CIRCUITRY

Local circuits within different cortical regions receive inputs from multiple distant brain regions. These inputs impact ongoing computations within, and thus the output from, local circuitry. In terms of input, a critical question is: what information is conveyed from distal brain regions to the local area? Several recent studies employed GECIs to record calcium transients in distal boutons of, for example cortico-cortical (Petreanu et al., 2012) and medial septal nucleus-hippocampal axons (Kaifosh et al., 2013) to address this question. Such studies have allowed unprecedented access to communication from one brain region to another with both cellular and genetic resolution.

Genetically encoded calcium indicators have also been used in addressing whether response properties of local cells within a region are a function of inputs received from hierarchically lower brain regions, or if those properties arise from local circuit interactions. For example, Glickfeld et al. (2013) demonstrated that the response properties of boutons projected from primary visual cortex in mouse to higher visual areas matched the response properties of cells within each region. This finding stands in contrast to the results from Fletcher et al. (2009) who demonstrated a *de novo* map of olfactory space that arises through local circuit interaction. In each case, GINAs were useful in disambiguating the degree to which local circuit computations result in new response properties.

Taken together, these studies point to the ways in which GINAs aid decoding of communication between brain regions, especially, revealing what message is sent between regions and how that message influences processing within the target structure. As probes of multiple colors become available for *in vivo* use, it will become possible to address such questions within a single experiment.

STABILITY AND PLASTICITY OF NEURAL CIRCUITRY

Neural circuitry is constantly reorganized structurally and functionally in response to experience and other influences on sensory input. Much effort has been dedicated in recent decades to determining under what conditions neural responses to a stimulus remain stable over time (Gerrow and Triller, 2010).

Genetically encoded indicators of neural activity are particularly well suited to the study of how neural responses to stimuli change over time. Because these probes express at roughly constant levels for periods as long as months, identified cells from a single organism can be repeatedly imaged over a long period of time (Mank et al., 2008; Tian et al., 2009; Kuhn et al., 2012; Margolis et al., 2012). As an example, Mank et al. (2008) showed that layer 2/3 cells in primary visual cortex of mice expressing TN-XXL exhibit stable tuning to orientation when imaged over the course of weeks. Another study, in contrast, found that at a cellular level, hippocampal place cell response to place fields is highly variable over a similar period of time. Despite the fact that most cells did not retain consistent mapping with respect to the place fields, at the population level an accurate spatial map was preserved (Ziv et al., 2013).

Genetically encoded calcium indicators has also been used to probe the dynamic changes of neural ensembles in response to learning. For example, it was found that as mice were trained to perform a sensorimotor task, preferred stimuli of individual L2/3 neurons expressing GCaMPs in vibrissal motor cortex shifted over time. At the population level, however, activity became increasingly stereotyped and time-locked to the stimulus and motor outputs (Huber et al., 2012). These results suggest that L2/3 neurons in mice motor cortex integrate sensory input to task-related motor programs.

Finally, sensory deprivation has been shown to result in a rapid rescaling of synaptic weights that act to preserve mean levels of neuronal activity around a homeostatically regulated set point via *in vivo* calcium imaging using GCaMPs.(Turrigiano et al., 1998; Bishop and Zito, 2013). In this study the activity of L2/3 and L5 neurons expressing GCAMP3/5 in primary visual cortex of mice was monitored. It was shown that bilateral retinal lesion resulted in a rapid decrease in population activity, followed by recovery to baseline activity levels over the course of the next 24 h (Bishop and Zito, 2013).

FUTURE PERSPECTIVES

In this review, we have presented a broad overview of the history, current use, and future prospects for the use of GINAs in imaging neural activity in the intact mammalian brain. Through iterative optimization, GINAs—and particularly GECIs—have come to represent an important tool set for systems neuroscientists.

Despite these gains, the power of GINAs in different experimental approaches remains to be fully realized. Of particular importance, optimizing GEVIs to the point that they are widely applicable for *in vivo* imaging is an active area of protein engineering research. Synaptic transmission is another rich area of research that can be better accessed optically through developing novel GINAs that permit probing neurotransmitters, neuropeptides and neuromodulators at the single neuron level as well as at circuit level. For all GINA classes, further development and optimization of color-shifted variants will enhance options for multiplexing optical genetic tools within a single experiment.

The lessons learned and disciplined methods used in optimizing GECIs can be easily adapted for optimizing properties of other GINA classes. As these goals are achieved in the coming years,

expect further fundamental contributions to our understanding of brain function to be derived through the use of GINAs in awake, behaving mammals.

REFERENCES

Ahrens, K. F., Heider, B., Lee, H., Isacoff, E. Y., and Siegel, R. M. (2012). Two-photon scanning microscopy of in vivo sensory responses of cortical neurons genetically encoded with a fluorescent voltage sensor in rat. *Front. Neural Circuits.* 6:15. doi: 10.3389/fncir.2012.00015

Ai, H. W., Baird, M. A., Shen, Y., Davidson, M. W., and Campbell, R. E. (2014). Engineering and characterizing monomeric fluorescent proteins for live-cell imaging applications. *Nat. Protoc.* 9, 910–928. doi: 10.1038/nprot.2014.054

Akemann, W., Mutoh, H., Perron, A., Rossier, J., and Knöpfel, T. (2010). Imaging brain electric signals with genetically targeted voltage-sensitive fluorescent proteins. *Nat. Methods* 7, 643–649. doi: 10.1038/nmeth.1479

Akemann, W., Sasaki, M., Mutoh, H., Imamura, T., Honkura, N., and Knöpfel, T. (2013). Two-photon voltage imaging using a genetically encoded voltage indicator. *Sci. Rep.* 3, 2231. doi: 10.1038/srep02231

Akerboom, J., Carreras Calderón, N., Tian, L., Wabnig, S., Prigge, M., Tolö, J., et al. (2013). Genetically encoded calcium indicators for multi-color neural activity imaging and combination with optogenetics. *Front. Mol. Neurosci.* 6:2. doi: 10.3389/fnmol.2013.00002

Akerboom, J., Chen, T. W., Wardill, T. J., Tian, L., Marvin, J. S., Mutlu, S., et al. (2012). Optimization of a GCaMP calcium indicator for neural activity imaging. *J. Neurosci.* 32, 13819–13840. doi: 10.1523/JNEUROSCI.2601-12.2012

Andermann, M. L., Kerlin, A. M., and Reid, R. C. (2010). Chronic cellular imaging of mouse visual cortex during operant behavior and passive viewing. *Front. Cell. Neurosci.* 4:3. doi: 10.3389/fncel.2010.00003

Aramuni, G., and Griesbeck, O. (2013). Chronic calcium imaging in neuronal development and disease. *Exp. Neurol.* 242, 50–56. doi: 10.1016/j.expneurol.2012.02.008

Aschauer, D. F., Kreuz, S., and Rumpel, S. (2013). Analysis of transduction efficiency, tropism and axonal transport of AAV serotypes 1, 2, 5, 6, 8 and 9 in the mouse brain. *PLoS ONE* 8:e76310. doi: 10.1371/journal.pone.0076310

Ashley, C. C., and Ridgway, E. B. (1968). Ridgway, Simultaneous recording of membrane potential, calcium transient and tension in single muscle fibers. *Nature* 219, 1168–1169. doi: 10.1038/2191168a0

Ataka, K., and Pieribone, V. A. (2002). A genetically targetable fluorescent probe of channel gating with rapid kinetics. *Biophys. J.* 82, 509–516. doi: 10.1016/S0006-3495(02)75415-5

Atasoy, D., Aponte, Y., Su, H. H., and Sternson, S. M. (2008). A FLEX switch targets Channelrhodopsin-2 to multiple cell types for imaging and long-range circuit mapping. *J. Neurosci.* 28, 7025–7030. doi: 10.1523/JNEUROSCI.1954-08.2008

Atkin, S. D., Patel, S., Kocharyan, A., Holtzclaw, L. A., Weerth, S. H., Schram, V., et al. (2009). Transgenic mice expressing a cameleon fluorescent Ca^{2+} indicator in astrocytes and Schwann cells allow study of glial cell Ca^{2+} signals in situ and in vivo. *J. Neurosci. Methods* 181, 212–226. doi: 10.1016/j.jneumeth.2009.05.006

Baird, G. S., Zacharias, D. A., and Tsien, R. Y. (1999). Circular permutation and receptor insertion within green fluorescent proteins. *Proc. Natl. Acad. Sci. U.S.A.* 96, 11241–11246. doi: 10.1073/pnas.96.20.11241

Baker, B. J., Lee, H., Pieribone, V. A., Cohen, L. B., Isacoff, E. Y., Knopfel, T., et al. (2007). Three fluorescent protein voltage sensors exhibit low plasma membrane expression in mammalian cells. *J. Neurosci. Methods* 161, 32–38. doi: 10.1016/j.jneumeth.2006.10.005

Balaji, J., and Ryan, T. A. (2007). Single-vesicle imaging reveals that synaptic vesicle exocytosis and endocytosis are coupled by a single stochastic mode. *Proc. Natl. Acad. Sci. U.S.A.* 104, 20576–20581. doi: 10.1073/pnas.0707574105

Barretto, R. P., Ko, T. H., Jung, J. C., Wang, T. J., Capps, G., Waters, A. C., et al. (2011). Time-lapse imaging of disease progression in deep brain areas using fluorescence microendoscopy. *Nat. Med.* 17, 223–228. doi: 10.1038/nm.2292

Ben Achour, S., Pont-Lezica, L., Béchade, C., and Pascual, O. (2010). Is astrocyte calcium signaling relevant for synaptic plasticity? *Neuron Glia Biol.* 6, 147–155. doi: 10.1017/S1740925X10000207

Bishop, H. I., and Zito, K. (2013). The downs and ups of sensory deprivation: evidence for firing rate homeostasis in vivo. *Neuron* 80, 247–249. doi: 10.1016/j.neuron.2013.10.011

Borrell, V., Yoshimura, Y., and Callaway, E. M. (2005). Targeted gene delivery to telencephalic inhibitory neurons by directional in utero electroporation. *J. Neurosci. Methods* 143, 151–158. doi: 10.1016/j.jneumeth.2004.09.027

Boulin, T., and Hobert, O. (2012). From genes to function: the *C. elegans* genetic toolbox. *Wiley Interdiscip. Rev. Dev. Biol.* 1, 114–137. doi: 10.1002/wdev.1

Bovetti, S., Moretti, C., and Fellin, T. (2014). Mapping brain circuit function *in vivo* using two-photon fluorescence microscopy. *Microsc. Res. Tech.* 77, 492–501. doi: 10.1002/jemt.22342

Bozza, T., McGann, J. P., Mombaerts, P., and Wachowiak, M. (2004). In vivo imaging of neuronal activity by targeted expression of a genetically encoded probe in the mouse. *Neuron* 42, 9–21. doi: 10.1016/S0896-6273(04)00144-8

Burger, C., Gorbatyuk, O. S., Velardo, M. J., Peden, C. S., Williams, P., Zolotukhin, S., et al. (2004). Recombinant AAV viral vectors pseudotyped with viral capsids from serotypes 1, 2, and 5 display differential efficiency and cell tropism after delivery to different regions of the central nervous system. *Mol. Ther.* 10, 302–317. doi: 10.1016/j.ymthe.2004.05.024

Buzsaki, G. (2004). Large-scale recording of neuronal ensembles. *Nat. Neurosci.* 7, 446–451. doi: 10.1038/nn1233

Cao, G., Platisa, J., Pieribone, V. A., Raccuglia, D., Kunst, M., and Nitabach, M. N. (2013). Genetically targeted optical electrophysiology in intact neural circuits. *Cell* 154, 904–913. doi: 10.1016/j.cell.2013.07.027

Cearley, C. N., and Wolfe, J. H. (2006). Transduction characteristics of adeno-associated virus vectors expressing cap serotypes 7, 8, 9, and Rh10 in the mouse brain. *Mol. Ther.* 13, 528–537. doi: 10.1016/j.ymthe.2005.11.015

Chen, J. L., Pfäffli, O. A., Voigt, F. F., Margolis, D. J., and Helmchen, F. (2013a). Online correction of licking-induced brain motion during two-photon imaging with a tunable lens. *J. Physiol.* 591(Pt 19), 4689–4698. doi: 10.1113/jphysiol.2013.259804

Chen, T. W., Wardill, T. J., Sun, Y., Pulver, S. R., Renninger, S. L., Baohan, A., et al. (2013b). Ultrasensitive fluorescent proteins for imaging neuronal activity. *Nature* 499, 295–300. doi: 10.1038/nature12354

Cheng, A., Gonçalves, J. T., Golshani, P., Arisaka, K., and Portera-Cailliau, C. (2011). Simultaneous two-photon calcium imaging at different depths with spatiotemporal multiplexing. *Nat. Methods* 8, 139–142. doi: 10.1038/nmeth.1552

Crochet, S., Poulet, J. F., Kremer, Y., and Petersen, C. C. (2011). Synaptic mechanisms underlying sparse coding of active touch. *Neuron* 69, 1160–1175. doi: 10.1016/j.neuron.2011.02.022

Cui, G., Jun, S. B., Jin, X., Pham, M. D., Vogel, S. S., Lovinger, D. M., et al. (2013). Concurrent activation of striatal direct and indirect pathways during action initiation. *Nature* 494, 238–242. doi: 10.1038/nature11846

Dahmen, H. J. (1980). A simple apparatus to investigate the orientation of walking insects. *Experientia* 36, 685–687. doi: 10.1007/BF01970140

Denk, W., Strickler, J. H., and Webb, W. W. (1990). Two-photon laser scanning fluorescence microscopy. *Science* 248, 73–76. doi: 10.1126/science.2321027

Díez-García, J., Matsushita, S., Mutoh, H., Nakai, J., Ohkura, M., Yokoyama, J., et al. (2005). Activation of cerebellar parallel fibers monitored in transgenic mice expressing a fluorescent Ca^{2+} indicator protein. *Eur. J. Neurosci.* 22, 627–635. doi: 10.1111/j.1460-9568.2005.04250.x

Dimitrov, D., He, Y., Mutoh, H., Baker, B. J., Cohen, L., Akemann, W., et al. (2007). Engineering and characterization of an enhanced fluorescent protein voltage sensor. *PLoS ONE* 2:e440. doi: 10.1371/journal.pone.0000440

Ding, J., Luo, A. F., Hu, L., Wang, D., and Shao, F. (2014). Structural basis of the ultrasensitive calcium indicator GCaMP6. *Sci. China Life Sci.* 57, 269–274. doi: 10.1007/s11427-013-4599-5

Ding, S. (2013). *In vivo* astrocytic Ca^{2+} signaling in health and brain disorders. *Future Neurol.* 8, 529–554. doi: 10.2217/fnl.13.38

Dombeck, D. A., Harvey, C. D., Tian, L., Looger, L. L., and Tank, D. W. (2010). Functional imaging of hippocampal place cells at cellular resolution during virtual navigation. *Nat. Neurosci.* 13, 1433–1440. doi: 10.1038/nn.2648

Dombeck, D. A., Khabbaz, A. N., Collman, F., Adelman, T. L., and Tank, D. W. (2007). Imaging large-scale neural activity with cellular resolution in awake, mobile mice. *Neuron* 56, 43–57. doi: 10.1016/j.neuron.2007.08.003

Felleman, D. J., and Van Essen, D. C. (1991). Distributed hierarchical processing in the primate cerebral cortex. *Cereb. Cortex* 1, 1–47. doi: 10.1093/cercor/1.1.1

Fenno, L. E., Mattis, J., Ramakrishnan, C., Hyun, M., Lee, S. Y., He, M., et al. (2014). Targeting cells with single vectors using multiple-feature Boolean logic. *Nat. Methods* 11, 763–772. doi: 10.1038/nmeth.2996

Ferezou, I., Bolea, S., and Petersen, C. C. (2006). Visualizing the cortical representation of whisker touch: voltage-sensitive dye imaging in freely moving mice. *Neuron* 50, 617–629. doi: 10.1016/j.neuron.2006.03.043

Fernández-Alfonso, T., Nadella, K. M., Iacaruso, M. F., Pichler, B., Roš, H., Kirkby, P. A., et al. (2014). Monitoring synaptic and neuronal activity in 3D with synthetic and genetic indicators using a compact acousto-optic lens two-photon microscope. *J. Neurosci. Methods* 222, 69–81. doi: 10.1016/j.jneumeth.2013.10.021

Fletcher, M. L., Masurkar, A. V., Xing, J., Imamura, F., Xiong, W., Nagayama, S., et al. (2009). Optical imaging of postsynaptic odor representation in the glomerular layer of the mouse olfactory bulb. *J. Neurophysiol.* 102, 817–830. doi: 10.1152/jn.00020.2009

Flusberg, B. A., Cocker, E. D., Piyawattanametha, W., Jung, J. C., Cheung, E. L., and Schnitzer, M. J. (2005). Fiber-optic fluorescence imaging. *Nat. Methods* 2, 941–950. doi: 10.1038/nmeth820

Flusberg, B. A., Nimmerjahn, A., Cocker, E. D., Mukamel, E. A., Barretto, R. P., Ko, T. H., et al. (2008). High-speed, miniaturized fluorescence microscopy in freely moving mice. *Nat. Methods* 5, 935–938. doi: 10.1038/nmeth.1256

Freeman, J., Vladimirov, N., Kawashima, T., Mu, Y., Sofroniew, N, J., Bennett, D. V., et al. (2014). Mapping brain activity at scale with cluster computing. *Nat. Methods* 11, 941–950. doi: 10.1038/nmeth.3041

Gerrow, K., and Triller, A. (2010). Synaptic stability and plasticity in a floating world. *Curr. Opin. Neurobiol.* 20, 631–639. doi: 10.1016/j.conb.2010.06.010

Ghosh, K. K., Burns, L. D., Cocker, E. D., Nimmerjahn, A., Ziv, Y., Gamal, A. E., et al. (2011). Miniaturized integration of a fluorescence microscope. *Nat. Methods* 8, 871–878. doi: 10.1038/nmeth.1694

Glickfeld, L. L., Andermann, M. L., Bonin, V., and Reid, R. C. (2013). Cortico-cortical projections in mouse visual cortex are functionally target specific. *Nat. Neurosci.* 16, 219–226. doi: 10.1038/nn.3300

Göbel, W., Kampa, B. M., and Helmchen, F. (2007). Imaging cellular network dynamics in three dimensions using fast 3D laser scanning. *Nat. Methods* 4, 73–79. doi: 10.1038/nmeth989

Gong, Y., Li, J. Z., and Schnitzer, M. J. (2013). Enhanced archaerhodopsin fluorescent protein voltage indicators. *PLoS ONE* 8:e66959. doi: 10.1371/journal.pone.0066959

Gong, Y., Wagner, M. J., Li, J. Z., and Schnitzer, M. J. (2014). Imaging neural spiking in brain tissue using FRET-opsin protein voltage sensors. *Nat. Commun.* 5, 3674. doi: 10.1038/ncomms4674

Gossen, M., and Bujard, H. (1992). Tight control of gene expression in mammalian cells by tetracycline-responsive promoters. *Proc. Natl. Acad. Sci. U.S.A.* 89, 5547–5551. doi: 10.1073/pnas.89.12.5547

Granseth, B., Odermatt, B., Royle, S. J., and Lagnado, L. (2006). Clathrin-mediated endocytosis is the dominant mechanism of vesicle retrieval at hippocampal synapses. *Neuron* 51, 773–786. doi: 10.1016/j.neuron.2006.08.029

Greenberg, D. S., and Kerr, J. N. (2009). Automated correction of fast motion artifacts for two-photon imaging of awake animals. *J. Neurosci. Methods* 176, 1–15. doi: 10.1016/j.jneumeth.2008.08.020

Grewe, B. F., Langer, D., Kasper, H., Kampa, B. M., and Helmchen, F. (2010). High-speed in vivo calcium imaging reveals neuronal network activity with near-millisecond precision. *Nat. Methods* 7, 399–405. doi: 10.1038/nmeth.1453

Grieger, J., and Samulski, R. (2005). "Adeno-associated virus as a gene therapy vector: vector development, production and clinical applications," in *Gene Therapy and Gene Delivery Systems,* eds D. Schaffer and W. Zhou (Heidelberg: Springer), 119–145.

Grutzendler, J., Kasthuri, N., and Gan, W. B. (2002). Long-term dendritic spine stability in the adult cortex. *Nature* 420, 812–816. doi: 10.1038/nature01276

Guizar-Sicairos, M., Thurman, S. T., and Fienup, J. R. (2008). Efficient subpixel image registration algorithms. *Opt. Lett.* 33, 156–158. doi: 10.1364/OL.33.000156

Gunaydin, L. A., Grosenick, L., Finkelstein, J. C., Kauvar, I. V., Fenno, L. E., Adhikari, A., et al. (2014). Natural neural projection dynamics underlying social behavior. *Cell* 157, 1535–1551. doi: 10.1016/j.cell.2014.05.017

Harvey, C. D., Coen, P., and Tank, D. W. (2012). Choice-specific sequences in parietal cortex during a virtual-navigation decision task. *Nature* 484, 62–68. doi: 10.1038/nature10918

Hasan, M. T., Friedrich, R. W., Euler, T., Larkum, M. E., Giese, G., Both, M., et al. (2004). Functional fluorescent Ca^{2+} indicator proteins in transgenic mice under TET control. *PLoS Biol.* 2:e163. doi: 10.1371/journal.pbio.0020163

Haustein, M. D., Kracun, S., Lu, X. H., Shih, T., Jackson-Weaver, O., Tong, X., et al. (2014). Conditions and constraints for astrocyte calcium signaling in the hippocampal mossy fiber pathway. *Neuron* 82, 413–429. doi: 10.1016/j.neuron.2014.02.041

Heider, B., Nathanson, J. L., Isacoff, E. Y., Callaway, E. M., and Siegel, R. M. (2010). Two-photon imaging of calcium in virally transfected striate cortical neurons of behaving monkey. *PLoS ONE* 5:e13829. doi: 10.1371/journal.pone.0013829

Helmchen, F., and Denk, W. (2005). Deep tissue two-photon microscopy. *Nat. Methods* 2, 932–940. doi: 10.1038/nmeth818

Helmchen, F., Fee, M. S., Tank, D. W., and Denk, W. (2001). A miniature head-mounted two-photon microscope. High-resolution brain imaging in freely moving animals. *Neuron* 31, 903–912. doi: 10.1016/S0896-6273(01)00421-4

Helmchen, F., Imoto, K., and Sakmann, B. (1996). Ca^{2+} buffering and action potential-evoked Ca^{2+} signaling in dendrites of pyramidal neurons. *Biophys. J.* 70, 1069–1081. doi: 10.1016/S0006-3495(96)79653-4

Higashijima, S., Masino, M. A., Mandel, G., and Fetcho, J. R. (2003). Imaging neuronal activity during zebrafish behavior with a genetically encoded calcium indicator. *J. Neurophysiol.* 90, 3986–3997. doi: 10.1152/jn.00576.2003

Hille, B. (2001). *Ion Channels of Excitable Membranes,* 3rd Edn. Sunderland, MA: Sinauer Associates Inc.

Hires, S. A., Zhu, Y., and Tsien, R. Y. (2008). Optical measurement of synaptic glutamate spillover and reuptake by linker optimized glutamate-sensitive fluorescent reporters. *Proc. Natl. Acad. Sci. U.S.A.* 105, 4411–4416. doi: 10.1073/pnas.0712008105

Holekamp, T. F. (2008). *A Novel High-Speed Sectioning Fluorescence Microscope Reveals Patterned Neural Responses to Pheromones*, Ph.D. thesis Program in Neurosciences, Washington University, Washington.

Holtmaat, A., Bonhoeffer, T., Chow, D. K., Chuckowree, J., De Paola, V., Hofer, S. B., et al. (2009). Long-term, high-resolution imaging in the mouse neocortex through a chronic cranial window. *Nat. Protoc.* 4, 1128–1144. doi: 10.1038/nprot.2009.89

Hoogland, T. M., Kuhn, B., Göbel, W., Huang, W., Nakai, J., Helmchen, F., et al. (2009). Radially expanding transglial calcium waves in the intact cerebellum. *Proc. Natl. Acad. Sci. U.S.A.* 106, 3496–3501. doi: 10.1073/pnas.0809269106

Horikawa, K., Yamada, Y., Matsuda, T., Kobayashi, K., Hashimoto, M., Matsuura, T., et al. (2010). Spontaneous network activity visualized by ultrasensitive Ca^{2+} indicators, yellow Cameleon-Nano. *Nat. Methods* 7, 729–732. doi: 10.1038/nmeth.1488

Hubel, D. H., and Wiesel, T. N. (1959). Receptive fields of single neurones in the cat's striate cortex. *J. Physiol.* 148, 574–591.

Huber, D., Gutnisky, D. A., Peron, S., O'Connor, D. H., Wiegert, J. S., Tian, L., et al. (2012). Multiple dynamic representations in the motor cortex during sensorimotor learning. *Nature* 484, 473–478. doi: 10.1038/nature11039

Ibraheem, A., and Campbell, R. E. (2010). Designs and applications of fluorescent protein-based biosensors. *Curr. Opin. Chem. Biol.* 14, 30–36. doi: 10.1016/j.cbpa.2009.09.033

Issa, J. B., Haeffele, B. D., Agarwal, A., Bergles, D. E., Young, E. D., and Yue, D. T. (2014). Multiscale optical Ca^{2+} imaging of tonal organization in mouse auditory cortex. *Neuron* 83, 944–959. doi: 10.1016/j.neuron.2014.07.009

Jin, L., Han, Z., Platisa, J., Wooltorton, J. R., Cohen, L. B., and Pieribone, V. A. (2012). Single action potentials and subthreshold electrical events imaged in neurons with a fluorescent protein voltage probe. *Neuron* 75, 779–785. doi: 10.1016/j.neuron.2012.06.040

Johnson, B. A., Woo, C. C., Hingco, E. E., Pham, K. L., and Leon, M. (1999). Multidimensional chemotopic responses to n-aliphatic acid odorants in the rat olfactory bulb. *J. Comp. Neurol.* 409, 529–548. doi: 10.1002/(SICI)1096-9861(19990712)409:4<529::AID-CNE2>3.0.CO;2-N

Joung, J. K., and Sander, J. D. (2013). TALENs: a widely applicable technology for targeted genome editing. *Nat. Rev. Mol. Cell Biol.* 14, 49–55. doi: 10.1038/nrm3486

Kaifosh, P., Lovett-Barron, M., Turi, G. F., Reardon, T. R., and Losonczy, A. (2013). Septo-hippocampal GABAergic signaling across multiple modalities in awake mice. *Nat. Neurosci.* 16, 1182–1184. doi: 10.1038/nn.3482

Katona, G., Szalay, G., Maák, P., Kaszás, A., Veress, M., Hillier, D., et al. (2012). Fast two-photon in vivo imaging with three-dimensional random-access scanning in large tissue volumes. *Nat. Methods* 9, 201–208. doi: 10.1038/nmeth.1851

Kerr, J. N., and Denk, W. (2008). Imaging in vivo: watching the brain in action. *Nat. Rev. Neurosci.* 9, 195–205. doi: 10.1038/nrn2338

Kerr, R., Lev-Ram, V., Baird, G., Vincent, P., Tsien, R. Y., and Schafer, W. R. (2000). Optical imaging of calcium transients in neurons and pharyngeal muscle of *C. elegans*. *Neuron* 26, 583–594. doi: 10.1016/S0896-6273(00)81196-4

Knöpfel, T. (2012). Genetically encoded optical indicators for the analysis of neuronal circuits. *Nat. Rev. Neurosci.* 13, 687–700. doi: 10.1038/nrn3293

Kobat, D., Horton, N. G., and Xu, C. (2011). In vivo two-photon microscopy to 1.6-mm depth in mouse cortex. *J. Biomed. Opt.* 16, 106014. doi: 10.1117/1.3646209

Koester, H. J., and Sakmann, B. (2000). Calcium dynamics associated with action potentials in single nerve terminals of pyramidal cells in layer 2/3 of the young rat neocortex. *J. Physiol.* 529(Pt 3), 625–646. doi: 10.1111/j.1469-7793.2000.00625.x

Komisaruk, B. R. (1970). Synchrony between limbic system theta activity and rhythmical behavior in rats. *J. Comp. Physiol. Psychol.* 70, 482–492. doi: 10.1037/h0028709

Kralj, J. M., Douglass, A. D., Hochbaum, D. R., Maclaurin, D., and Cohen, A. E. (2012). Optical recording of action potentials in mammalian neurons using a microbial rhodopsin. *Nat. Methods* 9, 90–95. doi: 10.1038/nmeth.1782

Kralj, J. M., Hochbaum, D. R., Douglass, A. D., and Cohen, A. E. (2011). Electrical spiking in *Escherichia coli* probed with a fluorescent voltage-indicating protein. *Science* 333, 345–348. doi: 10.1126/science.1204763

Kuhn, B., Ozden, I., Lampi, Y., Hasan, M. T., and Wang, S. S. (2012). An amplified promoter system for targeted expression of calcium indicator proteins in the cerebellar cortex. *Front. Neural Circuits* 6:49. doi: 10.3389/fncir.2012.00049

Laffray, S., Pagès, S., Dufour, H., De Koninck, P., De Koninck, Y., and Côté, D. (2011). Adaptive movement compensation for in vivo imaging of fast cellular dynamics within a moving tissue. *PLoS ONE* 6:e19928. doi: 10.1371/journal.pone.0019928

Li, H., Foss, S. M., Dobryy, Y. L., Park, C. K., Hires, S. A., Shaner, N. C., et al. (2011). Concurrent imaging of synaptic vesicle recycling and calcium dynamics. *Front. Mol. Neurosci.* 4:34. doi: 10.3389/fnmol.2011.00034

Li, Y., and Tsien, R. W. (2012). pHTomato, a red, genetically encoded indicator that enables multiplex interrogation of synaptic activity. *Nat. Neurosci.* 15, 1047–1053. doi: 10.1038/nn.3126

Liu, B. H., Li, P., Li, Y. T., Sun, Y. J., Yanagawa, Y., Obata, K., et al. (2009). Visual receptive field structure of cortical inhibitory neurons revealed by two-photon imaging guided recording. *J. Neurosci.* 29, 10520–10532. doi: 10.1523/JNEUROSCI.1915-09.2009

Looger, L. L., and Griesbeck, O. (2012). Genetically encoded neural activity indicators. *Curr. Opin. Neurobiol.* 22, 18–23. doi: 10.1016/j.conb.2011.10.024

Lundby, A., Mutoh, H., Dimitrov, D., Akemann, W., and Knöpfel, T. (2008). Engineering of a genetically encodable fluorescent voltage sensor exploiting fast Ci-VSP voltage-sensing movements. *PLoS ONE* 3:e2514. doi: 10.1371/journal.pone.0002514

Lütcke, H., Murayama, M., Hahn, T., Margolis, D. J., Astori, S., Zum Alten Borgloh, S. M., et al. (2010). Optical recording of neuronal activity with a genetically-encoded calcium indicator in anesthetized and freely moving mice. *Front. Neural Circuits* 4:9. doi: 10.3389/fncir.2010.00009

Mali, P., Esvelt, K. M., and Church, G. M. (2013). Cas9 as a versatile tool for engineering biology. *Nat. Methods* 10, 957–963. doi: 10.1038/nmeth.2649

Mank, M., Reiff, D. F., Heim, N., Friedrich, M. W., Borst, A., and Griesbeck, O. (2006). A FRET-based calcium biosensor with fast signal kinetics and high fluorescence change. *Biophys. J.* 90, 1790–1796. doi: 10.1529/biophysj.105.073536

Mank, M., Santos, A. F., Direnberger, S., Mrsic-Flogel, T. D., Hofer, S. B., Stein, V., et al. (2008). A genetically encoded calcium indicator for chronic in vivo two-photon imaging. *Nat. Methods* 5, 805–811. doi: 10.1038/nmeth.1243

Mante, V., Sussillo, D., Shenoy, K. V., and Newsome, W. T. (2013). Context-dependent computation by recurrent dynamics in prefrontal cortex. *Nature* 503, 78–84. doi: 10.1038/nature12742

Mao, B. Q., Hamzei-Sichani, F., Aronov, D., Froemke, R. C., and Yuste, R. (2001). Dynamics of spontaneous activity in neocortical slices. *Neuron* 32, 883–898. doi: 10.1016/S0896-6273(01)00518-9

Margolis, D. J., Lütcke, H., Schulz, K., Haiss, F., Weber, B., Kügler, S., et al. (2012). Reorganization of cortical population activity imaged throughout long-term sensory deprivation. *Nat. Neurosci.* 15, 1539–1546. doi: 10.1038/nn.3240

Marvin, J. S., Borghuis, B. G., Tian, L., Cichon, J., Harnett, M. T., Akerboom, J., et al. (2013). An optimized fluorescent probe for visualizing glutamate neurotransmission. *Nat. Methods* 10, 162–170. doi: 10.1038/nmeth.2333

Meister, M., and Bonhoeffer, T. (2001). Tuning and topography in an odor map on the rat olfactory bulb. *J. Neurosci.* 21, 1351–1360.

Miesenbock, G., De Angelis, D. A., and Rothman, J. E. (1998). Visualizing secretion and synaptic transmission with pH-sensitive green fluorescent proteins. *Nature* 394, 192–195. doi: 10.1038/28190

Miri, A., Daie, K., Arrenberg, A. B., Baier, H., Aksay, E., and Tank, D. W. (2011). Spatial gradients and multidimensional dynamics in a neural integrator circuit. *Nat. Neurosci.* 14, 1150–1159. doi: 10.1038/nn.2888

Mittmann, W., Wallace, D. J., Czubayko, U., Herb, J. T., Schaefer, A. T., Looger, L. L., et al. (2011). Two-photon calcium imaging of evoked activity from L5 somatosensory neurons in vivo. *Nat. Neurosci.* 14, 1089–1093. doi: 10.1038/nn.2879

Miyawaki, A. (2011). Development of probes for cellular functions using fluorescent proteins and fluorescence resonance energy transfer. *Annu. Rev. Biochem.* 80, 357–373. doi: 10.1146/annurev-biochem-072909-094736

Miyawaki, A., Griesbeck, O., Heim, R., and Tsien, R. Y. (1999). Dynamic and quantitative Ca^{2+} measurements using improved cameleons. *Proc. Natl. Acad. Sci. U.S.A.* 96, 2135–2140. doi: 10.1073/pnas.96.5.2135

Miyawaki, A., Llopis, J., Heim, R., McCaffery, J. M., Adams, J. A., Ikura, M., et al. (1997). Fluorescent indicators for Ca^{2+} based on green fluorescent proteins and calmodulin. *Nature* 388, 882–887. doi: 10.1038/42264

Mohamed, T. M., Abou-Leisa, R., Baudoin, F., Stafford, N., Neyses, L., Cartwright, E. J., et al. (2013). Development and characterization of a novel fluorescent indicator protein PMCA4-GCaMP2 in cardiomyocytes. *J. Mol. Cell. Cardiol.* 63, 57–68. doi: 10.1016/j.yjmcc.2013.07.007

Mukamel, E. A., Nimmerjahn, A., and Schnitzer, M. J. (2009). Automated analysis of cellular signals from large-scale calcium imaging data. *Neuron* 63, 747–760. doi: 10.1016/j.neuron.2009.08.009

Murata, Y., Iwasaki, H., Sasaki, M., Inaba, K., and Okamura, Y. (2005). Phosphoinositide phosphatase activity coupled to an intrinsic voltage sensor. *Nature* 435, 1239–1243. doi: 10.1038/nature03650

Muto, A., Ohkura, M., Abe, G., Nakai, J., and Kawakami, K. (2013). Real-time visualization of neuronal activity during perception. *Curr. Biol.* 23, 307–311. doi: 10.1016/j.cub.2012.12.040

Muto, A., Ohkura, M., Kotani, T., Higashijima, S., Nakai, J., and Kawakami, K. (2011). Genetic visualization with an improved GCaMP calcium indicator reveals spatiotemporal activation of the spinal motor neurons in zebrafish. *Proc. Natl. Acad. Sci. U.S.A.* 108, 5425–5430. doi: 10.1073/pnas.1000887108

Nagai, T., Sawano, A., Park, E. S., and Miyawaki, A. (2001). Circularly permuted green fluorescent proteins engineered to sense Ca^{2+}. *Proc. Natl. Acad. Sci. U.S.A.* 98, 3197–3202. doi: 10.1073/pnas.051636098

Nagai, T., Yamada, S., Tominaga, T., Ichikawa, M., and Miyawaki, A. (2004). Expanded dynamic range of fluorescent indicators for Ca^{2+} by circularly permuted yellow fluorescent proteins. *Proc. Natl. Acad. Sci. U.S.A.* 101, 10554–10559. doi: 10.1073/pnas.0400417101

Nakai, J., Ohkura, M., and Imoto, K. (2001). A high signal-to-noise Ca^{2+} probe composed of a single green fluorescent protein. *Nat. Biotechnol.* 19, 137–141. doi: 10.1038/84397

Niell, C. M., and Stryker, M. P. (2010). Modulation of visual responses by behavioral state in mouse visual cortex. *Neuron* 65, 472–479. doi: 10.1016/j.neuron.2010.01.033

Nikolenko, V., Watson, B. O., Araya, R., Woodruff, A., Peterka, D. S., and Yuste, R. (2008). SLM microscopy: scanless two-photon imaging and photostimulation with spatial light modulators. *Front. Neural Circuits* 2:5. doi: 10.3389/neuro.04.005.2008

Ohkura, M., Matsuzaki, M., Kasai, H., Imoto, K., and Nakai, J. (2005). Genetically encoded bright Ca^{2+} probe applicable for dynamic Ca^{2+} imaging of dendritic spines. *Anal. Chem.* 77, 5861–5869. doi: 10.1021/ac0506837

Ohkura, M., Sasaki, T., Sadakari, J., Gengyo-Ando, K., Kagawa-Nagamura, Y., Kobayashi, C., et al. (2012). Genetically encoded green fluorescent Ca^{2+} indicators with improved detectability for neuronal Ca^{2+} Signals. *PLoS ONE* 7:e51286. doi: 10.1371/journal.pone.0051286

Okumoto, S., Looger, L. L., Micheva, K. D., Reimer, R. J., Smith, S. J., and Frommer, W. B. (2005). Detection of glutamate release from neurons by genetically encoded surface-displayed FRET nanosensors. *Proc. Natl. Acad. Sci. U.S.A.* 102, 8740–8745. doi: 10.1073/pnas.0503274102

Oron, D., and Silberberg, Y. (2005). Spatiotemporal coherent control using shaped, temporally focused pulses. *Opt. Express* 13, 9903–9908. doi: 10.1364/OPEX.13.009903

Ouzounov, D. G., Horton, N., Wang, T., Feng, D., Nishimura, N., and Xu, C. (2014). "In vivo three-photon calcium imaging of brain activity from layer 6 neurons in mouse brain," in *CLEO, Postdeadline Paper Digest* (San Jose, CA: Optical Society of America). doi: 10.1364/CLEO_SI.2014.STh5C.2

Ozden, I., Lee, H. M., Sullivan, M. R., and Wang, S. S. (2008). Identification and clustering of event patterns from in vivo multiphoton optical recordings of neuronal ensembles. *J. Neurophysiol.* 100, 495–503. doi: 10.1152/jn.01310.2007

Packer, A. M., Roska, B., and Hausser, M. (2013). Targeting neurons and photons for optogenetics. *Nat. Neurosci.* 16, 805–815. doi: 10.1038/nn.3427

Palima, D., and Gluckstad, J. (2008). Comparison of generalized phase contrast and computer generated holography for laser image projection. *Opt. Express* 16, 5338–5349. doi: 10.1364/OE.16.005338

Palmer, A. E., Giacomello, M., Kortemme, T., Hires, S. A., Lev-Ram, V., Baker, D., et al. (2006). Ca^{2+} indicators based on computationally redesigned calmodulin-peptide pairs. *Chem. Biol.* 13, 521–530. doi: 10.1016/j.chembiol.2006.03.007

Palmer, A. E., Qin, Y., Park, J. G., and McCombs, J. E. (2011). Design and application of genetically encoded biosensors. *Trends Biotechnol.* 29, 144–152. doi: 10.1016/j.tibtech.2010.12.004

Papagiakoumou, E., Anselmi, F., Bègue, A., de Sars, V., Glückstad, J., Isacoff, E. Y., et al. (2010). Scanless two-photon excitation of channelrhodopsin-2. *Nat. Methods* 7, 848–854. doi: 10.1038/nmeth.1505

Paukert, M., and Bergles, D. E. (2012). Reduction of motion artifacts during in vivo two-photon imaging of brain through heartbeat triggered scanning. *J. Physiol.* 590(Pt 13), 2955–2963. doi: 10.1113/jphysiol.2012.228114

Perea, G., and Araque, A. (2005). Glial calcium signaling and neuron-glia communication. *Cell Calcium* 38, 375–382. doi: 10.1016/j.ceca.2005.06.015

Perron, A., Mutoh, H., Launey, T., and Knöpfel, T. (2009). Red-shifted voltage-sensitive fluorescent proteins. *Chem. Biol.* 16, 1268–1277. doi: 10.1016/j.chembiol.2009.11.014

Peterka, D. S., Takahashi, H., and Yuste, R. (2011). Imaging voltage in neurons. *Neuron* 69, 9–21. doi: 10.1016/j.neuron.2010.12.010

Petreanu, L., Gutnisky, D. A., Huber, D., Xu, N. L., O'Connor, D. H., Tian, L., et al. (2012). Activity in motor-sensory projections reveals distributed coding in somatosensation. *Nature* 489, 299–303. doi: 10.1038/nature11321

Polikov, V. S., Tresco, P. A., and Reichert, W. M. (2005). Response of brain tissue to chronically implanted neural electrodes. *J. Neurosci. Methods* 148, 1–18. doi: 10.1016/j.jneumeth.2005.08.015

Reid, R. C., Victor, J. D., and Shapley, R. M. (1997). The use of m-sequences in the analysis of visual neurons: linear receptive field properties. *Vis. Neurosci.* 14, 1015–1027. doi: 10.1017/S0952523800011743

Romoser, V. A., Hinkle, P. M., and Persechini, A. (1997). Detection in living cells of Ca^{2+}-dependent changes in the fluorescence emission of an indicator composed of two green fluorescent protein variants linked by a calmodulin-binding sequence. A new class of fluorescent indicators. *J. Biol. Chem.* 272, 13270–13274. doi: 10.1074/jbc.272.20.13270

Sakai, R., Repunte-Canonigo, V., Raj, C. D., and Knöpfel, T. (2001). Design and characterization of a DNA-encoded, voltage-sensitive fluorescent protein. *Eur. J. Neurosci.* 13, 2314–2318. doi: 10.1046/j.0953-816x.2001.01617.x

Sawinski, J., Wallace, D. J., Greenberg, D. S., Grossmann, S., Denk, W., and Kerr, J. N. (2009). Visually evoked activity in cortical cells imaged in freely moving animals. *Proc. Natl. Acad. Sci. U.S.A.* 106, 19557–19562. doi: 10.1073/pnas.0903680106

Seelig, J. D., Chiappe, M. E., Lott, G. K., Dutta, A., Osborne, J. E., Reiser, M. B., et al. (2010). Two-photon calcium imaging from head-fixed *Drosophila* during optomotor walking behavior. *Nat. Methods* 7, 535–540. doi: 10.1038/nmeth.1468

Shimomura, O., Johnson, F. H., and Saiga, Y. (1962). Extraction, purification and properties of aequorin, a bioluminescent protein from the luminous hydromedusan, *Aequorea*. *J. Cell. Comp. Physiol.* 59, 223–239. doi: 10.1002/jcp.1030590302

Siegel, M. S., and Isacoff, E. Y. (1997). A genetically encoded optical probe of membrane voltage. *Neuron* 19, 735–741. doi: 10.1016/S0896-6273(00)80955-1

Singer, J. H., and Diamond, J. S. (2006). Vesicle depletion and synaptic depression at a mammalian ribbon synapse. *J. Neurophysiol.* 95, 3191–3198. doi: 10.1152/jn.01309.2005

Souslova, E. A., Belousov, V. V., Lock, J. G., Strömblad, S., Kasparov, S., Bolshakov, A. P., et al. (2007). Single fluorescent protein-based Ca^{2+} sensors with increased dynamic range. *BMC Biotechnol.* 7:37. doi: 10.1186/1472-6750-7-37

Stosiek, C., Garaschuk, O., Holthoff, K., and Konnerth, A. (2003). In vivo two-photon calcium imaging of neuronal networks. *Proc. Natl. Acad. Sci. U.S.A.* 100, 7319–7324. doi: 10.1073/pnas.1232232100

St-Pierre, F., Marshall, J. D., Yang, Y., Gong, Y., Schnitzer, M. J., and Lin, M. Z. (2014). High-fidelity optical reporting of neuronal electrical activity with an ultrafast fluorescent voltage sensor. *Nat. Neurosci.* 17, 884–889. doi: 10.1038/nn.3709

Sun, X. R., Badura, A., Pacheco, D. A., Lynch, L. A., Schneider, E. R., Taylor, M. P., et al. (2013). Fast GCaMPs for improved tracking of neuronal activity. *Nat. Commun.* 4, 2170. doi: 10.1038/ncomms3170

Tabata, H., and Nakajima, K. (2001). Efficient in utero gene transfer system to the developing mouse brain using electroporation: visualization of neuronal migration in the developing cortex. *Neuroscience* 103, 865–872. doi: 10.1016/S0306-4522(01)00016-1

Tallini, Y. N., Ohkura, M., Choi, B. R., Ji, G., Imoto, K., Doran, R., et al. (2006). Imaging cellular signals in the heart in vivo: cardiac expression of the high-signal Ca^{2+} indicator GCaMP2. *Proc. Natl. Acad. Sci. U.S.A.* 103, 4753–4758. doi: 10.1073/pnas.0509378103

Tank, D. W., Sugimori, M., Connor, J. A., and Llinás, R. R. (1988). Spatially resolved calcium dynamics of mammalian Purkinje cells in cerebellar slice. *Science* 242, 773–777. doi: 10.1126/science.2847315

Theer, P., Hasan, M. T., and Denk, W. (2003). Two-photon imaging to a depth of 1000 microm in living brains by use of a Ti:Al2O3 regenerative amplifier. *Opt. Lett.* 28, 1022–1024. doi: 10.1364/OL.28.001022

Thestrup, T., Litzlbauer, J., Bartholomäus, I., Mues, M., Russo, L., Dana, H., et al. (2014). Optimized ratiometric calcium sensors for functional in vivo imaging of neurons and T lymphocytes. *Nat. Methods* 11, 175–182. doi: 10.1038/nmeth.2773

Tian, L., Hires, S. A., Mao, T., Huber, D., Chiappe, M. E., Chalasani, S. H., et al. (2009). Imaging neural activity in worms, flies and mice with improved GCaMP calcium indicators. *Nat. Methods* 6, 875–881. doi: 10.1038/nmeth.1398

Tsien, R. Y. (2005). Building and breeding molecules to spy on cells and tumors. *FEBS Lett.* 579, 927–932. doi: 10.1016/j.febslet.2004.11.025

Turrigiano, G. G., Leslie, K. R., Desai, N. S., Rutherford, L. C., and Nelson, S. B. (1998). Activity-dependent scaling of quantal amplitude in neocortical neurons. *Nature* 391, 892–896. doi: 10.1038/36103

Urnov, F. D., Rebar, E. J., Holmes, M. C., Zhang, H. S., and Gregory, P. D. (2010). Genome editing with engineered zinc finger nucleases. *Nat. Rev. Genet.* 11, 636–646. doi: 10.1038/nrg2842

Valmianski, I., Shih, A. Y., Driscoll, J. D., Matthews, D. W., Freund, Y., and Kleinfeld, D. (2010). Automatic identification of fluorescently labeled brain cells for rapid functional imaging. *J. Neurophysiol.* 104, 1803–1811. doi: 10.1152/jn.00484.2010

VanEngelenburg, S. B., and Palmer, A. E. (2008). Fluorescent biosensors of protein function. *Curr. Opin. Chem. Biol.* 12, 60–65. doi: 10.1016/j.cbpa.2008.01.020

Van Keuren, M. L., Gavrilina, G. B., Filipiak, W. E., Zeidler, M. G., and Saunders, T. L. (2009). Generating transgenic mice from bacterial artificial chromosomes: transgenesis efficiency, integration and expression outcomes. *Transgenic Res.* 18, 769–785. doi: 10.1007/s11248-009-9271-2

Vogelstein, J. T., Packer, A. M., Machado, T. A., Sippy, T., Babadi, B., Yuste, R., et al. (2010). Fast nonnegative deconvolution for spike train inference from population calcium imaging. *J. Neurophysiol.* 104, 3691–3704. doi: 10.1152/jn.01073.2009

Vogelstein, J. T., Watson, B. O., Packer, A. M., Yuste, R., Jedynak, B., and Paninski, L. (2009). Spike inference from calcium imaging using sequential Monte Carlo methods. *Biophys. J.* 97, 636–655. doi: 10.1016/j.bpj.2008.08.005

Wallace, D. J., Meyer zum Alten Borgloh, S., Astori, S., Yang, Y., Bausen, M., Kügler, S., et al. (2008). Single-spike detection in vitro and in vivo with a genetic Ca^{2+} sensor. *Nat. Methods* 5, 797–804. doi: 10.1038/nmeth.1242

Wang, D., McMahon, S., Zhang, Z., and Jackson, M. B. (2012). Hybrid voltage sensor imaging of electrical activity from neurons in hippocampal slices from transgenic mice. *J. Neurophysiol.* 108, 3147–3160. doi: 10.1152/jn.00722.2012

Wang, J. W., Wong, A. M., Flores, J., Vosshall, L. B., and Axel, R. (2003). Two-photon calcium imaging reveals an odor-evoked map of activity in the fly brain. *Cell* 112, 271–282. doi: 10.1016/S0092-8674(03)00004-7

Wardill, T. J., Chen, T. W., Schreiter, E. R., Hasseman, J. P., Tsegaye, G., Fosque, B. F., et al. (2013). A neuron-based screening platform for optimizing genetically-encoded calcium indicators. *PLoS ONE* 8:e77728. doi: 10.1371/journal.pone.0077728

Wurtz, R. H. (1968). Visual cortex neurons: response to stimuli during rapid eye movements. *Science* 162, 1148–1150. doi: 10.1126/science.162.3858.1148

Yaksi, E., and Friedrich, R. W. (2006). Reconstruction of firing rate changes across neuronal populations by temporally deconvolved Ca^{2+} imaging. *Nat. Methods* 3, 377–383. doi: 10.1038/nmeth874

Yamada, Y., Michikawa, T., Hashimoto, M., Horikawa, K., Nagai, T., Miyawaki, A., et al. (2011). Quantitative comparison of genetically encoded Ca indicators in

cortical pyramidal cells and cerebellar Purkinje cells. *Front. Cell. Neurosci.* 5:18. doi: 10.3389/fncel.2011.00018

Yin, L., Masella, B., Dalkara, D., Zhang, J., Flannery, J. G., Schaffer, D. V., et al. (2014). Imaging light responses of foveal ganglion cells in the living macaque eye. *J. Neurosci.* 34, 6596–6605. doi: 10.1523/JNEUROSCI.4438-13.2014

Zariwala, H. A., Borghuis, B. G., Hoogland, T. M., Madisen, L., Tian, L., De Zeeuw, C. I., et al. (2012). A Cre-dependent GCaMP3 reporter mouse for neuronal imaging in vivo. *J. Neurosci.* 32, 3131–3141. doi: 10.1523/JNEUROSCI.4469-11.2012

Zeng, H., and Madisen, L. (2012). Mouse transgenic approaches in optogenetics. *Prog. Brain Res.* 196, 193–213. doi: 10.1016/B978-0-444-59426-6.00010-0

Zhao, Y., Araki, S., Wu, J., Teramoto, T., Chang, Y. F., Nakano, M., et al. (2011). An expanded palette of genetically encoded Ca^{2+} indicators. *Science* 333, 1888–1891. doi: 10.1126/science.1208592

Ziv, Y., Burns, L. D., Cocker, E. D., Hamel, E. O., Ghosh, K. K., Kitch, L. J., et al. (2013). Long-term dynamics of CA1 hippocampal place codes. *Nat. Neurosci.* 16, 264–266. doi: 10.1038/nn.3329

Conflict of Interest Statement: The authors declare that the research was conducted in the absence of any commercial or financial relationships that could be construed as a potential conflict of interest.

Received: 28 August 2014; accepted: 15 November 2014; published online: 05 December 2014.

*Citation: Broussard GJ, Liang R and Tian L (2014) Monitoring activity in neural circuits with genetically encoded indicators. Front. Mol. Neurosci. **7**:97. doi: 10.3389/fnmol.2014.00097*

This article was submitted to the journal Frontiers in Molecular Neuroscience.

frontiers in
MOLECULAR NEUROSCIENCE

REVIEW ARTICLE
published: 18 November 2014
doi: 10.3389/fnmol.2014.00088

Putting a finishing touch on GECIs

Tobias Rose, Pieter M. Goltstein, Ruben Portugues and Oliver Griesbeck*

Max-Planck-Institute of Neurobiology, Martinsried, Germany

Edited by:
Yoshiyuki Yamada, University of Geneva, Switzerland

Reviewed by:
Johannes Hirrlinger, University of Leipzig, Germany
David J. Margolis, Rutgers University, USA

****Correspondence:***
Oliver Griesbeck, Max-Planck-Institute of Neurobiology, Am Klopferspitz 18, 82152 Martinsried, Germany
e-mail: griesbeck@neuro.mpg.de

More than a decade ago genetically encoded calcium indicators (GECIs) entered the stage as new promising tools to image calcium dynamics and neuronal activity in living tissues and designated cell types *in vivo*. From a variety of initial designs two have emerged as promising prototypes for further optimization: FRET (Förster Resonance Energy Transfer)-based sensors and single fluorophore sensors of the GCaMP family. Recent efforts in structural analysis, engineering and screening have broken important performance thresholds in the latest generation for both classes. While these improvements have made GECIs a powerful means to perform physiology in living animals, a number of other aspects of sensor function deserve attention. These aspects include indicator linearity, toxicity and slow response kinetics. Furthermore creating high performance sensors with optically more favorable emission in red or infrared wavelengths as well as new stably or conditionally GECI-expressing animal lines are on the wish list. When the remaining issues are solved, imaging of GECIs will finally have crossed the last milestone, evolving from an initial promise into a fully matured technology.

Keywords: buffering, calcium, fluorescent protein, FRET, imaging, neuronal activity, segmentation

INTRODUCTION

Genetically encoded calcium indicators (GECIs) have come of age. Since the first demonstration of FRET (Förster Resonance Energy Transfer)-based prototypical sensors such as the Cameleons (Miyawaki et al., 1997, 1999) and the first single fluorophore calcium sensors (Baird et al., 1999), these two major classes have evolved high performance variants in which signal strength was optimized in iterative steps of improvements and validation. Among FRET based sensors Cameleons, which exploit the interaction of Calmodulin with the binding peptide M13 as a calcium sensing mechanism, saw several rounds of improvements of their signal strength (Nagai et al., 2004; Horikawa et al., 2010). Troponin C has been used as a more biocompatible alternative to Calmodulin in FRET sensors (Heim and Griesbeck, 2004). These sensors also underwent several rounds of engineering (Mank et al., 2006, 2008). Among single fluorophore sensors GCaMP type sensors (Nakai et al., 2001) became the most popular class, chosen from several initial architectures. Variants with ever increasing sensitivity to neuronal activity were generated (Ohkura et al., 2005, 2012a; Tian et al., 2009; Akerboom et al., 2012), as were blue and red emitting color variants (Zhao et al., 2011; Akerboom et al., 2012; Ohkura et al., 2012b). Finally, large scale mutagenesis and screening approaches have resulted in GECIs that match or even exceed the *in vivo* sensitivity of the synthetic calcium dye OGB-1, often referred to as a standard against which response properties of new GECIs were compared to (Chen et al., 2013; Thestrup et al., 2014).

Genetically encoded calcium indicators finally made it possible to label specific types of neurons *in vivo* and even allowed targeting to subcellular compartments and repeated imaging of identified neurons over long periods of time. For several small genetically tractable organisms with strong body walls or cuticulae such as in *Caenorhabditis elegans* or *Drosophila*, which made access and loading of dyes from the outside challenging, expression of GECIs was the only feasible way to image neuronal activity. In many aspects imaging of GECIs has thus become a well-established technology that enables experiments that previously were not possible.

What is the ideal GECI for imaging neuronal physiology? Obviously this will depend on the experimental situation and the neuronal cell types to be imaged. Nevertheless, a number of general criteria may be derived that a GECI should strive to include in the ideal case. (i) It should be bright enough to identify expressing cells even at rest, allow an estimate of the amount of indicator expressed in a given cell after gene transfer, and possibly reveal fine details of its architecture. (ii) It should be readily expressed at sufficient levels by the standard methods for gene transfer and transgenesis. (iii) It should exhibit a linear relationship between the changes in free calcium and the fluorescence change of the indicator. (iv) For reporting neuronal activity it should be sensitive enough to faithfully report small calcium elevations due to firing of single action potentials (APs) in single trials *in vivo*, ideally at lower magnification and faster scanning rate to sample large numbers of neurons. (v) It should not perturb cells that express the indicator by buffering of physiological calcium or other unwanted biological side effects. (vi) It should minimize artifacts due to specimen movement, photobleaching, or other perturbing causes. (vii) Finally, it should have sufficiently fast binding kinetics to accurately follow calcium fluctuations, if it is used as a reporter of neuronal activity.

In view of these criteria we will discuss some of the current issues in quantifying neuronal signals with GECIs and point to some further desirable improvements to finally turn imaging of GECIs it into a mature, fully fledged technology for the study of neuronal function.

QUANTIFYING NEURONAL ACTIVITY WITH GECIs – DEALING WITH NON-LINEARITY

The biochemical and optical properties of the latest generation of GECIs rival and in some aspects even surpass those of synthetic calcium indicators (Chen et al., 2013; **Table 1**). It is now possible to detect the somatic calcium influx associated with individual APs with high reliability *in vivo*. Even calcium signals following synaptic activation can now be monitored chronically in live animals (Chen et al., 2013). Yet, in one point most GECIs are clearly inferior to their synthetic counterparts: linearity with respect to the actual calcium concentration. Indicator non-linearity renders the direct deduction of absolute changes in calcium from the relative changes in fluorescence challenging. Robust quantification with the commonly used calibration methods is only possible in the 'linear' regime of a calcium indicator (Grynkiewicz et al., 1985; Neher, 1995; Maravall et al., 2000; Yasuda et al., 2004), well below its K_d value (**Figure 1A**). Only in this range the fluorescence intensity (or fluorescence ratio) change $\Delta F/F$ or $\Delta R/R$ of the indicator is approximately proportional to the cellular Ca^{2+} concentration ($[Ca^{2+}]_i$). Most synthetic indicators with linear response curves (Hill coefficient ~1) show a simple saturation function of $\Delta F/F$ *or* $\Delta R/R$ vs. $[Ca^{2+}]$. The saturation fluorescence F_{max} in response to $[Ca^{2+}] >> K_d$ is used together with the indicator fluorescence F_{min} at zero $[Ca^{2+}]$ to calibrate the fluorescence response:

$$[Ca^{2+}] = [(F-F_{min})/(F_{max}-F)]^* K_d \quad \text{or}$$
$$[Ca^{2+}] = [(R - R_{min})/(R_{max} - R)]^* K_d \qquad (1)$$

However, if the Hill coefficient of the binding curve diverges strongly from 1 the assumptions underlying Eq. 1 are violated (**Figure 1A**).

Owing to four cooperative calcium-binding sites in most GECIs, response curves frequently are highly non-linear. For example, Hill coefficients of recent GCaMP5 or six variants range from 2.5 to 4 (Akerboom et al., 2012; Chen et al., 2013), as do those of many FRET-based Cameleons (Horikawa et al., 2010; **Table 1**). Quantification of $[Ca^{2+}]_i$ using the linear approximation (Eq. 1) is therefore impossible (**Figure 1A**). This will affect the ability to infer calcium transients from fluorescence data. Even if the non-linearity is taken into account computationally (Akerboom et al., 2012; Lütcke et al., 2013a), the sub-linearity in the low-calcium regime of the indicator is still of particular concern. The resting calcium concentration of a cell can vary depending on cell type, cell health, and exogenous ion concentrations (Schiller et al., 1995; Helmchen et al., 1996; Maravall et al., 2000). In the sub-linear regime of the indicator these differences will lead only to minor changes in resting fluorescence. The latest generation of GCaMP type single fluorophore sensors reached their exceptional signal to noise ratio (SNR) to a large degree thanks to a combination of increasing maximum brightness at saturation and decreasing the resting brightness F_0. Improving sensors by reducing F_0, however, makes it more challenging to quantify differences in resting calcium because the resulting minor fluctuations in resting fluorescence can essentially not be distinguished from variations in indicator expression level.

An additional complication for the quantitative use of GECIs is that it is not clear if the non-linear relation of F or R and calcium is constant, especially considering the variable expression levels over time and between subjects. The result is that the same absolute change in calcium may lead to highly variable changes in fluorescence depending on the actual resting calcium concentration (**Figure 1A**). As a result of this variability, establishing a 'ground truth' of single AP-evoked fluorescence in order to infer spike rate and timing from the fluorescence data is challenging: since it is unclear from which resting calcium level single AP transients are arising, generalizing a single waveform of this unitary event to an entire population of cells can be problematic. Of course, when the indicator affinity is high enough so that the calcium changes of interest largely fall in the linear range of the indicator, reliable spike inference should be possible. Careful *in situ* calibrations of indicator fluorescence change vs. simultaneously measured cellular activity under realistic indicator expression levels and imaging conditions need to be performed in order to deduce reliable spike timings from non-linear GECI data. In these cases one should consider if more linear ratiometric GECIs would provide a better quantifiable alternative. To increase the accuracy of methods for calcium measurement and AP inference, reducing calcium-binding sites as performed with recent ratiometric "Twitch" calcium sensors (Thestrup et al., 2014) should be a design goal for other future GECI developments.

BUFFERING AND EXPRESSION LEVEL

All calcium indicators act as calcium buffers. Therefore, expression of any type of GECI will inadvertently change the spatio-temporal dynamics of this ubiquitous secondary messenger. The degree to which an exogenous buffer affects cellular free calcium ($[Ca^{2+}]_i$) is well understood and largely depends on three main factors: its mobility, affinity (including binding rates), and concentration (Zhou and Neher, 1993; Neher, 1995; Helmchen et al., 1996).

If one aims at monitoring neuronal activity, i.e., calcium signals associated with APs or synaptic activation, one can either choose to minimize the effect of exogenous buffer on endogenous calcium signaling by minimizing the indicator concentration, or to maximize the SNR of the readout of calcium activity by finding the indicator concentration that yields optimal SNR.

Under ideal (i.e., photon shot noise limited) conditions, the measure of confidence that one can attribute to a change in fluorescence given the intrinsic variability in the measurement due to the Poisson statistics of light detection (i.e., the SNR), is directly proportional to the indicator's signal change over baseline fluorescence (i.e., ΔF or ΔR) and to the square root of the baseline fluorescence signal (Yasuda et al., 2004; Göbel and Helmchen, 2007):

$$\text{SNR} = \Delta F / F_0^{1/2} \qquad (2)$$

In the case of ratiometric indicators, the relative shot noise components of donor and emission fluorescence add so that for the same relative change in fluorescence ratio from a comparable baseline fluorescence level the SNR is worse than for single fluorophore GECIs that require only one noise-affected measurement. However, since FRET indicators are typically much brighter at rest this

Table 1 | Comparison of current generation genetically encoded calcium indicators (GECIs) for *in vivo* usage with OGB.

Indicator	Fluorophore(s)	Ca^{2+} sensing domain	*in vitro* K_D (nM)	Hill slope	Rise (s)	Decay (s)	Single AP ($\Delta F/F$ or $\Delta R/R$)	Description	Reference
Synthetic									
OGB	Oregon green	BAPTA	260	1.48	0.24[a] 0.09[b]	0.38[a] 2.11[b]	10.0 ± 0.9%[j] 5.2 ± 0.9%[k]	High linearity; high baseline brightness; fast kinetics; acute usage (<12 h)	Kerr et al. (2005), Hendel et al. (2008), Tada et al. (2014)
Cal-520	–	BAPTA	320	–	0.06[b]	0.69[b]	18.8 ± 0.8%[k]	Latest generation synthetic indicator	Tada et al. (2014)
Single FP									
GCaMP3	cpEGFP	Calmodulin	345–660	2.1–2.5	0.08[c]	0.61[c] 0.64[d]	7.9 ± 2.8%[j] 17.4 ± 3.5%[n]	–	Tian et al. (2009), Akerboom et al. (2012), Chen et al. (2013)
GCaMP5G	cpEGFP	Calmodulin	450–460	2.5	0.15[e]	0.61[e]	–	–	Akerboom et al. (2012), Chen et al. (2013)
GCaMP5K	cpEGFP	Calmodulin	189	3.8	0.06[f]	0.27[f]	3.6 ± 1.9%[l]	High affinity; High non-linearity	Akerboom et al. (2012), Chen et al. (2013)
GCaMP6	cpEGFP	Calmodulin	158	–	–	0.46[d]	27.9 ± 4.5%[n]	–	Ohkura et al. (2012b)
GCaMP8	cpEGFP	Calmodulin	200	–	–	0.43[d]	37.8 ± 5.2%[n]	–	Ohkura et al. (2012b)
GCaMP6f	cpEGFP	Calmodulin	375	2.27	0.14[e] 0.05[f]	0.38[e] 0.14[f]	19 ± 2.8%[l]	Medium–high affinity; low baseline brightness; faster kinetics	Chen et al. (2013)
GCaMP6m	cpEGFP	Calmodulin	167	2.96	0.14[e] 0.08[f]	0.87[e] 0.27[f]	13 ± 0.9%[l]	High affinity; low baseline brightness; intermediate kinetics	Chen et al. (2013)
GCaMP6s	cpEGFP	Calmodulin	144	2.90	0.16[e] 0.18[f]	1.14[e] 0.55[f]	23 ± 3.2%[l]	High affinity; low baseline brightness; slower kinetics	Chen et al. (2013)

(Continued)

Table 1 | Continued

Indicator	Fluorophore(s)	Ca^{2+} sensing domain	*in vitro* K_D (nM)	Hill slope	Rise (s)	Decay(s)	Single AP ($\Delta F/F$ or $\Delta R/R$)	Description	Reference
FRET									
YC3.60	ECFP/cpVenus	Calmodulin	250	1.7	0.82[g]	0.73[g]	$2.0 \pm 0.09\%$[k] $5.5 \pm 1.2\%$[m]	–	Nagai et al. (2004), Hendel et al. (2008), Horikawa et al. (2010), Lütcke et al. (2010)
YC-Nano15	ECFP/cpVenus	Calmodulin	15.8	3.1	–	~ 4[h]	$10.4 \pm 1.9\%$[m]	High affinity; high baseline brightness; slower kinetics	Horikawa et al. (2010), Thestrup et al. (2014)
TN-XXL	ECFP/cpCitrine	Troponin	800	1.5	1.04[g]	0.88[g]	$1.6 \pm 0.3\%$[n]	–	Mank et al. (2008), Thestrup et al. (2014)
Twitch2B	mCerulean3/ cpVenus	Troponin	200	1.31	–	2.11[i]	$26.5 \pm 3.8\%$[o]	High linearity; high baseline brightness; slower kinetics	Thestrup et al. (2014)
Twitch3	ECFP/cpCitrine	Troponin	250	1.42	–	2.05[i]	$5.7 \pm 0.7\%$[p]	High linearity; high baseline brightness; slower kinetics	Thestrup et al. (2014)

Overview of parameters describing the function of the commonly used GECIs, their predecessors and the 'golden standard' OGB.
K_D measured by stop-flow measurement using purified protein.
Rise and decay:
[a] *Single exponential fit (τ_{rise}, τ_{decay}), 40 APs (20 Hz) in drosophila larval neuromuscular junction (NMJ)* Hendel et al. (2008).
[b] *Rise time (10-90), decay time constant from double exponential fit to single AP in acute brain slices of mouse barrel cortex* Tada et al. (2014).
[c] *Half-rise time ($t_{1/2}$), half-decay time ($t_{1/2}$) for 10 APs (83Hz) in hippocampal slice culture* Tian et al. (2009).
[d] *Single exponential fit (decay $\tau_{1/2}$), 1 AP in hippocampal slice culture* Ohkura et al. (2012b).
[e] *Full-rise time, half-decay time ($t_{1/2}$), 20 Hz in drosophila larval NMJ* Chen et al. (2013).
[f] *Full-rise time, half-decay time ($t_{1/2}$) for single AP induced signals in mouse V1 in vivo* Akerboom et al. (2012) *or* Chen et al. (2013).
[g] *Single exponential fit (τ_{rise}, τ_{decay}), 80 APs (40 Hz) in drosophila larval NMJ* Hendel et al. (2008) *or* Mank et al. (2008).
[h] *Single exponential fit (τ_{decay}), for 10 APs (20 Hz) in mouse brain* Horikawa et al. (2010).
[i] *Single exponential fit (τ_{decay}), for 10 APs (83 Hz) in dissociated hippocampal culture* Thestrup et al. (2014).
Single AP $\Delta F/F$ or $\Delta R/R$ measured in:
[j] *Mouse M1 or S1 in vivo* Kerr et al. (2005) *or* Tian et al. (2009).
[k] *Mouse barrel cortex in vivo* Lütcke et al. (2010) *and* Tada et al. (2014).
[l] *Mouse V1 in vivo* Chen et al. (2013).
[m] *Mouse cortex, acute brain slices* Lütcke et al. (2010) *or* Horikawa et al. (2010).
[n] *Hippocampal slice culture* Mank et al. (2008) *and* Ohkura et al. (2012b).
[o] *Acute cortical slice* Thestrup et al. (2014).
[p] *Dissociated hippocampal culture* Thestrup et al. (2014).

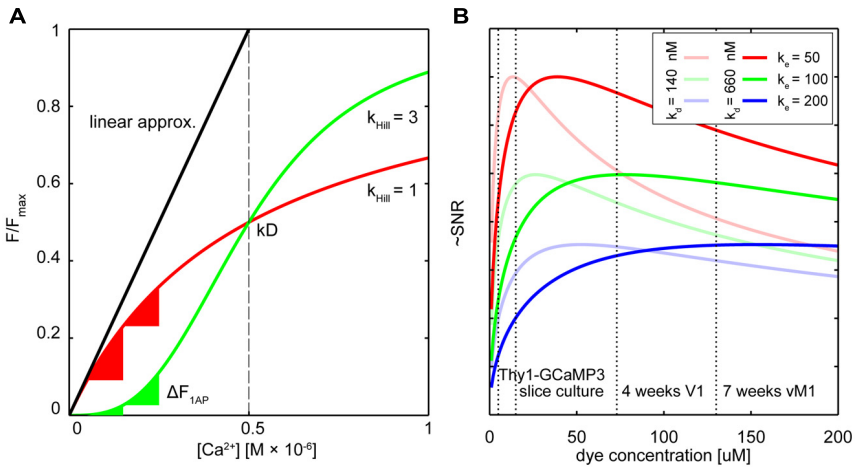

FIGURE 1 | Dealing with non-linearity and buffering. (A) Relative fluorescence changes of two hypothetical calcium indicators with similar affinity but different cooperativity (OGB-like: red trace, Hill slope (K_{hill}) = 1, GECI-like: green trace K_{hill} = 3) in response to varying calcium concentrations. The black line shows the commonly used linear calibration function (Eq. 1). Only for small changes in Ca^{2+} – well below the indicator K_d – this function describes the fluorescence response of the more linear indicator (red trace) well. Even though the non-linear indicator (green trace) responds approximately linear at intermediate Ca^{2+} levels around the K_d, the linear calibration function is left-shifted and therefore prominently underestimates the actual Ca^{2+} concentration from the measured fluorescence. Note that the same absolute change in Ca^{2+} starting from different resting calcium levels will lead to very different fluorescence changes of the non-linear indicator (green triangles) whereas the linear indicator responds with comparable changes (red triangles). **(B)** Hypothetical relation between added exogenous buffer capacity (i.e., increasing indicator concentrations) and signal-to-noise ratio (SNR; Göbel and Helmchen, 2007). Shown are different endogenous buffer capacities corresponding roughly to the range of reported values for pyramidal and subclasses of inhibitory neurons (red: κ_e = 50; green κ_e = 100; blue κ_e = 200; assumed resting $[Ca^{2+}]_i$ 50 nM). Two hypothetical indicators with different affinities similar to reported *in vitro* values for GCaMP3 and GCaMP6s are shown [bold lines: K_d = 660 nM, faded lines K_d = 140 nM; true *in vivo* K_d of genetically encoded calcium indicators (GECIs) may vary]. Note that SNR optimal indicator concentrations would be reached at ~25–50 μM. Here, 'balanced loading' is achieved where endogenous and exogenous buffer capacities are equal. Dashed vertical lines indicate four reported *in situ* indicator concentrations using different gene delivery methods and expression times for the GECI GCaMP3: Emx1-Cre:Ai38 mice, 5.4 μM (Zariwala et al., 2012); hippocampal slice culture after single-cell electroporation, 15 μM (Huber et al., 2012); primary visual cortex after 4 weeks of viral (AAV) infection, 72 μM (Zariwala et al., 2012); 7 weeks after AAV infection in vibrissal motor cortex (Huber et al., 2012), 130 μM.

disadvantage is largely compensated (but see Wilt et al., 2013). Increasing the concentration of a calcium indicator increases F and thereby improves SNR because more fluorescent molecules become available. Yet, a larger buffer concentration will also lead to a smaller fluorescence change: When the indicator is trying to bind more calcium than is entering the cell while at the same time competing with endogenous calcium buffers, the number of indicator molecules changing their emission from the baseline level decreases. The amplitude (ΔF or ΔR) and decay time constant (τ) of the calcium-dependent fluorescence change depend on the summed buffer capacity of the exogenous and endogenous buffers (Göbel and Helmchen, 2007):

$$\Delta F \propto F_0/(1 + \kappa_{endo} + \kappa_{dye}) \quad (3)$$

$$\tau \propto 1 + \kappa_{endo} + \kappa_{dye} \quad (4)$$

where κ_{endo} represents the buffer capacity of the endogenous buffers (fixed or mobile) and κ_{dye} represents the exogenous buffer capacity of the added calcium dye. The buffer capacity (or 'binding ratio') is the constant describing the fixed ratio between changes in free $[Ca^{2+}]$ and buffer-bound [CaB] calcium, which can be related to the effective dissociation constant (K_d) and concentration $[B]_{tot}$ of the respective buffer (Zhou and Neher, 1993; Neher, 1995):

$$(\kappa_{dye}) = \Delta[caB]/\Delta[Ca^{2+}]_i = (K_d{}^*[B]_{tot})/(K_d + [Ca^{2+}])^2 \quad (5)$$

What would be the optimal indicator concentration (or GECI expression level) to maximize SNR? F_0 is proportional to κ_{dye} and by substitution in Eq. 2 one yields (Borst and Helmchen, 1998; Göbel and Helmchen, 2007):

$$SNR = \Delta F/F_0^{1/2} \propto \kappa_{dye}/[(1 + \kappa_{endo} + \kappa_{dye})^*\kappa_{dye}{}^{1/2}]$$
$$= \kappa_{dye}^{1/2}/(1 + \kappa_{endo} + \kappa_{dye}) \quad (6)$$

It follows that maximal SNR is achieved under 'balanced loading' conditions where the endogenous and exogenous buffer capacities are equal ($\kappa_{endo} = \kappa_{dye}$; Borst and Helmchen, 1998; Göbel and Helmchen, 2007). **Figure 1B** shows this relation for various concentrations of two hypothetical GECIs at several endogenous buffer capacities that are similar to reported values for excitatory and inhibitory neurons. Also indicated are the approximated concentrations of the GECI GCaMP3 under different expression conditions. Note that for excitatory neurons (κ_{endo}~30–100; Helmchen et al., 1996; Maravall et al., 2000), concentrations of 25–50 μM would already yield near maximal SNR. For some classes of inhibitory neurons with high calcium binding ratio, 'balanced loading' would be reached at much higher

expression level (e.g., κ_{endo} ~285 in somatostatin positive bitufted interneurons in L2/3 of somatosensory cortex (Kaiser et al., 2001). Of course, without knowing the exact *in situ* values of all parameters (most notably the effective K_d, resting calcium concentrations and κ_{endo}), the actual optimal indicator concentration remains unknown. Complementing direct measurements of absolute indicator concentrations using purified protein as reference standard (Huber et al., 2012; Zariwala et al., 2012), the most relevant parameters for SNR-optimal 'balanced loading' – κ_{endo} and κ_{dye} – in various cell types could be experimentally obtained. By monitoring the amplitude and decay time of a step calcium signal with a calibrated second calcium indicator of different emission wavelength at different concentrations one could back-extrapolate to the apparent endogenous buffer capacity ($\kappa_{app} = \kappa_{endo} + \kappa_{dye}$) from the decreases in ΔF and τ (Eqs 3 and 4; Zhou and Neher, 1993; Neher, 1995; Helmchen et al., 1996; Matthews et al., 2013). If one would perform these experiments in cells acutely expressing the GECI ($\kappa_{app} = \kappa_{endo} + \kappa_{dye}$) and compared these to control cells without the GECI ($\kappa_{app} = \kappa_{endo}$) the buffer capacity added by overexpression of the GECI could be deduced and optimized. Of course, this would only be meaningful if the cell would not adjust its endogenous buffers in response to GECI expression in order to maintain buffer homeostasis – which in itself would be a highly relevant finding pointing toward potentially unwanted off-target effects of GECI expression. However, recent studies on gene expression profiling in mice globally expressing the FRET sensor TN-XXL (Direnberger et al., 2012) do not point in that direction. Nevertheless, more studies on the amount of buffering introduced into different neurons by various types of GECIs and gene transfer protocols would be highly desirable, especially when directly related to expression-correlated off-target effects of GECIs (see below). However, even with these data at hand, tailoring expression of GECIs toward SNR-optimal levels is difficult, especially when acute methods of gene transfer (e.g., viral transduction or electroporation) are used. Nevertheless, careful titration of the amount virus injected or DNA electroporated together with optimization of promoters, enhancers, or suppressors of expression should be considered to prevent unnecessary overexpression.

INDICATOR KINETICS

It had been noticed early on that the response kinetics of GECIs were slower than that of synthetic calcium dyes. Early prototypical Cameleon-1 had a measured on-rate k_{on} of about 10^6 M^{-1} s^{-1} compared to essentially diffusion-limited on-rates of 10^8 M^{-1} s^{-1} for fura-2 or fluo-3 (Kao and Tsien, 1988; Miyawaki et al., 1997; Naraghi, 1997). Accordingly, k_{off} numbers were also slower, with a value of 13 s^{-1} reported for the medium affinity Cameleon-1 (Miyawaki et al., 1997). Delayed kinetics compared to synthetic dyes were subsequently confirmed for other types of GECIs based on Cam-M13 or Troponin C, albeit at varying extent (Nakai et al., 2001; Pologruto et al., 2004; Tay et al., 2007; Horikawa et al., 2010). Engineering faster GECIs has been challenging, as on- and off rates, affinities and maximal fluorescence change are tightly linked to one another ($K_d = k_{off}/k_{on}$), and it is often not feasible to optimize one parameter without losing advantageous features of the other parameters. Engineering thus mostly focused either on calcium chelating residues within the EF-hand loops or on the binding interface of calmodulin with its binding peptide. For most types of mutagenesis an expected reciprocal relationship was found between calcium affinity and kinetics (Miyawaki et al., 1997; Mank et al., 2006; Horikawa et al., 2010; Chen et al., 2013; Sun et al., 2013; Thestrup et al., 2014). Will it be possible to engineer GECIs in which both on- and off-rates are enhanced to obtain high affinity rapid kinetics sensors comparable to dyes such as OGB-1? Some mutations in the interface between Calmodulin and its binding peptide allowed to generate G-CaMP type sensors with faster kinetics, only slightly altered affinity, but smaller maximal fluorescence change (Chen et al., 2013; Sun et al., 2013). Thus, hydrophobic interactions of Calmodulin with the peptide were identified as one rate-limiting step within these sensors. Other studies on Troponin C-based FRET sensors identified slow events close to the EF-hands as rate-limiting for dissociation, while addition of the donor and acceptor GFPs had no further negative effects on kinetics (Geiger et al., 2012). More detailed structural studies on the causes of slow intramolecular dynamics within GECIs appear necessary to finally break the apparent trade-off between sensitivity and speed.

Neurons in the mammalian CNS exhibit a wide range of firing rates, from sparse activity below 0.1 Hz (e.g., L2/3 cells in the barrel cortex, Kerr et al., 2005) to rates approaching 1 kHz (e.g., mossy fiber input to the cerebellum, Rancz et al., 2007). Even the latest generation of GECIs shows a fluorescence impulse response that rises and decays with time constants more than 100 times slower than the average inter-spike interval of the fastest neurons (**Table 1**). During high frequency activity this inevitably leads to overlapping fluorescence responses to individual APs. Once the cumulative fluorescence reaches indicator saturation level, information about the underlying neuronal activity is lost. Furthermore, experiments correlating neuronal activity with episodic sensory stimulation or behavioral events can suffer from response 'bleed-through': responses from previous episodes evoke activity that leads to fluorescence changes that are still present during the onset of the next episode, even though the underlying spike rate may have already decayed to baseline levels (**Figure 2C**). In these cases, raw fluorescence changes cannot be used for quantification of neuronal firing. Faster indicators lead to less response superposition and therefore allow simpler separation of individual activity events, thereby, for example, allowing shorter inter-trial intervals. However, for as long as cumulative fluorescence changes are not approaching full indicator saturation levels, the underlying spiking activity of synthetic indicators can often be resolved surprisingly well using non-linear methods of spike inference (Vogelstein et al., 2009; Grewe et al., 2010; Lütcke et al., 2013a). It remains to be established how well these methods perform with non-linear GECIs of the latest generation. The accuracy of spike inference methods depends on the actual spike rate, indicator speed, sampling rate, and all factors that affect the SNR of the measurement (see above). The complex interdependence of these factors has been extensively described elsewhere (Lütcke et al., 2013a; Wilt et al., 2013). These studies showed that faster is not always better: Depending on the frequency of expected responses, sparse sub-saturating

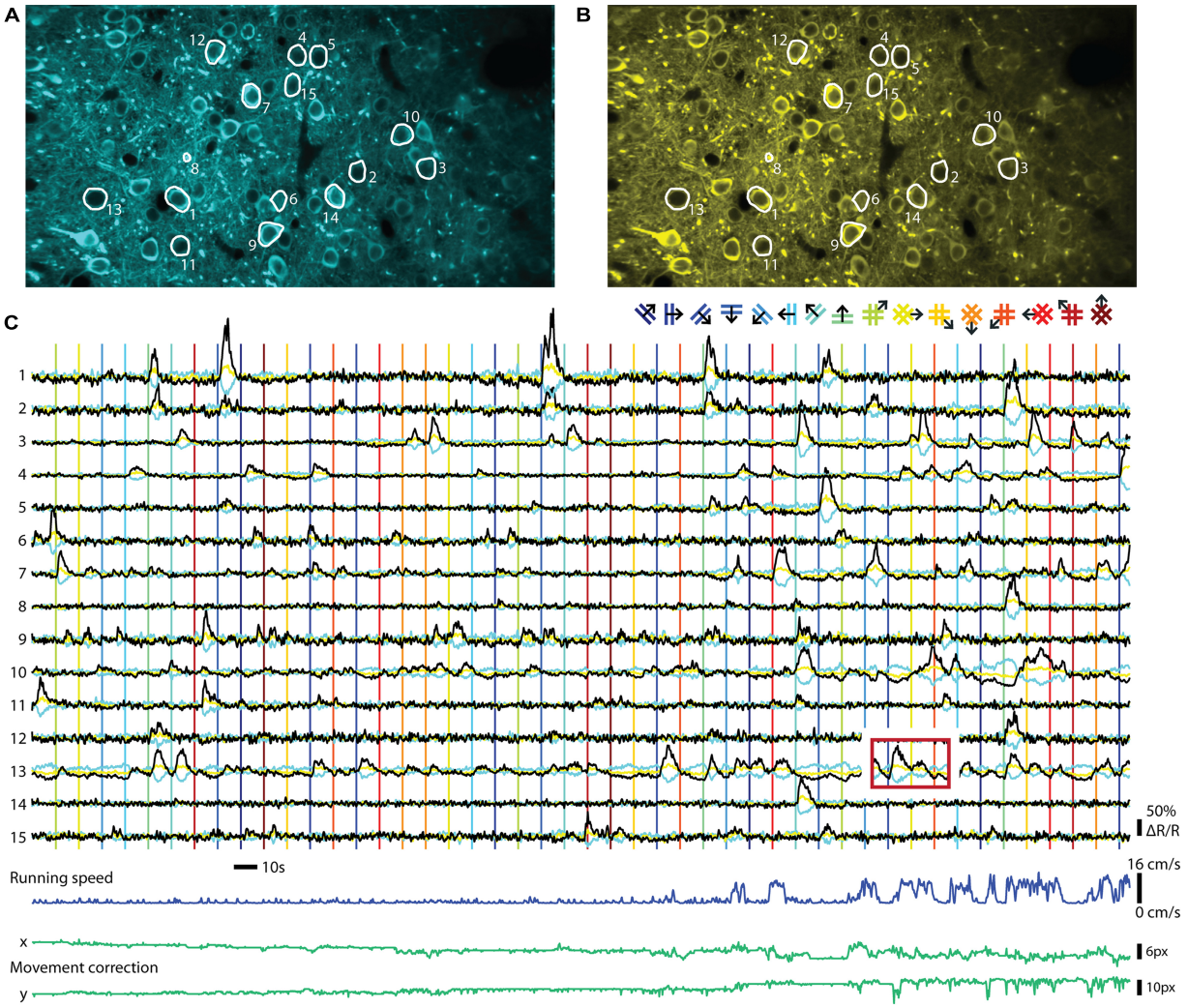

FIGURE 2 | Ratiometric imaging of neuronal activity in an awake mouse using the Twitch-2B calcium indicator. Two-photon imaging of layer II/III excitatory neurons, conditionally expressing Twitch-2B (CAG promoter, double-floxed inverted open reading frame, 28 days after transduction by AAV1) together with Cre-recombinase (CamKII promoter, AAV1), in V1 of an awake head-restrained mouse on a treadmill (see, e.g., Keller et al., 2012). Imaging frames were acquired at 30 Hz on a custom build two-photon microscope and corrected for movement artifacts (Guizar-Sicairos et al., 2008). **(A)** Frame-averaged image of donor fluorescence (467–499 nm). Region of interest (ROI's; white) were manually drawn for 15 active neurons. **(B)** Idem, but for acceptor fluorescence (519–549 nm). **(C)** Neuropil-subtracted (Kerlin et al., 2010) change in donor (cyan) and acceptor (yellow) fluorescence ($\Delta F/F$) for each ROI, referenced against a 60 s moving-average. Black traces display the change in ratio of the donor and acceptor fluorescence ($\Delta R/R$) over its 60 s moving-average. Time-series were smoothed using a 0.5 s moving average window. Vertical lines indicate onsets of visual stimuli, which were full-contrast sinusoidal moving gratings (spatial frequency: 0.045 cycle/degree; Speed: 1.5 cycle/s) or plaids (overlays of two orthogonal gratings; color of lines matches the legend above), presented on a gamma-corrected monitor at a distance of 20 cm. Stimulus presentation lasted 4.5 s, interleaved by a gray screen of equal brightness for 5.5 s. The red box over ROI 13 indicates an example of response bleed-through into the next stimulus episode. Running speed of the animal ranged from 0 to 16 cm/s (dark blue trace below). Image displacement (before correction) did not exceed 12 and 13 pixels on the x and y axes, respectively (green lines below). Data adapted from Thestrup et al. (2014).

activity will be detected with higher SNR using a slower indicator. Since imaging involves sampling at a fixed rate, more samples are collected for a fluorescence step response in the case of a slow indicator, increasing detection SNR by the square root of the number of samples acquired and preventing undersampling of short events. It is therefore non-trivial to decide – keeping all other indicator properties constant – what would be the optimal kinetics of an indicator. One needs to consider both the expected rates of activity and the sampling rate of available imaging hardware. Computational models as provided by Lütcke et al. (2013a) should ideally be consulted to make an informed decision.

RATIOING VERSUS SINGLE CHANNEL RECORDING

The two major classes of GECIs operate in different read-out modes. While single GFP-based sensors are imaged using a single channel for recording fluorescence, FRET-based indicators are ratiometric and require splitting the emitted light into two

channels that are recorded separately and the ratio of the two emission channel intensities taken as a measure of calcium concentrations. An example of a ratiometric *in vivo* recording can be seen in **Figure 2**. The indicator Twitch-2B was expressed in mouse primary visual cortex and ratiometric imaging of the activities of a group of neurons performed in awake mice. Both types of procedures have distinct advantages and disadvantages. Recording with a single channel is simpler and allows collecting all photons emitted from a probe, without any loss from emission filters or beam splitters. Such probes also occupy less bandwidth of the spectral range, allowing more multiplexing and co-labeling of neuronal cell types with different colors. Ratiometric, FRET based probes use two fluorescent proteins as fluorophores, and therefore occupy a larger area of spectral bandwidth for a given sensor. Ratioing has, however, a number of advantages if quantification of neuronal activity is desired. The ratio formed between the two channels is, in principle, independent of expression levels. Thus, heterogeneities in indicator expression levels between cells, as occur with AAV-mediated gene delivery into the brain (Aschauer et al., 2014) and other gene delivery methods, can be more easily addressed. As indicator expression levels directly affect both amplitudes and time constants of calcium signals (see, e.g., Helmchen et al., 1996), it may be necessary to correct for these differences. Direct acceptor excitation is an unambiguous way to read out indicator expression levels independent of the calcium concentration. It may also facilitate the definition of regions of interest because it will not display increased signal intensity for more active cells. During long-term imaging over months, fluctuations in excitation light intensity, changes of indicator expression levels or changes in optical path length due to tissue growth may also occur, which could be addressed by ratioing. As long noted, ratiometric imaging is beneficial when movement artifacts are a concern, such as in moving preparations or awake animals, because correlated artifacts affecting both channels in the same way are effectively canceled out due to the processing. Ratiometric imaging also corrects for further changes in optical path length resulting from vasoconstriction and -dilation. These vascular artifacts are often correlated with neuronal activity and are therefore of particular concern (Shen et al., 2012). While movement-related artifacts could also be addressed by simple co-expression of a second, preferably red fluorescent protein together with the GFP-based sensors, truly ratiometric FRET probes have the advantage that the resting ratio of the indicator can be used to directly quantify the resting calcium level. This is especially of interest for some classes of inhibitory neurons that fire APs at high rate under 'resting' conditions (Klausberger and Somogyi, 2008; see also Thestrup et al., 2014). Thus, the choice of indicator and read-out mode will depend on the type of experiment and the available expression systems and promoters to drive expression.

SEGMENTATION

The main objective of calcium imaging experiments is to monitor neuronal activity via variations in fluorescence. Having performed the experiment, the next step is to make sense of the fluorescence data. Traditional methods involve hand-picking a region of interest (ROI) in the anatomy and finding the fluorescence time-series within this ROI. This method can easily be implemented when sparse labeling makes it straight forward to manually segment the anatomical ROI and is particularly useful in experiments where the experimenter knows what particular ROIs are of interest in order to answer questions such as: Is this specific neuron active in my experiment?

In certain cases though, it is more appropriate to use an automated method to select ROIs, in particular when seeking an unbiased, large-throughput way of processing the data. These methods can be said to fall roughly into two categories, those that use anatomical information and those that use functional data for the segmentation. We briefly discuss both below.

Anatomical segmentation methods greatly rely on the specimen being imaged and the labeling of the tissue. Issues such as whether the calcium indicator is expressed in the nucleus or the cytoplasm, whether the labeling is dense or sparse and whether neurons are morphologically similar or vary widely in shape and size all enter the design of the particular algorithm. In regions where the morphology of the anatomy is homogenous, algorithms can be quite effective. **Figure 3A** shows an example from the optic tectum of a larval zebrafish expressing GCaMP5G under the pan-neuronal promoter *elavl3*. The neurons have their cytoplasm labeled, are densely packed and of similar size. In order to perform automated segmentation, the anatomical image is spatially filtered with a filter whose width is in the order of the diameter d of a typical neuron, for example a Gaussian filter with standard deviation d. This removes local spatial inhomogeneities and emphasizes the important features that will be used for segmentation. In this case these are the bright cytoplasms, which can be used to identify boundaries between cells and the dark nuclei which can be used to identify the centers of the cells (**Figure 3B**, left). One may then perform a watershed algorithm on this image that will identify the "ridges" in this image, namely the bright cytoplasms. This will segment the image into ROIs, many of which will be individual cells (**Figure 3B**, right). By placing constraints on the morphology of these ROIs, such as a lower and upper limit on their size it is possible to ensure that most of the ROIs that are kept are actual neurons. The fluorescence time-series for all the ROIs can then be extracted using these ROIs as masks. **Figure 3C** shows this process for the 627 automatically segmented neurons in **Figure 3B**. These algorithms are not perfect. As can be observed in **Figure 3B**, right, they will fail to identify *bona-fide* neurons and will identify ROIs that are not actual neurons (akin to type II and type I statistical errors, respectively). By placing further constraints, errors can be minimized, but simple algorithms like the ones described are able to correctly identify a large fraction of neurons within seconds. These methods have been used (Akerboom et al., 2012; Panier et al., 2013) to identify 1000s of neurons in the brain of larval zebrafish. The expression of calcium indicators can also be restricted to the nucleus using a nuclear localization sequence (NLS). This will remove labeling in neuropil and will generally make it easier to segment the signals, simply by identifying particles in the anatomical image (Prevedel et al., 2014). Alternatively, adding a spectrally separated nuclear co-label, for instance by co-expression of a red protein, would help greatly with morphological segmentation for the same reasons.

A second class of algorithms involves functional segmentation. This idea relies on the fact that pixels that belong to the same

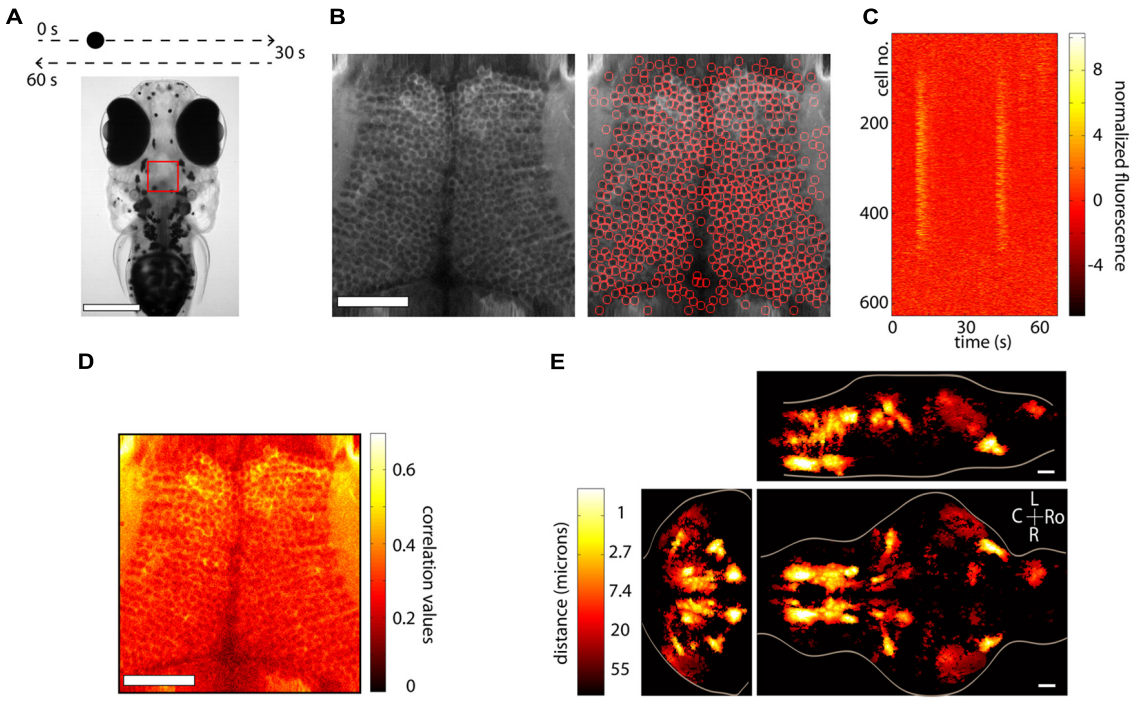

FIGURE 3 | Segmentation and whole-brain imaging. (A) Head of a 7-day-old larval zebrafish that was embedded in agarose and was presented with a visual stimulus: a dot moving at constant speed from left to right of its visual field and then back to the left. The red square shows the area that was imaged at 7.5 Hz in the medial optic tectum. Scale bar = 250 μm. **(B)** Anatomical image of the region imaged, generated by summing all the frames acquired in one plane (left). The image can then be automatically segmented using the methods described in the text (right). In this case 627 neurons were identified. Scale bar = 50 μm. **(C)** Raster plot of the responses of the 627 automatically segmented neurons in **(B)**. **(D)** The method of computing the correlation of the fluorescence time-series of a pixel with its eight neighboring pixels is shown. This image can be used as a basis for determining functionally active cells by determining a threshold (following a shuffling-control) followed by segmentation. **(E)** How similar is activity during behavior across different animals? This question was addressed by imaging the whole brain of 13 behaving larval zebrafish discretized in over 500 × 800 × 400 voxels and then morphing the brains onto a reference brain (Portugues et al., 2014). Functionally active units were segmented using correlation-based methods described in the text. For every active voxel, how far on average must one look in other brains to find a similarly active voxel, i.e., one displaying similar activity patterns? The figure shows that in regions such as the ventral hindbrain neuropil, the cerebellum and certain retinal ganglion cell arborization fields, the answer is surprisingly less than 1 μm. Ro, rostral; L, left; R, right; C, caudal; scale bar = 50 μm.

neuron will have highly correlated fluorescence time-series. Naturally, if a neuron is not active, the time-series of the pixels that comprise it will involve mainly independent noisy fluctuations that will exhibit low correlation. These algorithms will therefore identify contiguous regions that are active in a correlated way. Explicitly the algorithms work as follows. For every pixel one can compute the correlation of its time-series with the sum of the time-series of its eight closest neighbors (in the case of 2D segmentation). This can be repeated for every pixel in the image, such that the result is an anatomical image of correlation values. In **Figure 3D** we perform this analysis for the same dataset as **Figures 3B,C**. This image can then be further processed in one of two ways (potentially following spatial filtering). The easiest way is to perform a threshold operation (set a threshold and set to 0 all the pixels with values below the threshold) and then identify particles within the thresholded image. In this case the threshold can be set either by hand, or more rigorously, by performing a shuffling control, comparing the distributions of the un-shuffled and the shuffled correlations and using the correlation value that implements a certain confidence interval of choice (i.e., this correlation value is 20 times more common in the un-shuffled versus the shuffled data).

Alternatively, the correlation image can be used to determine the seeds of a region-growing algorithm. The first step is to look for local maxima in the correlation image. The highest maximum is then used as a seed of the first ROI, and neighboring pixels are added to the ROI if their correlation with the already existing pixels in the ROI exceeds a threshold, which should ideally be determined by again performing a shuffled control. This process is repeated until no more pixels are aggregated and then one proceeds to the second highest maximum, which becomes the seed of the second ROI. It is once more possible to place constraints on the size and shape of these ROIs to ensure that certain requirements are met, for example, that they have the morphology of neurons. This method will only produce *active* ROIs, as opposed to the anatomical segmentation mentioned before, and has been recently used in (Portugues et al., 2014) to automatically identify 3D ROIs throughout the brains or larval zebrafish.

In the case of the dataset shown in **Figures 3A–D**, this method would not work particularly well to identify individual neurons, because many contiguous neurons are active and would be clumped into the same ROI. On the other hand, using this

algorithm will identify activity in regions which are not morphologically different from their anatomical surrounding, such as neuropil.

No single method is superior to the others and which one should be implemented depends on many factors, such as the biological questions that need to be answered, the specific expression pattern of the indicator or the signal to noise of the measurement. These are by no means the only algorithms possible. Functional segmentation can be performed using maximum DF/F instead of correlation with neighboring pixels as a measure of activity and then centering ROIs that are the size and shape of typical neurons on the spatial locations of maxima that exceed a threshold (Ahrens et al., 2012), methods involving independent component analysis have been developed (Mukamel et al., 2009), and of course it is always possible to mix and match.

CHRONIC IMAGING

Neuronal circuits adapt in response to sensory experience, mature during development and change due to disease processes in time scales which vary from milliseconds to months. While fast events are easily captured with electrophysiology techniques and imaging of synthetic calcium dyes, events that extended more than a few hours in time were up to now hard or impossible to follow due to technical limitations. Long term imaging of structural changes within the nervous system (see e.g., Grutzendler et al., 2002; Trachtenberg et al., 2002) have been performed routinely using anatomic labeling with fluorescent protein variants, but these studies lacked a physiology component. GECIs were soon identified as a suitable means to follow activity of identified groups of neurons in repeated sessions over long periods (for review see Aramuni and Griesbeck, 2013; Lütcke et al., 2013b). After the first demonstration of chronic imaging of sensory induced activity in mouse visual cortex over weeks (Mank et al., 2008) a number of studies have extended the paradigm to other brain areas and increased the intervals between imaging sessions up to a month or longer (Tian et al., 2009; Andermann et al., 2010; Dombeck et al., 2010; Minderer et al., 2012). By now, numerous high-end applications reveal new insights into reconfiguration of network properties as a consequence of learning and plasticity. Huber et al. (2012) followed populations of neurons in motor cortex over weeks while mice learned a new object detection task. They reported strengthening of the task representation at the level of the population, which was stable despite of the dynamics at the single neuron level. In another study (Margolis et al., 2012) populations of neurons in barrel cortex were followed over time after sensory deprivation, demonstrating the power of chronic long term calcium imaging to monitor response dynamics within individual neurons and across whole populations of neurons as they undergo plasticity. Exciting recent papers describe re-organization of population activity in motor cortex after standardized learning of a somatosensory task (Masamizu et al., 2014). With the advent of GECIs with exquisite sensitivities and established biocompatibility it is expected that a plethora of new studies on long term physiology will provide new insights into long standing questions, e.g., on how the brain manages to balance between stable representations and adaptation due to sensory experience, on how it couples sensory input to behavioral output, on how it fine-tunes circuitry during development, how it uses population coding to represent, store and retrieve information of the outside world, and finally also on how pathologic change and circuit dysfunction in the brain is causally manifested.

WHOLE-BRAIN IMAGING

The dream of a systems' neuroscientist is to be able to record the spiking activity (the membrane potential would even be more preferable) of all the neurons in a brain while the animal is actively engaged in a behavior. Recent studies now show that this is a very real possibility, at least in certain model organisms.

The nematode *C. elegans* and the larval zebrafish are transparent organisms, small enough so that a large fraction of their nervous system fits within the field of view of an objective. They have cells that on average range from 3 to 10 microns in diameter, although *C. elegans* have 302 and zebrafish in the order of 150,000. Traditional approaches involving point scanning microscopy required several presentations of the same experimental paradigm per plane in order to determine the calcium response properties of the cells in the imaging plane. However, the signal to noise properties of the latest GECIs (Akerboom et al., 2012; Chen et al., 2013; Thestrup et al., 2014) allows the unambiguous determination of neuronal activity from single trials. This reduces the imaging time by three- to ten-fold, allowing the imaging of a whole brain in the order of 4–10 h, with x, y, and z resolution of ∼1 micron. When dealing with robust behaviors, such as the optokinetic reflex, this can be used to obtain functional maps with single-cell resolution of neuronal activity throughout a single brain and create whole-brain anatomical maps of both stimulus and motor related activity (Portugues et al., 2014). In many instances the neuronal activity shows correlation values with these variables exceeding 0.7. These neuronal networks are sparse, with around 5% of the brain showing consistent activity, yet highly stereotyped across individuals, often within the extent of a single cell body (**Figure 3E**). These experiments revealed some more surprising features, such as spatial gradients of temporal activation along neuropil regions in both the hindbrain and retinal ganglion cell arborization fields, highly asymmetric activity mostly in the left habenula, and a small number of individual cells in the optic tectum which, despite receiving direct retinal input only from the contralateral eye, displayed binocular responses.

Scanning microscopy nevertheless has its limitations. The activity during single trial learning, for example, cannot be observed in every imaging plane. The nuclear targeting of calcium indicators and the implementation of more recently developed volumetric imaging techniques such as fast z-scanning with piezos (Göbel et al., 2007), electrically tunable lenses (Grewe et al., 2011), acousto-optic deflectors (Grewe et al., 2010), light-sheet imaging (Ahrens et al., 2013; Panier et al., 2013), temporal focusing of sculpted light (Schrödel et al., 2013), and light-field imaging (Prevedel et al., 2014) have opened the door to the possibility of monitoring whole-brain activity with an improved temporal resolution: 1 brain every 0.5 s as opposed to every several hours, at the expense of slightly reduced spatial resolution. Although

certain technical difficulties still need to be overcome, it is clear that the calcium indicators now available are contributing to turn the dream into a reality.

OFF-TARGET EFFECTS OF GECIs

A major problem for previous GECIs has been that SNR-optimal indicator concentrations often could not be reached without leading to obvious signs of deterioration of cell health or compromises on indicator function. Indeed, already early versions of Cameleons showed sensor inactivation or formation of aggregates when expressed in transgenic mice (Hasan et al., 2004; Nagai et al., 2004). Contemporary viral or non-viral expression methods (e.g., *in utero* electroporation) lead to high and often steadily increasing chronic expression levels. By comparing the fluorescence of purified protein with the fluorescence of GECI-expressing cells, the actual indicator concentration has been determined under various conditions for GCaMP2 and GCaMP3 (Hires et al., 2008; Huber et al., 2012; Zariwala et al., 2012). Expression levels that are likely to exceed SNR-optimal concentrations have been achieved after 7 weeks of viral transduction of cortical neurons with GCaMP3 (Huber et al., 2012; **Figure 1B**). This high expression level led to breakdown of nuclear exclusion of the indicator in a considerable number of cells, a phenomenon that is known to correlate with clear signs of changed cellular response properties. A variable degree of nuclear filling has been observed for essentially all indicator classes, with the Troponin-based TN-XXL showing the smallest tendency for nuclear accumulation (Tian et al., 2009). Also in the case of GCaMP5 and GCaMP6, long-term high-level expression led to a large number of cells with affected nuclear exclusion and atypical cellular responsiveness (Tian et al., 2009; Akerboom et al., 2012; Chen et al., 2013). Overexpression using AAVs at the viral titers available at public virus repositories led to a steadily increasing fraction of 'filled' cells in mouse visual cortex that correlated with aberrant cellular tuning responses (**Figure 4A**). Further comparative research into the biocompatibility of various GECIs at different expression levels is clearly warranted.

Either by means of changed expression strategies or serendipitous improvement of indicator properties, general cytotoxicity of the GCaMP family of indicators appears to have been reduced over time. Constitutive expression of GCaMP2 in mice led to unwanted phenotypes like cardiac hypertrophy (Tallini et al., 2006), whereas similar effects have not been noted for later conditional or neuron-specific GCaMP2, GCaMP3, and GCaMP5 transgenic mouse lines (Chen et al., 2012; Zariwala et al., 2012; Gee et al., 2014). While GCaMPs were readily expressed in transgenic flies and fish, currently available mouse lines for GCaMP3, however, still suffer from relatively low expression levels, that so far have prevented their widespread use in the community. Early versions of Troponin C based sensors could be expressed functionally and stably in transgenic mice at high levels (Heim et al., 2007), but their lower signal strength made them unsuitable for a number of high end applications. Healthy animal models constitutively or conditionally expressing an SNR-optimal concentration of a high performance GECI would be desirable. The first generation of publicly available mouse lines expressing GCaMP6 (GCaMP6s, GCaMP6f under the Thy1-promoter) has just been released (Dana et al., 2014). GECIs now have reached a state of maturity that makes waiting for the 'next-best' version less tempting. Given suitable expression levels and patterns, we expect that mouse lines like these will become widely popular in the future.

Stably or conditionally expressing animal models greatly simplify imaging by rendering invasive acute transfection methods unnecessary and by improving the repeatability of experiments. Probably even more importantly, they ameliorate issues resulting from the unavoidable ramping up of expression after viral transduction that render long-term chronic imaging of the same cell-populations problematic. Chronic imaging of stably expressing neuronal populations is indispensable, though, to study experience-dependent plasticity on the single cell level. Changes in intracellular calcium determine the sign and amplitude of synaptic plasticity (Shouval et al., 2002). GECI overexpression has therefore always been suspected to affect neuronal plasticity. While plastic changes during learning have now repeatedly been observed using chronic GECI expression over weeks (Huber et al., 2012; Masamizu et al., 2014) and months (Margolis et al., 2012), the observed experience-dependent changes could in principle also have occurred in associated, untransfected upstream circuits. However, experiments on hippocampal slice culture that expressed GCaMP3 at moderate levels have shown that early phase long-term potentiation (LTP) is indistinguishable from non-expressing control (Huber et al., 2012; **Figure 4B**). Still it is necessary that further experiments compare the achievable levels of *in vitro* synaptic plasticity between expressing and non-expressing cells in brain slices from the very animals, brain regions, cell types, and expression levels used for the chronic experiments – ideally accompanied by estimates of added buffer capacity and put in relation to adverse phenomena like nuclear filling.

REASONS FOR RED

The most recent optimization efforts in the field of GECI engineering are centered on expanding the spectral palette of high-performance GECIs. While indicators emitting in the blue range of the visible spectrum have been developed as well (Zhao et al., 2011), most work so far focused on the development of viable probes emitting in the red (Ohkura et al., 2012b; Akerboom et al., 2013; Wu et al., 2013). The reason for this is that red indicators would have desirable properties that go beyond the most obvious advantage of being able to spectrally multiplex different cellular populations expressing GECIs of different color. Current generation GECIs have their single photon excitation maximum around 440–480 nm. This, however, poses a problem if one tries to use these optogenetic sensors together with optogenetic actuators like Channelrhodopsin-2 (ChR2; Akerboom et al., 2013; Wu et al., 2013). While two-photon laser scanning microscopy can be used to largely prevent co-excitation of ChR2 (Zhang and Oertner, 2006), single photon activation of ChR2 inadvertently strongly excites most GECIs due to excitation spectral overlap. This not only affects the functional fluorescence readout but may also lead to unnecessary photobleaching and damage. Red proteins usually require green excitation light (550–560 nm), which renders cross-excitation less critical but not entirely unproblematic: ChR2

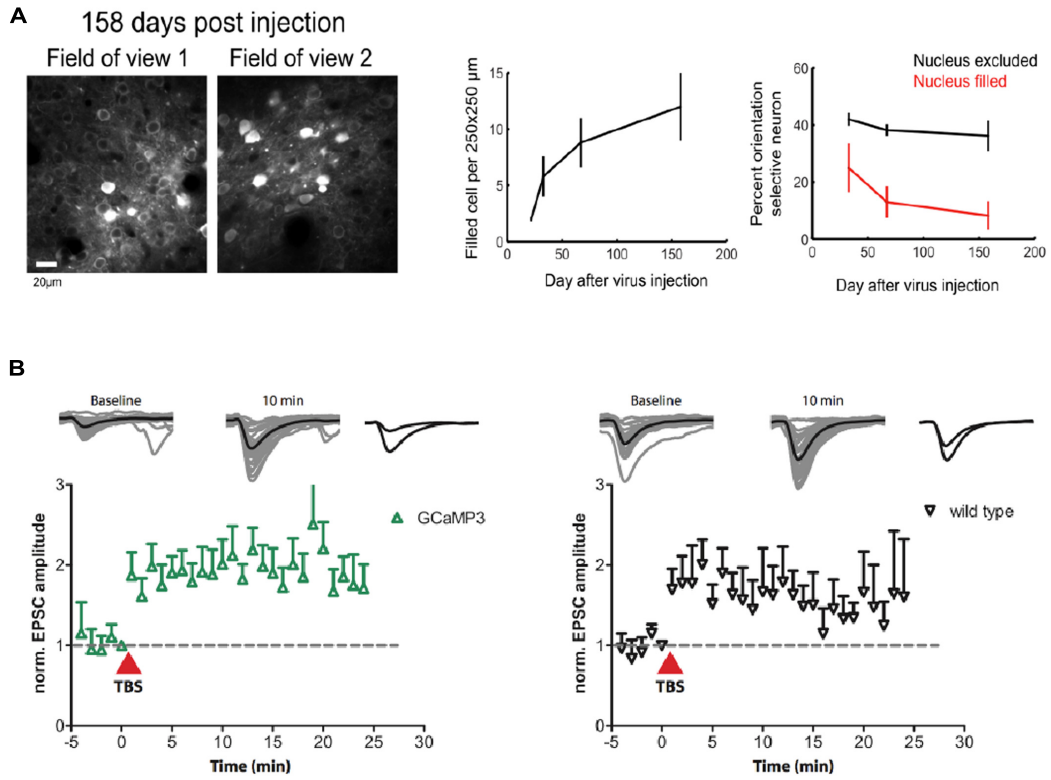

FIGURE 4 | Biocompatibility and off-target effects of GECIs. (A) Long-term high-level expression of a GECI (GCaMP6s) leads to breakdown of nuclear exclusion of the indicator. The number of 'filled' cells is a function of time after viral transduction (middle panel). Cells with 'filled' nucleus show atypical functional responses (right panel): neurons in primary visual cortex with 'filled' nuclei lose their orientation selectivity in response to moving grating stimulation. **(B)** GCaMP3 expression at moderate levels (~15 µM) in CA1 neurons in rat hippocampal slice culture does not affect the early phase of long-term potentiation (LTP) in the short run. [Figures reproduced from Huber et al. (2012) and Chen et al. (2013) with permission (pending)].

can still be effectively excited by intense green light given suitable expression levels (Zhang and Oertner, 2006). A further benefit of red GECIs would be that they would allow imaging deeper with less excitation power. Light scattering is strongly wavelength-dependent. The shorter the wavelength, the higher the probability of photons straying off-course from their ballistic path. As a very coarse approximation, both excitation and emission light (in both the single and two-photon excitation regime) could travel roughly twice as far without being scattered due to refractive index mismatches in brain tissue if excitation and emission light would be shifted 100 nm to the red in comparison to commonly used 'green' probes (Helmchen and Denk, 2005). Further red-shifted probes may even allow for near infrared intravital imaging of Ca^{2+} signals through skin and bone. In addition to increased depth penetration, red-shifted excitation in both single- and two-photon imaging modes leads to a reduction in the background signal resulting from the excitation of autofluorescence, thereby increasing SNR. If the overall GECI fluorescence is low, activity-dependent changes in autofluorescence (e.g., of flavoprotein oxidation) can become a major source of signal contamination. Intrinsic changes in flavoprotein fluorescence are widely used to map cortical responses to sensory stimuli (Shibuki et al., 2003; Michael et al., 2014). The sign of the signal change as well as excitation and emission wavelengths of flavoprotein autofluorescence overlap with those of 'green' GECIs. Red GECIs would therefore be especially helpful for wide-field single photon imaging where the source of the fluorescent signal cannot be confirmed spatially. So far, however, red single fluorophore GECIs like R-GECO and RCaMP have not reached the same performance as their green counterparts and still suffer from low SNR, strong photobleaching and even photoswitching artifacts that have so far prevented their wide-spread use (Yamada and Mikoshiba, 2012; Akerboom et al., 2013; Wu et al., 2013). An alternative might be red-shifted FRET indicators based on new engineered bright green or yellow (as donors) and orange or red fluorescent proteins (as acceptors; Tsutsui et al., 2008; Lam et al., 2012; Shaner et al., 2013). Incorporation into current designs such as "Twitch" indicators will require some substantial re-engineering of the indicators, but further increases in brightness, a better separation of donor and acceptor emission channels and the overall red-shift promise a significant boost in sensitivity of these sensors.

CONCLUSION

Genetically encoded calcium indicators have come a long way since the presentations of the initial designs. Cycles of iterative improvements, biophysical, and structural analysis and testing have led to variants with ever increasing signal strength. Recent engineering efforts have also aimed at both lowering calcium buffering by

the sensors and improving linearity of responses. Finally, large-scale mutagenesis and screening approaches have resulted in high performance variants in both FRET-based and GCaMP indicator families. In particular, these latter efforts provide a viable example for improving some of the other genetically encoded sensors that neuroscience is interested in, for example sensors of membrane potential. With the remaining issues clarified, as pointed out in this article, imaging of GECIs will finally become a tremendously valuable and mature set of tools for analyzing neuronal circuits and their plasticity and pathology.

ACKNOWLEDGMENTS

Ruben Portugues would like to that Michael B. Orger and Claudia E. Feierstein for help with collecting data and extremely useful discussions. Tobias Rose, Pieter M. Goltstein, and Oliver Griesbeck acknowledge Pia Sipilä for support and helpful discussion. We all would like to thank the Max-Planck-Society for support.

REFERENCES

Ahrens, M. B., Li, J. M., Orger, M. B., Robson, D. N., Schier, A. F., Engert, F., et al. (2012). Brain-wide neuronal dynamics during motor adaptation in zebrafish. *Nature* 485, 471–477. doi: 10.1038/nature11057

Ahrens, M. B., Orger, M. B., Robson, D. N., Li, J. M., and Keller, P. J. (2013). Whole-brain functional imaging at cellular resolution using light-sheet microscopy. *Nat. Methods* 10, 413–420. doi: 10.1038/nmeth.2434

Akerboom, J., Carreras Calderón, N., Tian, L., Wabnig, S., Prigge, M., Tolö, J., et al. (2013). Genetically encoded calcium indicators for multi-color neural activity imaging and combination with optogenetics. *Front. Mol. Neurosci.* 6:2. doi: 10.3389/fnmol.2013.00002

Akerboom, J., Chen, T.-W., Wardill, T. J., Tian, L., Marvin, J. S., Mutlu, S., et al. (2012). Optimization of a GCaMP calcium indicator for neural activity imaging. *J. Neurosci.* 32, 13819–13840. doi: 10.1523/JNEUROSCI.2601-12.2012

Andermann, M. L., Kerlin, A. M., and Reid, R. C. (2010). Chronic cellular imaging of mouse visual cortex during operant behavior and passive viewing. *Front. Cell. Neurosci.* 4:3. doi: 10.3389/fncel.2010.00003

Aramuni, G., and Griesbeck, O. (2013). Chronic calcium imaging in neuronal development and disease. *Exp. Neurol.* 242, 50–56. doi: 10.1016/j.expneurol.2012.02.008

Aschauer, D. F., Kreuz, S., and Rumpel, S. (2014). Analysis of transduction efficiency, tropism and axonal transport of AAV serotypes 1, 2, 5, 6, 8 and 9 in the mouse brain. *PLoS ONE* 8:e76310. doi: 10.1371/journal.pone.0076310

Baird, G. S., Zacharias, D. A., and Tsien, R. Y. (1999). Circular permutation and receptor insertion within green fluorescent proteins. *Proc. Natl. Acad. Sci. U.S.A.* 97, 11984–11989. doi: 10.1073/pnas.97.22.11984

Borst, J. G., and Helmchen, F. (1998). Calcium influx during an action potential. *Methods Enzymol.* 293, 352–371. doi: 10.1016/S0076-6879(98)93023-3

Chen, Q., Cichon, J., Wang, W., Qiu, L., Lee, S.-J. R., Campbell, N. R., et al. (2012). Imaging neural activity using Thy1-GCaMP transgenic mice. *Neuron* 76, 297–308. doi: 10.1016/j.neuron.2012.07.011

Chen, T.-W., Wardill, T. J., Sun, Y., Pulver, S. R., Renninger, S. L., Baohan, A., et al. (2013). Ultrasensitive fluorescent proteins for imaging neuronal activity. *Nature* 499, 295–300. doi: 10.1038/nature12354

Dana, H., Chen, T. W., Hu, A., Shields, B. C., Gua, C., Looger, L. L., et al. (2014). Thy1-GCaMP6 transgenic mice for neuronal population imaging in vivo. *PLoS ONE* 9:e108697. doi: 10.1371/journal.pone.0108697

Direnberger, S., Mues, M., Micale, V., Wotjak, C. T., Dietzel, S., Schubert, M., et al. (2012). Biocompatibility of a genetically encoded calcium indicator in a transgenic mouse model. *Nat. Commun.* 3, 1031. doi: 10.1038/ncomms2035

Dombeck, D. A., Harvey, C. D., Tian, L., Looger, L. L., and Tank, D. W. (2010). Functional imaging of hippocampal place cells at cellular resolution during virtual navigation. *Nat. Neurosci.* 13, 1433–1440. doi: 10.1038/nn.2648

Gee, J. M., Smith, N. A., Fernandez, F. R., Economo, M. N., Brunert, D., Rothermel, M., et al. (2014). Imaging activity in neurons and glia with a Polr2a-based and cre-dependent GCaMP5G-IRES-tdtomato reporter mouse. *Neuron* 83, 1058–1072. doi: 10.1016/j.neuron.2014.07.024

Geiger, A., Russo, L., Gensch, T., Thestrup, T., Becker, S., Hopfner, K.-P., et al. (2012). Correlating calcium binding, Förster resonance energy transfer, and conformational change in the biosensor TN-XXL. *Biophys. J.* 102, 2401–2410. doi: 10.1016/j.bpj.2012.03.065

Göbel, W., and Helmchen, F. (2007). In vivo calcium imaging of neural network function. *Physiology (Bethesda)* 22, 358–365. doi: 10.1152/physiol.00032.2007

Göbel, W., Kampa, B. M., and Helmchen, F. (2007). Imaging cellular network dynamics in three dimensions using fast 3D scanning. *Nat. Methods* 4, 73–79. doi: 10.1038/nmeth989

Grewe, B. F., Langer, D., Kasper, H., Kampa, B. M., and Helmchen, F. (2010). High-speed in vivo calcium imaging reveals neuronal network activity with near-millisecond precision. *Nat. Methods* 7, 399–405. doi: 10.1038/nmeth.1453

Grewe, B. F., Voigt, F. F., van't Hoff, M., and Helmchen, F. (2011). Fast two-layer two-photon imaging of neuronal populations using an electrically tunable lens. *Biomed. Opt. Express* 2, 2035–2046. doi: 10.1364/BOE.2.002035

Grutzendler., J., Kasthuri., N., and Gan, W. B. (2002). Long-term dendritic spine stability in the adult cortex. *Nature* 420, 812–816. doi: 10.1038/nature01276

Grynkiewicz, G., Poenie, M., and Tsien, R. Y. (1985). A new generation of Ca^{2+} indicators with greatly improved fluorescence properties. *J. Biol. Chem.* 260, 3440–3450.

Guizar-Sicairos, M., Thurman, S. T., and Fienup, J. R. (2008). Efficient subpixel image registration algorithms. *Opt. Lett.* 33, 156–158. doi: 10.1364/OL.33.000156

Hasan, M. T., Friedrich, R. W., Euler, T., Larkum, M. E., Giese, G., Both, M., et al. (2004). Functional fluorescent Ca^{2+} indicator proteins in transgenic mice under TET control. *PLoS Biol.* 2:e163. doi: 10.1371/journal.pbio.0020163

Heim, N., Garaschuk, O., Friedrich, M. W., Mank, M., Milos, R. I., Kovalchuk, Y., et al. (2007). Improved calcium imaging in transgenic mice expressing a troponin C-based biosensor. *Nat. Methods* 4, 127–129. doi: 10.1038/nmeth1009

Heim, N., and Griesbeck, O. (2004). Genetically encoded indicators of cellular calcium dynamics based on troponin C and green fluorescent protein. *J. Biol. Chem.* 279, 14280–14286. doi: 10.1074/jbc.M312751200

Helmchen, F., and Denk, W. (2005). Deep tissue two-photon microscopy. *Nat. Methods* 2, 932–940. doi: 10.1038/nmeth818

Helmchen, F., Imoto, K., and Sakmann, B. (1996). Calcium buffering and action potential-evoked calcium signaling in dendrites of pyramidal neurons. *Biophys. J.* 70, 1069–1081. doi: 10.1016/S0006-3495(96)79653-4

Hendel, T., Mank, M., Schnell, B., Griesbeck, O., Borst, A., and Reiff, D. F. (2008). Fluorescence changes of genetic calcium indicators and OGB-1 correlated with neural activity and calcium in vivo and in vitro. *J. Neurosci.* 28, 7399–7411. doi: 10.1523/JNEUROSCI.1038-08.2008

Hires, S. A., Tian, L., and Looger, L. L. (2008). Reporting neural activity with genetically encoded calcium indicators. *Brain Cell. Biol.* 36, 69–86. doi: 10.1007/s11068-008-9029-4

Horikawa, K., Yamada, Y., Matsuda, T., Kobayashi, K., Hashimoto, M., Matsuura, T., et al. (2010). Spontaneous network activity visualized by ultrasensitive Ca^{2+} indicators, yellow Cameleon-Nano. *Nat. Methods* 7, 729–732. doi: 10.1038/nmeth.1488

Huber, D., Gutnisky, D. A., Peron, S., O'Connor, D. H., Wiegert, J. S., Tian, L., et al. (2012). Multiple dynamic representations in the motor cortex during sensorimotor learning. *Nature* 484, 473–478. doi: 10.1038/nature11039

Kaiser, K. M. M., Zilberter, Y., and Sakmann, B. (2001). Back-propagating action potentials mediate calcium signalling in dendrites of bitufted interneurons in layer 2/3 of rat somatosensory cortex. *J. Physiol.* 535, 17–31. doi: 10.1111/j.1469-7793.2001.t01-1-00017.x

Kao, J. P., and Tsien, R. Y. (1988). Ca^{2+} binding kinetics of fura-2 and azo-1 from temperature-jump relaxation measurements. *Biophys. J.* 53, 635–639. doi: 10.1016/S0006-3495(88)83142-4

Keller, G. B., Bonhoeffer, T., and Hübener, M. (2012). Sensorimotor mismatch signals in primary visual cortex of the behaving mouse. *Neuron* 74, 809–815. doi: 10.1016/j.neuron.2012.03.040

Kerlin, A. M., Andermann, M. L., Berezovskii, V. K., and Reid, R. C. (2010). Broadly tuned response properties of diverse inhibitory neuron subtypes in mouse visual cortex. *Neuron* 67, 858–871. doi: 10.1016/j.neuron.2010.08.002

Kerr, J. N. D., Greenberg, D., and Helmchen, F. (2005). Imaging input and output of neocortical networks in vivo. *Proc. Natl. Acad. Sci. U.S.A.* 102, 14063–14068. doi: 10.1073/pnas.0506029102

Klausberger, T., and Somogyi, P. (2008). Neuronal diversity and temporal dynamics: the unity of hippocampal circuit operations. *Science* 321, 53–57. doi: 10.1126/science.1149381

Lam, A. J., St-Pierre, F., Gong, Y., Marshall, J. D., Cranfill, P. J., Baird, M. A., et al. (2012). Improving FRET dynamic range with bright green and red fluorescent proteins. *Nat. Methods* 9, 1005–1012. doi: 10.1038/nmeth.2171

Lütcke, H., Gerhard, F., Zenke, F., Gerstner, W., and Helmchen, F. (2013a). Inference of neuronal network spike dynamics and topology from calcium imaging data. *Front. Neural Circuits* 7:201. doi: 10.3389/fncir.2013.00201

Lütcke, H., Margolis, D. J., and Helmchen, F. (2013b). Steady or changing? Long-term monitoring of neuronal population activity. *Trends Neurosci.* 36, 375–384. doi: 10.1016/j.tins.2013.03.008

Lütcke, H., Murayama, M., Hahn, T., Margolis, D. J., Astori, S., Zum Alten Borgloh, S. M., et al. (2010). Optical recording of neuronal activity with a genetically-encoded calcium indicator in anesthetized and freely moving mice. *Front. Neural Circuits* 4:9. doi: 10.3389/fncir.2010.00009

Mank, M., Reiff, D. F., Heim, N., Friedrich, M. W., Borst, A., and Griesbeck, O. (2006). A FRET-based calcium biosensor with fast signal kinetics and high fluorescence change. *Biophys. J.* 90, 1790–1796. doi: 10.1529/biophysj.105.073536

Mank, M., Santos, A. F., Direnberger, S., Mrsic-Flogel, T. D., Hofer, S. B., Stein, V., et al. (2008). A genetically encoded calcium indicator for chronic in vivo two-photon imaging. *Nat. Methods* 5, 805–811. doi: 10.1038/nmeth.1243

Maravall, M., Mainen, Z. F., Sabatini, B. L., and Svoboda, K. (2000). Estimating intracellular calcium concentrations and buffering without wavelength ratioing. *Biophys. J.* 78, 2655–2667. doi: 10.1016/S0006-3495(00)76809-3

Margolis, D. J., Lütcke, H., Schulz, K., Haiss, F., Weber, B., Kügler, S., et al. (2012). Reorganization of cortical population activity imaged throughout long-term sensory deprivation. *Nat. Neurosci.* 15, 1539–1546. doi: 10.1038/nn.3240

Masamizu, Y., Tanaka, Y. R., Tanaka, Y. H., Hira, R., Ohkubo, F., Kitamura, K., et al. (2014). Two distinct layer-specific dynamics of cortical ensembles during learning of a motor task. *Nat. Neurosci.* 17, 987–994. doi: 10.1038/nn.3739

Matthews, E. A., Schoch, S., and Dietrich, D. (2013). Tuning local calcium availability: cell-type-specific immobile calcium buffer capacity in hippocampal neurons. *J. Neurosci.* 33, 14431–14445. doi: 10.1523/JNEUROSCI.4118-12.2013

Michael, N., Bischof, H. J., and Löwel, S. (2014). Flavoprotein autofluorescence imaging of visual system activity in zebra finches and mice. *PLoS ONE* 9:e85225. doi: 10.1371/journal.pone.0085225

Minderer, M., Liu, W., Sumanovski, L. T., Kügler, S., Helmchen, F., and Margolis, D. J. (2012). Chronic imaging of cortical sensory map dynamics using a genetically encoded calcium indicator. *J. Physiol.* 590, 99–107. doi: 10.1113/jphysiol.2011.219014

Miyawaki, A., Griesbeck, O., Heim, R., and Tsien, R. Y. (1999). Dynamic and quantitative calcium measurements using improved cameleons. *Proc. Natl. Acad. Sci. U.S.A.* 96, 2135–2140. doi: 10.1073/pnas.96.5.2135

Miyawaki, A., Llopis, J., Heim, R., McCaffery, J. M., Adams, J. A., Ikura, M., et al. (1997). Fluorescent indicators for Ca^{2+} based on green fluorescent proteins and calmodulin. *Nature* 388, 882–887. doi: 10.1038/42264

Mukamel, E. A., Nimmerjahn, A., and Schnitzer, M. J. (2009). Automated analysis of cellular signals from large-scale calcium imaging data. *Neuron* 63, 747–760. doi: 10.1016/j.neuron.2009.08.009

Nagai, T., Yamada, S., Tominaga, T., Ichikawa, M., and Miyawaki, A. (2004). Expanded dynamic range of fluorescent indicators for Ca^{2+} by circularly permuted yellow fluorescent proteins. *Proc. Natl. Acad. Sci. U.S.A.* 101, 10554–10559. doi: 10.1073/pnas.0400417101

Nakai, J., Ohkura, M., and Imoto, K. (2001). A high signal-to-noise calcium probe comosed of a single green fluorescent protein. *Nat. Biotechnol.* 19, 137–141. doi: 10.1038/84397

Naraghi, M. (1997). T-jump study of calcium binding kinetics of calcium chelators. *Cell Calcium* 22, 255–268. doi: 10.1016/S0143-4160(97)90064-6

Neher, E. (1995). The use of fura-2 for estimating Ca buffers and Ca fluxes. *Neuropharmacology* 34, 1423–1442. doi: 10.1016/0028-3908(95)00144-U

Ohkura, M., Matsuzaki, M., Kasai, H., Imoto, K., and Nakai, J. (2005). Genetically encoded bright calcium probe applicable for dynamic calcium imaging of dendritic spines. *Anal. Chem.* 77, 5861–5869. doi: 10.1021/ac0506837

Ohkura, M., Sasaki, T., Sadakari, J., Gengyo-Ando, K., Kagawa-Nagamura, Y., Kobayashi, C., et al. (2012a). Genetically encoded green fluorescent calcium indicators with improved detectability for neuronal calcium signals. *PLoS ONE* 7:e51286. doi: 10.1371/journal.pone.0051286

Ohkura, M., Sasaki, T., Kobayashi, C., Ikegaya, Y., and Nakai, J. (2012b). An improved genetically encoded red fluorescent calcium indicator for detecting optically evoked action potentials. *PLoS ONE* 7:e39933. doi: 10.1371/journal.pone.0039933

Panier, T., Romano, S. A., Olive, R., Pietri, T., Sumbre, G., Candelier, R., et al. (2013). Fast functional imaging of multiple brain regions in intact zebrafish larvae using selective plane illumination microscopy. *Front. Neural Circuits* 7:65. doi: 10.3389/fncir.2013.00065

Pologruto, T. A., Yasuda, R., and Svoboda, K. (2004). Monitoring neural activity and $[Ca^{2+}]$ with genetically encoded Ca^{2+} indicators. *J. Neurosci.* 24, 9572–9579. doi: 10.1523/JNEUROSCI.2854-04.2004

Portugues, R., Feierstein, C. E., Engert, F., and Orger, M. B. (2014). Whole-brain activity maps reveal stereotyped, distributed networks for visuomotor behavior. *Neuron* 81, 1328–1343. doi: 10.1016/j.neuron.2014.01.019

Prevedel, R., Yoon, Y. G., Hoffmann, M., Pak, N., Wetzstein, G., Kato, S., et al. (2014). Simultaneous whole-animal 3D imaging of neuronal activity using light-field microscopy. *Nat. Methods* 11, 727–730. doi: 10.1038/nmeth.2964

Rancz, E. A., Ishikawa, T., Duguid, I., Chadderton, P., Mahon, S., and Häusser, M. (2007). High-fidelity transmission of sensory information by single cerebellar mossy fibre boutons. *Nature* 450, 1245–1248. doi: 10.1038/nature05995

Schiller, J., Helmchen, F., and Sakmann, B. (1995). Spatial profile of dendritic calcium transients evoked by action potentials in rat neocortical pyramidal neurones. *J. Physiol.* 487 (Pt 3), 583–600.

Schrödel, T., Prevedel, R., Aumayr, K., Zimmer, M., and Vaziri, A. (2013). Brain-wide 3D imaging of neuronal activity in *Caenorhabditis elegans* with sculpted light. *Nat. Methods* 10, 1013–1020. doi: 10.1038/nmeth.2637

Shaner, N. C., Lambert, G. G., Chammas, A., Ni, Y., Baird, M. A., Selland, B. R., et al. (2013). A bright monomeric green fluorescent protein derived from *Branchiostoma lanceolatum*. *Nat. Methods* 10, 407–409. doi: 10.1038/nmeth.2413

Shen, Z., Lu, Z., Chhatbar, P. Y., O'Herron, P., and Kara, P. (2012). An artery-specific fluorescent dye for studying neurovascular coupling. *Nat. Methods* 9, 273–276. doi: 10.1038/nmeth.1857

Shibuki, K., Hishida, R., Murakami, H., Kudoh, M., Kawaguchi, T., Watanabe, M., et al. (2003). Dynamic imaging of somatosensory cortical activity in the rat visualized by flavoprotein autofluorescence. *J. Physiol.* 549, 919–927. doi: 10.1113/jphysiol.2003.040709

Shouval, H. Z., Bear, M. F., and Cooper, L. N. (2002). A unified model of NMDA receptor-dependent bidirectional synaptic plasticity. *Proc. Natl. Acad. Sci. U.S.A.* 99, 10831–10836. doi: 10.1073/pnas.152343099

Sun, X. R., Badura, A., Pacheco, D. A., Lynch, L. A., Schneider, E. R., Taylor, M. P., et al. (2013). Fast GCaMPS for improved tracking of neuronal activity. *Nat. Commun.* 4, 2170. doi: 10.1038/ncomms3170

Tada, M., Takeuchi, A., Hashizume, M., Kitamura, K., and Kano, M. (2014). A highly sensitive fluorescent indicator dye for calcium imaging of neural activity in vitro and in vivo. *Eur. J. Neurosci.* 39, 1720–1728. doi: 10.1111/ejn.12476

Tallini, Y. N., Ohkura, M., Choi, B.-R. R., Ji, G., Imoto, K., Doran, R., et al. (2006). Imaging cellular signals in the heart in vivo: cardiac expression of the high-signal Ca2+ indicator GCaMP2. *Proc. Natl. Acad. Sci. U.S.A.* 103, 4753–4758. doi: 10.1073/pnas.0509378103

Tay, L. H., Griesbeck, O., and Yue, D. T. (2007). Live-cell transforms between Ca^{2+} transients and FRET responses for a troponin-C-based Ca^{2+} sensor. *Biophys. J.* 93, 4031–4040. doi: 10.1529/biophysj.107.109629

Thestrup, T., Litzlbauer, J., Bartholomäus, I., Mues, M., Russo, L., Dana, H., et al. (2014). Optimized ratiometric calciumsensors for functional in vivo imaging of neurons and T-lymphocytes. *Nat. Methods* 11, 175–182. doi: 10.1038/nmeth.2773

Tian, L., Hires, S. A., Mao, T., Huber, D., Chiappe, M. E., Chalasani, S. H., et al. (2009). Imaging neural activity in worms, flies and mice with improved GCaMP calcium indicators. *Nat. Methods* 6, 875–881. doi: 10.1038/nmeth.1398

Trachtenberg, J. T., Chen, B. E., Knott, G. W., Feng, G., Sanes, J. R., Welker, E., et al. (2002). Long-term in vivo imaging of experience-dependent

synaptic plasticity in adult cortex. *Nature* 420, 788–794. doi: 10.1038/nature01273

Tsutsui, H., Karasawa, S., Okamura, Y., and Miyawaki, A. (2008). Improving membrane voltage measurements using FRET with new fluorescent proteins. *Nat. Methods* 5, 683–685. doi: 10.1038/nmeth.1235

Vogelstein, J. T., Watson, B. O., Packer, A. M., Yuste, R., Jedynak, B., and Paninski, L. (2009). Spike inference from calcium imaging using sequential Monte Carlo methods. *Biophys. J.* 97, 636–655. doi: 10.1016/j.bpj.2008.08.005

Wilt, B. A., Fitzgerald, J. E., and Schnitzer, M. J. (2013). Photon shot noise limits on optical detection of neuronal spikes and estimation of spike timing. *Biophys. J.* 104, 51–62. doi: 10.1016/j.bpj.2012.07.058

Wu, J., Liu, L., Matsuda, T., Zhao, Y., Rebane, A., Drobizhev, M., et al. (2013). Improved orange and red Ca^{2+} indicators and photophysical considerations for optogenetic applications. *ACS Chem. Neurosci.* 4, 963–972. doi: 10.1021/cn400012b

Yamada, Y., and Mikoshiba, K. (2012). Quantitative comparison of novel GCaMP-type genetically encoded Ca^{2+} indicators in mammalian neurons. *Front. Cell. Neurosci.* 6:41. doi: 10.3389/fncel.2012.00041

Yasuda, R., Nimchinsky, E. A., Scheuss, V., Pologruto, T. A., Oertner, T. G., Sabatini, B. L., et al. (2004). Imaging calcium concentration dynamics in small neuronal compartments. *Sci. STKE* 2004, pl5.

Zariwala, H. A., Borghuis, B. G., Hoogland, T. M., Madisen, L., Tian, L., De Zeeuw, C. I., et al. (2012). A Cre-Dependent GCaMP3 reporter mouse for neuronal imaging in vivo. *J. Neurosci.* 32, 3131–3141. doi: 10.1523/JNEUROSCI.4469-11.2012

Zhang, Y.-P. P., and Oertner, T. G. (2006). Optical induction of synaptic plasticity using a light-sensitive channel. *Nat. Methods* 4, 139–141. doi: 10.1038/nmeth988

Zhao, Y., Araki, S., Wu, J., Teramoto, T., Chang, Y.-F., Nakano, M., et al. (2011). An expanded palette of genetically encoded Ca^{2+} indicators. *Science* 333, 1888–1891. doi: 10.1126/science.1208592

Zhou, Z., and Neher, E. (1993). Mobile and immobile calcium buffers in bovine adrenal chromaffin cells. *J. Physiol.* 469, 245–273.

Conflict of Interest Statement: The authors declare that the research was conducted in the absence of any commercial or financial relationships that could be construed as a potential conflict of interest.

Received: 19 August 2014; paper pending published: 07 September 2014; accepted: 29 October 2014; published online: 18 November 2014.

Citation: Rose T, Goltstein PM, Portugues R and Griesbeck O (2014) Putting a finishing touch on GECIs. Front. Mol. Neurosci. 7:88. doi: 10.3389/fnmol.2014.00088

This article was submitted to the journal Frontiers in Molecular Neuroscience.

frontiers in
MOLECULAR NEUROSCIENCE

OPINION ARTICLE
published: 25 November 2014
doi: 10.3389/fnmol.2014.00090

Genetically encoded Ca^{2+} indicators; expanded affinity range, color hue and compatibility with optogenetics

Takeharu Nagai[1,2]*, Kazuki Horikawa[3], Kenta Saito[4] and Tomoki Matsuda[1]

[1] *Department of Biomolecular Science and Engineering, The Institute of Scientific and Industrial Research, Osaka University, Osaka, Japan*
[2] *PRESTO, Japan Science and Technology Agency, Tokyo, Japan*
[3] *Division for Bioimaging, Institute of Health Biosciences, The University of Tokushima Graduate School, Tokushima, Japan*
[4] *Department of Systems Neuroscience, Centre for Brain Integration Research, Tokyo Medical and Dental University Graduate School of Medical and Dental Sciences, Bunkyo-ku, Tokyo, Japan*
**Correspondence: ng1@sanken.osaka-u.ac.jp*

Edited by:
Katsuhiko Mikoshiba, RIKEN Brain Science Institute, Japan

Reviewed by:
Christian D. Wilms, University College London, UK
Hideaki Mizuno, KU Leuven, Belgium

Keywords: genetically encoded calcium ion indicator, Ca^{2+} imaging, FRET, fluorescence, bioluminescence

INTRODUCTION

Fluorescent protein-based indicators are invaluable tools for functional imaging of living cells and organisms. Genetically encoded calcium indicators (GECIs) such as derivatives of yellow cameleons (YCs) and GCaMPs/pericams (Miyawaki et al., 1997; Nagai et al., 2001; Nakai et al., 2001) are a highly advanced class of indicators. Continued efforts for improvement of the performance of GECIs have resulted in brighter indicators with better photostability and expanded dynamic range, thus improving the sensitivity of detection. Fine-tuning of other properties, including Ca^{2+} affinity and Hill constant, have also contributed to increase the detectability of Ca^{2+} dynamics. Emerging optogenetic technology has forced the spectrally compatible GECI color variants. In this *opinion*, we highlight the recent development of GECIs including photo-switchable Ca^{2+} indicators and bioluminescence-based Ca^{2+} indicator, mainly invented in our group, focusing especially on the parameters determining their performance in order to provide a guideline for the selection of appropriate GECI for a given experiment.

AFFINITY VARIANT

After the first reports regarding design concept of YCs and GCaMPs/pericams (Miyawaki et al., 1997; Nagai et al., 2001; Nakai et al., 2001), their properties have been modified in term of dynamic range of signal change, pH sensitivity and color hue, and so on. However, application of these GECIs had been still limited in certain experimental targets. One of the critical limitations of these GECIs was their relatively poor repertoire of affinity variants. Because the Ca^{2+} concentration ($[Ca^{2+}]$) at resting state and the amplitude of $[Ca^{2+}]$ change differ significantly within the subcellular locations, cell types, and organisms, a diverse set of affinity variants of GECIs covering dissociation constants (K_ds) from nM to mM would be needed for studying a wide range of research targets.

While moderate- and low-affinity variants of YCs ($K_d > 0.1\,\mu M$) were developed successfully by either site-directed mutagenesis of the Ca^{2+} binding domain in the indicator (Miyawaki et al., 1997) or by the rearrangement of the overall molecular structure of the indicator (Truong et al., 2001) (**Table 1**), there was no systematic way for engineering a high-affinity variant. *In vitro* analysis revealed that free calmodulin (CaM) and its binding peptide M13 had much higher Ca^{2+} affinity (K_d of 20 nM) than that of the CaM and M13 fusion protein linked with two amino acid linkers (K_d of 80 nM) (Porumb et al., 1994). This suggested that steric hindrance might prevent efficient interaction of Ca^{2+}-CaM with M13 in YCs. This possibility was examined by serial increment of the length of the linker from 2 to 5 amino acids. Flexible linkers with 3, 4, and 5 amino acids yielded K_ds of 60 nM, 30 nM, and 15 nM, respectively. Linker elongation also worked for YC 3.60, yielding five YC variants covering K_ds from 15 nM to 140 nM (**Table 1**). These affinity variants of YCs called YC-Nano showed increased sensitivity and could detect subtle changes in $[Ca^{2+}]$ in pyramidal neurons (Horikawa et al., 2010; Yamada et al., 2011) (**Table 1**), becoming an ideal toolbox to efficiently monitor the novel Ca^{2+} dynamics in cases where the concentration range of Ca^{2+} is poorly described (**Table 1**). Recent identification of Ca^{2+} twinkle, which is a localized Ca^{2+} transient in the fine astrocytic processes, is one of the examples (Kanemaru et al., 2014).

So far, high-affinity variants of the GCaMP and pericam families are not available (smallest K_d of 160 nM for B-GECO) (Zhao et al., 2011) (**Table 1**). Although these single FP-based Ca^{2+} indicators have distinct structural design unlike YCs, it will be interesting to examine whether elongation of linkers, which connect the sensor modules, contributes to increased Ca^{2+} affinity, as in the case of YC-Nano.

POSSIBLE SIDE EFFECTS OF GECI

One might worry that the strong Ca^{2+} chelating effect of YC-Nano would affect endogenous Ca^{2+} homeostasis. Depletion of target molecules or ions by loaded indicators is often problematic for imaging of non-buffered signaling molecules, such as cyclic nucleotides and NO, but this is not the case for Ca^{2+}. Like H^+, cytosolic free $[Ca^{2+}]$ is maintained

Table 1 | *In vitro* properties of color variants of single-FP GECIs, selected.

Indicator	Backbone	Ex/Em apo.	Ex/Em sat.	*D*	K_d, μM	*n*	τ, ms	p$K_a$apo./ sat.	References
YC2.60	ECFP, cp173Venus	430/480(530)	–	6.6	0.04	2.4	–	–	Nagai et al., 2004
YC3.60	ECFP, cp173Venus	430/480(530)	–	6.6	0.25 |0.22/0.78	1.7 |3.6/1.2	2940	–	Nagai et al., 2004 |Horikawa et al., 2010
YC4.60	ECFP, cp173Venus	430/480(530)	–	4.6	0.06/14.4	1.7/0.9	–	–	Nagai et al., 2004
YC-Nano140	ECFP, cp173Venus	430/480(530)	–	14	0.14/0.75	2.0/0.9	3030	–	Horikawa et al., 2010
YC-Nano65	ECFP, cp173Venus	430/480(530)	–	14	0.06/1.4	1.6/1.8	–	–	Horikawa et al., 2010
YC-Nano50	ECFP, cp173Venus	430/480(530)	–	13.5	0.05/0.4	2.5/1.0	–	–	Horikawa et al., 2010
YC-Nano30	ECFP, cp173Venus	430/480(530)	–	13.5	0.03/0.2	2.4/1.3	–	–	Horikawa et al., 2010
YC-Nano15	ECFP, cp173Venus	430/480(530)	–	15.5	0.016/0.3	3.1/0.6	–	–	Horikawa et al., 2010
D2cpV	ECFP, cp173Venus	430/480(535)	–	5.3	0.03/3.0	–	–	–	Palmer et al., 2006
D3cpV	ECFP, cp173Venus	430/480(535)	–	5.1	0.6	–	–	–	Palmer et al., 2006
D4cpV	ECFP, cp173Venus	430/480(535)	–	3.8	64	–	–	–	Palmer et al., 2006
TN-L15	ECFP, Citrine	430/480(535)	–	2.4	1.2	1	1330	–	Heim and Griesbeck, 2004
TN-XL	ECFP, cp174Citrine	430/480(535)	–	5	2.5	1.7	240	–	Mank et al., 2006
TN-XXL	ECFP, cp174Citrine	430/480(535)	–	3.3	0.8	1.5	620	–	Mank et al., 2008
PA-TNXL	PA-GFP, cp173DimVenus	504/517	–	0.18	0.22	1.4	–	–	Matsuda et al., 2013
GFP-Aequorin	Aequorin, EGFP	– /510	–	–	–	–	–	–	Baubet et al., 2000
BRAC	Venus, RLuc8	– /480(530)	–	0.6	1.9	1.3	210	–	Saito et al., 2010
Nano-lantern (Ca^{2+}), CaM-2G	Venus, RLuc8_S257G	– /530	–	2	0.08/0.31	3.5/1.4	–	–	Saito et al., 2012
Nano-lantern (Ca^{2+}), CaM-2GS	Venus, RLuc8_S257G	– /530	–	2	0.054/0.29	3.5/1.6	–	–	Saito et al., 2012
Nano-lantern (Ca^{2+}), CaM-4GS	Venus, RLuc8_S257G	– /530	–	2	0.017/0.354	1.9/1.7	–	–	Saito et al., 2012
Nano-lantern (Ca^{2+}), CaM(E104Q)-2G	Venus, RLuc8_S257G	– /530	–	2	0.62	1.4	–	–	Saito et al., 2012
Nano-lantern (Ca^{2+}), CaM(E104Q)-3GS	Venus, RLuc8_S257G	– /530	–	2	0.32	1.4	–	–	Saito et al., 2012
Nano-lantern (Ca^{2+}), CaM(E104Q)-4GS	Venus, RLuc8_S257G	– /530	–	2	0.065/0.321	2.5/0.7	–	–	Saito et al., 2012
G-GECO1	GCaMP3	496*/512	496*/512	26	0.75	3	700	10.0/7.6	Zhao et al., 2011
G-GECO1.1	GCaMP3 x mApple	496*/512	496*/512	27	0.62	2	700	10.0/7.5	Zhao et al., 2011
G-GECO1.2	GCaMP3 x f-pericam x mApple	498*/513	498*/513	24	1.15	2.1	700	10.0/7.2	Zhao et al., 2011
B-GECO	GCaMP3 x f-pericam x mApple	378* /446	378* /446	8	0.16	2.6	490	10.0/5.6	Zhao et al., 2011
R-GECO	cp146mApple	577*/600	561*/589	17	0.48	2	752 |173	10.0/6.6	Zhao et al., 2011 |Akerboom et al., 2013
GEX-GECO1	GCaMP3 x f-pericam x mApple	397* /512	390*/ 506	27	0.32	2.8	1030	6.0	Zhao et al., 2011
GEM-GECO1	GCaMP3 x f-pericam x mApple	397* / 511	390*/455	111	0.34	2.9	225	6.2	Zhao et al., 2011
R-CaMP1.07	R-GECO	–	562*/ 584	28.7	∼ 0.15	–	920	–	Ohkura et al., 2012
BCaMP1c	cpBFP	–	–	2	0.5	2.7	–	5.1/4.2	Akerboom et al., 2013
CyCaMP1b	cpCFP	–	–	2.6	0.42	1.7	–	7.1/8.9	Akerboom et al., 2013
YCaMP1b	cpYFP	–	–	9.2	0.8	1.7	–	7.1/8.9	Akerboom et al., 2013
RCaMP1h	cp159mRuby	575*/602	571*/594	10.5	1.3	2.5	410	– /4.9	Akerboom et al., 2013

(Continued)

Table 1 | Continued

Indicator	Backbone	Ex/Em apo.	Ex/Em sat.	*D*	K_d, μM	*n*	τ, ms	p$K_a$apo./ sat.	References
GR-GECO1.1	cpmMaple145								Hoi et al., 2013
(Green)		487/508	491/506	3.4	0.086	2.0	1866	9.0/8.5	
(red)		559/582	564/583	3.2	0.054	2.6	1718	8.3/7.8	
GR-GECO1.2	cpmMaple145								Hoi et al., 2013
(Green)		488/506	488/506	2.2	0.074	1.7	–	9.2/8.8	
(red)		558/581	558/582	4.6	0.090	1.7	–	8.4/7.5	
	Backbone	Ex/Em apo.	Ex/Em sat.	*D*	K_d, μM	*n*	τ, ms	p$K_a$apo./ sat.	references

*Ex/Em, excitation and emission wavelength; apo/sat, Ca^{2+}-free/saturated condition; D, dynamic range; K_d, dissociation constant; n, Hill constant; τ, time constant of the dissociation reaction at 20–25° C, pK_a, acidity constant at room temperature (20–25° C). Dissociation time constant is given by $\tau = \Theta/k_{off}$, assuming $\Theta = 1$. * for Ex is a peak absorption. Values from different references are separated by vertical bar. Modified from Pérez Koldenkova and Nagai (2013).*

dynamically through the balancing action of Ca^{2+} buffers (i.e., Ca^{2+} binding proteins), which exist in abundance within the cell. Of course, excessive loading of Ca^{2+} indicator/chelator beyond the buffering capacity of these buffers does affect cellular Ca^{2+} homeostasis. In cases where more than mM concentrations of EGTA were loaded to observe subcellularly localized Ca^{2+}, Ca^{2+} puffs and blips were generated (Cheng and Lederer, 2008). Moderate loading/expression at sub-μM concentration of YC-Nano never affected the viability of fish embryos including a set of neurons (Horikawa et al., 2010).

On the other hand, functional interference of GECIs with endogenous Ca^{2+} binding proteins and their targets could pose a problem. The CaM of YCs potentially trans-activate endogenous CaM targets. *In vitro* analysis reported that excessive amounts of CaM affect the dynamic range of conventional YCs in a dose-dependent manner (Palmer et al., 2006). To avoid these side effects, computational re-design of Ca^{2+} sensing motifs was performed. Modified binding interface of the synthetic CaM and its target prevented intermolecular interaction. The resulting YCs, named D2/3/4cpV, have been demonstrated to be insensitive to large excesses of CaM, while maintaining a K_d of 0.03–64 μM and a large dynamic range of 3.8- to 5.3-fold (Palmer et al., 2006) (**Table 1**).

An alternate way to avoid uncontrolled interaction of GECI with endogenous proteins is to employ a different Ca^{2+}-binding motif. While CaM has a variety of downstream targets, troponin C (TnC), a skeletal and cardiac muscle-specific Ca^{2+}-binding protein, is known to limit its interaction to just troponin I and troponin T. Indicators incorporating TnC from avian skeletal muscle or human cardiac muscle were generated, based on molecular design similar to that of cameleon. The resulting TN-L15 and TN-hTnC displayed a moderate Ca^{2+} affinity but a lower Ca^{2+} specificity (due to its cross reactivity with Mg^{2+}) and a small signal change (due to the lack of its binding peptide which enhances the conformational change of sensor motif) (Heim and Griesbeck, 2004) (**Table 1**). As with YCs, further improvements have been introduced to TN-L15. Mg^{2+} reactivity was eliminated by site directed mutagenesis on TnC, and the dynamic range was increased by replacing the Citrine acceptor with its cp174 variant, eventually yielding TN-XL (Mank et al., 2006). Low affinity of TN-XL was improved in TN-XXL by replacing TnC moiety with a concatenate of its high affinity C-lobe (**Table 1**). Although the *in vitro* dynamic range of TN-XXL was small, its *in vivo* performance was acceptable, suggesting the advantages of using TnC with reduced interference (Mank et al., 2008) (**Table 1**).

PHOTOACTIVATABLE GECI

To visualize Ca^{2+} dynamics in specific cell types, tissues, or organs, targeted expression of GECI gene is imperative. Although many promoters for cell/tissue/organ-specific expression are available, they do not cover all types of cell/tissue/organ. Photoswitchable GECIs (PS-GECI) can help overcome this limitation. Fluorescence status of PS-GECIs can be switched through light irradiation in arbitrary cell/tissue/organ, enabling cell/tissue/organ-specific visualization of Ca^{2+} dynamics. This "highlighted Ca^{2+} imaging" is beneficial in elucidating the activity of a single cell in the convoluted cell population of the neuronal network. There are only two reported PS-GECIs: a photoactivatable GECI, PA-TNXL (Matsuda et al., 2013), and a photoconvertible GECI, GR-GECO (Hoi et al., 2013) (**Supplementary Image 1**). The PA-TNXL was developed by replacing the donor and the acceptor fluorescent proteins in the TN-XL with a PA-GFP (photoactivatable GFP) and a dim yellow fluorescent protein DimVenus, respectively (**Supplementary Image 1A** and **Table 1**). Fluorescence of PA-TNXL can be switched on by violet light (∼ 400 nm) irradiation. The fluorescence of the photoactivated PA-TNXL dims upon Ca^{2+} binding. GR-GECO has a similar design as GCaMPs/pericams. It has an mMaple, which can change fluorescence wavelength from green to red on being irradiated with violet light (∼ 400 nm) (McEvoy et al., 2012; Hoi et al., 2013) (**Supplementary Image 1B** and **Table 1**). The intensity of both green and red fluorescence gets brighter with increase in $[Ca^{2+}]$. For a wider range of applications, new PS-GECIs showing larger change in fluorescence intensity on photostimulation, higher dynamic range, broader Ca^{2+} affinity range, and/or reversible photoswitching are required.

GECIs FOR OPTOGENETICS

In neuroscience, a paradigm shift has been brought about by optogenetics. Channel rhodopsin (ChR), a light-gated ion channel, and halorhodopsin (HR), a pump, allow us to control the activity of neural circuits with fine spatio-temporal resolution (Boyden et al., 2005; Zhang et al., 2007). As ChR and HR are activated by blue (400–500 nm) and yellow (500–600 nm) light, respectively; spectrally separated GECIs are necessary for combinatorial application of optogenetics with Ca^{2+} imaging. GECOs are the first reported color variants of single-FP GECIs based on cpGFPs and cpmApple (Zhao et al., 2011). Large-scale screening carried out by utilizing bacterial periplasmic expression system helped identify blue and red color variants of GECOs, including green and ratio metric alternates. In addition to the expanded color pallet, GECOs are also show sizable signal change (111-fold for GEM-GECO1), sensitizing them for the detection of subtle Ca^{2+} response. Structure guided evolution of GCaMP yielded BCaMP1c, CyCaM1a, YCaMP1b, and a series of RCaMPs (Akerboom et al., 2013). Compatibility of GECI color variants with optogenetic control was demonstrated by using CA3 pyramidal neuron co-expressing ChR2 and RCaMP1.07, which was in turn developed by the site-directed mutagenesis of R-GECO1 (Ohkura et al., 2012).

Bioluminescence-based Ca^{2+} imaging is an alternate and ideal strategy that is highly compatible with optogenetics. As bioluminescent indicators do not require excitation with light, observation can be free from functional crosstalk between optogenetic actuators. The limitation of this indicator was their dim signal as in the case of Ca^{2+} sensitive Aequorin and its emission-enhanced variants such as GA (Baubet et al., 2000). A considerable increase of emission signal was, however, achieved in BRAC and Nano-lantern (Ca^{2+}), the latest version of bioluminescence-based GECIs (Saito et al., 2010, 2012) (**Supplementary Image 1C** and **Table 1**). BRAC is the cameleon like fluorescence resonance energy transfer (FRET)-based indicator harboring CaM-M13 moiety fused with an improved luciferase (RLuc8) derived from *Renilla reniformis*, which acts as a donor, and Venus, which acts as an acceptor. BRAC displays Ca^{2+} dependent FRET emission change (**Supplementary Image 1C**, left). Using BRAC, Ca^{2+} signaling was successfully visualized in plant leaves, in which fluorescence-based Ca^{2+} indicators cannot be applied due to their strong autofluorescence and intrinsic photosensitivity.

Nano-lantern (Ca^{2+}) was constructed by direct fusion of Venus with RLuc8, which is split by insertion of CaM-M13. Ca^{2+} binding to CaM-M13 induces reconstitution of the split Rluc8. This leads to FRET from reconstituted Rluc to Venus, resulting in a large increase in emission signal (**Supplementary Image 1C**, right and **Table 1**). Thus, Ca^{2+} dynamics is monitored as a total intensity change, from both RLuc8 and FRET-enhanced emission of Venus. In the state-of-the-art demonstration by using cultured hippocampal neurons, Ca^{2+}, transiently triggered by photo-activated ChR2, were imaged at 10 Hz with high SNR, showing the good compatibility of bioluminescence imaging with optogenetics (Saito et al., 2012) (**Supplementary Images 1D,E**).

CONCLUSION AND PERSPECTIVE

GECIs are advantageous over synthetic Ca^{2+} dyes in their targetability and reliability for chronic imaging. However, there remains room for further improvement on several parameters. Suboptimal kinetic property, non-linearity due to cooperativity, and pH sensitivity of single-FP based indicator should be improved to perform reliable detection of Ca^{2+}. The future development of GECI is, regardless of the faults, promising, because of its evolvability. As a result of the past and the current attempts, not only have the basic property of GECIs been optimized, but also of new family of GECIs have been successfully developed, including color variants and self-illuminating GECIs. Future experiments will focus on improving the compatibility of GECIs with optogenetic tools. GECIs, used in collaboration with latest imaging platform such as a deep tissue imaging and ultra-fast and large-scale recording systems, will pave way to deepening our understanding of the supple ability our brain to learn and to memorize.

ACKNOWLEDGMENTS

The authors would like to acknowledge funding from Grant-in-Aid for Scientific Research on Innovative Areas, "Spying minority in biological phenomena" (No. 3306) from MEXT, a grant from the Cooperative Research Program of "Network Joint Research Center for Medical Devices," and PRESTO and SENTAN from JST.

SUPPLEMENTARY MATERIAL

The Supplementary Material for this article can be found online at: http://www.frontiersin.org/journal/10.3389/fnmol.2014.00090/abstract

Supplementary Image S1 | Schematic representation of photoactivatable, photoconvertible or bioluminescent Ca^{2+} indicators. (A) PA-TNXL is composed of a troponin C (TnC) linked to a photoactivatable GFP (PA-GFP) at the N-terminal and a dim variant of Venus (DimVenus) at the C-terminal. On violet light irradiation, TnC starts fluorescing green. As the Ca^{2+} concentration increases, the intensity of fluorescence decreases proportionately due to FRET from PA-GFP to DimVenus **(B)** GR-GECO was developed from a photoconvertible FP mMaple, whose fluorescence changes from green to red on violet light irradiation. Circular permutation was introduced into mMaple and then linked to calmodulin (CaM) and M13 to create GR-GECO. The fluorescence in both green and red state increases proportionally with an increase in Ca^{2+} concentration. **(C)** A schematic representation of bioluminescence-based GECIs BRAC and Nano-lantern (Ca^{2+}) for detecting Ca^{2+}: Calmodulin (CaM) and M13 are used as Ca^{2+} binding domain for both of them. (Left) BRAC has Venus and RLuc8 at N- and C-terminal of CaM-M13, respectively. It causes wavelength shift from cyan to yellow thorough FRET on Ca^{2+} biding. (Right) A split RLuc is used for Nano-lantern (Ca^{2+}). Each half of RLuc is linked to the terminals of CaM-M13. Compaction of CaM-M13 by Ca^{2+} binding reconstitutes the whole structure of RLuc, and luminescence intensity increases. Luminescence from RLuc is enhanced by VenusΔC10 located at N-terminal of the Nano-lantern (Ca^{2+}). An increase in Ca^{2+} can therefore be observed as FRET results in an increase in the intensity of yellow fluorescence. **(D, E)** Ca^{2+} imaging in the rat hippocampal neuron co-expressing Nano-lantern (Ca^{2+}) and ChR2. **(D)** Ratio image (L/L_0) of the Nano-lantern (Ca^{2+}) without (i and iii) and with (ii and iv) activation of ChR2. **(E)** Time course of the ratio change. ChR2 is activated during the time period marked in gray.

REFERENCES

Akerboom, J., Carreras Calderón, N., Tian, L., Wabnig, S., Prigge, M., Tolö, J. et al. (2013). Genetically encoded calcium indicators for multi-color neural activity imaging and combination with optogenetics. *Front. Mol. Neurosci.* 6:2. doi: 10.3389/fnmol.2013.00002

Baubet, V., Le Mouellic, H., Campbell, A. K., Lucas-Meunier, E., Fossier, P., and Brúlet, P. (2000). Chimeric green fluorescent protein-aequorin as bioluminescent Ca^{2+} reporters at the single-cell level. *Proc. Natl. Acad. Sci. U.S.A.* 97, 7260–7265. doi: 10.1073/pnas.97.13.7260

Boyden, E. S., Zhang, F., Bamberg, E., Nagel, G., and Deisseroth, K. (2005). Millisecond-timescale, genetically targeted optical control of neural activity. *Nat. Neurosci.* 8, 1263–1268. doi: 10.1038/nn1525

Cheng, H., and Lederer, W. J. (2008). Calcium sparks. *Physiol. Rev.* 88, 1491–1545. doi: 10.1152/physrev.00030.2007

Heim, N., and Griesbeck, O. (2004). Genetically encoded indicators of cellular calcium dynamics based on troponin C and green fluorescent protein. *J. Biol. Chem.* 279, 14280–14286. doi: 10.1074/jbc.M312751200

Hoi, H., Matsuda, T., Nagai, T., and Campbell, R. E. (2013). Highlightable Ca^{2+} indicators for live cell imaging. *J. Am. Chem. Soc.* 135, 46–49. doi: 10.1021/ja310184a

Horikawa, K., Yamada, Y., Matsuda, T., Kobayashi, K., Hashimoto, M., Matsu-ura, T., et al. (2010). Spontaneous network activity visualized by ultra-sensitive Ca^{2+} indicators, yellow Cameleon-Nano. *Nat. Methods* 7, 729–732. doi: 10.1038/nmeth.1488

Kanemaru, K., Sekiya, H., Xu, M., Satoh, K., Kitajima, N., Yoshida, K., et al. (2014). *In vivo* visualization of subtle, transient, and local activity of astrocytes using an ultrasensitive Ca2+ indicator. *Cell Rep.* 8, 311–318. doi: 10.1016/j.celrep.2014.05.056

Mank, M., Reiff, D. F., Heim, N., Friedrich, M. W., Borst, A., and Griesbeck, O. (2006). A FRET-based calcium biosensor with fast signal kinetics and high fluorescence change. *Biophys. J.* 90, 1790–1796. doi: 10.1529/biophysj.105.073536

Mank, M., Santos, A. F., Direnberger, S., Mrsic-Flogel, T. D., Hofer, S. B., Stein, V., et al. (2008). A genetically encoded calcium indicator for chronic *in vivo* two-photon imaging. *Nat. Methods* 5, 805–811. doi: 10.1038/nmeth.1243

Matsuda, T., Horikawa, K., Saito, K., and Nagai, T. (2013). Highlighted Ca^{2+} imaging with a genetically encoded 'caged' indicator. *Sci. Rep.* 3:1398. doi: 10.1038/srep01398

McEvoy, A. L., Hoi, H., Bates, M., Platonova, E., Cranfill, P. J., Baird, M. A., et al. (2012). mMaple: a photoconvertible fluorescent protein for use in multiple imaging modalities. *PLoS ONE* 7:e51314. doi: 10.1371/journal.pone.0051314

Miyawaki, A., Llopis, J., Heim, R., McCaffery, J. M., Adams, J. A., Ikura, M., et al. (1997). Fluorescent indicators for Ca^{2+} based on green fluorescent proteins and calmodulin. *Nature* 388, 882–887. doi: 10.1038/42264

Nagai, T., Sawano, A., Park, E. S., and Miyawaki, A. (2001). Circularly permuted green fluorescent proteins engineered to sense Ca^{2+}, Proc. *Proc. Natl. Acad. Sci. U.S.A.* 98, 3197–3202. doi: 10.1073/pnas.051636098

Nagai, T., Yamada, S., Tominaga, T., Ichikawa, M., and Miyawaki, A. (2004). Expanded dynamic range of fluorescent indicators for Ca^{2+} by circularly permuted yellow fluorescent proteins. *Proc. Natl. Acad. Sci. U.S.A.* 101, 10554–10559. doi: 10.1073/pnas.0400417101

Nakai, J., Ohkura, M., and Imoto, K. (2001). A high signal-to-noise Ca^{2+} probe composed of a single green fluorescent protein. *Nat. Biotechnol.* 19, 137–141. doi: 10.1038/84397

Ohkura, M., Sasaki, T., Kobayashi, C., Ikegaya, Y., and Nakai, J. (2012). An improved genetically encoded red fluorescent Ca^{2+} indicator for detecting optically evoked action potentials. *PLoS ONE* 7:e39933. doi: 10.1371/journal.pone.0039933

Palmer, A. E., Giacomello, M., Kortemme, T., Hires, S. A., Lev-Ram, V., Baker, D., et al. (2006). Ca^{2+} indicators based on computationally redesigned calmodulin-peptide pairs. *Chem. Biol.* 13, 521–530. doi: 10.1016/j.chembiol.2006.03.007

Pérez Koldenkova, V., and Nagai, T. (2013). Genetically encoded Ca^{2+} indicators: properties and evaluation. *Biochim. Biophys. Acta* 1833, 1787–1797. doi: 10.1016/j.bbamcr.2013.01.011

Porumb, T., Yau, P., Harvey, T. S., and Ikura, M. (1994). A calmodulin-target peptide hybrid molecule with unique calcium-binding properties. *Protein Eng.* 7, 109–115. doi: 10.1093/protein/7.1.109

Saito, K., Chang, Y. F., Horikawa, K., Hatsugai, N., Higuchi, Y., Hashida, M., et al. (2012). Luminescent proteins for high-speed single-cell and whole-body imaging. *Nat. Commun.* 3, 1262. doi: 10.1038/ncomms2248

Saito, K., Hatsugai, N., Horikawa, K., Kobayashi, K., Matsu-Ura, T., Mikoshiba, K., et al. (2010). Auto-luminescent genetically-encoded ratiometric indicator for real-time Ca^{2+} imaging at the single cell level. *PLoS ONE* 5:e9935. doi: 10.1371/journal.pone.0009935

Truong, K., Sawano, A., Mizuno, H., Hama, H., Tong, K. I., Mal, T. K., et al. (2001). FRET-based *in vivo* Ca^{2+} imaging by a new calmodulin-GFP fusion molecule. *Nat. Struct. Biol.* 8, 1069–1073. doi: 10.1038/nsb728

Yamada, Y., Michikawa, T., Hashimoto, M., Horikawa, K., Nagai, T., Miyawaki, A., et al. (2011). Quantitative comparison of genetically encoded Ca^{2+} indicators in cortical pyramidal cells and cerebellar purkinje cells. *Front. Cell. Neurosci.* 5:18. doi: 10.3389/fncel.2011.00018

Zhang, F., Wang, L. P., Brauner, M., Liewald, J. F., Kay, K., Watzke, N., et al. (2007). Multimodal fast optical interrogation of neural circuitry. *Nature* 446, 633–639. doi: 10.1038/nature05744

Zhao, Y., Araki, S., Wu, J., Teramoto, T., Chang, Y. F., Nakano, M., et al. (2011). An expanded palette of genetically encoded Ca^{2+} indicators. *Science* 333, 1888–1891. doi: 10.1126/science.1208592

Conflict of Interest Statement: The authors declare that the research was conducted in the absence of any commercial or financial relationships that could be construed as a potential conflict of interest.

Received: 15 September 2014; accepted: 30 October 2014; published online: 25 November 2014.

Citation: Nagai T, Horikawa K, Saito K and Matsuda T (2014) Genetically encoded Ca^{2+} indicators; expanded affinity range, color hue and compatibility with optogenetics. Front. Mol. Neurosci. 7:90. doi: 10.3389/fnmol.2014.00090

This article was submitted to the journal Frontiers in Molecular Neuroscience.

frontiers in Molecular Neuroscience

REVIEW
published: 21 July 2015
doi: 10.3389/fnmol.2015.00037

Investigating neuronal function with optically controllable proteins

*Xin X. Zhou[1], Michael Pan[2] and Michael Z. Lin[1,2]**

[1] Department of Bioengineering, Stanford University, Stanford, CA, USA, [2] Department of Pediatrics, Stanford University, Stanford, CA, USA

In the nervous system, protein activities are highly regulated in space and time. This regulation allows for fine modulation of neuronal structure and function during development and adaptive responses. For example, neurite extension and synaptogenesis both involve localized and transient activation of cytoskeletal and signaling proteins, allowing changes in microarchitecture to occur rapidly and in a localized manner. To investigate the role of specific protein regulation events in these processes, methods to optically control the activity of specific proteins have been developed. In this review, we focus on how photosensory domains enable optical control over protein activity and have been used in neuroscience applications. These tools have demonstrated versatility in controlling various proteins and thereby cellular functions, and possess enormous potential for future applications in nervous systems. Just as optogenetic control of neuronal firing using opsins has changed how we investigate the function of cellular circuits *in vivo*, optical control may yet yield another revolution in how we study the circuitry of intracellular signaling in the brain.

Keywords: optogenetics, optobiology, signal transduction, transcription, development

OPEN ACCESS

Edited by:
Yoshiyuki Yamada, University of Geneva, Switzerland

Reviewed by:
Michael R. Bruchas, Washington University in St. Louis, USA
Alexandre Mourot, Université Pierre et Marie Curie, France

****Correspondence:***
Michael Z. Lin, Department of Pediatrics and Department of Bioengineering, Stanford University, 269 Campus Drive, CCSR 2105, Stanford, CA 94305, USA
mzlin@stanford.edu

Received: *30 March 2015*
Accepted: *09 July 2015*
Published: *21 July 2015*

Citation:
Zhou XX, Pan M and Lin MZ (2015) Investigating neuronal function with optically controllable proteins. Front. Mol. Neurosci. 8:37. doi: 10.3389/fnmol.2015.00037

Introduction

The field of neuroscience is now in the 10th year of the optogenetics revolution. It was one decade ago that excitation of a microbial opsin functioning as a light-activated cation channel was first shown to successfully control neuronal excitability (Boyden et al., 2005; Li et al., 2005). Subsequently, a variety of light-activated cation channels, chloride pumps, and proton pumps have been isolated and employed as neurobiological tools. Opsins have been engineered for improved expression, larger currents, red-shifted absorbance, and altered ion selectivity (Bernstein and Boyden, 2011; Fenno et al., 2011; Yizhar et al., 2011; Zhang et al., 2011; Lin et al., 2013a; Chuong et al., 2014; Klapoetke et al., 2014). It is now routine to activate or inactivate specific genetically labeled neurons in living animals, enabling neuroscientists to determine the functions of specific pathways or cell types in sensation, decision-making, or behavior.

In recent years, the term optogenetics, originally coined to describe combining light and genetics to control the electrical activity of neurons using opsins, has been increasingly used to describe the application of light and genetics to control protein functions. As genomic and proteomic technologies can now delineate the entire cast of proteins responsible for carrying out cellular regulatory processes, scientists are increasingly turning toward investigating how proteins function within signaling networks and how protein activities are restricted in space and time. Optical control of protein function, when available, allows for modulation of protein activities with exquisite spatial and temporal resolution, enabling researchers to study the effects of localized or transient protein

activities on downstream signaling pathways or cellular behavior (Riggsbee and Deiters, 2010). Thus, research in adapting natural photosensory modules or creating new ones to control signaling proteins in animals has progressed at an intense pace. In particular, the number of studies that have used light-controlled proteins to investigate specific aspects of neuronal development or function has been growing rapidly.

In this present review, we will summarize how optical control of protein activities using genetically encoded protein tools has already been used in neuroscientific applications to improve the spatial or temporal resolution of experiments. These experiments have involved natural photoreceptor domains from the opsin, sensors of blue light using flavin adenine dinucleotide (BLUF), light-oxygen-voltage (LOV), cryptochrome, phytochrome, and UV response (UVR) families, establishing a wide panel of tools for manipulating specific biochemical processes in neurons with light. The growing availability of tools for optical control of protein function is extending the paradigm of optogenetic control beyond only neuronal electrical activity to cover a wide variety of biochemical events in nervous system development and function. We will also discuss new optical control strategies that could be considered by neuroscientists for future applications.

Opsins

Opsins are a family of light-sensitive transmembrane proteins that covalently bind to a retinal cofactor. Upon light illumination, the cofactor isomerizes and the protein subsequently undergoes a series of conformational relaxations. Microbial opsins that are light-gated ion channels or pumps, such as ChRs and NpHRs, have well-established uses in controlling neuronal excitability (Deisseroth et al., 2006). For specific information on this use of opsins, the reader can refer to recent reviews (Fenno et al., 2011; Duebel et al., 2015). Animal visual opsins found in rods and cones are G-protein-coupled receptors (GPCRs) that activate the $G_{i/o}$ subclass of G proteins. Indeed, their ability to naturally activate the G protein-coupled inward rectifying potassium channel (GIRK) has been used to suppress neuronal activity indirectly (Li et al., 2005). Activation of $G_{i/o}$ by natural animal visual opsins has also been used to enhance neurite outgrowth in neurons, likely via PIP_3 production (Karunarathne et al., 2013). We discuss below uses of engineered animal opsins for controlling neuronal physiology with enhanced specificity for signaling pathways of interest.

Light-Induced Control of G_q and G_s Signaling in Neurons

Based on the structural and functional similarities found in other families of GPCRs and vertebrate visual opsins, and following earlier work by the Khorana lab (Kim et al., 2005), Airan et al. (2009) proposed optoXRs, engineered opsins that control specific G proteins and downstream second messengers (Kim et al., 2005). They exchanged the intracellular loops of bovine visual opsin, which activates the G-protein family member $G_{i/o}$, with those of the α_{1a}-adrenergic receptor, which activates the G-protein family member G_q, to create opto-α_1AR. Likewise, they exchanged the intracellular loops of bovine visual opsin with those of the β_2-adrenergic receptor, which specifically activates G_s, to create opto-β_2AR (**Figure 1A**). Upon blue-cyan light illumination, opto-α_1AR activated phospholipase C via G_q, leading to increased inositol trisphosphate (IP_3) levels, and opto-β_2AR activated adenylate cyclase via G_s, leading to increased cyclic adenosine monophosphate (cAMP) levels. Mice expressing opto-α_1AR in nucleus accumbens (NAc) exhibited light-induced increases in spike firing, and light was sufficient to induce conditioned place preference in a behavior study. In contrast, opto-β_2AR expression in the NAc reduced spontaneous firing.

A potential limitation of optoXRs using visual opsins is that they are unable to regenerate 11-*cis*-retinal from the photoisomerized all-*trans*-retinal (Bailes et al., 2012). A natural G_s-coupled opsin that can regenerate 11-*cis*-retinal may provide an alternative means for optical control of cAMP production. Bailes et al. (2012) used the opsin from box jellyfish, the only animal opsin known to couple to G_s, to increase cAMP levels in response to light. Box jellyfish opsin was able to signal with addition of only all-*trans*-retinal, implying it was capable of regenerating 11-*cis*-retinal, and enabled repeated optical activation of cAMP production with less fatigue than opto-β_2AR (Bailes et al., 2012).

Control of Opioid Signaling Pathways

In a recent study, Siuda et al. (2015) generated another chimeric protein from an animal visual opsin and a GPCR to impose optical control upon mu-opioid signaling pathways. Understanding of opioid functions in the brain has been hampered by the poor cell-type specificity and temporal resolution of pharmacological stimulation. Siuda et al. (2015) constructed a photosensitive mu-opioid-like chimeric receptor (opto-MOR) by swapping the intracellular segments of rat visual opsin with those of mu-opioid receptor. While both receptors activate $G_{i/o}$, these segments may specifically confer localization or regulation by GPCR kinases and arrestins in a mu-opioid receptor-like manner (Siuda et al., 2015). Opto-MOR activation in neurons suppressed cAMP production and increased currents through GIRK upon light stimulation (**Figure 1B**). Opto-MOR activation in selected GABAergic neurons in mouse induced reward or aversion behaviors. While more work is needed to verify that the details of signaling downstream of opto-MOR mimic those of opioid receptors specifically, these results suggest that the chimeric opsin concept can confer specificity to signaling outputs beyond G protein subtypes.

Control of Serotonin Receptor Pathways

Serotonin (5-HT) modulates anxiety circuits through various receptors that couple to different subtypes of G proteins. As pharmacologic activation lacks selectivity for different receptor subtypes and their different downstream pathways, Herlitze and colleagues engineered light-controllable 5-HT receptors to investigate the role of specific receptor types in the regulation of anxiety (**Figure 1C**; Oh et al., 2010; Masseck et al., 2014;

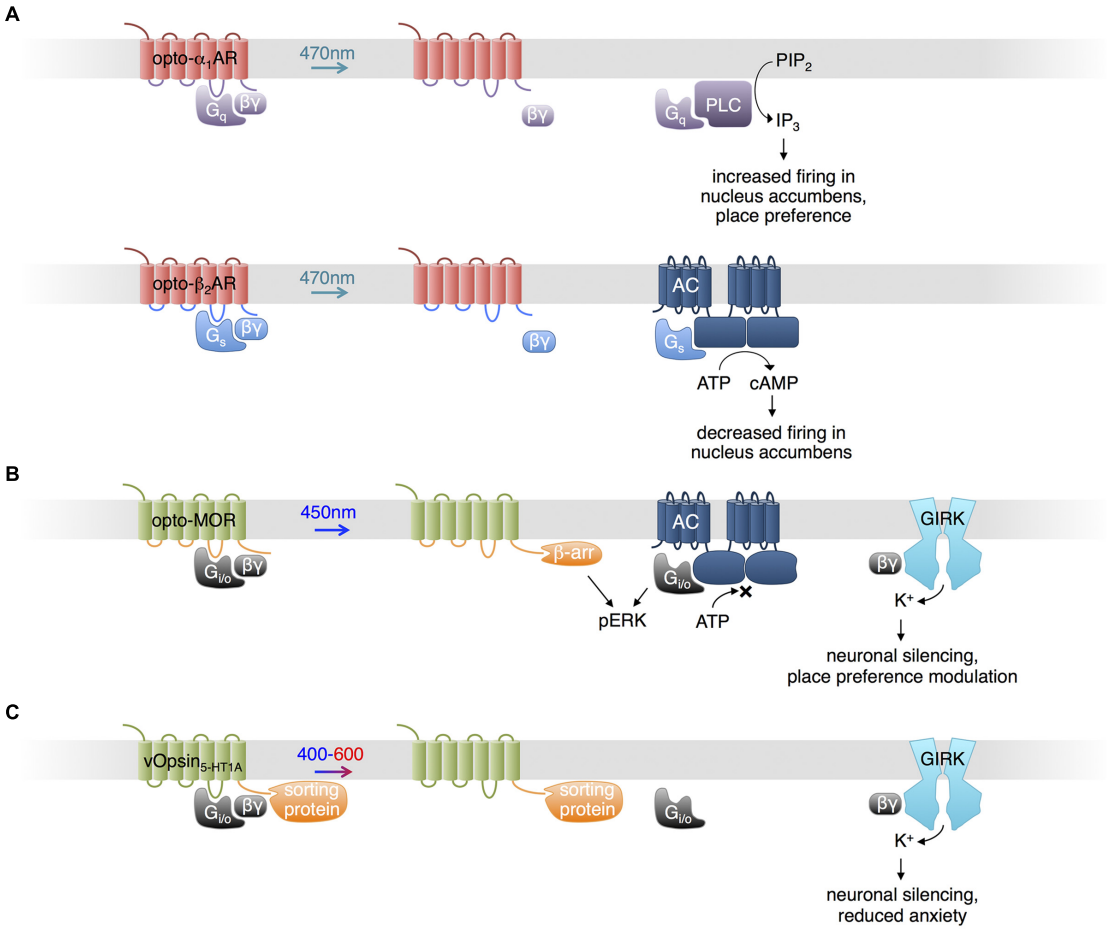

FIGURE 1 | Uses of opsins. (A) Opto-α_1-AR consists of bovine visual opsin with the intracellular loops of G_q-coupled human α_{1a}-adrenergic receptor. Opto-β_2-AR consists of bovine visual opsin with the intracellular loops of G_s-coupled hamster β_2-adrenergic receptor. When excited with blue light, opto-α_1-AR and opto-β_2-AR activate production of IP_3 and cAMP, increasing and decreasing neuronal firing *in vivo*, respectively. **(B)** Opto-MOR consists of rat visual opsin with the intracellular loops of the mu-opioid receptor. Optical stimulation results in inhibition of adenylate cyclase via $G_{i/o}$, activation of ERK via β-arrestin and $G_{i/o}$, and activation of GIRK via Gβγ. **(C)** Photoactivatable serotonin receptors can be produced by conjugating light-sensitive vertebrate opsins (here, denoted vOpsins) at various excitation wavelengths with the C terminal portion of a specific serotonin receptor subtype, which mediates proper localization within the cell via sorting proteins. Excitation with 400–600 nm light triggers activation of GIRK via Gβγ, decreasing neuronal firing.

Spoida et al., 2014). Oh et al. (2010) fused the C-terminal domain of 5-HT_{1A} receptor, which mediates sorting to somatodendritic locations via binding to Yif1B, to the C-terminus of the rat rod opsin RO4. The chimeric construct (vRh-$CT_{5\text{-}HT1A}$) was distributed similarly to 5-HT_{1A} receptor and functionally restored 5-HT_{1A} $G_{i/o}$-mediated GIRK activation in the absence of the native receptor upon excitation at 475 nm (Oh et al., 2010). However, vRh-$CT_{5\text{-}HT1A}$ showed declining activity with sustained or repetitive stimulation. Masseck et al. (2014) developed more robust light-controllable 5-HT_{1A} receptors using short- and long-wavelength vertebrate cone opsins ($vSWO_{5\text{-}HT1A}$ and $vLWO_{5\text{-}HT1A}$, excited at 450 and 590 nm, respectively), and found that activation in the dorsal raphe nucleus (DRN) suppresses neuronal firing and modulates anxiety behaviors. Spoida et al. (2014) similarly created a chimeric protein (vMo-$CT_{5\text{-}HT2C}$) from vertebrate melanopsin and 5-HT_{2c} receptor, both of which are G_q-linked. Activation of vMo-$CT_{5\text{-}HT2C}$ with light at 485 nm in GABAergic neurons in the DRN, which normally expresses 5-HT_{2C} receptors, decreased firing of serotonergic neurons in the DRN and relieved anxiety behavior in mice, likely due to GABAergic neuron activation and subsequent inhibition of serotonergic neurons (Spoida et al., 2014).

BLUF Domain Regulation of Adenylate Cyclases

The BLUF domain is a protein domain found prevalently in prokaryotes (Christie et al., 2012). BLUF domains bind flavin adenine dinucleotide (FAD) in a cleft formed by two α helices and a β sheet. Blue light causes rearrangements in hydrogen bonds between FAD and the protein, inducing a conformational change in the BLUF domain that can be propagated to adjacent protein domains allosterically. Activation is spontaneously reversed

within seconds to minutes in the dark (Barends et al., 2009; Zoltowski and Gardner, 2011).

Euglena gracilis expresses a photoactivated adenylate cyclase that consists of α and β subunits (euPACα and euPACβ), each of which contains two BLUF domains. Each subunit can be expressed in heterologous organisms to mediate light-induced cAMP production, with the α subunit showing higher activity (**Figure 2A**; Efetova and Schwarzel, 2015). In adult *Drosophila*, activation of euPACα throughout the brain resulted in hyperactivity and freezing, demonstrating some ability to modulate neuronal function (Schroder-Lang et al., 2007). In *Drosophila* larvae, illumination of euPACα-expressing olfactory receptor neurons (ORNs) mimicked odorant-induced ORN activation (Bellmann et al., 2010). Light stimulation of specific euPACα-expressing ORNs induced attractive or repellent behaviors, indicating that the attractive or repulsive behaviors are determined by the ORNs but not by the receptors which detect the odorants. In *Caenorhabditis elegans*, pre-synaptic cAMP signaling plays a vital role in the regulation of locomotion, and photoactivation of euPACα in cholinergic neurons resulted in a rise in swimming frequency and speed of locomotion, and a decrease in the number of backward locomotion episodes (Weissenberger et al., 2011).

More recently, a PAC from the bacterium *Beggiatoa* (bPAC) was characterized that is smaller and more soluble than euPACα (**Figure 2B**; Stierl et al., 2011). In rat hippocampal pyramidal cells, bPAC induced larger currents than euPACα. Light induced faster inhibition of behavior in flies expressing bPAC pan-neuronally than in flies expressing euPACα. In contrast to euPACα expressing flies, bPAC-expresing flies were not affected by the phosphodiesterase inhibitor IBMX alone, implying less basal cAMP production by bPAC. In freely behaving larval zebrafish, light stimulation of bPAC in pituitary cells induced activation of corticotropin-releasing-hormone receptor, release of glucocorticoid hormone, and subsequent stress responses (De Marco et al., 2013). One disadvantage of bPAC is its slower inactivation kinetics of 19 s compared to 3 s for euPACα (Stierl et al., 2011).

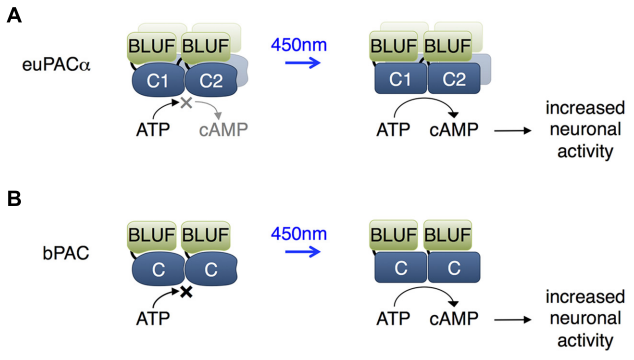

FIGURE 2 | Blue light using flavin adenine dinucleotide (BLUF) domain-regulated adenylate cyclases. (A) The euPACα polypeptide is composed of two BLUF and two catalytic domains in the order BLUF1, C1, BLUF2, C2, and likely dimerizes or tetramerizes when expressed heterologously. The C1 and C2 catalytic domains associate to form the adenylate cyclase active site. BLUF domains N-terminal to each catalytic domain enhance catalysis in response to light. **(B)** The bPAC is composed of a single BLUF and a single catalytic domain, and likely dimerizes when expressed, so that an adenylate cyclase active site forms at the interface of the catalytic domains. The BLUF domain enhances catalysis in response to light.

LOV Domains

In the past few years, one of the most extensively used photosensory domains has been the LOV sensing domain. LOV domains are small (~15 kD) monomeric domains with terminal α helices and a central β sheet that binds flavin chromophores, either flavin mononucleotide (FMN) or FAD (Crosson and Moffat, 2001; Harper et al., 2003). Upon illumination by blue light (400–480 nm), the flavin cofactor forms a covalent thioether bond with a cysteine residue in the LOV domain, leading to conformational changes in the β sheet, resulting in dissociation of one of the α helices (Zoltowski and Gardner, 2011). This process reverses spontaneously within seconds to minutes in the dark (Losi, 2007).

PA-Rac: Control of Synaptic Plasticity

Light-oxygen-voltage domains undergo versatile light dependent interactions. In the best-studied LOV domain, LOV2 from *Avena sativa* phototropin, light-induced thioeither bond formation between a cysteine residue and the FMN chromophore leads to partial unfolding of the C-terminal α-helix (named Jα) from the rest of the LOV2 domain (Harper et al., 2004). This conformation change has been widely used to construct light-controllable proteins in allosteric or steric manners (Lee et al., 2008; Strickland et al., 2008; Moglich et al., 2009; Wu et al., 2009; Ohlendorf et al., 2012). Wu et al. (2009) constructed photoactivatable small GTPase Rac1 (PA-Rac1; **Figure 3A**), which has since been widely used (Walters et al., 2010; Wang et al., 2010; Yoo et al., 2010; Dietz et al., 2012; Ramel et al., 2013; Schwechter et al., 2013). Wu et al. (2009) screened different linkages of the LOV2 domain to the N-terminus of Rac1 and selected the construct that showed light-mediated protein activation. The resulting construct, PA-Rac1, optically controlled membrane ruffling and migration of animal cells. A crystal structure of PA-Rac1 in the dark state revealed that Rac1's binding sites for downstream effectors are blocked by close interaction with LOV2. The light-triggered unwinding of Jα likely releases Rac1 from LOV2 interaction, leading to the binding of Rac1 to its effectors and activation of downstream signaling proteins.

Dietz et al. (2012) utilized PA-Rac1 to investigate the essential role of Rac1 in cocaine-induced structural plasticity in neurons. Cocaine induces the formation of long thin spines in medium spiny neurons of the NAc, and the authors found that cocaine negatively regulated Rac1 activity in a transient manner. To probe whether this transient reduction in Rac1 activity is responsible for the cocaine-induced dendritic arborization, Dietz et al. (2012) photostimulated PA-Rac1 following cocaine injections in mice transduced intra-NAc with

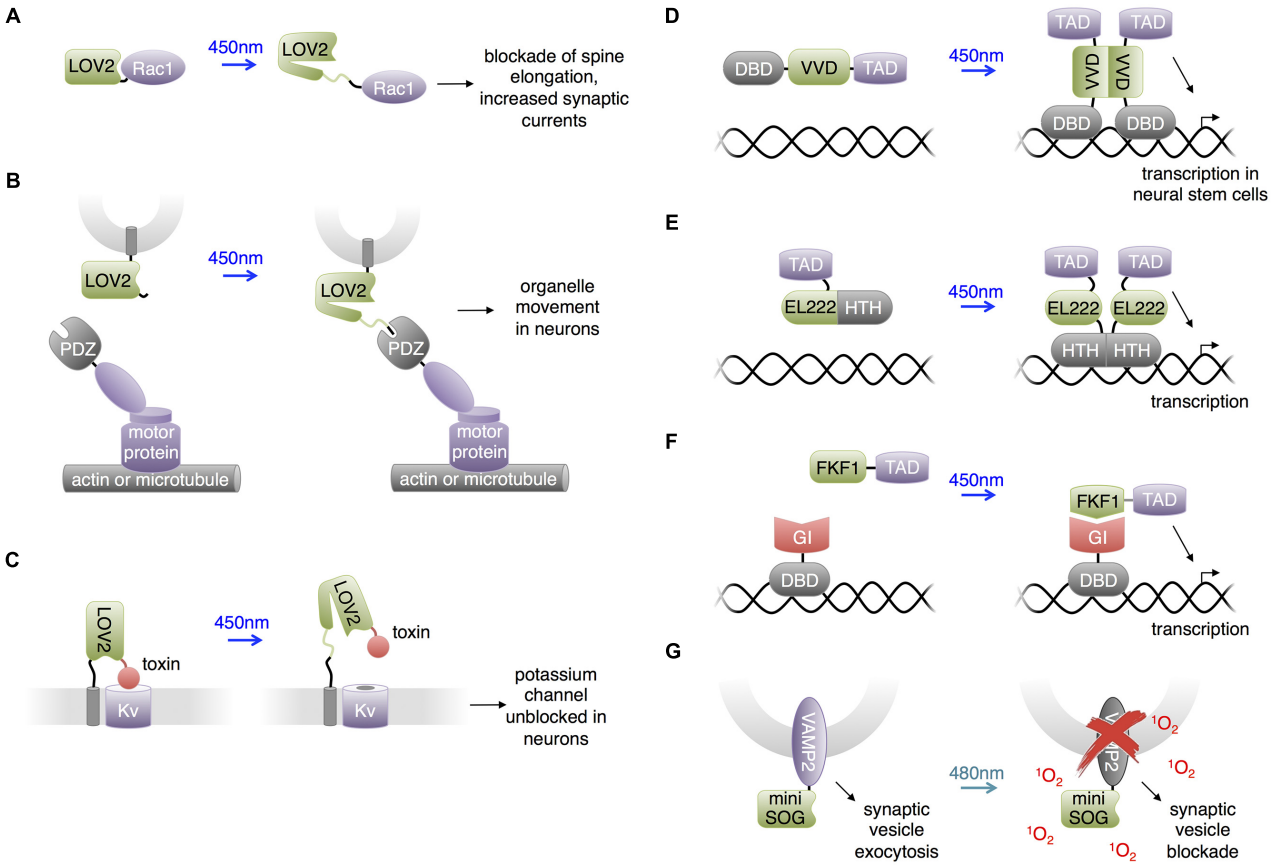

FIGURE 3 | Uses of LOV domains. (A) Photoactivation of PA-Rac1 by blue light has been shown to prevent cocaine-induced increase in spine elongation and, separately, to increase synaptic currents. **(B)** Blue light-mediated LOV2-PDZ interaction can recruit motor proteins for locomotion of targeted organelles. PDZ-kinesin would produce anterograde movement of the organelle, while PDZ-dynein would produce retrograde movement of the organelle. **(C)** Lumitoxins are fusions of a channel-blocking peptide toxin, a flexible linker, the LOV2 domain, and a transmembrane helix. When excited by blue light, unfolding of the Jα helix is believed to lengthen the linkage to the membrane, decreasing the local concentration of the toxin near the ion channels. **(D)** The LightON transcription system fuses a truncated Gal4 DNA-binding domain (DBD) to the Vivid (VVD) LOV domain to produce a construct that homodimerizes upon excitation with blue light and binds to Gal4's cognate DNA, activating downstream transcription. TAD is a transcription-activating domain. **(E)** A similar homodimerizing optobiological tool for transcription control. Bacterial transcription factor EL222's light-sensitive LOV domain and helix-turn-helix (HTH) DBD are conjugated to a nuclear localizing sequence and VP16 transcription activating domain (TAD). The compound protein homodimerizes upon excitation with blue light to bind cognate C120 DNA sequences and activate downstream transcription. **(F)** Interaction between FKF1 and GIGANTEA (GI) domains can produce blue light-activatable transcription employing the VP16 TAD and the Gal4 DBD. **(G)** Proteins fused to miniSOG, a singlet oxygen-generating mutant of LOV2, can be destroyed by chromophore-assisted light inactivation (CALI). In the case of a VAMP2-miniSOG fusion, light results in blockade of synaptic transmission.

PA-Rac1 vector. They observed that photoactivation of PA-Rac1 prevented cocaine-induced development of new spines on neurons and reward behavior in living mice. These studies involving PA-Rac1 provided evidence that the cocaine-induced transient downregulation of Rac1 activity is required for the normal rewarding effects of cocaine, illustrating the experimental designs made possible by the temporal resolution achieved using optically controllable proteins. Separately, Schwechter et al. (2013) studied the effects of PA-Rac1 in modulating synaptic strength in neurons. They found that PA-Rac1 activation in the post-synaptic neuron induces increased synaptic transmission frequency and post-synaptic currents, supporting the hypothesis that activators of Rac1 induce long-term potentiation.

LOVpep: Control of Organelle Movement and Axonal Extension

Strickland et al. (2012) developed a light-inducible heterodimerization system based on interaction between a fusion of a slightly truncated LOV2 domain to a PDZ-binding peptide (LOVpep) and a PDZ domain. Upon illumination, unfolding of the Jα helix uncages the peptide epitope, which interacts with the PDZ domain. The affinity and kinetics of this interaction are tunable by mutations. In a similar approach, Lungu et al. (2012) engineered a fusion of truncated LOV2 to the bacterial SsrA peptide which becomes capable of binding SspB upon illumination. In neural studies, van Bergeijk et al. (2015) utilized the LOVpep system to transport and position organelles (**Figure 3B**). The engineered LOV2

domain was fused to the organelle targeting signals, and the PDZ domain was fused to plus/minus-end-directed motor proteins. Photostimulation recruited motors to organelles and drove organelle movements. This approach enabled localized and repeatable induction and cessation of the motility of peroxisomes, recycling endosomes, and mitochondria, allowing investigation of the relationships between organelle positioning/dynamics and cellular functions. For instance, van Bergeijk et al. (2015) demonstrated the linkage between local positioning of recycling endosomes and axon growth in primary rat hippocampal neurons by showing that dynein-driven removal or kinesin-driven enrichment of endosomes within axonal growth cones reversibly suppressed or enhanced axon growth, respectively.

Lumitoxins: Light-Inhibited Neurotoxins

Schmidt et al. (2014) created "lumitoxins" as fusions of an ion channel-specific peptide toxin to a LOV2 domain tethered to the cell membrane. Prior to photoactivation, the toxin peptide blocks the activity of voltage-gated potassium channels. Illumination reverses the blockade, possibly due to unwinding of the Jα helix causing an increase in the distance between the toxin and the channels in the membrane (**Figure 3C**). The unblocked channels then can be activated by membrane depolarization. This method was shown to exhibit specificity toward different subsets of voltage-gated potassium channels. Schmidt proposed that localized specificity such as axon or dendrite localization could be facilitated by the addition of subcellular protein trafficking motifs. Compared to other LOV2-domain based approaches, lumitoxin does not require customization for each target, and the dynamic range could be altered through adjusting the length of the Jα helix. Lumitoxins thus may serve as a modular and tunable architecture that could be potentially generalized to other classes of ion channels and membrane proteins. As little as 10 $\mu W/mm^2$ of light was able to activate lumitoxins compared to >1000 $\mu W/mm^2$ for other optogenetic tools such as ChR2. A potential advantage of modulating native channels over using exogenous opsins is that responsiveness of channels to endogenous neuronal activity and localization to specific subcellular compartments can be preserved.

Control of Transcription and Neuronal Differentiation

The LOV domain of the Vivid protein from *Neurospora crassa* homodimerizes upon blue light illumination. Bond formation between the FAD cofactor and the cysteine residue in the Vivid LOV domain induces dimerization via an N-terminus helix (Zoltowski et al., 2007). Wang et al. (2012) utilized Vivid to create a light activated transcription system named "LightON" (**Figure 3D**). They fused the Vivid LOV domain to a Gal4 DNA-binding domain (DBD) that only weakly binds its cognate DNA sequence due to removal of its dimerization region. Light-mediated dimerization of this fusion protein activated DNA binding and transcriptional activation with very high inducibility (>200-fold). Imayoshi et al. (2013) used this "LightON" approach to investigate the role of the bHLH gene Ascl1 in neuronal progenitor cells. They observed that prolonged light-driven transcription of Ascl1 induces neuronal differentiation while oscillatory light-driven transcription maintains cell proliferation.

Light-oxygen-voltage domain proteins other than Vivid have also been used for transcriptional regulation in non-neuronal cells and presumably could be applied to study the nervous system. Motta-Mena et al. (2014) reported an optogenetic gene expression system based on EL222, a bacterial transcription factor that dimerizes and increases its affinity for its cognate DNA sequence upon light stimulation (**Figure 3E**). EL222 contains a photosensory LOV domain and a helix-turn-helix (HTH) DNA-binding domain. In the dark, the LOV domain binds and covers the HTH 4α helix essential to dimerization and DNA binding. Light illumination releases the steric caging and results in protein dimerization and DNA binding. To adapt this system for eukaryotic applications, Motta-Mena et al. (2014) fused a minimal regulatory element of EL222 to the VP16 transcriptional activation domain and a nuclear localization signal sequence to create VP-EL222. Compared to the functionally similar LightON system, VP-EL222 has similar dynamic range and appears to have faster turn-off kinetics, but habituates to baseline levels when continuously stimulated by light. Earlier, Yazawa et al. (2009) demonstrated that light-induced interaction between the LOV domain of *Arabidopsis thaliana* FKF1 and GIGANTEA can be used to drive transcription via recruitment of a transcriptional activation domain to a DBD (**Figure 3F**). This system has on-rates of minutes, which is fast enough for transcriptional regulation, and has very slow or negligible reversibility which can be useful for sustained transcription. Polstein and Gersbach (2012) subsequently adapted this system to activate transcription from zinc-finger DNA-binding domains and thereby regulate endogenous genes.

Destructive Inactivation of Synaptic Transmission

Chromophore assisted light inactivation (CALI) is a technique to inactive proteins in proximity to a chromophore (Jay, 1988; Marek and Davis, 2002; Tour et al., 2003). In CALI, reactive oxygen species generated by the chromophore upon illumination oxidize nearby susceptible residues including tryptophan, tyrosine, histidine, cysteine and methionine, thereby disrupting protein function. In a repurposing of the LOV domain from its natural function, Shu et al. (2011) engineered the *Arabidopsis* phototropin LOV2 domain to enhance its generation of reactive oxygen species rather than undergo reversible conformational changes upon illumination. They mutated the reactive cysteine near the FMN chromophore to glycine, eliminating photoadduct formation. The resulting space near the chromophore may allow oxygen to approach, facilitating the generation of reactive oxygen species. The resulting domain, named miniSOG, generated singlet oxygen upon blue light illumination with higher efficiency than previous CALI probes based on fluorescent proteins. Lin et al. (2013b) found that fusions of miniSOG to the SNARE protein synaptobrevin 2 (VAMP2) or synaptophysin (SYP1), allowed 480-nm light

to inhibit synaptic release (**Figure 3G**). Light effectively blocked synaptic transmission in neurons in hippocampal slices expressing SYP1-miniSOG, and reduced movement of worms expressing VAMP2-miniSOG in all neurons. As inhibition of synaptic release did not require replacing endogenous synaptic vesicle proteins, it is possible that the CALI effect extends from the transfected proteins to endogenous ones. One limitation of this approach is the irreversibility of inactivation. For example, recovery of movement in worms occurred 20–22 h after illumination, which would be consistent with replacement of reacted proteins with newly synthesized copies.

Cryptochromes

Another extensively studied photosensory protein is cryptochrome, a FAD-binding protein that regulates growth processes in plants and circadian clocks in animals (Liu et al., 2008). Blue light induces FAD reduction and protein conformational changes. In *Arabidopsis* cryptochrome 2 (CRY2), this light-induced conformational change initiates the interaction between CRY2 and cryptochrome-interacting basic-helix-loop-helix 1 (CIB1; Liu et al., 2008) as well as self-oligomerization of CRY2 domains (Bugaj et al., 2013). The interaction features subsecond on-rates and fast spontaneous reversibility. A new variant, called CRY2olig, undergoes clustering significantly more quickly and with lower illumination intensity than wild-type CRY2 (Taslimi et al., 2014). The following examples adapted these two light-induced interactions for applications in neurosciences.

Activation of Neurotropin Receptors and Filopodia by CRY2 Clustering

Following the observation that light-induced clustering of proteins fused to CRY2 can be applied to activate the small GTPase RhoA (Bugaj et al., 2013), Chang et al. (2014) engineered light activatable TrkB by fusion to CRY2 in neurons (**Figure 4A**). TrkB belongs to the tropomyosin-related kinase family, which activates through brain-derived neurotrophic factor (BDNF)-mediated homodimerization at the plasma membrane. TrkB mediates multiple downstream signaling pathways and contributes to neuronal survival, neurite outgrowth and synaptic plasticity. Chang et al. (2014) fused the photolyase homology region (CRY2PHR) of CRY2 to the intracellular region of TrkB, such that light-induced oligomerization of the CRY2PHR domain induced the dimerization of TrkB and activated the protein. This photoactivatable TrkB, named optoTrkB, was used in primary neurons to induce the formation and growth of filopodia, the actin-structure linked to dendrite creation when new synapses are formed in the brain (Maletic-Savatic et al., 1999). OptoTrkB features rapid, transient, and localized activation of the signaling pathway, and only requires expression of a single protein chain. CRY2 oligomerization was also used to induce clustering of the cytoplasmic domain of a different receptor tyrosine kinase, the fibroblast growth factor receptor FGFR1, to trigger PI3K activation in non-neuronal cells (Kim et al., 2014). Omission of the extracellular domain prevented activation by endogenous ligands.

Control of Kinases and Neuronal Differentiation by CRY2-CIB1

Plasma membrane localization activates many signaling proteins, and the light-induced heterodimerizing interaction between CRY2 and CIB1 can introduce optical control to these proteins. Typically, the CRY2 domain is fused to the protein of interest (POI) and expressed in the cytoplasm, and the CIB1 domain is membrane-localized by fusion with a membrane trafficking motif, e.g., the C-terminal K-Ras CaaX domain (Willumsen et al., 1984). With light stimulation, the CRY2-CIB1 interaction activates the POI by membrane localization.

Following this strategy, Zhang et al. (2014) constructed light activated Raf1 kinase (**Figure 4B**). Raf1 phosphorylates upon membrane localization and activates the MAPK signaling pathway. The MAPK signaling pathway plays vital roles in various cellular processes, and different activation kinetics regulate the specific functional output of the pathway. Using the photoactivatable Raf1, Zhang et al. (2014) investigated the role of Raf1 activation in mediating PC12 differentiation into neuron-like cells. They observed that photoactivated Raf1 could independently induce PC12 differentiation in the absence of growth factors, and the neurite outgrowth reached the maximum length if the off-time duration in an intermittent on/off illumination pattern was shorter than 45 min. This application provides another example of the high specificity and temporal resolution that light activated proteins provide when dissecting the kinetics of pathway activations.

Control of PIP_3 and Axonal Extension by CRY2-CIB1

Adapting the same strategy, Kakumoto and Nakata (2013) constructed a phosphatidylinositol 3-kinase (PI3K) photoswitch and used it to study the spatiotemporal function of phosphatidylinositol-3,4,5-trisphosphate (PIP_3) in developing neurons (**Figure 4C**). PI3K produces PIP_3 on the plasma membrane, and this intracellular signaling lipid's function is closely related to its spatial distribution. Kakumoto and Nakata (2013) fused the K-ras CaaX motif to the CIB1 domain and fused the CRY2PHR domain to the inter-SH2 domain of p85b, the regulatory subunit of PI3K (CRY2PHR-iSH). In the dark, CRY2PHR-iSH interacted with endogenous p110, the catalytic subunit of PI3K, and light stimulation localized the CRY2PHR-iSH-p110 complex to the plasma membrane, triggering the production of PIP_3. Kakumoto and Nakata (2013) then used the PI3K photoswitch to probe the local dynamics and primary functions of PIP_3 in developing neurons by optically inducing production of PIP_3 at neurite tips in mouse hippocampal neurons. The studies indicated that PIP_3 production at neurite tips induced filopodia and lamellipodia formation and growth cone expansion but not neurite elongation. It was also observed that ectopic PIP_3 elevation caused membranes to form actin-based structures whose behavior was similar to that of growth-cone-like 'waves,'

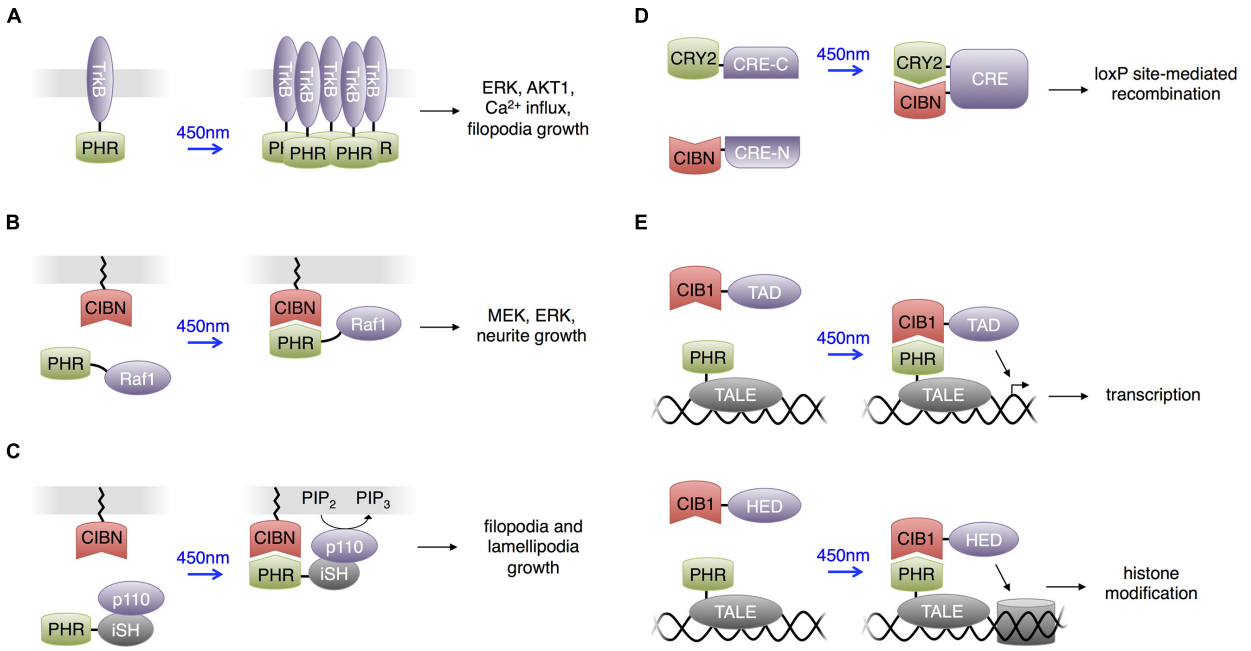

FIGURE 4 | Uses of CRY2 domains. For all panels, CRY2 and CIB1 are the full-length domains. PHR is the photolyase homology region of CRY2 (a truncated CRY2) and CIBN is the N terminal portion of CIB1 (a truncated CIB1). **(A)** Light-sensitive receptor tyrosine kinases. Upon excitation with blue light, PHR homodimerizes to activate downstream components in the Trk signaling pathway. **(B)** Heterodimerization between PHR and CIBN used to produce light-activated Raf1 for optogenetic control of the Raf1/MEK/ERK pathway in PC12 cells. Membrane localization of Raf1 activated downstream kinases and eventually stimulated neurite growth in PC12 cells. **(C)** Light-activated phosphatidylinositol 3-kinase (PI3K). CIBN is membrane-localized and PHR is fused to the inter-SH2 domain of p85b, the regulatory subunit of PI3K kinase (iSH). The catalytic p110 component of PI3K was supplied endogenously by the cell expressing these two constructs. Blue light excitation recruited the PHR-iSH-p110 complex to the membrane, where it would produce PIP_3 from PIP_2. **(D)** Light-induced heterodimerization between CRY2 and CIBN can assemble a functional protein if an appropriate half of the protein is fused to each of CRY2 and CIBN. Fusing half of cre recombinase to CRY2 and CIBN produces light-dependent loxP site recombination. **(E)** The light-inducible transcriptional effector (LITE) system allows optical control of transcription or chromatin structure. Transcription activator-like effectors (TALEs) serve as modular DNA-binding domains. TALE fused to PHR comprises one component of LITE. An effector domain (TAD or HED, a histone effector domain) fused to CIB1 comprises the other component of LITE.

and that endocytosis regulates effective PIP_3 membrane concentration.

Control of Cre-Mediated Recombination in Neurons by CRY2-CIB1

Similar to the concept of engineering optically inducible protein–protein interactions, Kennedy et al. (2010) used the CRY2-CIB1 interaction to induce recombination of split proteins with light. Kennedy et al. (2010) fused CRY2 and CIB1 to each half of a split Cre recombinase, and the close proximity between the fusion proteins during light-mediated interaction reassembled the two Cre fragments (**Figure 4D**).

One could envision various applications of this light activated Cre in selectively controlling gene expression in neurons with excellent spatiotemporal resolution. For instance, LOLLIbow combines this approach with the Brainbow technique in *Drosophila* to permit developmental scientists to label stochastically cells of interest at a desired time point during development for visualization (Boulina et al., 2013). Brainbow causes neurons to randomly express red, green, or blue fluorescent proteins through the stochastic action of recombinases on arrays of genes encoding these proteins (Livet et al., 2007). The fluorescent labels improve neuronal tracing, because individual neurons can be distinguished from neighboring cells.

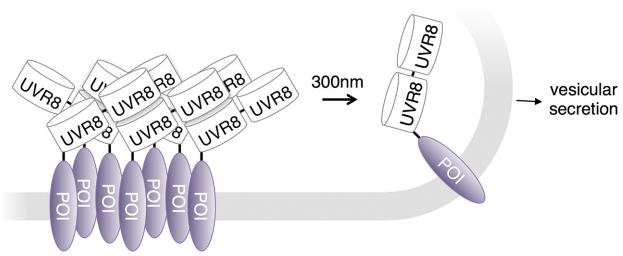

FIGURE 5 | UVR8 in regulation of protein export. The Ultraviolet Response 8 (UVR8) plant photoreceptor forms homodimers in the dark and dissociates into monomers upon excitation with UV-B light. A protein secretion control system conjugates tandem UVR8 tags to a protein of interest (POI). As a result, these conjugates form aggregates in the ER and remain stationary until dissociated by UV-B light.

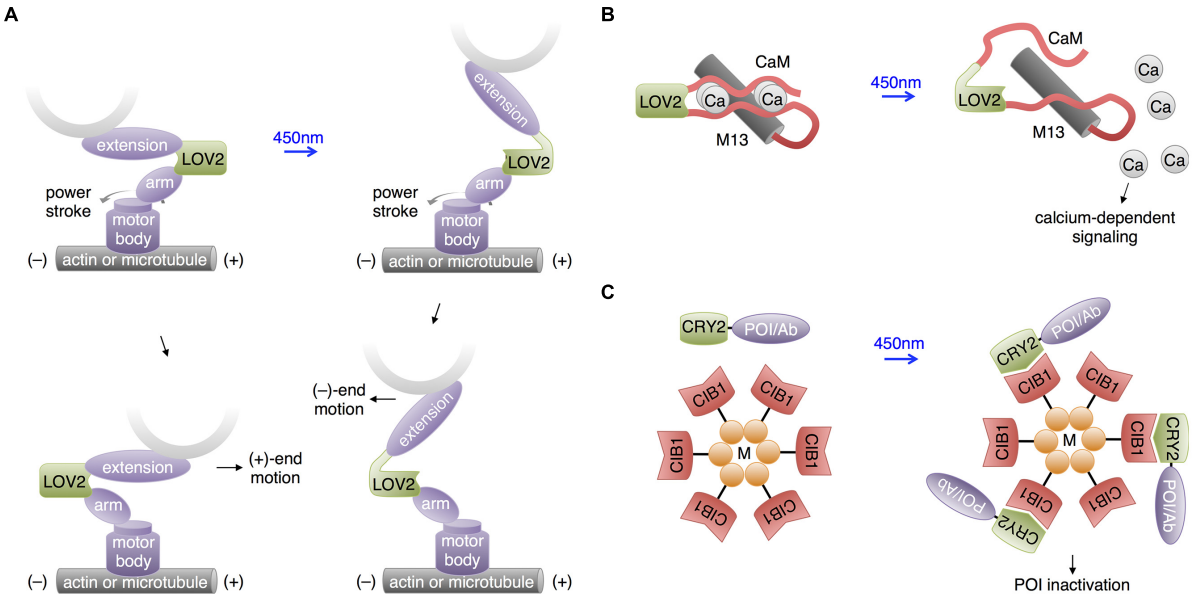

FIGURE 6 | Recent uses of LOV and CRY2 domains with potential neuroscience applications. (A) Motor protein direction can be modified by changing the lever arm length using a LOV2 domain. An artificial lever arm was made by fusing two α-actinin structural elements (arm and extension) to LOV2, then this was attached to a motor protein's catalytic domain (motor body). Change in lever arm geometry upon illumination resulted in a change in motor direction. **(B)** Light-induced LOV2 conformational change was also used to disrupt the folding of two fragments of calmodulin, allowing light-induced release of calcium. **(C)** The LARIAT method enables temporary inactivation of a POI by sequestration. LARIAT consists of CRY2 conjugated to a POI or an antibody fragment recognizing the POI (Ab) and CIB1 conjugated to a multimerizing protein (M). Blue light excitation causes the POI to aggregate to the multimer clusters formed by the CIB1-M construct.

Control of Transcription of Endogenous Genes by CRY2-CIB1

Konermann et al. (2013) created light-inducible transcriptional effectors (LITEs), using the light-inducible CRY2-CIB1 interaction to recruit transcriptional regulators to endogenous promoters. They fused CRY2 to transcription activator-like effectors (TALEs), customized DNA binding domains, and CIB1 to transcriptional activation or histone effector domains (**Figure 4E**). Light could then be used to induce transcriptional activation or epigenetic modulations on targeted genes. This approach was applied in primary mouse neurons and the brains of awake mice *in vivo* to control a variety of endogenous transcriptional and epigenetic processes. Recently a CRISPR associated protein 9 (Cas9) domain deficient in DNA cleavage was used in place of TALEs for genomic targeting in a similar strategy. This also enabled light-induced transcription of endogenous genes in non-neuronal cells and presumably could be applied in the nervous system (Nihongaki et al., 2015; Polstein and Gersbach, 2015). As Cas9 is directed to a DNA sequence by a single guide RNA (Jinek et al., 2012), targeting to new DNA sequences only requires alteration of the sgRNA sequence, which is easier than engineering new custom TALEs.

UVR8 in Control of Vesicular Secretion

The plant protein Ultraviolet Response 8 (UVR8) undergoes an ultraviolet (UV)-light-mediated transition from homodimer to monomer. It subsequently binds to the Constitutively Morphogenetic 1 (COP1) protein, leading to the activation of genes that provide protection from UV light (Favory et al., 2009). UVR8 does not require any cofactor; instead the chromophore in UVR8 is a pair of tryptophan residues that interact with arginine residues at the dimeric interface through cation-π interactions. Light absorption results in the excitation of the tryptophan indole rings, leading to destabilization of the cation-π interactions and subsequent breakage at the homodimeric interface (Rizzini et al., 2011; Wu et al., 2012). As with other light-inducible dimerization systems, UVR8-COP1 heterodimerization has been used to activate transcription in response to light (Crefcoeur et al., 2013; Muller et al., 2014). Despite its potential phototoxicity, the UV wavelengths recognized by UVR8 avoid spectral overlap with other photoactivatable and fluorescent proteins, thus allowing orthogonal multicolor activation and imaging (Muller et al., 2014). Interestingly, in mammalian cells, UVR8 dissociation and COP1 association is irreversible. *Arabidopsis* proteins that promote UVR8 redimerization and COP1 dissociation have been identified, suggesting the future possibility of engineering reversible UVR8-based systems for optical control in mammalian cells using these proteins (Heijde and Ulm, 2013).

Photodissociation of UVR8 has been used to control protein secretion in neuronal cells. Chen et al. (2013) observed that fusing tandem copies of UVR8 to secreted proteins caused sequestration in the endoplasmic reticulum. A brief pulse of UV light released the high-order oligomerizing interactions and

allowed cargo trafficking to the Golgi apparatus and ultimately the plasma membrane (**Figure 5**). Chen et al. (2013) used this approach to study local trafficking of secretory cargo near dendritic branch points in neurons. Their data suggest that cargo released from the endoplasmic reticulum near branch points is preferentially trafficked to nearby dendritic Golgi membranes.

Future Possibilities

In this review, we have focused on examples in which optogenetic systems utilizing chromophores present in animal cells were used to control protein activity in the nervous system. However, the same systems have been applied to control an even broader variety of signaling processes in living cells, and these applications could in principle be useful for studying the nervous system as well. In addition, other light-controllable systems have recently been developed that may be promising systems for exploring protein function in the nervous system with high spatiotemporal resolution.

A fairly generalizable way to use the LOV2 domain has been to cage the function of small peptides. In addition to controlling small peptides that mediate protein–protein interactions as mentioned above (Lungu et al., 2012; Strickland et al., 2012), LOV2 can also be used to control small peptides that function in nuclear localization (Niopek et al., 2014) and protein degradation (Renicke et al., 2013; Bonger et al., 2014) when they are appended to the Jα helix or replace a portion of it. Application of these tools to neurons should be possible. Likely, optically controlled peptides could potentially be designed to inhibit a variety of protein–protein interactions in the nervous system.

In a unique use of the LOV2 domain, Nakamura et al. (2014) used the light-regulatable hinge nature of LOV2 to construct cytoskeletal motor proteins that speed up, slow down, or change trafficking direction in response to blue light (**Figure 6A**). Cytoskeletal motor proteins consist of a catalytic domain that hydrolyzes ATP to move along a component of the cytoskeleton (e.g., myosin moves along microfilaments and kinesin moves along microtubules) and a lever arm domain that connects the catalytic domain to the motor protein's cargo. The difference between the center of mass of the lever arm before and after the powerstroke influences the direction and speed of the motor. Nakamura et al. (2014) constructed an artificial lever arm consisting of the LOV2 domain flanked by α-actinin structural elements, and attached this lever arm to a myosin catalytic domain. The LOV2 domain acts as a light-actuated hinge; the light-induced loosening of the LOV2 domain changes the exit angle of the distal part of the lever arm and thus the center of mass of the lever arm. Nakamura et al. (2014) found that this artificial lever arm was modular and could introduce light-dependent speed/direction control into a variety of motor proteins, including myosin and kinesin. Such optogenetic control of a cell's organelle trafficking activities could be useful for study of neurons, in which cytoskeleton-directed organelle trafficking is required for neurite extension and synaptic maintenance and plasticity.

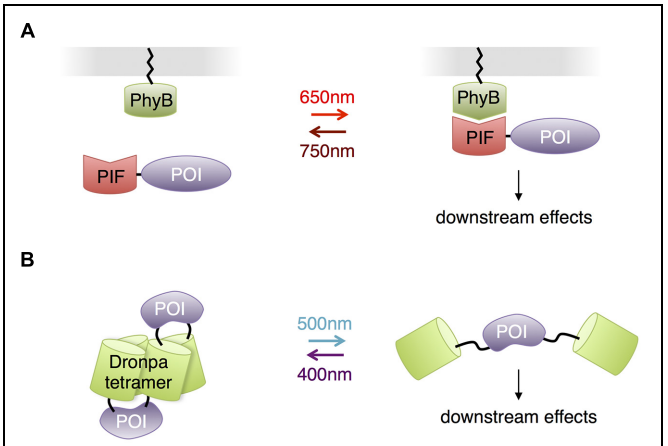

FIGURE 7 | Other photosensory modules with potential benefits for neurobiological applications. (A) Phytochrome – PIF based protein membrane translocation. Phytochrome (PhyB) is localized at plasma membrane by fusing to a membrane-trafficking peptide, and a POI is in fusion with the PIF domain. Red light-mediated PhyB-PIF interaction drives the POI to the plasma membrane, initiating downstream reactions. **(B)** Dronpa system for optogenetic control of protein function through steric blockade. Dronpa(K145N) forms tetramers. A POI is flanked by Dronpa on either terminus. When Dronpa is in multimeric form, the protein is caged and unable to perform its normal functions. Exposure to cyan light causes Dronpa to monomerize, uncaging the protein. A subsequent exposure to violet light will cause Dronpa to multimerize, again caging the protein.

Interestingly, Fukuda et al. (2014) pursued a similar idea of using LOV2 as a light-activated hinge to create PACR, a photoactivatable calcium-releasing protein (**Figure 6B**). Here, two fragments of calmodulin were fused to the two termini of LOV2, with the calmodulin-binding peptide M13 following the C-terminal calmodulin fragment. At baseline, PACR bound calcium with a dissociation constant of ∼20 nM, indicating that the calmodulin fragments were able to assemble. Upon illumination, however, affinity was reduced 200-fold, likely due to LOV2 assuming an open conformation promoting calmodulin disassembly and loss of the proper geometry for calcium chelation. As calcium induces multiple biochemical pathways via calmodulin, including ion channel modulation and kinase activation, PACR may have applications in controlling synaptic strength or neuronal growth.

In addition to its use in activating proteins, CRY2-CIB1 heterodimerization has been applied to inactivate proteins. In a technique named LARIAT (**Figure 6C**), CRY2 is fused to the POI, while CIB1 is conjugated to the multimerizing domain of CaMKIIa (Lee et al., 2014). Light induces formation of large clusters containing both fusion proteins, causing loss of activity from the POI via sequestration. In an interesting variation, a GFP-binding antibody fragment was fused to CRY2 so that the activity of GFP fusion proteins could be inhibited by light, introducing a readily applicable method for regulating proteins already tagged with GFP in transgenic mouse lines. While functional disruption has yet to be demonstrated in neurons,

TABLE 1 | Comparison of optogenetic systems.

Protein domain	Chromophore	Stimulus and time	Forward reaction	Reversibility and time	Demonstrated applications
UVR8	Tryptophan	300 nm, subsecond	Homodimer to monomer then heterodimer with COP1	Negligible in non-plant cells	Release of membrane cargo from aggregates in ER, transcription
BLUF	FAD	450 nm, subsecond	Conformational change	Spontaneous, ~3 (euPACα) or 19 s (bPAC)	Activation of naturally linked adenylate cyclase
phototropin LOV2	FMN	450 nm, subsecond	Jα helix bound to unbound	Spontaneous, ~1 min*	Uncaging of fused peptide, activation of fused protein function
EL222 LOV-HTH	FMN	450 nm, subsecond	Monomer to homodimer via HTH domain	Spontaneous, ~1 min	Transcription
FKF1 LOV	FMN	450 nm, minutes	Monomer to heterodimer with GIGANTEA	Spontaneous, days	Activation through membrane recruitment, transcription
VVD LOV	FAD	450 nm, subsecond	Monomer to homodimer	Spontaneous, ~5 h**	Transcription
CRY2	FAD	450 nm, subsecond	Monomer to homooligomer and complex with CIB1	Spontaneous, minutes	Activation through oligomerization, membrane recruitment, or fragment assembly, inactivation through aggregation, transcription
miniSOG	FMN	480 nm, minutes	Generate reactive oxygen species	Irreversible protein inactivation	Inactivating proteins through oxidizing adjacent residues
Dronpa K145N	GFP chromophore	500 nm, seconds	Homotetramer to monomer	Spontaneous in minutes, or seconds with 400 nm	Caging and uncaging of proteins
Opsins	Retinal	400–600 nm, minutes	Heteromer with GαGβγ to monomer	Negligible	Activation of G-protein effectors
PhyB	phyto-chromobilin	650 nm, subsecond	Homodimer to complex with PIF	Spontaneous in minutes, or seconds with 700 nm	Activation through membrane recruitment, transcription

*Major characteristics of representative optogenetic systems, grouped by photosensory module and ordered by excitation wavelength. Indicated times are reaction half-times with typical illumination powers on a microscope, i.e., 0.1–10 W/cm^2. *Tunable to ~3 s to 17 min with mutations (Zoltowski et al., 2009). **Tunable to ~30 s to 2 days with mutations (Zoltowski et al., 2009).*

CIB1-dependent aggregation of CRY2 fusions does occur. It may be useful to use a multimerizing domain other than that of CaMKIIa for LARIAT to prevent detrimental effects on endogenous CaMKIIa signaling.

Optogenetic control of protein activities can be extended to control specific types of ion channels regulated through protein–protein interactions or second messengers. For example, the FKF1-GIGANTEA interaction was used to control the activity of a voltage-gated calcium channel in cardiomyocytes (Dixon et al., 2012). Light-induced dimerization of $Ca_v1.2$-FKF1 and $Ca_v1.2$-GIGANTEA led to increased voltage sensitivity and calcium currents, mimicking clustering of $Ca_v1.2$ channels by the protein AKAP150. Membrane recruitment and activation of PI3K via a CRY2-CIB1 interaction has been used to modulate $K_V7.2/7.3$ potassium channels in non-neuronal cells (Idevall-Hagren et al., 2012). PI3K membrane recruitment resulted in rapid cessation of $K_V7.2/7.3$ currents, presumably because these channels require $PI(4,5)P_2$ to remain open, and PI3K activity lowers $PI(4,5)P_2$ levels. Light can thus be used to modulate the activity of specific channels native to animals, as opposed to light-gated microbial opsin ion channels or pumps, the concept that originally gave rise to the term optogenetics (Deisseroth et al., 2006). A potential advantage of modulating native-type channels is preservation of the channel responses to endogenous neuronal activity and localization to specific subcellular compartments. This could represent an alternative approach to lumitoxins to modulate the activity of specific channels that are native to animals.

Other than opsins, all the photosensory domains discussed so far use either flavin compounds or tryptophan residues as chromophores, necessitating the use of blue or UV light. This may be problematic for illuminating large regions of the brain or for prolonged stimulation, as these wavelengths of light are less penetrating and more phototoxic than redder wavelengths. Indeed, the presence of FMN and FAD in essential cellular enzymes, the reason for their ubiquity in all kingdoms of life, is also the cause of blue light-mediated phototoxicity, and UV light is efficiently absorbed by protein and DNA. However, other photosensory domains exist that use redder wavelengths of light, and these have the potential to allow multichromatic control of a variety of biological events in neurons, or optical control with less phototoxicity. Phytochromes are a family of red-absorbing photoreceptors found in plants, fungi and bacteria that use tetrapyrrole cofactors as chromophores. Plant phytochromes bind to phytochrome interaction factors (PIFs) in response to light (Li et al., 2011). This interaction was used for light control of transcription and protein localization in yeast (Shimizu-Sato et al., 2002; Yang et al., 2013) and membrane trafficking of signaling proteins in mammalian cells

(Levskaya et al., 2009; Toettcher et al., 2013; **Figure 7A**). The phytochromobilin cofactor used by plant phytochromes is not present in yeast and animal cells but can be added to cell culture. Recently, expression of the synthetic enzymes for phytochromobilin in mammalian cells was found to produce enough phytochromobilin for phytochrome maturation (Muller et al., 2013), suggesting that plant phytochromes could be usable in mice as well. Alternatively, phytochromes that use biliverdin, a natural degradation product of heme, may be adaptable to control mammalian proteins. A fusion of a biliverdin-utilizing bacterial phytochrome to a phosphodiesterase was recently shown to allow light control of cAMP levels in mammalian cells and zebrafish embryos (Gasser et al., 2014). However, light-dependent binding partners of biliverdin-utilizing phytochromes have not yet been described. The unique red absorption characteristic of phytochromes enables its usage in combination with a violet- or blue-absorbing light activated system, so that two or three processes can be controlled concurrently, potentially allowing roles of multiple proteins in complex cell signaling pathways to be disentangled (Muller et al., 2014).

In contrast to adapting photosensory proteins that naturally function in light-mediated signaling, Zhou et al. (2012) engineered the green monomeric fluorescent protein Dronpa for optogenetic control of protein function. A K145N mutant of Dronpa is a tetrameric protein that monomerizes when exposed to cyan light (500 nm) and reassembles when exposed to violet light (400 nm). Fusion of Dronpa K145N to both termini of proteins caged proteins through steric blockade of interaction sites, and photodissociation of Dronpa K145N activated the proteins (**Figure 7B**). These fluorescent light-inducible proteins (FLiPs) have a few unique properties derived from using a traditional autocatalytic fluorescent protein as the photosensory domain. FLiPs are activated by cyan light, which is not absorbed by endogenous proteins in animal cells. The chromophore in Dronpa is autocatalytically synthesized, so performance is independent of the concentration of cofactors. Finally, FLiPs are self-reporting, as the monomerization of Dronpa K145N corresponds with its photoswitching into a dark state.

Summary

The last few years have seen the rapid development of optogenetic methods for controlling protein activities (**Table 1**). As reviewed here, some of these have already been successfully applied to the study of nervous system development and function. Unlike drug control, optogenetic control allows for modulation of protein activity relatively rapidly (sub-second to minutes) or in localized subcellular regions. The methods that have been used in neurons so far either take advantage of cofactors that are available in animal cells (retinal, FAD, and FMN), or use a natural amino acid as a chromophore (tryptophan in the case of UVR8). Many examples of optogenetic control of protein activities in the brains of animals now exist.

For some mechanisms of protein regulation, multiple light-controlled systems are available, allowing experimenters to choose the system best suited for their needs. For example, the Vivid LOV domain and CRY2 both mediate light-induced protein homodimerization. For light-induced heterodimerization, e.g., for membrane recruitment of signaling proteins or split protein recombination, the LOVpep-PDZ, LOV2SsrA-SspB, FKF-GIGANTEA, CRY2-CIB1, or PhyB-PIF interactions can be used. The CRY2-CIB interaction features fast activation (sub-second) and by many reports is robust and reproducible, but aggregation of CRY2 in response to light may activate some functions while inhibiting others. This could create some uncertainty when CRY2 is fused to a protein capable of interacting with other proteins or with enzymatic activity. It may be useful when inducing any particular protein interaction to use multiple systems for cross-validation. Interestingly, LOV2-pep, CRY2-CIB1, and PhyB-PIF systems were recently compared in a transcriptional activation assay and found to function in the same general range (Pathak et al., 2014).

Optogenetic strategies for controlling protein activity continue to grow in diversity and number. For example, recent research has extended optical control beyond simply inducing protein oligomerization or localization via heterodimerization. The LOV domain can also be used as a light-openable hinge (Nakamura et al., 2014), the CRY2-CIB1 interaction can be used to sequester proteins (Lee et al., 2014), and autocatalytic fluorescent proteins can be used to cage and uncage the function of individual proteins (Zhou et al., 2012). The next few years will undoubtedly see the development of more methods for harnessing light to control biological activities in animal cells, and additional interesting applications of optogenetic control of protein activity to the development and function of nervous systems.

Acknowledgments

XZ is supported by a Howard Hughes International Graduate Fellowship and a Stanford Graduate Fellowship. ML is supported by NIH Pioneer Award 1DP1OD017209, the Rita Allen Foundation, and the Burroughs Wellcome Foundation.

References

Airan, R. D., Thompson, K. R., Fenno, L. E., Bernstein, H., and Deisseroth, K. (2009). Temporally precise in vivo control of intracellular signalling. *Nature* 458, 1025–1029. doi: 10.1038/nature07926

Bailes, H. J., Zhuang, L. Y., and Lucas, R. J. (2012). Reproducible and sustained regulation of Galphas signalling using a metazoan opsin as an optogenetic tool. *PLoS ONE* 7:e30774. doi: 10.1371/journal.pone.0030774

Barends, T. R., Hartmann, E., Griese, J. J., Beitlich, T., Kirienko, N. V., Ryjenkov, D. A., et al. (2009). Structure and mechanism of a bacterial light-regulated cyclic nucleotide phosphodiesterase. *Nature* 459, 1015–1018. doi: 10.1038/nature07966

Bellmann, D., Richardt, A., Freyberger, R., Nuwal, N., Schwarzel, M., Fiala, A., et al. (2010). Optogenetically induced olfactory stimulation in *Drosophila larvae* reveals the neuronal basis of odor-aversion behavior. *Front. Behav. Neurosci.* 4:27. doi: 10.3389/fnbeh.2010.00027

Bernstein, J. G., and Boyden, E. S. (2011). Optogenetic tools for analyzing the neural circuits of behavior. *Trends Cogn. Sci.* 15, 592–600. doi: 10.1016/j.tics.2011.10.003

Bonger, K. M., Rakhit, R., Payumo, A. Y., Chen, J. K., and Wandless, T. J. (2014). General method for regulating protein stability with light. *ACS Chem. Biol.* 9, 111–115. doi: 10.1021/cb400755b

Boulina, M., Samarajeewa, H., Baker, J. D., Kim, M. D., and Chiba, A. (2013). Live imaging of multicolor-labeled cells in *Drosophila*. *Development* 140, 1605–1613. doi: 10.1242/dev.088930

Boyden, E. S., Zhang, F., Bamberg, E., Nagel, G., and Deisseroth, K. (2005). Millisecond-timescale, genetically targeted optical control of neural activity. *Nat. Neurosci.* 8, 1263–1268. doi: 10.1038/nn1525

Bugaj, L. J., Choksi, A. T., Mesuda, C. K., Kane, R. S., and Schaffer, D. V. (2013). Optogenetic protein clustering and signaling activation in mammalian cells. *Nat. Methods* 10, 249–252. doi: 10.1038/nmeth.2360

Chang, K. Y., Woo, D., Jung, H., Lee, S., Kim, S., Won, J., et al. (2014). Light-inducible receptor tyrosine kinases that regulate neurotrophin signalling. *Nat. Commun.* 5:4057. doi: 10.1038/ncomms5057

Chen, D., Gibson, E. S., and Kennedy, M. J. (2013). A light-triggered protein secretion system. *J. Cell Biol.* 201, 631–640. doi: 10.1083/jcb.201210119

Christie, J. M., Gawthorne, J., Young, G., Fraser, N. J., and Roe, A. J. (2012). LOV to BLUF: flavoprotein contributions to the optogenetic toolkit. *Mol. Plant* 5, 533–544. doi: 10.1093/mp/sss020

Chuong, A. S., Miri, M. L., Busskamp, V., Matthews, G. A., Acker, L. C., Sorensen, A. T., et al. (2014). Noninvasive optical inhibition with a red-shifted microbial rhodopsin. *Nat. Neurosci.* 17, 1123–1129. doi: 10.1038/nn.3752

Crefcoeur, R. P., Yin, R., Ulm, R., and Halazonetis, T. D. (2013). Ultraviolet-B-mediated induction of protein-protein interactions in mammalian cells. *Nat. Commun.* 4:1779. doi: 10.1038/ncomms2800

Crosson, S., and Moffat, K. (2001). Structure of a flavin-binding plant photoreceptor domain: insights into light-mediated signal transduction. *Proc. Natl. Acad. Sci. U.S.A.* 98, 2995–3000. doi: 10.1073/pnas.051520298

De Marco, R. J., Groneberg, A. H., Yeh, C. M., Castillo Ramirez, L. A., and Ryu, S. (2013). Optogenetic elevation of endogenous glucocorticoid level in larval zebrafish. *Front. Neural Circuits* 7:82. doi: 10.3389/fncir.2013.00082

Deisseroth, K., Feng, G., Majewska, A. K., Miesenbock, G., Ting, A., and Schnitzer, M. J. (2006). Next-generation optical technologies for illuminating genetically targeted brain circuits. *J. Neurosci.* 26, 10380–10386. doi: 10.1523/JNEUROSCI.3863-06.2006

Dietz, D. M., Sun, H., Lobo, M. K., Cahill, M. E., Chadwick, B., Gao, V., et al. (2012). Rac1 is essential in cocaine-induced structural plasticity of nucleus accumbens neurons. *Nat. Neurosci.* 15, 891–896. doi: 10.1038/nn.3094

Dixon, R. E., Yuan, C., Cheng, E. P., Navedo, M. F., and Santana, L. F. (2012). Ca^{2+} signaling amplification by oligomerization of L-type Cav1.2 channels. *Proc. Natl. Acad. Sci. U.S.A.* 109, 1749–1754. doi: 10.1073/pnas.1116731109

Duebel, J., Marazova, K., and Sahel, J. A. (2015). Optogenetics. *Curr. Opin. Ophthalmol.* 26, 226–232. doi: 10.1097/ICU.0000000000000140

Efetova, M., and Schwarzel, M. (2015). Photoactivatable adenylyl cyclases (PACs) as a tool to study cAMP signaling in vivo: an overview. *Methods Mol. Biol.* 1294, 131–135. doi: 10.1007/978-1-4939-2537-7_10

Favory, J. J., Stec, A., Gruber, H., Rizzini, L., Oravecz, A., Funk, M., et al. (2009). Interaction of COP1 and UVR8 regulates UV-B-induced photomorphogenesis and stress acclimation in *Arabidopsis*. *EMBO J.* 28, 591–601. doi: 10.1038/emboj.2009.4

Fenno, L., Yizhar, O., and Deisseroth, K. (2011). The development and application of optogenetics. *Annu. Rev. Neurosci.* 34, 389–412. doi: 10.1146/annurev-neuro-061010-113817

Fukuda, N., Matsuda, T., and Nagai, T. (2014). Optical control of the Ca^{2+} concentration in a live specimen with a genetically encoded Ca^{2+}-releasing molecular tool. *ACS Chem. Biol.* 9, 1197–1203. doi: 10.1021/cb400849n

Gasser, C., Taiber, S., Yeh, C. M., Wittig, C. H., Hegemann, P., Ryu, S., et al. (2014). Engineering of a red-light-activated human cAMP/cGMP-specific phosphodiesterase. *Proc. Natl. Acad. Sci. U.S.A.* 111, 8803–8808. doi: 10.1073/pnas.1321600111

Harper, S. M., Christie, J. M., and Gardner, K. H. (2004). Disruption of the LOV-Jalpha helix interaction activates phototropin kinase activity. *Biochemistry* 43, 16184–16192. doi: 10.1021/bi048092i

Harper, S. M., Neil, L. C., and Gardner, K. H. (2003). Structural basis of a phototropin light switch. *Science* 301, 1541–1544. doi: 10.1126/science.1086810

Heijde, M., and Ulm, R. (2013). Reversion of the *Arabidopsis* UV-B photoreceptor UVR8 to the homodimeric ground state. *Proc. Natl. Acad. Sci. U.S.A.* 110, 1113–1118. doi: 10.1073/pnas.1214237110

Idevall-Hagren, O., Dickson, E. J., Hille, B., Toomre, D. K., and De Camilli, P. (2012). Optogenetic control of phosphoinositide metabolism. *Proc. Natl. Acad. Sci. U.S.A.* 109, E2316–E2323. doi: 10.1073/pnas.1211305109

Imayoshi, I., Isomura, A., Harima, Y., Kawaguchi, K., Kori, H., Miyachi, H., et al. (2013). Oscillatory control of factors determining multipotency and fate in mouse neural progenitors. *Science* 342, 1203–1208. doi: 10.1126/science.1242366

Jay, D. G. (1988). Selective destruction of protein function by chromophore-assisted laser inactivation. *Proc. Natl. Acad. Sci. U.S.A.* 85, 5454–5458. doi: 10.1073/pnas.85.15.5454

Jinek, M., Chylinski, K., Fonfara, I., Hauer, M., Doudna, J. A., and Charpentier, E. (2012). A programmable dual-RNA-guided DNA endonuclease in adaptive bacterial immunity. *Science* 337, 816–821. doi: 10.1126/science.1225829

Kakumoto, T., and Nakata, T. (2013). Optogenetic control of PIP3: PIP3 is sufficient to induce the actin-based active part of growth cones and is regulated via endocytosis. *PLoS ONE* 8:e70861. doi: 10.1371/journal.pone.0070861

Karunarathne, W. K., Giri, L., Kalyanaraman, V., and Gautam, N. (2013). Optically triggering spatiotemporally confined GPCR activity in a cell and programming neurite initiation and extension. *Proc. Natl. Acad. Sci. U.S.A.* 110, E1565–E1574. doi: 10.1073/pnas.1220697110

Kennedy, M. J., Hughes, R. M., Peteya, L. A., Schwartz, J. W., Ehlers, M. D., and Tucker, C. L. (2010). Rapid blue-light-mediated induction of protein interactions in living cells. *Nat. Methods* 7, 973–975. doi: 10.1038/nmeth.1524

Kim, J. M., Hwa, J., Garriga, P., Reeves, P. J., RajBhandary, U. L., and Khorana, H. G. (2005). Light-driven activation of beta 2-adrenergic receptor signaling by a chimeric rhodopsin containing the beta 2-adrenergic receptor cytoplasmic loops. *Biochemistry* 44, 2284–2292. doi: 10.1021/bi048328i

Kim, N., Kim, J. M., Lee, M., Kim, C. Y., Chang, K. Y., and Heo, W. D. (2014). Spatiotemporal control of fibroblast growth factor receptor signals by blue light. *Chem. Biol.* 21, 903–912. doi: 10.1016/j.chembiol.2014.05.013

Klapoetke, N. C., Murata, Y., Kim, S. S., Pulver, S. R., Birdsey-Benson, A., Cho, Y. K., et al. (2014). Independent optical excitation of distinct neural populations. *Nat. Methods* 11, 338–346. doi: 10.1038/nmeth.2836

Konermann, S., Brigham, M. D., Trevino, A. E., Hsu, P. D., Heidenreich, M., Cong, L., et al. (2013). Optical control of mammalian endogenous transcription and epigenetic states. *Nature* 500, 472–476. doi: 10.1038/nature12466

Lee, J., Natarajan, M., Nashine, V. C., Socolich, M., Vo, T., Russ, W. P., et al. (2008). Surface sites for engineering allosteric control in proteins. *Science* 322, 438–442. doi: 10.1126/science.1159052

Lee, S., Park, H., Kyung, T., Kim, N. Y., Kim, S., Kim, J., et al. (2014). Reversible protein inactivation by optogenetic trapping in cells. *Nat. Methods* 11, 633–636. doi: 10.1038/nmeth.2940

Levskaya, A., Weiner, O. D., Lim, W. A., and Voigt, C. A. (2009). Spatiotemporal control of cell signalling using a light-switchable protein interaction. *Nature* 461, 997–1001. doi: 10.1038/nature08446

Li, J., Li, G., Wang, H., and Wang Deng, X. (2011). Phytochrome signaling mechanisms. *Arabidopsis Book* 9:e0148. doi: 10.1199/tab.0148

Li, X., Gutierrez, D. V., Hanson, M. G., Han, J., Mark, M. D., Chiel, H., et al. (2005). Fast noninvasive activation and inhibition of neural and network activity by vertebrate rhodopsin and green algae channelrhodopsin. *Proc. Natl. Acad. Sci. U.S.A.* 102, 17816–17821. doi: 10.1073/pnas.0509030102

Lin, J. Y., Knutsen, P. M., Muller, A., Kleinfeld, D., and Tsien, R. Y. (2013a). ReaChR: a red-shifted variant of channelrhodopsin enables deep transcranial optogenetic excitation. *Nat. Neurosci.* 16, 1499–1508. doi: 10.1038/nn.3502

Lin, J. Y., Sann, S. B., Zhou, K., Nabavi, S., Proulx, C. D., Malinow, R., et al. (2013b). Optogenetic inhibition of synaptic release with chromophore-assisted light inactivation (CALI). *Neuron* 79, 241–253. doi: 10.1016/j.neuron.2013.05.022

Liu, H., Yu, X., Li, K., Klejnot, J., Yang, H., Lisiero, D., et al. (2008). Photoexcited CRY2 interacts with CIB1 to regulate transcription and floral initiation in *Arabidopsis*. *Science* 322, 1535–1539. doi: 10.1126/science.1163927

Livet, J., Weissman, T. A., Kang, H., Draft, R. W., Lu, J., Bennis, R. A., et al. (2007). Transgenic strategies for combinatorial expression of fluorescent proteins in the nervous system. *Nature* 450, 56–62. doi: 10.1038/nature06293

Losi, A. (2007). Flavin-based blue-Light photosensors: a photobiophysics update. *Photochem. Photobiol.* 83, 1283–1300. doi: 10.1111/j.1751-1097.2007.00196.x

Lungu, O. I., Hallett, R. A., Choi, E. J., Aiken, M. J., Hahn, K. M., and Kuhlman, B. (2012). Designing photoswitchable peptides using the AsLOV2 domain. *Chem. Biol.* 19, 507–517. doi: 10.1016/j.chembiol.2012.02.006

Maletic-Savatic, M., Malinow, R., and Svoboda, K. (1999). Rapid dendritic morphogenesis in CA1 hippocampal dendrites induced by synaptic activity. *Science* 283, 1923–1927. doi: 10.1126/science.283.5409.1923

Marek, K. W., and Davis, G. W. (2002). Transgenically encoded protein photoinactivation (FlAsH-FALI): acute inactivation of synaptotagmin I. *Neuron* 36, 805–813. doi: 10.1016/S0896-6273(02)01068-1

Masseck, O. A., Spoida, K., Dalkara, D., Maejima, T., Rubelowski, J. M., Wallhorn, L., et al. (2014). Vertebrate cone opsins enable sustained and highly sensitive rapid control of Gi/o signaling in anxiety circuitry. *Neuron* 81, 1263–1273. doi: 10.1016/j.neuron.2014.01.041

Moglich, A., Ayers, R. A., and Moffat, K. (2009). Design and signaling mechanism of light-regulated histidine kinases. *J. Mol. Biol.* 385, 1433–1444. doi: 10.1016/j.jmb.2008.12.017

Motta-Mena, L. B., Reade, A., Mallory, M. J., Glantz, S., Weiner, O. D., Lynch, K. W., et al. (2014). An optogenetic gene expression system with rapid activation and deactivation kinetics. *Nat. Chem. Biol.* 10, 196–202. doi: 10.1038/nchembio.1430

Muller, K., Engesser, R., Timmer, J., Nagy, F., Zurbriggen, M. D., and Weber, W. (2013). Synthesis of phycocyanobilin in mammalian cells. *Chem. Commun. (Camb.)* 49, 8970–8972. doi: 10.1039/c3cc45065a

Muller, K., Engesser, R., Timmer, J., Zurbriggen, M. D., and Weber, W. (2014). Orthogonal optogenetic triple-gene control in Mammalian cells. *ACS Synth. Biol.* 3, 796–801. doi: 10.1021/sb500305v

Nakamura, M., Chen, L., Howes, S. C., Schindler, T. D., Nogales, E., and Bryant, Z. (2014). Remote control of myosin and kinesin motors using light-activated gearshifting. *Nat. Nanotechnol.* 9, 693–697. doi: 10.1038/nnano.2014.147

Nihongaki, Y., Yamamoto, S., Kawano, F., Suzuki, H., and Sato, M. (2015). CRISPR-Cas9-based photoactivatable transcription system. *Chem. Biol.* 22, 169–174. doi: 10.1016/j.chembiol.2014.12.011

Niopek, D., Benzinger, D., Roensch, J., Draebing, T., Wehler, P., Eils, R., et al. (2014). Engineering light-inducible nuclear localization signals for precise spatiotemporal control of protein dynamics in living cells. *Nat. Commun.* 5:4404. doi: 10.1038/ncomms5404

Oh, E., Maejima, T., Liu, C., Deneris, E., and Herlitze, S. (2010). Substitution of 5-HT1A receptor signaling by a light-activated G protein-coupled receptor. *J. Biol. Chem.* 285, 30825–30836. doi: 10.1074/jbc.M110.147298

Ohlendorf, R., Vidavski, R. R., Eldar, A., Moffat, K., and Moglich, A. (2012). From dusk till dawn: one-plasmid systems for light-regulated gene expression. *J. Mol. Biol.* 416, 534–542. doi: 10.1016/j.jmb.2012.01.001

Pathak, G. P., Strickland, D., Vrana, J. D., and Tucker, C. L. (2014). Benchmarking of optical dimerizer systems. *ACS Synth. Biol.* 3, 832–838. doi: 10.1021/sb500291r

Polstein, L. R., and Gersbach, C. A. (2012). Light-inducible spatiotemporal control of gene activation by customizable zinc finger transcription factors. *J. Am. Chem. Soc.* 134, 16480–16483. doi: 10.1021/ja3065667

Polstein, L. R., and Gersbach, C. A. (2015). A light-inducible CRISPR-Cas9 system for control of endogenous gene activation. *Nat. Chem. Biol.* 11, 198–200. doi: 10.1038/nchembio.1753

Ramel, D., Wang, X., Laflamme, C., Montell, D. J., and Emery, G. (2013). Rab11 regulates cell–cell communication during collective cell movements. *Nat. Cell Biol.* 15, 317–324. doi: 10.1038/ncb2681

Renicke, C., Schuster, D., Usherenko, S., Essen, L. O., and Taxis, C. (2013). A LOV2 domain-based optogenetic tool to control protein degradation and cellular function. *Chem. Biol.* 20, 619–626. doi: 10.1016/j.chembiol.2013.03.005

Riggsbee, C. W., and Deiters, A. (2010). Recent advances in the photochemical control of protein function. *Trends Biotechnol.* 28, 468–475. doi: 10.1016/j.tibtech.2010.06.001

Rizzini, L., Favory, J. J., Cloix, C., Faggionato, D., O'Hara, A., Kaiserli, E., et al. (2011). Perception of UV-B by the *Arabidopsis* UVR8 protein. *Science* 332, 103–106. doi: 10.1126/science.1200660

Schmidt, D., Tillberg, P. W., Chen, F., and Boyden, E. S. (2014). A fully genetically encoded protein architecture for optical control of peptide ligand concentration. *Nat. Commun.* 5:3019. doi: 10.1038/ncomms4019

Schroder-Lang, S., Schwarzel, M., Seifert, R., Strunker, T., Kateriya, S., Looser, J., et al. (2007). Fast manipulation of cellular cAMP level by light in vivo. *Nat. Methods* 4, 39–42. doi: 10.1038/nmeth975

Schwechter, B., Rosenmund, C., and Tolias, K. F. (2013). RasGRF2 Rac-GEF activity couples NMDA receptor calcium flux to enhanced synaptic transmission. *Proc. Natl. Acad. Sci. U.S.A.* 110, 14462–14467. doi: 10.1073/pnas.1304340110

Shimizu-Sato, S., Huq, E., Tepperman, J. M., and Quail, P. H. (2002). A light-switchable gene promoter system. *Nat. Biotechnol.* 20, 1041–1044. doi: 10.1038/nbt734

Shu, X., Lev-Ram, V., Deerinck, T. J., Qi, Y., Ramko, E. B., Davidson, M. W., et al. (2011). A genetically encoded tag for correlated light and electron microscopy of intact cells, tissues, and organisms. *PLoS Biol.* 9:e1001041. doi: 10.1371/journal.pbio.1001041

Siuda, E. R., Copits, B. A., Schmidt, M. J., Baird, M. A., Al-Hasani, R., Planer, W. J., et al. (2015). Spatiotemporal control of opioid signaling and behavior. *Neuron* 86, 923–935. doi: 10.1016/j.neuron.2015.03.066

Spoida, K., Masseck, O. A., Deneris, E. S., and Herlitze, S. (2014). Gq/5-HT2c receptor signals activate a local GABAergic inhibitory feedback circuit to modulate serotonergic firing and anxiety in mice. *Proc. Natl. Acad. Sci. U.S.A.* 111, 6479–6484. doi: 10.1073/pnas.1321576111

Stierl, M., Stumpf, P., Udwari, D., Gueta, R., Hagedorn, R., Losi, A., et al. (2011). Light modulation of cellular cAMP by a small bacterial photoactivated adenylyl cyclase, bPAC, of the soil bacterium *Beggiatoa*. *J. Biol. Chem.* 286, 1181–1188. doi: 10.1074/jbc.M110.185496

Strickland, D., Lin, Y., Wagner, E., Hope, C. M., Zayner, J., Antoniou, C., et al. (2012). TULIPs: tunable, light-controlled interacting protein tags for cell biology. *Nat. Methods* 9, 379–384. doi: 10.1038/nmeth.1904

Strickland, D., Moffat, K., and Sosnick, T. R. (2008). Light-activated DNA binding in a designed allosteric protein. *Proc. Natl. Acad. Sci. U.S.A.* 105, 10709–10714. doi: 10.1073/pnas.0709610105

Taslimi, A., Vrana, J. D., Chen, D., Borinskaya, S., Mayer, B. J., Kennedy, M. J., et al. (2014). An optimized optogenetic clustering tool for probing protein interaction and function. *Nat. Commun.* 5:4925. doi: 10.1038/ncomms5925

Toettcher, J. E., Weiner, O. D., and Lim, W. A. (2013). Using optogenetics to interrogate the dynamic control of signal transmission by the Ras/Erk module. *Cell* 155, 1422–1434. doi: 10.1016/j.cell.2013.11.004

Tour, O., Meijer, R. M., Zacharias, D. A., Adams, S. R., and Tsien, R. Y. (2003). Genetically targeted chromophore-assisted light inactivation. *Nat. Biotechnol.* 21, 1505–1508. doi: 10.1038/nbt914

van Bergeijk, P., Adrian, M., Hoogenraad, C. C., and Kapitein, L. C. (2015). Optogenetic control of organelle transport and positioning. *Nature* 518, 111–114. doi: 10.1038/nature14128

Walters, K. B., Green, J. M., Surfus, J. C., Yoo, S. K., and Huttenlocher, A. (2010). Live imaging of neutrophil motility in a zebrafish model of WHIM syndrome. *Blood* 116, 2803–2811. doi: 10.1182/blood-2010-03-276972

Wang, X., He, L., Wu, Y. I., Hahn, K. M., and Montell, D. J. (2010). Light-mediated activation reveals a key role for Rac in collective guidance of cell movement in vivo. *Nat. Cell Biol.* 12, 591–597. doi: 10.1038/ncb2061

Wang, X., Chen, X., and Yang, Y. (2012). Spatiotemporal control of gene expression by a light-switchable transgene system. *Nat. Methods* 9, 266–269. doi: 10.1038/nmeth.1892

Weissenberger, S., Schultheis, C., Liewald, J. F., Erbguth, K., Nagel, G., and Gottschalk, A. (2011). PACalpha–an optogenetic tool for in vivo manipulation of cellular cAMP levels, neurotransmitter release, and behavior in *Caenorhabditis elegans*. *J. Neurochem.* 116, 616–625. doi: 10.1111/j.1471-4159.2010.07148.x

Willumsen, B. M., Christensen, A., Hubbert, N. L., Papageorge, A. G., and Lowy, D. R. (1984). The p21 ras C-terminus is required for transformation and membrane association. *Nature* 310, 583–586. doi: 10.1038/310583a0

Wu, D., Hu, Q., Yan, Z., Chen, W., Yan, C., Huang, X., et al. (2012). Structural basis of ultraviolet-B perception by UVR8. *Nature* 484, 214–219. doi: 10.1038/nature10931

Wu, Y. I., Frey, D., Lungu, O. I., Jaehrig, A., Schlichting, I., Kuhlman, B., et al. (2009). A genetically encoded photoactivatable Rac controls the motility of living cells. *Nature* 461, 104–108. doi: 10.1038/nature08241

Yang, X., Jost, A. P., Weiner, O. D., and Tang, C. (2013). A light-inducible organelle-targeting system for dynamically activating and inactivating signaling in budding yeast. *Mol. Biol. Cell* 24, 2419–2430. doi: 10.1091/mbc.E13-03-0126

Yazawa, M., Sadaghiani, A. M., Hsueh, B., and Dolmetsch, R. E. (2009). Induction of protein-protein interactions in live cells using light. *Nat. Biotechnol.* 27, 941–945. doi: 10.1038/nbt.1569

Yizhar, O., Fenno, L. E., Prigge, M., Schneider, F., Davidson, T. J., O'Shea, D. J., et al. (2011). Neocortical excitation/inhibition balance in information processing and social dysfunction. *Nature* 477, 171–178. doi: 10.1038/nature10360

Yoo, S. K., Deng, Q., Cavnar, P. J., Wu, Y. I., Hahn, K. M., and Huttenlocher, A. (2010). Differential regulation of protrusion and polarity by PI (3) K during neutrophil motility in live zebrafish. *Dev. Cell* 18, 226–236. doi: 10.1016/j.devcel.2009.11.015

Zhang, F., Vierock, J., Yizhar, O., Fenno, L. E., Tsunoda, S., Kianianmomeni, A., et al. (2011). The microbial opsin family of optogenetic tools. *Cell* 147, 1446–1457. doi: 10.1016/j.cell.2011.12.004

Zhang, K., Duan, L., Ong, Q., Lin, Z., Varman, P. M., Sung, K., et al. (2014). Light-mediated kinetic control reveals the temporal effect of the Raf/MEK/ERK pathway in PC12 cell neurite outgrowth. *PLoS ONE* 9:e92917. doi: 10.1371/journal.pone.0092917

Zhou, X. X., Chung, H. K., Lam, A. J., and Lin, M. Z. (2012). Optical control of protein activity by fluorescent protein domains. *Science* 338, 810–814. doi: 10.1126/science.1226854

Zoltowski, B. D., and Gardner, K. H. (2011). Tripping the light fantastic: blue-light photoreceptors as examples of environmentally modulated protein-protein interactions. *Biochemistry* 50, 4–16. doi: 10.1021/bi101665s

Zoltowski, B. D., Schwerdtfeger, C., Widom, J., Loros, J. J., Bilwes, A. M., Dunlap, J. C., et al. (2007). Conformational switching in the fungal light sensor Vivid. *Science* 316, 1054–1057. doi: 10.1126/science.1137128

Zoltowski, B. D., Vaccaro, B., and Crane, B. R. (2009). Mechanism-based tuning of a LOV domain photoreceptor. *Nat. Chem. Biol.* 5, 827–834. doi: 10.1038/nchembio.210

Conflict of Interest Statement: The authors declare that the research was conducted in the absence of any commercial or financial relationships that could be construed as a potential conflict of interest.

frontiers in
MOLECULAR NEUROSCIENCE

ORIGINAL RESEARCH ARTICLE
published: 29 September 2014
doi: 10.3389/fnmol.2014.00078

Exploration of genetically encoded voltage indicators based on a chimeric voltage sensing domain

Yukiko Mishina[1,2], Hiroki Mutoh[1,3], Chenchen Song[4] and Thomas Knöpfel[1,4]*

[1] *Laboratory for Neuronal Circuit Dynamics, RIKEN Brain Science Institute, Wako, Japan*
[2] *Centre for Global Communication Strategies, The University of Tokyo, Tokyo, Japan*
[3] *Department of Neurophysiology, Hamamatsu University School of Medicine, Shizuoka, Japan*
[4] *Division of Brain Sciences, Department of Medicine, Imperial College London, London, UK*

Edited by:
Katsuhiko Mikoshiba, RIKEN Brain Science Institute, Japan

Reviewed by:
Manuel L. Covarrubias, Thomas Jefferson University, USA
Alexandre Mourot, Université Pierre et Marie Curie, France

Correspondence:
Thomas Knöpfel, Division of Brain Sciences, Department of Medicine, Imperial College London, Hammersmith Hospital Campus, Du Cane Road, London W12 0NN, UK
e-mail: t.knopfel@imperial.ac.uk

Deciphering how the brain generates cognitive function from patterns of electrical signals is one of the ultimate challenges in neuroscience. To this end, it would be highly desirable to monitor the activities of very large numbers of neurons while an animal engages in complex behaviors. Optical imaging of electrical activity using genetically encoded voltage indicators (GEVIs) has the potential to meet this challenge. Currently prevalent GEVIs are based on the voltage-sensitive fluorescent protein (VSFP) prototypical design or on the voltage-dependent state transitions of microbial opsins. We recently introduced a new VSFP design in which the voltage-sensing domain (VSD) is sandwiched between a fluorescence resonance energy transfer pair of fluorescent proteins (termed VSFP-Butterflies) and also demonstrated a series of chimeric VSD in which portions of the VSD of *Ciona intestinalis* voltage-sensitive phosphatase are substituted by homologous portions of a voltage-gated potassium channel subunit. These chimeric VSD had faster sensing kinetics than that of the native Ci-VSD. Here, we describe a new set of VSFPs that combine chimeric VSD with the Butterfly structure. We show that these chimeric VSFP-Butterflies can report membrane voltage oscillations of up to 200 Hz in cultured cells and report sensory evoked cortical population responses in living mice. This class of GEVIs may be suitable for imaging of brain rhythms in behaving mammalians.

Keywords: optogenetics, mouse model, optical imaging, voltage imaging, FRET sensors

INTRODUCTION

Deciphering how the brain generates cognitive function from patterns of electrical signals is one of the ultimate challenges in neuroscience. Advances toward this goal require a better understanding of the "neuronal code," and being able to monitor electrical signals of very large neuronal populations with fine temporal resolution is central to the progress. Even when restricted to relatively simple behaviors (such as goal-directed motor actions in response to sensory stimuli), observing only cortical activities, and in small animals such as mice, the monitoring of electrical activities must cover mesoscopic areas of tissue (dimensions measured at the millimeter scale). Optical voltage imaging methods have, at least in principle, the spatio-temporal resolution necessary for this endeavor (Ross et al., 1974; Grinvald et al., 1977; Grinvald and Hildesheim, 2004). In particular, voltage-sensitive dyes have been fruitfully employed in widefield epifluorescence imaging (Shoham et al., 1999; Petersen et al., 2003a; Grinvald and Hildesheim, 2004), and this approach has contributed much to the understanding of cortical circuit dynamics, especially in visual and somatosensory areas (Shoham et al., 1999; Kenet et al., 2003; Petersen et al., 2003a,b; Grinvald and Hildesheim, 2004).

Recently developed genetically-encoded voltage indicators (GEVIs) promise to improve upon classical voltage-sensitive dyes in at least four aspects: (i) they allow for non-invasive transcranial imaging in species with thin craniums (such as mice), which eliminates the previously compulsory craniotomies for dye staining; (ii) they provide reliable recordings from the same neuronal population in a subject over prolonged periods of time for multiple sessions; (iii) they genetically target specific cell populations, so the signals originate only from specific neurons of interest in an otherwise diverse population; (iv) they enable transgenic expression strategies that provide highly reproducible expression of protein indicators in different animals to eliminate between-subject variability.

There are two classes of conceptual designs of GEVIs currently being pursued. The first type is the microbial opsin-based GEVIs that exhibit voltage-dependent state-transitions in their photocycles (Kralj et al., 2012; Maclaurin et al., 2013). These opsin-based probes were initially limited by their low brightness (Mutoh et al., 2012; Mutoh and Knöpfel, 2013), but this issue has been successfully addressed in very recent work (Gong et al., 2014; Zou et al., 2014). The second type is the voltage-sensitive fluorescent protein (VSFP) class of GEVIs. These utilize the voltage-dependent structural rearrangement of voltage-sensing domains (VSDs), which are homologous to the S1–S4 transmembrane segment of Kv potassium channels. Thus far, several VSFP derivatives have enabled voltage imaging in brain slices as well as in intact mouse brain (Akemann et al., 2010, 2012; Mutoh et al., 2012; St-Pierre et al., 2014).

The first VSFPs (VSFP1 and VSFP2.x) exploited the voltage-dependent VSD structural rearrangement to modulate fluorescence resonance energy transfer (FRET) efficacy between a tandem

pair of fluorescent proteins (Sakai et al., 2001; Dimitrov et al., 2007). Dissection of a FRET independent component of the voltage response led to the development of the monochromatic (single fluorescent protein) VSFP3.x (Lundby et al., 2008; Perron et al., 2009a,b). More recently, we introduced VSFP-Butterflies, in which two fluorescent proteins are positioned so that the VSD is now sandwiched between the FRET pair (Akemann et al., 2012). These VSFP-Butterflies permitted imaging of sub-threshold activity *in vivo* in specific neuronal populations in awake behaving mice (Akemann et al., 2012). The VSFP2.x, VSFP3.x, and the VSFP-Butterfly scaffolds were adopted for other fluorescent proteins (Tsutsui et al., 2008, 2013; Jin et al., 2012).

The first VSFP with robust signals in mammalian cells used the voltage sensor of *Ciona intestinalis* voltage-sensitive phosphatase (Ci-VSP) whose VSD is homologous to that of Kv potassium channels (VSFP2.1; Dimitrov et al., 2007). Subsequent VSFP type of GEVIs [e.g., VSFP2.3 and VSFP3.1 (Lundby et al., 2008); VSFP2.4 (Akemann et al., 2010); VSFP-mUKG-mKOκ (Tsutsui et al., 2008); VSFP-CR (Lam et al., 2012); ArcLight (Jin et al., 2012)], and ASAP1 (St-Pierre et al., 2014) generally substituted different fluorescent proteins or VSDs and varied the linking arrangements of the two components.

In order to overcome the limited response kinetics of current VSFPs, we developed chimeric VSDs in which portions of the Ci-VSP VSD was replaced by homologous portions of the Kv3.1 voltage-gated potassium channel subunit (Mishina et al., 2012). Insertion of these chimeric VSDs into the VSFP2.3 scaffold led to a series of chimeric VSFP variants, many of which efficiently target to the membrane of PC12 and human embryonic kidney (HEK) cells and exhibit optimized kinetics which retained Kv3.1 characteristics.

Here, we describe a new set of VSFPs that combine the chimeric VSDs with the VSFP-Butterfly structure. We show that these chimeric VSFP-Butterflies can report membrane voltage oscillations of up to 200 Hz in cultured cells and report sensory evoked cortical population responses in living mice. These variants of GEVIs may be suitable for imaging of brain rhythms in awake, behaving mammals.

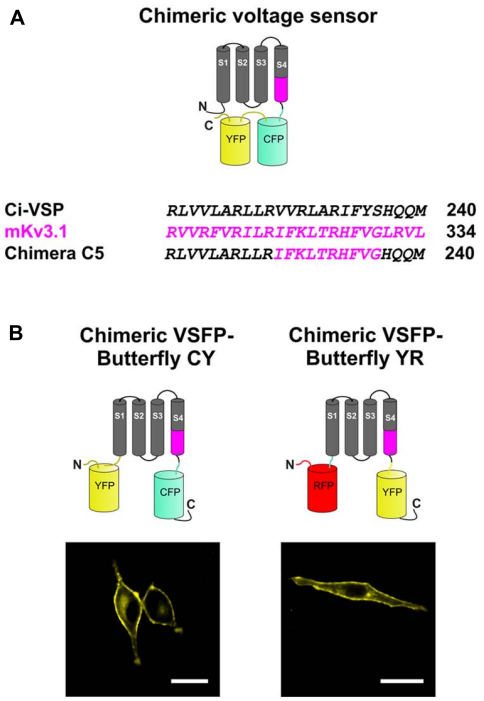

FIGURE 1 | Design of a chimeric voltage sensor by transferring a fragment of Kv3.1 to *Ciona intestinalis* voltage-sensitive phosphatase (Ci-VSP) in the S4 transmembrane segment. (A) Schematic depiction **(top)** of a chimeric voltage sensor, Chimera C5, in which a section of the voltage-sensing domain (VSD) of Ci-VSP is exchanged with amino acids from the S4 transmembrane segment of Kv3.1 **(bottom)**. The fluorescent proteins that are attached to the C-terminus of the chimeric construct enables visualization of membrane targeting and monitoring of voltage-dependent fluorescence changes due to movements of the VSD. **(B)** Modifications in the pair of the fluorescent proteins and localization of the constructs at the plasma membrane. The donor fluorescent protein was kept at the C-terminus, whereas the acceptor fluorescence was attached to the N-terminus. The donor/acceptor pairs were mCerulean/mCitrine for Chimeric voltage-sensitive fluorescent protein (VSFP)-Butterfly cyan–yellow (CY; **left)** and mCitrine/mKate2 for Chimeric VSFP-Butterfly yellow–red (YR; **right)**. Scale bar, 20 μm.

MATERIALS AND METHODS

MOLECULAR BIOLOGY

The chimeric Butterfly constructs were based on previously published versions of VSFPs, namely a combination of Chimera C5 (Mishina et al., 2012), in which a region of the VSD of Ci-VSP was substituted with that of the Kv3.1 potassium channel and VSFP-Butterfly 1.2 (Akemann et al., 2012; **Figure 1**). Both Chimeric VSFP-Butterfly cyan–yellow (CY; mCerulean/mCitrine) and Chimeric VSFP-Butterfly yellow–red (YR; mCitrine/mKate2) were generated using sequential polymerase chain reactions following the previously published protocols (Lundby et al., 2008; Mutoh et al., 2009; Akemann et al., 2012; Mishina et al., 2012). Briefly, Chimeric VSFP-Butterfly YR was generated by substituting the Ci-VSP VSD sequence of VSFP-Butterfly 1.2 (Akemann et al., 2012) with that of Kv3.1 VSD. This was performed by introducing restriction sites (XhoI and EcoRV) at the terminal ends of the VSD in both VSFP-Butterfly 1.2 and Chimera C5 (Mishina et al., 2012) as silent mutations and substituting the Chimera C5 VSD into the VSFP-Butterfly 1.2. In addition, a single mutation, K234R of mKate2, was introduced by site-directed mutagenesis for decreased intracellular aggregation and enhanced brightness (Perron and Knöpfel, unpublished observations). Chimeric VSFP-Butterfly CY was designed to incorporate the mCerulean/mCitrine fluorescence reporters, rather than the mCitrine/mKate pair (Mutoh et al., 2009). Similar to the VSFP-Butterfly 1.0 (Akemann et al., 2012), the mCitrine FRET acceptor was attached to the VSD at position 70 by overlap extension polymerase chain reactions after removal of the mCitrine of VSFP2.3. All constructs were subsequently subcloned into both pcDNA3.1(−; for functional imaging in cell culture) and pCAG vectors (for *in vivo* imaging; Lundby et al., 2008; Akemann et al., 2012) by utilizing NheI and AflII restriction endonucleases. DNA sequences for all of the constructs were confirmed by DNA sequencing analysis.

Chimeric VSFP-Butterfly CY and chimeric VSFP-Butterfly YR are deposited at Addgene (pCAG-Chimeric_Butterfly_CY_1.0, 59800; pCAG-Chimeric_Butterfly_YR_1.0, 59801).

CELL CULTURE, *IN VITRO* OPTICAL IMAGING, AND *IN UTERO* ELECTROPORATION

PC12 cells were cultured in Dulbecco's modified Eagle's medium supplemented with 10% horse serum, 5% fetal bovine serum, and 1% penicillin and streptomycin (GIBCO) at 37°C. HEK293T cells were cultured in Dulbecco's modified Eagle's medium supplemented with 10% fetal bovine serum and 1% penicillin and streptomycin (GIBCO) at 37°C. Cells were grown on poly-D-lysine coated coverslips and transfected 24 h after plating using Lipofectamine 2000 reagent (Invitrogen) and washed daily. Experiments were performed 2–3 days after transfection. PC12 cell images were obtained with a confocal laser scanning microscope (C1si/FN1, Nikon) for expression screening. *In utero* electroporation were performed as previously described (Akemann et al., 2010).

ELECTROPHYSIOLOGY AND FUNCTIONAL OPTICAL IMAGING

The voltage clamp recordings were performed on the instrumental set-up as previously described (Akemann et al., 2010, 2012). Briefly, voltage-dependent fluorescence recordings from both PC12 and HEK cells were performed by combining voltage clamp (under the whole-cell configuration of the patch-clamp technique) with dual-emission microfluorometry. Electrical and optical data were acquired using pCLAMP 10.1 software (Axon Instruments). PC12 or HEK cells were continuously perfused (1.5–2 ml/min) with a bathing solution containing (in mM) 150 NaCl, 4 KCl, 2 $CaCl_2$, 1 $MgCl_2$, 5 Glucose, 5 HEPES (pH 7.4 with NaOH). Patch electrodes had resistances of 3–5 MΩ when filled with intracellular solution containing (in mM) 130 CsCl, 1 $MgCl_2$, 20 HEPES, 5 EGTA, 3 MgATP (pH 7.2 with CsOH). All data were low-pass filtered with a cutoff frequency of 5 kHz and digitized at 5 kHz using a Digidata 1322 analog-to-digital converter (Axon Instruments). Fluorescence was illuminated by light from a computer-controlled monochromator (Polychrome IV, T.I.L.L. Photonics). For VSFP2.3, Chimera C5 and Chimeric VSFP-Butterfly CY, excitation light (440 nm) was reflected and first passed through a 458-nm dichroic mirror (FF458-Di01, Semrock). Emitted fluorescence was then split by a 506-nm dichroic mirror (FF506-Di03, Semrock) onto two photodiodes (T.I.L.L. Photonics) behind Cerulean- and Citrine- specific filters (BP 482 ± 35 nm: FF01-482/35-25 and LP 514 nm: LP02-514RU-25, Semrock). For Chimeric VSFP-Butterfly YR, excitation light (488 nm) was reflected and first passed through a 506-nm dichroic mirror (FF506-Di03, Semrock). Emitted fluorescence was then split by a 593-nm dichroic mirror (FF593-Di03, Semrock) onto two photodiodes (T.I.L.L. Photonics) behind Citrine- and mKate2- specific filters (BP 542 ± 13.5 nm: FF01-542/27-25 and LP 594 nm: BLP01-594R-25, Semrock).

The following protocol was used to test the voltage-dependence of the constructs (**Figure 2**). From a holding potential of −60 mV, cells were held for 500 ms at voltages between −140 mV and 120 mV in 20 mV steps to elicit fluorescence signals from mCerulean and mCitrine (VSFP2.3, Chimera C5, and Chimeric VSFP-Butterfly CY) or mCitrine and mKate2 (Chimeric VSFP-Butterfly YR). Finally, to test the frequency response of the constructs, sinusoidal voltage oscillations (20 mV amplitude) from −70 were generated in voltage clamp mode at frequencies of 10, 50, 100, and 200 Hz.

For all optical data, background data were obtained from a region on the coverslips devoid of fluorescent proteins. Photobleaching was corrected by division of a double exponential fit of the fluorescence trace at the holding potential. The ratiometric fluorescent signals were obtained by dividing the signals from the two fluorescent proteins. Calculations, including time constants, dynamic range, and $V_{1/2}$ were calculated as previously described (Akemann et al., 2012). Data are expressed as mean ± SEM, with *n* specifying the number of independent experiments. For each cell and voltage protocol 6–10 traces were averaged.

In vivo optical imaging was performed on mice (over 60 days old) *in utero* electroporated with expression plasmids. A glass window was implanted under surgical anesthesia (pentobarbital by intraperitoneal injection) as previously described (Akemann et al., 2012). Briefly, after exposing the cranial bone by removing the soft tissue, the left somatosensory cortex was carefully thinned using a dental drill and a cover glass was mounted over the cortex. A metal bolt was fixed on the frontal–medial cranium with dental cement. For imaging, mice were mounted onto a custom-made stereotaxic frame for stabilization and the body temperature was kept at 37°C (Fine Science Tools, Tokyo). The stimulus to the contralateral whisker C1 was delivered by a focal air puff system (100 ms, Picospritzer III, Parker Hannifin). Dual-emission optical imaging was performed using two synchronized CCD cameras (Sensicam, PCO) at 50 frames/s. Excitation light was provided by a high-power halogen lamp (Moritex). The following filters and splitters were used for optical recording: mCitrine excitation (FF01 483/32-25), mCitrine emission (F01 542/27-25), mKate2 emission (BLP01 594R-25), LP506 nm (FF 506-Di03) as excitation beam splitter, and LP593 nm (FF 593-Di03) as detection splitter, all installed onto the THT macroscopy system (Brainvision, Tokyo). Images were acquired using a custom-made macros using ImagePro6.2.

Animal experiments were performed under the Institutional Animal Care and Use Committee of the RIKEN Wako Research Center.

RESULTS

CHIMERIC VSFP-BUTTERFLIES

We previously systematically replaced portions of the Ci-VSP VSD with homologous sections of the Kv3.1 potassium channel subunit, yielding chimeric VSDs that we termed Chimera Cx (x running from 1 to 40) and demonstrated that this replacement leads to an acceleration of voltage sensing movements in a subgroup of constructs (Mishina et al., 2012). For the present study, we used the construct Chimera C5, in which 10 consecutive amino acid segments from the C-terminal portion of the S4 of Kv3.1 replaced the homologous region in VSFP2.3 (**Figure 1A**).

The choice of the fluorescent protein pair for FRET measurements and the positioning relative to the VSD can

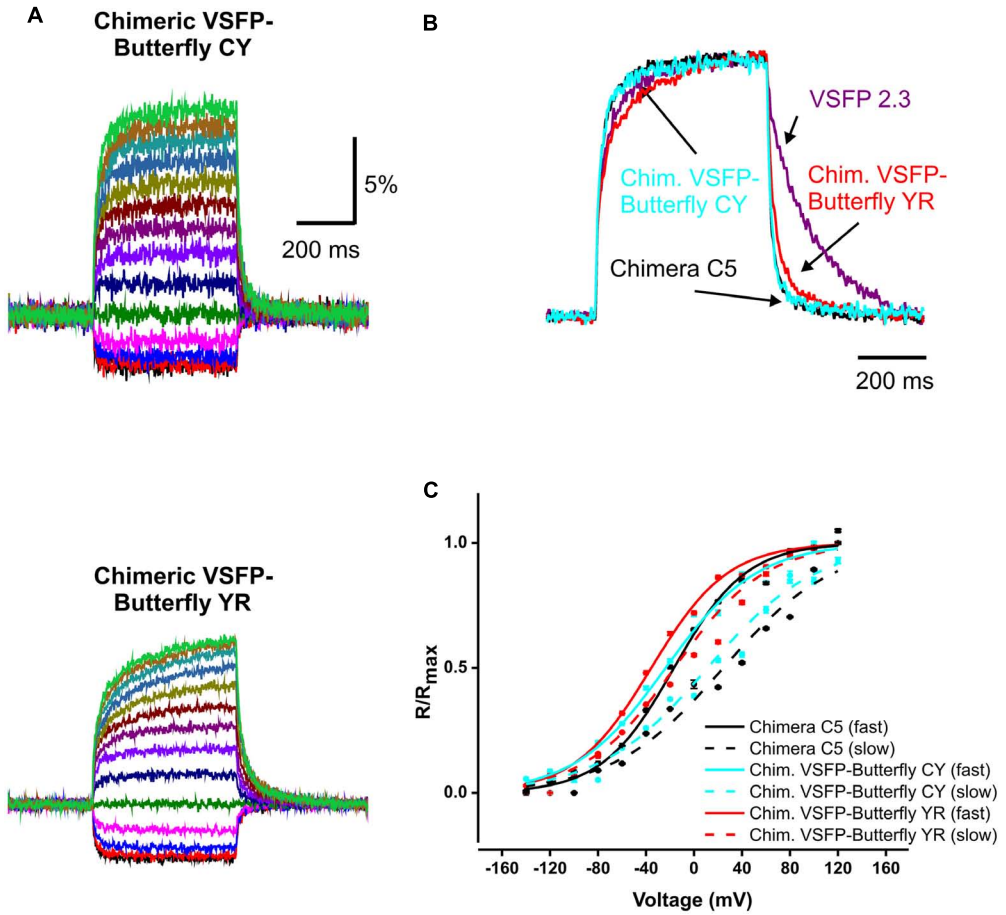

FIGURE 2 | Kinetics of voltage dependency of Chimeric VSFP-Butterfly CY and Chimeric VSFP-Butterfly YR in PC12 cells. (A) Comparison of ratiometric fluorescence signals of Chimeric VSFP-Butterfly CY **(upper)** and Chimeric VSFP-Butterfly YR **(lower)** in response to a family of voltage steps from a holding potential of −60 mV, and 20 mV step increments from −140 to 120 mV. ($n = 6$). **(B)** Normalized responses to depolarization from −60 to 20 mV and responses to return for VSFP2.3 (magenta), Chimera C5 (black), Chimeric VSFP-Butterfly CY (blue), and Chimeric VSFP-Butterfly YR (red). **(C)** Amplitude of normalized optical signal (ΔR/R) versus membrane voltage for the fast (solid line) and slow (dotted line) components of Chimera C5 (black), Chimeric VSFP-Butterfly CY (blue), and Chimeric VSFP-Butterfly YR (red). Responses (ΔR/R) to families of voltage steps (as in **A**) were fitted with the function $y = y0 + A1*\exp(-t/\tau1\_on) + A2*\exp(-t/\tau2\_on)$ where t is time, τ1_on the faster on time constant and τ2_on the slower on time constant. A1 and A2 are the amplitudes of fast and slow response components and are plotted against the step voltage. $N = 6–7$; error bars ± SEM.

Table 1 | Summary of the FRET response properties of chimeric voltage-sensitive fluorescent protein (VSFP)-Butterflies and previously published VSFPs.

	τ_1 on	τ_2 on	% τ_1	τ off	$V_{1/2}$ fast (mV)	$V_{1/2}$ slow (mV)	ΔR/R (%)#
Chimeric VSFP-Butterfly cyan–yellow (CY)	2.1 ± 0.2	36.7 ± 1.1	60.0	14.6 ± 0.5	−24.0 ± 0.5	≥20	14.7 ± 0.2
Chimeric VSFP-Butterfly yellow–red (YR)	2.3 ± 0.2	81.2 ± 2.7	55.4	25.1 ± 0.9	−33.7 ± 0.3	−9.1 ± 0.4	12.7 ± 0.1
Chimera C5*	2.1 ± 0.2	36.8 ± 0.9	60.1	13.4 ± 0.5	−17.9 ± 0.4	≥20	14.8 ± 0.1
VSFP2.3*	3.0 ± 0.2	69.2 ± 1.8	26.6	91.6 ± 1.7	−28.3 ± 0.5	−48.6 ± 0.5	15.2 ± 0.1
Butterfly 1.2**	1.0 ± 0.7	12.2 ± 0.7	40.0	89.9 ± 5.2	−79 ± 2	−58.2 ± 5.3	15.0 ± 0.7

**From Mishina et al. (2012); **From Akemann et al. (2012); # % ΔR/R values were obtained from the maximal and minimal acceptor/donor florescence ratio responses between −140 and 120 mV from a holding potential of −70 mV.*
Time constants τ on was calculated from a response from −70 mV holding potential to a 60 mV step, and τ off was calculated from a return to −70 mV. n = 6–9; Errors ± SEM.

significantly affect the biophysical properties of FRET-based genetically encoded indicator proteins (Alford et al., 2013). By moving the FRET acceptor from the C-terminus of the donor to the N-terminal end of the VSD, we generated and characterized two new Butterfly variants of the Chimera C5 construct. The two Butterfly variants were designed with mCerulean/mCitrine ("CY") and mCitrine/mKate2 ("YR") fluorescent protein FRET pairs (**Figure 1B**) and they were named Chimeric VSFP-Butterfly CY and Chimeric VSFP-Butterfly YR, respectively.

We first tested whether the VSFP-Butterfly conformation preserved the kinetic properties found for Chimera C5 described in Mishina et al. (2012; **Figure 2**; **Table 1**). We found no significant (t-test, $p = 0.1$–0.5; **Table 1**) difference between chimera C5 and Chimeric VSFP-Butterfly CY in terms of the response time constants and the overall ratiometric signal amplitudes. The Chimeric VSFP-Butterfly YR version exhibited a slightly larger second on time constant and a slower off time constant when compared to Chimera C5 (t-test, $p < 0.001$ for both, **Table 1**).

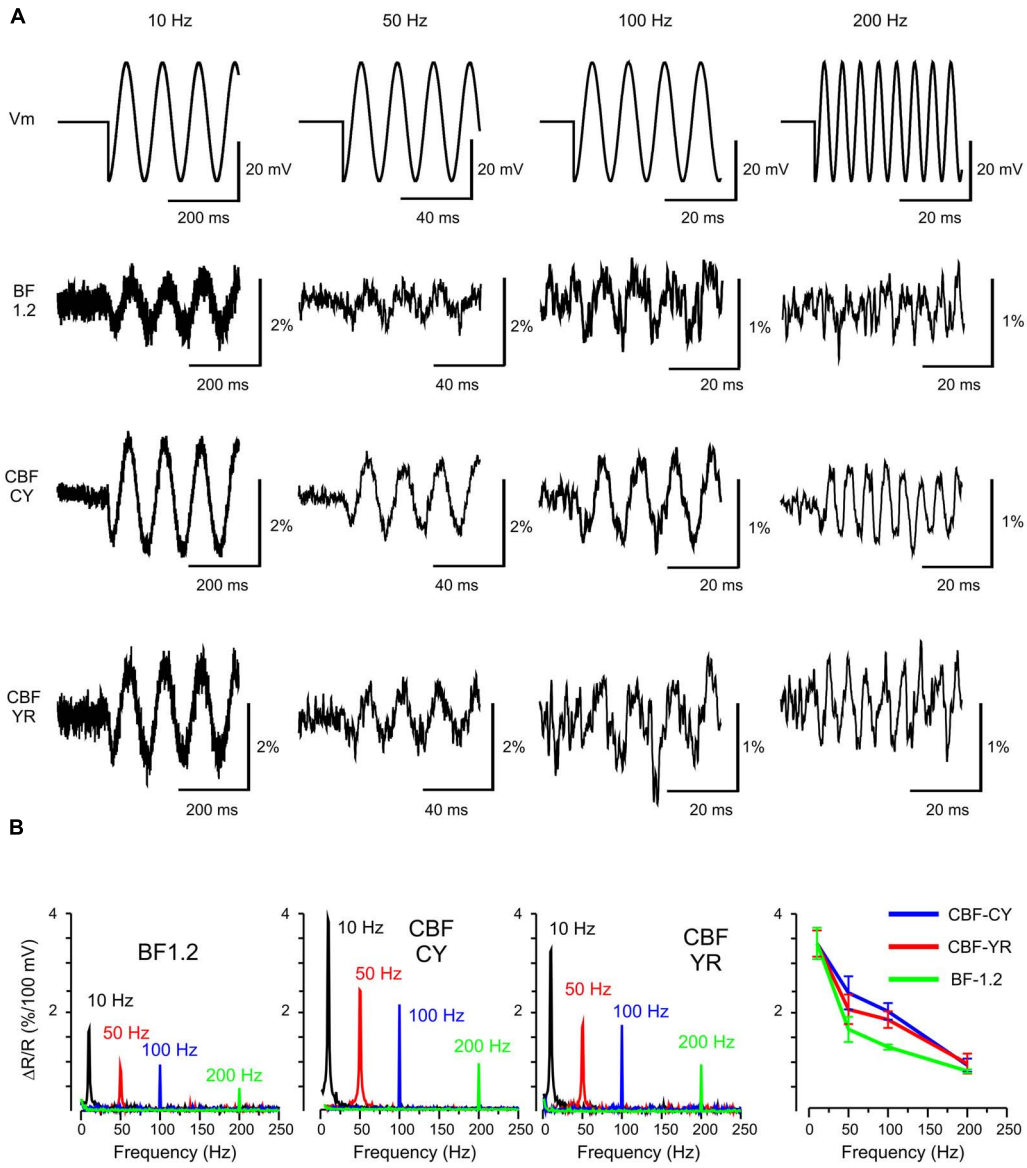

FIGURE 3 | Frequency response of VSFP Butterfly constructs to membrane voltage oscillations at 10, 50, 100, and 200 Hz in human embryonic kidney (HEK) cells. (A) The upper row shows the command waveform of 20 mV oscillations around −70 mV. The second to fourth row depict the VSFP-Butterfly 1.2 (BF 1.2) Chimeric VSFP-Butterfly CY (CBF CY) and the Chimeric VSFP-Butterfly YR (CBF YR) ratiometric response signals (example recordings from one cell for each construct; average over 3–30 sweeps). **(B)** First three panels: Amplitude spectrograms for each oscillation frequency for each construct. Right panel: mean and SEM of the optical response at different frequencies.

One of the advantageous features of our previous VSFP Butterfly 1.2 was a left shifted $V_{1/2}$ value (as compared to its precursor VSFP2.42), increasing the sensitivity around the resting membrane potential (Akemann et al., 2012). A significant left shift of the $V_{1/2}$ values was found for Chimeric VSFP-Butterfly YR when compared to Chimera C5 (t-test, $p < 0.001$; **Table 1**). A clear improvement of the Chimeric VSFP-Butterfly YR as compared to VSFP Butterfly 1.2 was a significant shortening of the off time constant (25.1 ± 0.9 versus 89.9 ± 5.2 ms; Akemann et al., 2012, $p < 0.005$). The faster off response was even more pronounced for Chimeric VSFP-Butterfly CY (14.6 ± 0.5, significant smaller than the value of Chimeric VSFP-Butterfly YR, t-test, $p < 0.001$; **Table 1**).

These characteristic parameters are summarized in **Table 1** along with previous published measurements for VSFP2.3 (Lundby et al., 2008, 2010; Akemann et al., 2010) and VSFP Butterfly 1.2 (Akemann et al., 2012).

RESPONSES OF THE CHIMERIC VSFP-BUTTERFLY CONSTRUCTS TO OSCILLATORY MEMBRANE VOLTAGES

To evaluate the use of chimeric VSFP-Butterflies for the potential to image brain rhythms in behaving mammalians, optical responses to oscillatory membrane potential were studied. To this end, PC12 and HEK cells were voltage clamped with an oscillatory voltage command. These experiments show that chimeric VSFP-Butterflies follow sinusoidal membrane voltage oscillations of up to 200 Hz, confirming the above initial assessment of these constructs demonstrating optimized kinetics relative to VSFP-Butterfly 1.2 (Akemann et al., 2012; **Figure 3A**). Compared to VSFP-Butterfly 1.2 (Akemann et al., 2012), chimeric VSFP-Butterflies show a larger gain (sensitivity) at frequencies between 10 and 200 Hz ($p < 0.05$, t-test; **Figure 3**). The less pronounced loss of gain observed with chimeric VSFP-Butterflies between steady state sensitivity and report of oscillatory membrane voltage

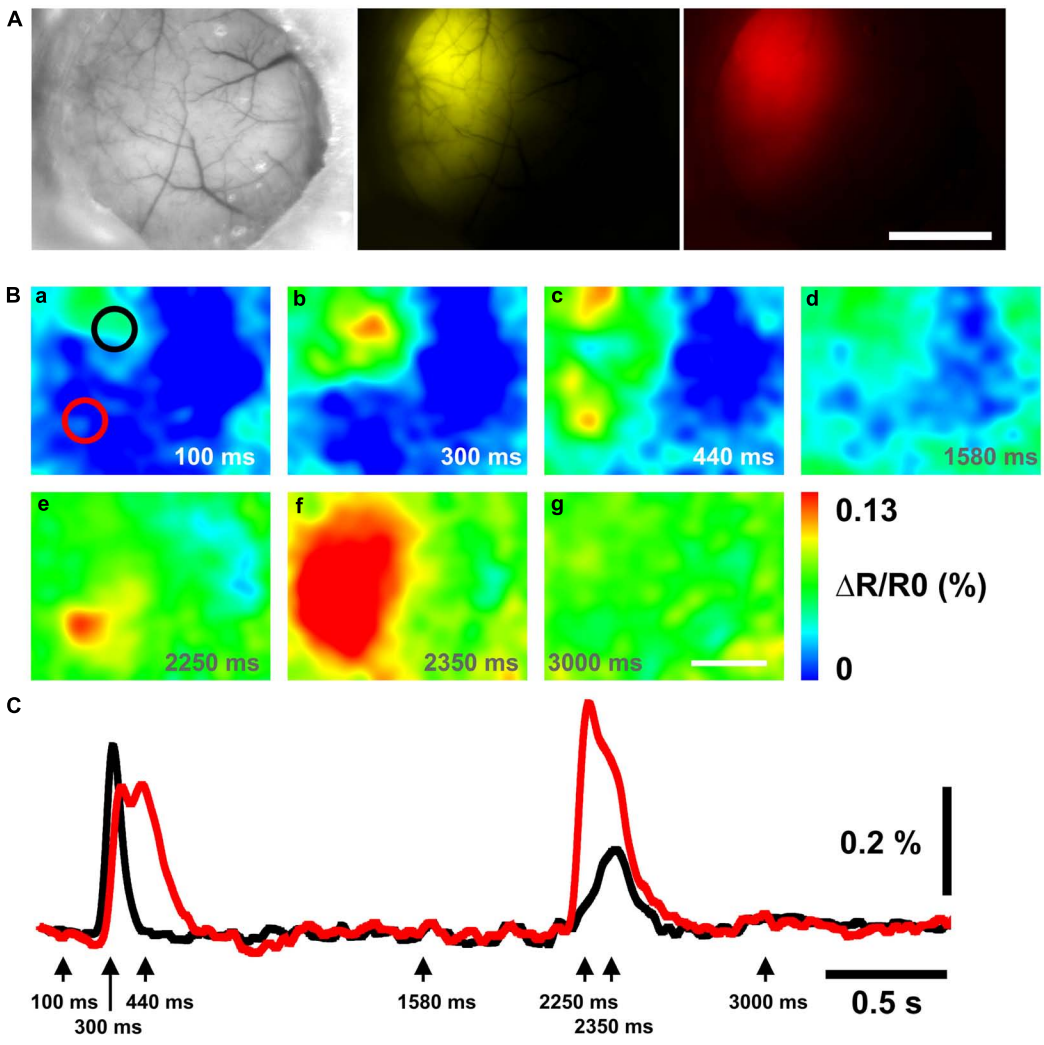

FIGURE 4 | Chimeric VSFP-Butterfly YR voltage imaging of cortical responses to whisker deflection and light flash. (A) Brightfield **(left)** image and the expression pattern of mCitrine **(middle)** and mKate2 **(right)** of the left hemisphere. **(B)** Ratiometric images obtained before and after a single deflection of the C1 whisker and a brief flash of light. Scale bar, 2 mm. **(C)** Black and red traces of the ratiometric signal are taken from the black (somatosensory cortex) and red (visual cortex) circles in **(B-a)**, respectively. The arrows indicate the time points of the ratiometric images in **(B)**.

fluctuations (at 10 Hz or higher frequencies) can be explained by the larger contribution of the faster component of the on response (τ1 on) and the much faster off time constant (τ1 off; **Table 1**).

IN VIVO DEMONSTRATION OF THE FUNCTIONAL POTENTIALS OF THE CHIMERIC CONSTRUCTS

Chimeric VSFP-Butterfly YR was taken as a representative chimeric construct to explore performance *in vivo.* A relatively large transcranial window covering the left hemisphere of mice electroporated with the Chimeric VSFP-Butterfly YR construct exhibited strong fluorescence signals (**Figure 4A**). Under anesthesia, the signal of the Chimeric VSFP-Butterfly YR on the somatosensory cortex could be induced from baseline (**Figure 4B-a**) by a single C1 whisker deflection (**Figure 4B-b**) and the signal propagated to other discrete cortical areas (motor cortex and secondary somatosensory cortex, **Figure 4B-c**), and eventually faded (**Figure 4B-d**). Stimulation using brief flashes of light also activated the visual cortex area (**Figure 4B-e**) which propagated through the hemisphere toward the rostral area (**Figure 4B-f**) also then gradually faded (**Figure 4B-g**). **Figure 4C** shows how those voltage signals propagated in two distinct cortices, the somatosensory cortex and the visual cortex.

DISCUSSION

We generated and characterized a new set of VSFPs that combine a chimeric VSD with the VSFP-Butterfly structure. We show that these chimeric VSFP-Butterflies can report membrane voltage oscillations of up to 200 Hz in cultured cells. We also demonstrate that these GEVIs report sensory evoked cortical population responses in living mice. The *in vivo* assay is particularly important as some previously reported VSFP derivatives (e.g., "Mermaid") were functional in transfected cultured cells but failed to provide robust voltage signals in equivalent *in vivo* assays (Akemann et al., 2012). Similarly, it remains to be seen whether the recently reported monochromatic green fluorescent VSFPs with high *in vitro* sensitivity such as ASAP1 (St-Pierre et al., 2014) are suitable for rodent *in vivo* imaging experiments where modulation of green indicator fluorescence is significantly affected by hemodynamic effects (Diez-Garcia et al., 2007) and where movement artifacts are a major challenge.

The present study addresses the need for GEVIs with fast kinetics. Previous work has indicated that the kinetics of FRET-based VSFP is limited by properties of the voltage-sensitive protein that undergoes a slower state transition into a relaxed state after an initial, relatively fast on response (Lundby et al., 2010). To overcome this kinetic limit, VSDs from various species have also been explored. In particular, the chick homolog of Ci-VSP appears to provide a scaffold that lead to VSFPs with faster kinetics (Han et al., 2013; St-Pierre et al., 2014). The advantage of chimeras between Ci-VSP and Kv potassium channel subunits, as introduced and employed here, is that Kv channels are among the best studied membrane proteins with a wealth of structural understanding (Villalba-Galea et al., 2008; Vargas et al., 2012). This will likely instigate a more rational approach in the fine-tuning of the voltage sensing portion of GEVIs.

Improvements of GEVIs will continue as they are essential tools in studies where processing of synaptic inputs and action potentials at frequencies greater than 10 Hz are of interest. We expect that voltage imaging will be instrumental when linking neuronal information flows across large cortical areas and complex behavior GEVIs are likely on their way to replace the current low molecular weight voltage-sensitive dyes used in such long-term mesoscopic (circuit-centric) imaging approaches (Knöpfel, 2012). In this brain mapping research domain, GEVIs will become central to bridging the gap between single-neuron and whole-brain recordings as they are able to target specific cell populations and are able to provide consistent recordings over extended periods at the same locations.

The new VSFPs reported here outperform previously published GEVIs with demonstrated *in vivo* performance that are based on coupling a VSD with a FRET pair of fluorescent proteins by a factor of two in response time while keeping former advantages and strengths such as utilizing ratiometric outputs and brightness necessary for robust, high-resolution signals. Future fine-tuning of the chimeric Butterflies introduced here may include further enhancements in VSD kinetics and dynamic range, and may involve varied fluorescent proteins for increased brightness and photostability.

ACKNOWLEDGMENTS

We would like to thank the members of the Knöpfel lab for scientific advice and insightful discussions. We also would like to thank GlaxoSmithKline for their financial support.

REFERENCES

Akemann, W., Mutoh, H., Perron, A., Park, Y. K., Iwamoto, Y., and Knöpfel, T. (2012). Imaging neural circuit dynamics with a voltage-sensitive fluorescent protein. *J. Neurophysiol.* 108, 2323–2337. doi: 10.1152/jn.00452.2012

Akemann, W., Mutoh, H., Perron, A., Rossier, J., and Knöpfel, T. (2010). Imaging brain electric signals with genetically targeted voltage-sensitive fluorescent proteins. *Nat. Methods* 7, 643–649. doi: 10.1038/nmeth.1479

Alford, S. C., Wu, J., Zhao, Y., Campbell, R. E., and Knöpfel, T. (2013). Optogenetic reporters. *Biol. Cell* 105, 14–29. doi: 10.1111/boc.201200054

Diez-Garcia, J., Akemann, W., and Knöpfel, T. (2007) In vivo calcium imaging from genetically specified target cells in mouse cerebellum. *Neuroimage* 34, 859–869. doi: 10.1016/j.neuroimage.2006.10.021

Dimitrov, D., He, Y., Mutoh, H., Baker, B. J., Cohen, L., Akemann, W., et al. (2007). Engineering and characterization of an enhanced fluorescent protein voltage sensor. *PLoS ONE* 2:e440. doi: 10.1371/journal.pone.0000440

Gong, Y., Wagner, M. J., Zhong, L. J., and Schnitzer, M. J. (2014). Imaging neural spiking in brain tissue using FRET-opsin protein voltage sensors. *Nat. Commun.* 5, 3674. doi: 10.1038/ncomms4674

Grinvald, A., and Hildesheim, R. (2004). VSDI: a new era in functional imaging of cortical dynamics. *Nat. Rev. Neurosci.* 5, 874–885. doi: 10.1038/nrn1536

Grinvald, A., Salzberg, B. M., and Cohen, L. B. (1977). Simultaneous recording from several neurones in an invertebrate central nervous system. *Nature* 268, 140–142. doi: 10.1038/268140a0

Han, Z., Jin, L., Platisa, J., Cohen, L. B., Baker, B. J., and Pieribone, V. A. (2013). Fluorescent protein voltage probes derived from ArcLight that respond to membrane voltage changes with fast kinetics. *PLoS ONE* 8:e81295. doi: 10.1371/journal.pone.0081295

Jin, L., Han, Z., Platisa, J., Wooltorton, J. R., Cohen, L. B., and Pieribone, V. A. (2012). Single action potentials and subthreshold electrical events imaged in neurons with a fluorescent protein voltage probe. *Neuron* 75, 779–785. doi: 10.1016/j.neuron.2012.06.040

Kenet, T., Bibitchkov, D., Tsodyks, M., Grinvald, A., and Arieli, A. (2003). Spontaneously emerging cortical representations of visual attributes. *Nature* 425, 954–956. doi: 10.1038/nature02078

Knöpfel, T. (2012). Genetically encoded optical indicators for the analysis of neuronal circuits. *Nat. Rev. Neurosci.* 13, 687–700. doi: 10.1038/nrn3293

Kralj, J. M., Douglass, A. D., Hochbaum, D. R., Maclaurin, D., and Cohen, A. E. (2012). Optical recording of action potentials in mammalian neurons using a microbial rhodopsin. *Nat. Methods* 9, 90–95. doi: 10.1038/nmeth.1782

Lam, A. J., St-Pierre, F., Gong, Y., Marshall, J. D., Cranfill, P. J., Baird, M. A., et al. (2012). Improving FRET dynamic range with bright green and red fluorescent proteins. *Nat. Methods* 9, 1005–1012. doi: 10.1038/nmeth.2171

Lundby, A., Akemann, W., and Knöpfel, T. (2010). Biophysical characterization of the fluorescent protein voltage probe VSFP2.3 based on the voltage-sensing domain of Ci-VSP. *Eur. Biophys. J.* 39, 1625–1635. doi: 10.1007/s00249-010-0620-0

Lundby, A., Mutoh, H., Dimitrov, D., Akemann, W., and Knöpfel, T. (2008). Engineering of a genetically encodable fluorescent voltage sensor exploiting fast Ci-VSP voltage-sensing movements. *PLoS ONE* 3:e2514. doi: 10.1371/journal.pone.0002514

Maclaurin, D., Venkatachalam, V., Lee, H., and Cohen, A. E. (2013). Mechanism of voltage-sensitive fluorescence in a microbial rhodopsin. *Proc. Natl. Acad. Sci. U.S.A.* 110, 5939–5944. doi: 10.1073/pnas.1215595110

Mishina, Y., Mutoh, H., and Knöpfel, T. (2012). Transfer of Kv3.1 voltage sensor features to the isolated Ci-VSP voltage-sensing domain. *Biophys. J.* 103, 669–676. doi: 10.1016/j.bpj.2012.07.031

Mutoh, H., Akemann, W., and Knöpfel, T. (2012). Genetically engineered fluorescent voltage reporters. *ACS Chem. Neurosci.* 3, 585–592. doi: 10.1021/cn300041b

Mutoh, H., and Knöpfel, T. (2013). Probing neuronal activities with genetically encoded optical indicators: from a historical to a forward-looking perspective. *Pflugers Arch.* 465, 361–371. doi: 10.1007/s00424-012-1202-z

Mutoh, H., Perron, A., Dimitrov, D., Iwamoto, Y., Akemann, W., Chudakov, D. M., et al. (2009). Spectrally-resolved response properties of the three most advanced FRET based fluorescent protein voltage probes. *PLoS ONE* 4:e4555. doi: 10.1371/journal.pone.0004555

Perron, A., Mutoh, H., Akemann, W., Gautam, S. G., Dimitrov, D., Iwamoto, Y., et al. (2009a). Second and third generation voltage-sensitive fluorescent proteins for monitoring membrane potential. *Front. Mol. Neurosci.* 2:5. doi: 10.3389/neuro.02.005.2009

Perron, A., Mutoh, H., Launey, T., and Knöpfel, T. (2009b). Red-shifted voltage-sensitive fluorescent proteins. *Chem. Biol.* 16, 1268–1277. doi: 10.1016/j.chembiol.2009.11.014

Petersen, C. C., Grinvald, A., and Sakmann, B. (2003a). Spatiotemporal dynamics of sensory responses in layer 2/3 of rat barrel cortex measured in vivo by voltage-sensitive dye imaging combined with whole-cell voltage recordings and neuron reconstructions. *J. Neurosci.* 23, 1298–1309.

Petersen, C. C., Hahn, T. T., Mehta, M., Grinvald, A., and Sakmann, B. (2003b). Interaction of sensory responses with spontaneous depolarization in layer 2/3 barrel cortex. *Proc. Natl. Acad. Sci. U.S.A.* 100, 13638–13643. doi: 10.1073/pnas.2235811100

Ross, W. N., Salzberg, B. M., Cohen, L. B., and Davila, H. V. (1974). A large change in dye absorption during the action potential. *Biophys. J.* 14, 983–986. doi: 10.1016/S0006-3495(74)85963-1

Sakai, R., Repunte-Canonigo, V., Raj, C. D., and Knöpfel, T. (2001). Design and characterization of a DNA-encoded, voltage-sensitive fluorescent protein. *Eur. J. Neurosci.* 13, 2314–2318. doi: 10.1046/j.0953-816x.2001.01617.x

Shoham, D., Glaser, D. E., Arieli, A., Kenet, T., Wijnbergen, C., Toledo, Y., et al. (1999). Imaging cortical dynamics at high spatial and temporal resolution with novel blue voltage-sensitive dyes. *Neuron* 24, 791–802. doi: 10.1016/S0896-6273(00)81027-2

St-Pierre, F., Marshall, J. D., Yang, Y., Gong, Y., Schnitzer, M. J., and Lin, M. Z. (2014). High-fidelity optical reporting of neuronal electrical activity with an ultrafast fluorescent voltage sensor. *Nat. Neurosci.* 17, 884–889. doi: 10.1038/nn.3709

Tsutsui, H., Jinno, Y., Tomita, A., Niino, Y., Yamada, Y., Mikoshiba, K., et al. (2013). Improved detection of electrical activity with a voltage probe based on a voltage-sensing phosphatase. *J. Physiol.* 591, 4427–4437. doi: 10.1113/jphysiol.2013.257048

Tsutsui, H., Karasawa, S., Okamura, Y., and Miyawaki, A. (2008). Improving membrane voltage measurements using FRET with new fluorescent proteins. *Nat. Methods* 5, 683–685. doi: 10.1038/nmeth.1235

Vargas, E., Yarov-Yarovoy, V., Khalili-Araghi, F., Catterall, W. A., Klein, M. L., Tarek, M., et al. (2012). An emerging consensus on voltage-dependent gating from computational modeling and molecular dynamics simulations. *J. Gen. Physiol.* 140, 587–594. doi: 10.1085/jgp.201210873

Villalba-Galea, C. A., Sandtner, W., Starace, D. M., and Bezanilla, F. (2008). S4-based voltage sensors have three major conformations. *Proc. Natl. Acad. Sci. U.S.A.* 105, 17600–17607. doi: 10.1073/pnas.0807387105

Zou, P., Zhao, Y., Douglass, A. D., Hochbaum, D. R., Brinks, D., Werley, C. A., et al. (2014). Bright and fast multicoloured voltage reporters via electrochromic FRET. *Nat. Commun.* 5, 4625. doi: 10.1038/ncomms5625

Conflict of Interest Statement: The Associate Editor Katsuhiko Mikoshiba declares that, despite being affiliated to the same institution as authors, the review process was handled objectively and no conflict of interest exists. The authors declare that the research was conducted in the absence of any commercial or financial relationships that could be construed as a potential conflict of interest.

Received: 19 June 2014; accepted: 14 September 2014; published online: 29 September 2014.

Citation: Mishina Y, Mutoh H, Song C and Knöpfel T (2014) Exploration of genetically encoded voltage indicators based on a chimeric voltage sensing domain. Front. Mol. Neurosci. 7:78. doi: 10.3389/fnmol.2014.00078

This article was submitted to the journal Frontiers in Molecular Neuroscience.

frontiers in
MOLECULAR NEUROSCIENCE

ORIGINAL RESEARCH ARTICLE
published: 27 November 2014
doi: 10.3389/fnmol.2014.00093

Engineering a genetically-encoded SHG chromophore by electrostatic targeting to the membrane

Yuka Jinno[1], Keiko Shoda[2], Emiliano Rial-Verde[3], Rafael Yuste[3], Atsushi Miyawaki[2] and Hidekazu Tsutsui[2,4,5]*

[1] *Laboratory of Integrative Physiology, Graduate School of Medicine, Osaka University, Suita, Japan*
[2] *Laboratory for Cell Function Dynamics, Brain Science Institute, RIKEN, Wako, Japan*
[3] *Department of Biological Sciences, Neurotechnology Center, Columbia University, New York, NY, USA*
[4] *Formation of and Information Processing by Neural Networks, and Control, PRESTO, Japan Science and Technology Agency (JST), Kawaguchi, Japan*
[5] *Department of Material Science, Japan Advanced Institute of Science and Technology, Nomi, Japan*

Edited by:
Nicola Maggio, The Chaim Sheba Medical Center, Israel

Reviewed by:
Eduard Korkotian, The Weizmann Institute of Science, Israel
Hideaki Mizuno, KU Leuven, Belgium

***Correspondence:**
Hidekazu Tsutsui, Department of Material Science, Japan Advanced Institute of Science and Technology, Asahidai 1-1, Nomi, Ishikawa 923-1211, Japan
e-mail: tsutsui@jaist.ac.jp

Although second harmonic generation (SHG) microscopy provides unique imaging advantages for voltage imaging and other biological applications, genetically-encoded SHG chromophores remain relatively unexplored. SHG only arises from non-centrosymmetric media, so an anisotropic arrangement of chromophores is essential to provide strong SHG signals. Here, inspired by the mechanism by which K-Ras4B associates with plasma membranes, we sought to achieve asymmetric arrangements of chromophores at the membrane-cytoplasm interface using the fluorescent protein mVenus. After adding a farnesylation motif to the C-terminus of mVenus, nine amino acids composing its β-barrel surface were replaced by lysine, forming an electrostatic patch. This protein (mVe9Knus-CVIM) was efficiently targeted to the plasma membrane in a geometrically defined manner and exhibited SHG in HEK293 cells. In agreement with its design, mVe9Knus-CVIM hyperpolarizability was oriented at a small angle (~7.3°) from the membrane normal. Genetically-encoded SHG chromophores could serve as a molecular platform for imaging membrane potential.

Keywords: fluorescence protein, mutagenesis, electrostatic surface potential, second harmonic generation

INTRODUCTION

Second harmonic generation (SHG), or frequency-doubling, is a second-order non-linear optical phenomena, in which light with twice the frequency of the incident light is generated upon the interaction of matter and intense light (Shen, 1989). Second-harmonic imaging microscopy (SHIM; Campagnola et al., 2001; Millard et al., 2003a) uses SHG as a contrast mechanism and shares some advantages with two-photon excited fluorescence microscopy, such as 3D optical sectioning, a critical benefits for biological applications. But an important feature of SHIM which is not shared by two-photon microscopy (itself a third-order non-linear optical technique) is that SHG signals arise only from non-centrosymmetric media, such as oriented polymers or interfaces. Also, because SHG is a coherent scattering process, SHIM does not necessarily require exogenous dyes. In fact, endogenous microtubule, myosin and collagen fibers produce significant SHG signals (Campagnola et al., 2002). SHIM from membranes and other interfaces, however, generally requires labeling with exogenous π-conjugated chromophores possessing substantial non-linear hyperpolarizabilities.

Taking advantage of its sensitivity to local centrosymmetry, SHIM has been used to distinguish juxtaposed regions of membrane vesicles from un-adhered region (Moreaux et al., 2000) and to detect the exocytotic wave at fertilization in a sea urchin egg (Millard et al., 2005). Such measurements are not easily achievable with two photon excitation microscopy. In addition, SHG offers remarkable advantages for neuroscience because the second harmonics from membrane-bound dyes can be sensitive to trans-membrane voltage (Campagnola et al., 1999; Millard et al., 2003b, 2004; Nemet et al., 2004). This has enabled measuring membrane potential in small membrane structures such as dendritic spines (Nuriya et al., 2006) and axons (Nuriya and Yasui, 2010). For FM4-64, a diffusible SHG indicator, this voltage sensitivity is due to an electro-optic effect (Jiang et al., 2007).

In spite of such potential advantages of SHIM, the development of genetically-encoded SHG chromophore remains in its infancy. Since GFP-like chromophores exhibit non-linear hyperpolarizability, they have been explored as candidates for SHG (Lewis et al., 1999; Khatchatouriants et al., 2000; Roorda et al., 2004; Asselberghs et al., 2008). In past work, signals at the second-harmonic band have been reported in *C. elegans* expressing GFP tagged with a transmembrane protein (Lewis et al., 1999; Khatchatouriants et al., 2000). But the nature of chromophore arrangement at the membrane interface, the most critical factor in the design of SHG chromophores, remained unclear. Also, this construct was not expressed in mammalian cells. Attempting to generate a defined geometry of GFP chromophores at the membrane interface, Roorda et al. (2004) generated a dually tagged EGFP by incorporating prenylation and palmitoylation signal sequences simultaneously into the EGFP sequence. While the resultant protein showed oriented membrane targeting (Lazar et al., 2011), the detection of SHG signal remained elusive.

In this paper, we report our successful effort in engineering a genetically-encoded SHG chromophore. Our approach is inspired by the mechanism by which Kirsten Ras4B (K-Ras4B) interacts with plasma membranes (Welman et al., 2000). K-Ras4B, a member of the four Ras homologs which are expressed ubiquitously (H-Ras, N-Ras, K-Ras4A, and K-Ras4B), undergo switching between GDP-bound inactive and GTP-bound active states, and modulate cellular signaling of cell growth and differentiation. Ras proteins generally consist of a conserved N-terminal region and a C-terminal hyper-variable domain. The conserved N-terminal region is involved in the binding of GTP/GDP as well as the associations with effector proteins such as PI3 kinase, Raf kinase, Ral GDS, and AF6 (Welman et al., 2000). The C-terminal hyper variable domain is involved in the association with plasma-membrane. Unlike the other three members, the hypervariable domain of K-Ras4B contains a polybasic region in conjunction to the farnesylation target, which is conferred though an alternate mRNA splicing and provides the synergistic electrostatic and hydrophobic mechanism to associate with plasma-membranes (Hancock et al., 1990, 1991; Welman et al., 2000). Because electrostatic interactions of a protein with membrane surface electric-field occurs only at a short distance from the membrane, we explored whether the mechanism found in K-Ras4B may be utilized to engineer chromophores which are tightly oriented at the membrane-cytoplasm interface, a critical step toward building optical indicators of membrane potential.

MATERIALS AND METHODS

MOLECULAR BIOLOGY, CELL CULTURE, AND PROTEIN MODELING

We used a custom modified pCS2+ vector for heterologous expression experiments in mammalian cells. Site-directed mutagenesis was performed as described previously (Sawano and Miyawaki, 2000). HEK293T cells were cultured in Dulbecco's Modified Eagle Medium supplemented with 10% fetal bovine serum in a standard incubator (5% CO_2, 37°C). Transfection was performed using Lipofectamine 2000 reagent (Thermo Fisher Scientific, MA) according to the manufacturer's protocol. The crystal structure for Venus (PDB#:1MYV; Rekas et al., 2002) was used as a template for molecular modeling. The mutant models were generated by using Swiss PDB Viewer software (Guex and Peitsch, 1997; http://www.expasy.org/spdbv/). The electrostatic surface potential maps for the mutant models were generated by the web-based software, eF-surf (http://ef-site.protein.osaka-u.ac.jp/eF-surf/top.do).

WIDE-FIELD FLUORESCENCE MICROSCOPY

Cells were imaged at 24∼36 h post-transfection on an inverted microscope (IX71, Olympus, Tokyo, Japan) equipped with a 75 W xenon lamp and a CMOS camera (Orca-Flash2.8, Hamamatsu Photonics, Hamamatsu, Japan). Excitation, dichroic, and emission filters used were ex500/24, dm520, and em542/27 (Semrock, N.Y.), respectively. A rotatable polarizer in the excitation light path (Sigma-Koki, Tokyo, Japan) was used to study polarization angle dependency. A 40× objective lens with a moderately low numerical aperture (UPlanFLN 40x, NA 0.75, Olympus, Tokyo, Japan) was used to minimize aperture effect. Intrinsic angle-dependency of the imaging system (g-factor) was calibrated using isotropic solution of fluorescein deposited between two coverslips.

SECOND HARMONIC AND TWO-PHOTON EXCITED FLUORESCENCE MICROSCOPY

We used two setups of laser scanning microscope. One (Columbia University) was a custom-made two-photon laser scanning microscope based on the Olympus FV-300 system (FV-300 side-mounted to a BX50WI microscope with a 60X, N.A. 1.1water immersion objective, LUMFLN 60XW) and a Ti:sapphire laser (Chameleon Ultra, Coherent). Details for the instrumentations have been described elsewhere (Nikolenko et al., 2003). Fluorescence was detected with a top-mounted Hamamatsu H7422-P40 PMT connected to a Hamamatsu C7319 preamplifier whose output was connected to a Fluoview system (Olympus). SHG was detected with a bottom-mounted similar PMT. The polarization of fundamental light was modified by a quartz zero-order half-wave plate (Newport Corporation). The other (RIKEN) is a multi-photon excitation imaging system (FV1000MPE, Olympus, Tokyo, Japan) at RIKEN BSI-Olympus Collaboration Center, equipped with a Ti-sapphire pulsed laser (InSight, Spectra-Physics, CA), an upright microscope, and a water immersion objective (LUMPlanFL/IR 60XW, N.A. 0.9, Olympus, Tokyo, Japan). Second harmonics emitted to the forward direction was collected by a condenser lens (N.A. 0.9) and detected with a photomultiplier module (Hamamatsu Photonics, Hamamatsu, Japan) in the transmission light path through a narrow band-pass filter of appropriate band. Two-photon excited fluorescence was detected using a detector in the reflection light path.

RESULTS

DESIGNING A FLUORESCENCE PROTEIN WITH AN ELECTROSTATIC SURFACE PATCH

The hypervariable domain of K-Ras4B consists of the polybasic region followed by the tetra- peptides, Cys-Val-Ile-Met ("CVIM" in a single-letter code), which acts as the farnesylation signal (**Figure 1A**). It has been shown that this synergistic membrane localizing mechanism can be applicable for other host proteins such as a fluorescence protein (Welman et al., 2000). In this study, we were first interested in exploring whether the polybasic region is separable from the C-terminal farnesylation target, and transferred onto the host protein surface, constituting an electrostatic patch, so that the host is oriented to the membrane in a geometrically defied manner (**Figures 1B–D**).

A previous study has revealed that the amount of basic amino acids in the polybasic region, rather than the specific sequence, is essential for efficient membrane localization (Welman et al., 2000). Our experiments also confirmed this conclusion. An artificial hypervariable domain consisting of 12 lysines followed by CVIM was fused after mVenus (i.e., a yellow fluorescence protein carrying A206K mutation; Nagai et al., 2002; Zacharias et al., 2002). We found that this chimeric protein was efficiently targeted to plasma membrane in HEK293T cells (mVenus-12K-CVIM; **Figures 1A,E**). The removal of the polybasic region (i.e., 12 × Lys) resulted in totally cytosolic expression (mVenus-CVIM; **Figures 1A,E**). These observations are thus in consistent with the

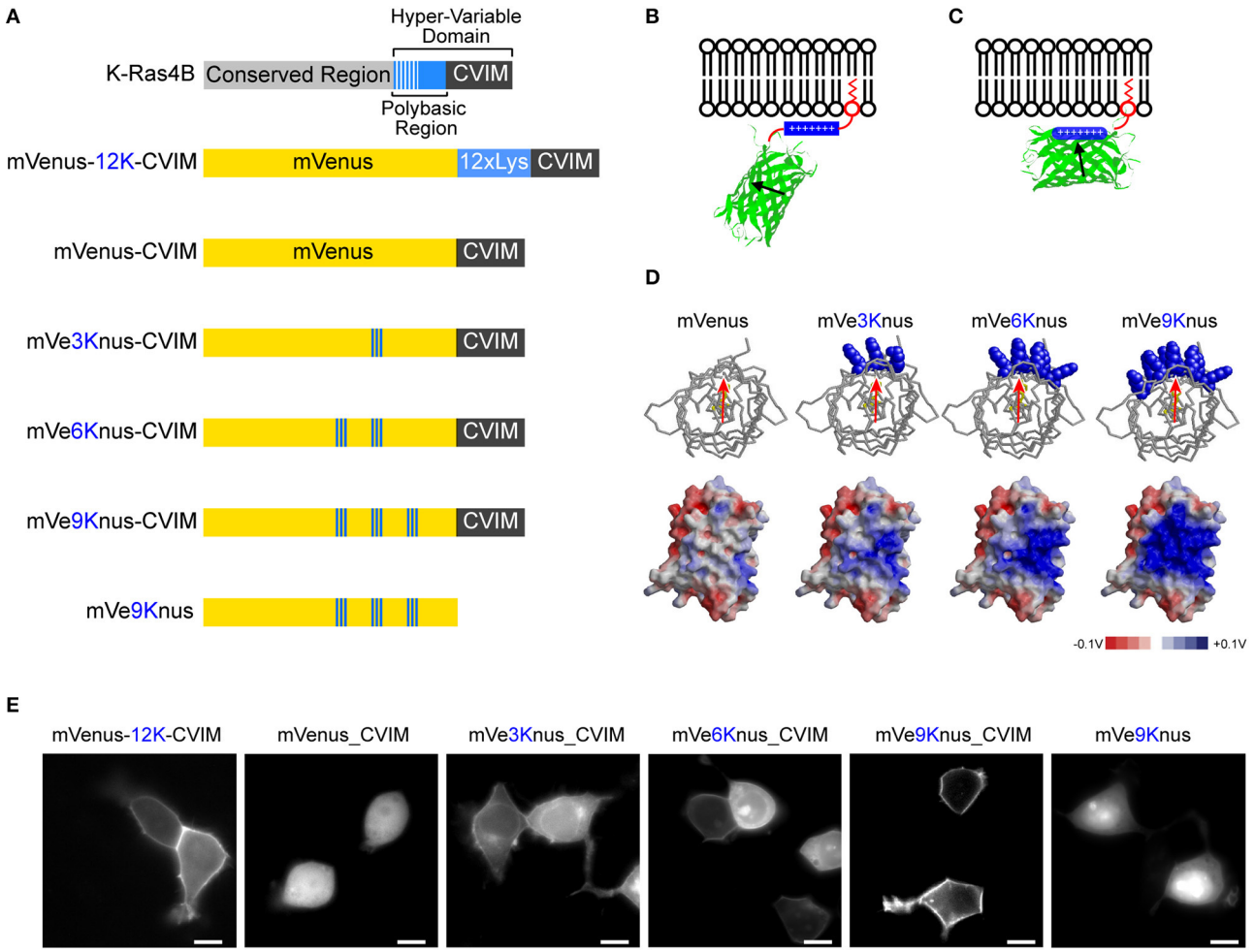

FIGURE 1 | Engineering of mVe9Knus-CVIM. (A) Primary structures of K-ras4B as well as the six mVenus-based constructs studied. "CVIM" in the gray box represents the farnesylation signal. The engineered lysine resides in mVenus-based constructs are highlighted in blue. **(B,C)** The design of these constructs consists in transferring the polybasic region to the surface of mVenus, aiming to orient it in a geometrically defined manner at the membrane-cytoplasm interface. **(D)** ***Top:*** Top views of mVenus and the three mutant models. The introduced lysine residues are highlighted in the blue, space-filled models. The red arrow approximates the transition dipole moment. ***Bottom:*** Side views of electrostatic surface potential maps in these models. **(E)** Representative images of HEK293 cells expressing the corresponding constructs. Bars = 10 μm.

previous study (Welman et al., 2000) and verified the functional significance of the positive charges in the hypervariable domain of K-Ras4B.

Using mVenus-CVIM as a template, we then mutated to lysine the amino acids that build the surface of the β-barrel in order to introduce a positively charged, electrostatic patch. It has been postulated that the transition dipole moment of the GFP chromophore subtends slight angles with the vector that joins the phenolic and imidazolinone oxygen atoms of the chromophore (Rosell and Boxer, 2003; Shi et al., 2007). Aiming to direct this vector roughly perpendicular to the membrane, we generated three variants which carried three (Y200K, S202K, Q204K), six (Y200K, S202K, Q204K, S147K, N149K, Y151K), and nine (Y200K, S202K, Q204K, S147K, N149K, Y151K, L221K, F223K, T225K) substations and named them as mVe3Knus-CVIM, mVe6Knus-CVIM, and mVe9Knus-CVIM, respectively (**Figures 1A,D**). These residues were determined basing on the crystal structure of Venus (PDB# 1MYV). In particular, the first three amino acids (Y200, S202, and Q204) are located on the opposite side of Tyr^{203} whose phenolic group interacts with the chromophore though π-stacking. The effects of the substitutions on membrane localization were tested by expressing in HEK293 cells (**Figure 1E**). Membrane localizations were only partially recovered in mVe3Knus-CVIM and mVe6Knus-CVIM, but was totally recovered in mVe9Knus-CVIM (**Figure 1E**), demonstrating significance of the area size of electrostatic patch (**Figure 1D**). Finally, the effect of removing the farnesylation target from mVe9Knus-CVIM was examined in order to discriminate whether its membrane localization relies on the synergistic mechanism as before, or is just as a result of the enlarged electrostatic patch. The removed construct, mVe9Knus, did not show membrane localizations but rather showed partial nuclear localization (**Figure 1E**), which supported the former view.

POLARIZATION DEPENDENCE OF mVe9Knus-CVIM FLUORESCENCE

Next, the polarization dependency of cellular fluorescence was analyzed in order to evaluate an effect of the electrostatic patch on the transition dipole orientations with respect to the membrane normal (**Figure 2**). The fluorescence profiles in the two images, one acquired with horizontally-polarized and the other with vertically-polarized excitation light reflected a substantial flexibility in the orientations of the transition dipole moment and were almost identical for a cell expressing mVenus-12K-CVIM, (**Figure 2A**). In contrast, in cells expressing mVe9Knus-CVIM, fluorescence was critically dependent on the polarization angle (**Figure 2B**). The merged image as well as the profile (**Figure 2B**) showed that mVe9Knus-CVIM at the membrane was more efficiently excited when the polarization angle was close to the membrane normal; indicating that the transition dipoles were not randomly distributed but rather oriented parallel to the membrane normal, on average. Such observed geometrical constrain was consistent with our protein design of electrostatic surface patch (**Figure 1D**).

SECOND HARMONIC GENERATION BY mVe9Knus-CVIM

Cells expressing mVe9Knus-CVIM were then subject to SHIM. Laser wavelengths from 780 to 1064 nm were examined. The SHG band (exactly half of the fundamental wavelength) and the two-photon excited fluorescence band (480∼550 nm) were separated by narrow band-pass filters. This required the fundamental wavelength to be shorter than 960 nm. SHG was extremely weak or undetectable at wavelengths below 900 nm, suggesting a resonant enhancement by electronic excitation. Under such constrains, the optimal wavelengths to obtain SHG signals were 940∼950 nm. Typically, a field of view of 70 × 70 μm was scanned as a 320 × 320 pixel image at a pixel dwell time of 40 μs. Laser power as large as 30∼40 mW at the sample was normally needed to detect clear second harmonic signals. Representative two-photon fluorescence and SHG image upon illumination at 940 nm are shown (**Figures 3A,B**). The possibility that the signal through a 470/10 nm band-pass filter (**Figure 3B**) originates from blue-edge of the two-photon excited fluorescence was excluded because the replacement by a 480/10 nm filter practically eliminated the signal (**Figure 3C**). SHG signals were not detected from membrane of the cells expressing mVenus-12K-CVIM (**Figures 3D–E**), reflecting the critical importance of the anisotropic orientation control of the chromophores. Weak endogenous SHG signals were occasionally detected from the center of the cells where no fluorescence was observed (**Figures 3B,E**). They could reflect SHG from endogenous structural proteins such as microtubules (Campagnola et al., 2002). In addition, the sensitivity to local centrosymmetry, the nature of SHG signal, was confirmed in the cells overexpressing mVe9Knus-CVIM (**Figure 4**). In these cases, although most of the protein was concentrated inside the cell rather than at the membrane-cytoplasm interface, as revealed by the pseudo-colored fluorescence image, second harmonic signals only arise from the interface, where the inversion symmetry is broken. Finally, we quantitatively addressed the orientation of mVe9Knus-CVIM at the membrane-cytoplasm interface. Under the simplifying assumption that the hyperpolarizability tensor of the chromophore is dominated by an element along its long molecular axis, the dependency of SHG from membrane-bound dyes on the polarization angle can be analytically expressed as Jiang et al. (2007):

$$SHG \propto \left\{ \left[< \cos^3\theta > \cos^2\phi + < \cos\theta \sin^2\theta > \sin^2\phi/2 \right]^2 + < \cos\theta \sin^2\theta >^2 \sin^2\phi \cos^2\phi \right\}, \quad (1)$$

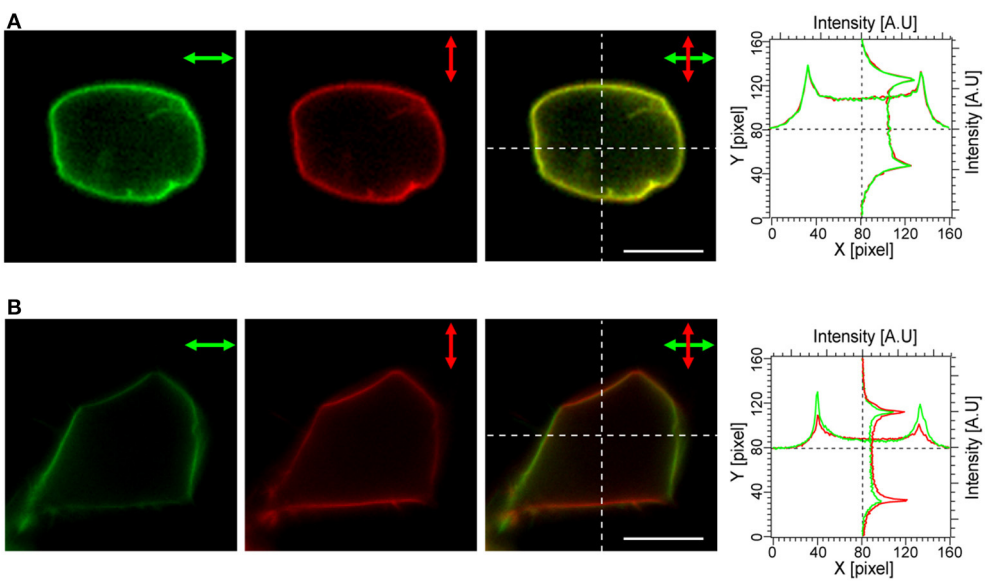

FIGURE 2 | Polarization dependency of mVe9Knus-CVIM Fluorescence. The panels show cellular fluorescence upon excitation with horizontally (green) and vertically (red) polarized light, the merged images, as well as intensity profiles along the dotted lines for the two constructs: mVenus-12K-CVIM **(A)** and mVe9Knus-CVIM **(B)**. Bars = 10 μm.

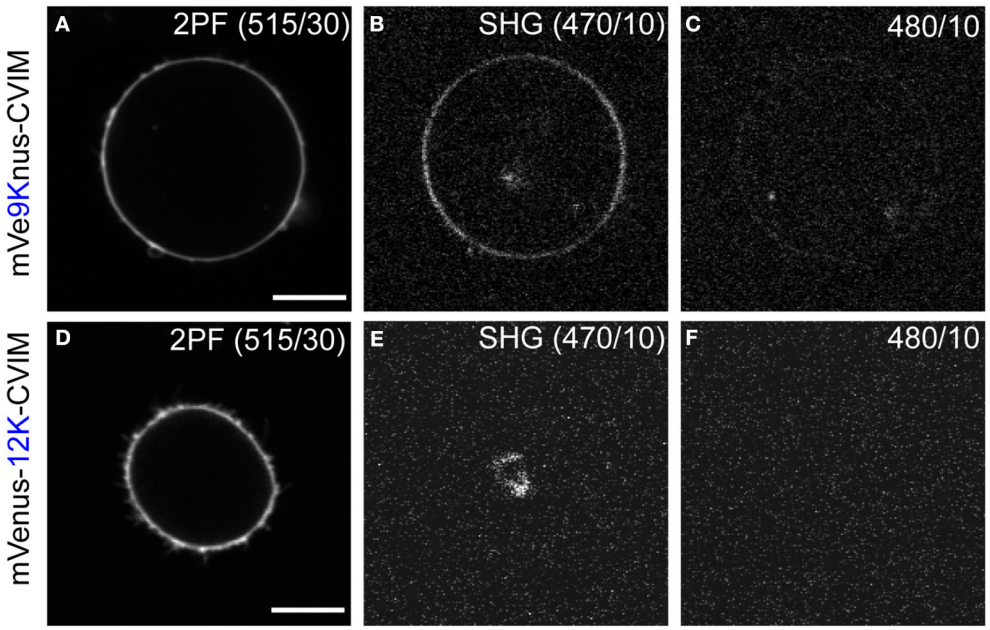

FIGURE 3 | Second harmonic imaging of mVe9Knus-CVIM. (A–C) Images showing two-photon excited fluorescence (2PF), SHG, and off-band signals from a cell expressing mVe9Knus-CVIM, respectively. **(D–F)** Same for a cell expressing mVenus-12K-CVIM. Fundamental wavelength was 940 nm. **(B,C,E,F)** Used the same brightness/contrast settings to allow direct comparisons. Actual optical filters used were indicated in the images. Bars = 10 μm.

where θ and ϕ are the angles of membrane normal subtended from the dye axis, and that from the polarization plane of fundamental light, respectively (**Figure 5A**). The angle brackets denote ensemble average. **Figures 5B,C** show representative and pooled data, respectively. When a fixed θ value was assumed for the ensemble, the curve fitting resulted in the tilt angle θ of $\sim 7.3°$.

DISCUSSION

In this study we have successfully engineered a GFP-based SHG membrane chromophore, even though one may not in principle expect strong SHG from GFP-based membrane proteins, because the SHG intensity from a chromophore is proportional to the square of its density (Shen, 1989) and the maximum dipole density is intrinsically limited by the size of β-barrel (Roorda et al., 2004). These difficulties were likely compensated by a highly-ordered protein orientation at the membrane-cytoplasm interface. For mVe9Knus-CVIM, the tile angle ($\theta =\sim 7.3°$) was smaller than that measured for the styryl dye FM4-64 ($\theta =\sim 36°$) (Jiang et al., 2007), although the insertion mechanisms of FM4-64 and mVe9Knus-CVIM are very different (lipophilic attachment for FM4-64 vs. electrostatic for mVe9Knus-CVIM).

FM4-64 and other organic dyes bound in cell membrane produce robust voltage dependent second harmonics (Campagnola et al., 1999; Millard et al., 2003b, 2004; Nemet et al., 2004), and have been successfully applied to monitor electrical activity in fine membrane structures (Nuriya et al., 2006). Various effects, from direct to rather indirect ones, could serve as the mechanisms for voltage sensitivity, including electro optic, or chromic effect, translocation, reorientation, and redistribution (Moreaux et al., 2003; Pons et al., 2003; Jiang et al., 2007). It would be interesting to ascertain whether the second harmonics from mVe9Knus-CVIM is sensitive to transmembrane voltage. Because the Debye length in physiological ionic condition is probably smaller than 10 Å, the chromophore may lie outside of the substantial surface field. At the same time, it is possible

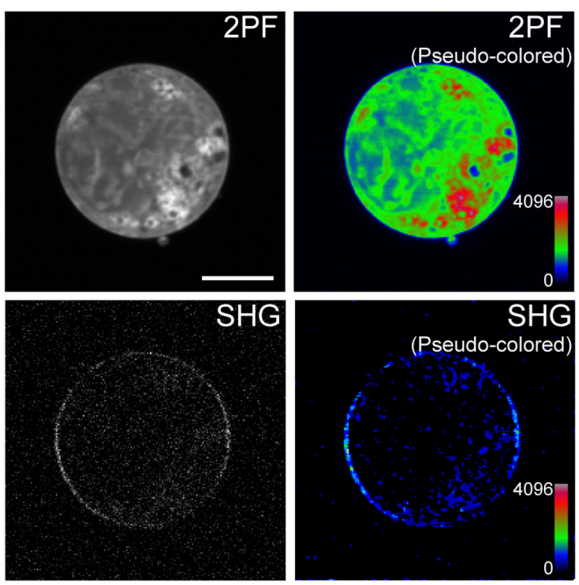

FIGURE 4 | Sensitivity of mVe9Knus-CVIM SHG to inversion symmetry. Images show two-photon excited fluorescence (2PF) and SHG signals from an overexpressing cell in gray and pseudocolor. Proteins are more densely distributed inside the cell than at the membrane. Despeckle filter was applied prior to generate the pseudocolored SHG image (lower right panel). Bar = 10 μm.

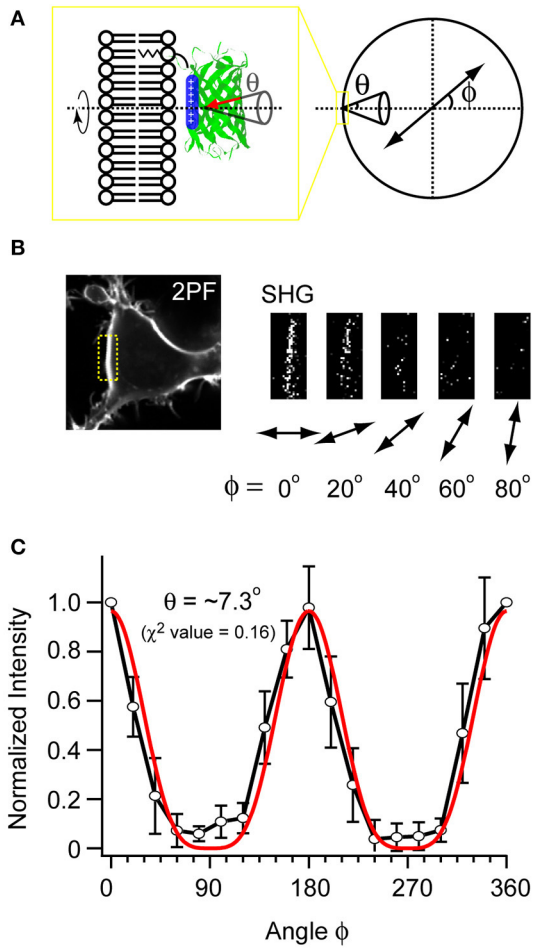

FIGURE 5 | Measuring the orientation of mVe9Knus-CVIM at the membrane interface. (A) A scheme illustrating the parameters. ϕ: angle of the polarization plane with respect to the membrane normal. θ: tilt angle of chromophore's uniaxial hyperpolarizability with respect to the membrane normal. The cone represents the distributions on ensemble. **(B)** Example images obtained with five different polarization angles (ϕ). **(C)** The pooled data (black plot; average ± SD; $n = 6$), and its fit (red plot).

that, like it has been estimated for nanoparticles (Dr. J. Owen, personal communication), the electric field could protrude from the membrane and engulf a molecule that excludes ions. Indirect effects cannot be ruled out also, since our protein is actually oriented to the membrane through the electrostatic interaction with the short-distance field. In principle, the degree of interaction and orientation could be subject to modulation. Assuming membrane capacitance C of ∼1 μF/cm^2, a voltage change ΔV of ∼100 mV will associate change in the surface charge:

$$\Delta Q = C\Delta V \approx 10^{-7}[C/cm^2] \approx 1/15000[e/Å^2], \qquad (2)$$

which is equivalent to ∼1% of net cytoplasmic surface charge of typical phospholipid composition (1/100∼1/200 [e/Å^2]; Smith et al., 1993; Xu and Loew, 2003). In preliminary experiments, we performed pilot experiments of simultaneous patch-clamp and SHG measurements, but have not detected clear voltage dependent signals so far. Nevertheless, we consider that a solid conclusion regarding this issue has not been obtained since poor signal-to-noise ratio, which has hampered us to perform precise measurements. Use of higher laser power may not be appropriate since our second harmonic signal most likely relies on resonant enhancement through electronic excitation. Notably, SHG is proportional to square of the dipole density, and thus our signal is highly sensitive to chromophore destruction. In spite of this, we envision two future directions toward improvements. The first is to exploit the diversity of GFP-like proteins, which could differ widely not only in chromatic properties, but also in non-linear properties. In fact, the protonated form of Dronpa, a photo-switchable coral fluorescence protein (Ando et al., 2004), has been shown to exhibit large high non-linear hyperpolarizability (Asselberghs et al., 2008). At this point, many other GFP-like proteins still remain unevaluated for SHG. Thus, performing a proper survey with subsequent protein engineering as in the present study could lead to a better performing SHG chromophores. The second direction for future improvement is more precise control of the electrostatic property of the β-barrel surface in terms of the area size and also the position. As observed in the constructs with less surface lysine (**Figures 1D,E**), the protein order at the interface alters the balance between the electrostatic energy stabilization and the thermal relaxation. By considering derivate of the Equation (1), it is anticipated that the response to the electrostatic perturbation will depend on basal tile angle, θ. Thus, there might be an optimal surface electrostatic condition where ΔQ would most effectively influence the signal.

In addition, in terms of mechanisms of protein-membrane association, there are some other proteins (e.g., Src, MARCKS, HIV-1 gag) which are known to rely on the electrostatic mechanism similar to K-Ras4B. While all these proteins likewise possess apparent basic clusters in their primary structures, the present study clearly demonstrated that the basic amino acids are not necessarily clustered in the primary structure whenever they constitute a basic patch in the tertiary structure. Thus, might be more natural proteins which have not yet been recognized to interact electrostatically.

Compared to the recent achievements building genetically-encoded probes basing on fluorescence (Miyawaki, 2011), the design of protein probes based on SHG has remained behind. In this study, as a first step, we show that genetically-encoded chromophores can be in fact anisotropically arranged beneath the membrane through the artificial control of the electrostatic properties of the protein surface. Although still faint, the second harmonic signals from mVe9Knus-CVIM could be improved for wider biological use. Using this strategy for orientation control of membrane chromophores could enable further development of genetically-encoded probes for membrane potential imaging.

ACKNOWLEDGMENTS

This work was supported by grants from MEXT and JST-PRESTO to Hidekazu Tsutsui. Initial part of this study was supported by the Special Postdoctoral Researcher Program of RIKEN (Hidekazu Tsutsui). The Rafael Yuste lab was supported by the NEI (DP1EY024503), NIHM (R01MH101218) and the Keck Foundation. This material is based upon work supported

by, or in part by, the U. S. Army Research Laboratory and the U. S. Army Research Office under contract number W911NF-12-1-0594 (MURI). We thank all the members of Yuste's lab for the support during the stay of Hidekazu Tsutsui.

REFERENCES

Ando, R., Mizuno, H., and Miyawaki, A. (2004). Regulated fast nucleocytoplasmic shuttling observed by reversible protein highlighting. *Science* 306, 1370–1373. doi: 10.1126/science.1102506

Asselberghs, I., Flors, C., Ferrighi, L., Botek, E., Champagne, B., Mizuno, H., et al. (2008). Second-harmonic generation in GFP-like proteins. *J. Am. Chem. Soc.* 130, 15713–15719. doi: 10.1021/ja805171q

Campagnola, P. J., Clark, H. A., Mohler, W. A., Lewis, A., and Loew, L. M. (2001). Second-harmonic imaging microscopy of living cells. *J. Biomed. Opt.* 6, 277–286. doi: 10.1117/1.1383294

Campagnola, P. J., Millard, A. C., Terasaki, M., Hoppe, P. E., Malone, C. J., and Mohler, W. A. (2002). Three-dimensional high-resolution second-harmonic generation imaging of endogenous structural proteins in biological tissues. *Biophys. J.* 82, 493–508. doi: 10.1016/S0006-3495(02)75414-3

Campagnola, P. J., Wei, M. D., Lewis, A., and Loew, L. M. (1999). High-resolution nonlinear optical imaging of live cells by second harmonic generation. *Biophys. J.* 77, 3341–3349. doi: 10.1016/S0006-3495(99)77165-1

Guex, N., and Peitsch, M. C. (1997). SWISS-MODEL and the Swiss-PdbViewer: an environment for comparative protein modelling. *Electrophoresis* 18, 2714–2723. doi: 10.1002/elps.1150181505

Hancock, J. F., Cadwallader, K., Paterson, H., and Marshall, C. J. (1991). A CAAX or a CAAL motif and a second signal are sufficient for plasma membrane targeting of ras proteins. *EMBO J.* 10, 4033–4039.

Hancock, J. F., Paterson, H., and Marshall, C. J. (1990). A polybasic domain or palmitoylation is required in addition to the CAAX motif to localize p21ras to the plasma membrane. *Cell* 63, 133–139. doi: 10.1016/0092-8674(90)90294-O

Jiang, J., Eisenthal, K. B., and Yuste, R. (2007). Second harmonic generation in neurons: electro-optic mechanism of membrane potential sensitivity. *Biophys. J.* 93, L26–L28. doi: 10.1529/biophysj.107.111021

Khatchatouriants, A., Lewis, A., Rothman, Z., Loew, L., and Treinin, M. (2000). GFP is a selective non-linear optical sensor of electrophysiological processes in Caenorhabditis elegans. *Biophys. J.* 79, 2345–2352. doi: 10.1016/S0006-3495(00)76480-0

Lazar, J., Bondar, A., Timr, S., and Firestein, S. J. (2011). Two-photon polarization microscopy reveals protein structure and function. *Nat. Methods* 8, 684–690. doi: 10.1038/nmeth.1643

Lewis, A., Khatchatouriants, A., Treinin, M., Chen, Z., Peleg, G., Friedman, N., et al. (1999). Second harmonic generation of biological interfaces: probing the membrane protein bacteriorhodopsin and imaging membrane potential around GFP molecules at specific sites in neuronal cells of C. *elegans. Chem. Phys.* 245, 133–144. doi: 10.1016/S0301-0104(99)00128-7

Millard, A. C., Campagnola, P. J., Mohler, W., Lewis, A., and Loew, L. M. (2003a). Second harmonic imaging microscopy. *Methods Enzymol.* 361, 47–69. doi: 10.1016/S0076-6879(03)61005-0

Millard, A. C., Jin, L., Lewis, A., and Loew, L. M. (2003b). Direct measurement of the voltage sensitivity of second-harmonic generation from a membrane dye in patch-clamped cells. *Opt. Lett.* 28, 1221–1223. doi: 10.1364/OL.28.001221

Millard, A. C., Jin, L., Wei, M. D., Wuskell, J. P., Lewis, A., and Loew, L. M. (2004). Sensitivity of second harmonic generation from styryl dyes to transmembrane potential. *Biophys. J.* 86, 1169–1176. doi: 10.1016/S0006-3495(04)74191-0

Millard, A. C., Terasaki, M., and Loew, L. M. (2005). Second harmonic imaging of exocytosis at fertilization. *Biophys. J.* 88, L46–L48. doi: 10.1529/biophysj.105.063768

Miyawaki, A. (2011). Development of probes for cellular functions using fluorescent proteins and fluorescence resonance energy transfer. *Annu. Rev. Biochem.* 80, 357–373. doi: 10.1146/annurev-biochem-072909-094736

Moreaux, L., Pons, T., Dambrin, V., Blanchard-Desce, M., and Mertz, J. (2003). Electro-optic response of second-harmonic generation membrane potential sensors. *Opt. Lett.* 28, 625–627. doi: 10.1364/OL.28.000625

Moreaux, L., Sandre, O., Blanchard-Desce, M., and Mertz, J. (2000). Membrane imaging by simultaneous second-harmonic generation and two-photon microscopy. *Opt. Lett.* 25, 320–322. doi: 10.1364/OL.25.000320

Nagai, T., Ibata, K., Park, E. S., Kubota, M., Mikoshiba, K., and Miyawaki, A. (2002). A variant of yellow fluorescent protein with fast and efficient maturation for cell-biological applications. *Nat. Biotechnol.* 20, 87–90. doi: 10.1038/nbt0102-87

Nemet, B., Nikolenko, V., and Yuste, R. (2004). Second harmonic retinal imaging of membrane potential (SHRIMP). *J. Biomed. Opt.* 9, 873–881. doi: 10.1117/1.1783353

Nikolenko, V., Nemet, B., and Yuste, R. (2003). A two-photon and second-harmonic microscope. *Methods* 30, 3–15. doi: 10.1016/S1046-2023(03)00003-3

Nuriya, M., Jiang, J., Nemet, B., Eisenthal, K. B., and Yuste, R. (2006). Imaging membrane potential in dendritic spines. *Proc. Natl. Acad. Sci. U.S.A.* 103, 786–790. doi: 10.1073/pnas.0510092103

Nuriya, M., and Yasui, M. (2010). Membrane potential dynamics of axons in cultured hippocampal neurons probed by second-harmonic-generation imaging. *J. Biomed. Opt.* 15:020503. doi: 10.1117/1.3365135

Pons, T., Moreaux, L., Mongin, O., Blanchard-Desce, M., and Mertz, J. (2003). Mechanisms of membrane potential sensing with second-harmonic generation microscopy. *J. Biomed. Opt.* 8, 428–431. doi: 10.1117/1.1581871

Rekas, A., Alattia, J. R., Nagai, T., Miyawaki, A., and Ikura, M. (2002). Crystal structure of venus, a yellow fluorescent protein with improved maturation and reduced environmental sensitivity. *J. Biol. Chem.* 277, 50573–50578. doi: 10.1074/jbc.M209524200

Roorda, R. D., Hohl, T. M., Toledo-Crow, R., and Miesenböck, G. (2004). Video-rate nonlinear microscopy of neuronal membrane dynamics with genetically encoded probes. *J. Neurophysiol.* 92, 609–621. doi: 10.1152/jn.00087.2004

Rosell, F. I., and Boxer, S. G. (2003). Polarized absorption spectra of green fluorescent protein single crystals: transition dipole moment directions. *Biochemistry* 42, 177–183. doi: 10.1021/bi0266535

Sawano, A., and Miyawaki, A. (2000). Directed evolution of green fluorescent protein by a new versatile PCR strategy for site-directed and semi-random mutagenesis. *Nucleic Acids Res.* 28:E78. doi: 10.1093/nar/28.16.e78

Shen, Y. R. (1989). Surface properties probed by second-harmonic and sum-frequency generation. *Nature* 337, 519–525. doi: 10.1038/337519a0

Shi, X., Basran, J., Seward, H. E., Childs, W., Bagshaw, C. R., and Boxer, S. G. (2007). Anomalous negative fluorescence anisotropy in yellow fluorescent protein (YFP 10C): quantitative analysis of FRET in YFP dimers. *Biochemistry* 46, 14403–14417. doi: 10.1021/bi701575n

Smith, P. A., Aschroft, F. M., and Fewtrell, C. M. (1993). Permeation and gating properties of the L-type calcium channel in mouse pancreatic beta cells. *J. Gen. Physiol.* 101, 767–797. doi: 10.1085/jgp.101.5.767

Welman, A., Burger, M. M., and Hagmann, J. (2000). Structure and function of the C-terminal hypervariable region of K-Ras4B in plasma membrane targetting and transformation. *Oncogene* 19, 4582–4591. doi: 10.1038/sj.onc.1203818

Xu, C., and Loew, L. M. (2003). The effect of asymmetric surface potentials on the intramembrane electric field measured with voltage-sensitive dyes. *Biophys. J.* 84, 2768–2780. doi: 10.1016/S0006-3495(03)75081-4

Zacharias, D. A., Violin, J. D., Newton, A. C., and Tsien, R. Y. (2002). Partitioning of lipid-modified monomeric GFPs into membrane microdomains of live cells. *Science* 296, 913–916. doi: 10.1126/science.1068539

Conflict of Interest Statement: The authors declare that the research was conducted in the absence of any commercial or financial relationships that could be construed as a potential conflict of interest.

Received: 02 September 2014; accepted: 08 November 2014; published online: 27 November 2014.

Citation: Jinno Y, Shoda K, Rial-Verde E, Yuste R, Miyawaki A and Tsutsui H (2014) Engineering a genetically-encoded SHG chromophore by electrostatic targeting to the membrane. Front. Mol. Neurosci. 7:93. doi: 10.3389/fnmol.2014.00093

This article was submitted to the journal Frontiers in Molecular Neuroscience.

frontiers in Molecular Neuroscience

METHODS
published: 15 April 2015
doi: 10.3389/fnmol.2015.00010

Imaging activity in astrocytes and neurons with genetically encoded calcium indicators following *in utero* electroporation

J. Michael Gee[1,2], *Meredith B. Gibbons*[3,4], *Marsa Taheri*[1], *Sierra Palumbos*[5], *S. Craig Morris*[1,5], *Roy M. Smeal*[3], *Katherine F. Flynn*[3], *Michael N. Economo*[1], *Christian G. Cizek*[1,5], *Mario R. Capecchi*[5,6], *Petr Tvrdik*[5], *Karen S. Wilcox*[3]* and *John A. White*[1]*

[1] Neuronal Dynamics Laboratory, Department of Bioengineering, University of Utah, Salt Lake City, UT, USA, [2] MD-PhD Program, University of Utah, Salt Lake City, UT, USA, [3] Glial-Neuronal Interactions in Epilepsy Laboratory, Department of Pharmacology and Toxicology, University of Utah, Salt Lake City, UT, USA, [4] Interdepartmental Program in Neuroscience, University of Utah, Salt Lake City, UT, USA, [5] Mario Capecchi Laboratory, Department of Human Genetics, University of Utah, Salt Lake City, UT, USA, [6] Department of Human Genetics, Howard Hughes Medical Institute, University of Utah, Salt Lake City, UT, USA

OPEN ACCESS

Edited by:
Katsuhiko Mikoshiba,
RIKEN Brain Science Institute, Japan

Reviewed by:
Masayuki Miura,
The University of Tokyo, Japan
Kenji Tanaka,
Keio University, Japan

***Correspondence:**
Karen S. Wilcox,
Department of Pharmacology and Toxicology, University of Utah, 417 Wakara Way, Rm 3211, Salt Lake City, UT 84108, USA
karen.wilcox@hsc.utah.edu;
John A. White,
Department of Bioengineering, University of Utah, Sorenson Molecular Biotechnology Building, 36 S Wasatch Dr., Rm 3100, Salt Lake City, UT 84112, USA
john.white@utah.edu

Received: 22 February 2015
Paper pending published: 03 March 2015
Accepted: 23 March 2015
Published: 15 April 2015

Citation:
Gee JM, Gibbons MB, Taheri M, Palumbos S, Morris SC, Smeal RM, Flynn KF, Economo MN, Cizek CG, Capecchi MR, Tvrdik P, Wilcox KS and White JA (2015) Imaging activity in astrocytes and neurons with genetically encoded calcium indicators following in utero electroporation. Front. Mol. Neurosci. 8:10. doi: 10.3389/fnmol.2015.00010

Complex interactions between networks of astrocytes and neurons are beginning to be appreciated, but remain poorly understood. Transgenic mice expressing fluorescent protein reporters of cellular activity, such as the GCaMP family of genetically encoded calcium indicators (GECIs), have been used to explore network behavior. However, in some cases, it may be desirable to use long-established rat models that closely mimic particular aspects of human conditions such as Parkinson's disease and the development of epilepsy following status epilepticus. Methods for expressing reporter proteins in the rat brain are relatively limited. Transgenic rat technologies exist but are fairly immature. Viral-mediated expression is robust but unstable, requires invasive injections, and only works well for fairly small genes (<5 kb). *In utero* electroporation (*IUE*) offers a valuable alternative. *IUE* is a proven method for transfecting populations of astrocytes and neurons in the rat brain without the strict limitations on transgene size. We built a toolset of *IUE* plasmids carrying GCaMP variants 3, 6s, or 6f driven by CAG and targeted to the cytosol or the plasma membrane. Because low baseline fluorescence of GCaMP can hinder identification of transfected cells, we included the option of co-expressing a cytosolic tdTomato protein. A binary system consisting of a plasmid carrying a *piggyBac* inverted terminal repeat (ITR)-flanked CAG-GCaMP-IRES-tdTomato cassette and a separate plasmid encoding for expression of *piggyBac* transposase was employed to stably express GCaMP and tdTomato. The plasmids were co-electroporated on embryonic days 13.5–14.5 and astrocytic and neuronal activity was subsequently imaged in acute or cultured brain slices prepared from the cortex or hippocampus. Large spontaneous transients were detected in slices obtained from rats of varying ages up to 127 days. In this report, we demonstrate the utility of this toolset for interrogating astrocytic and neuronal activity in the rat brain.

Keywords: GCaMP6, rat model, GCaMP3, calcium imaging, astroglia, neural network, gene expression, tdTomato

Introduction

The brain comprises networks of glia and neurons. Investigation of glial and neuronal network dynamics is necessary for understanding complex behavior and disease. The rat brain is particularly well-suited for modeling neurophysiology and neuropathology. The predominant use of rats throughout the history of neuroscience research has already created a wealth of knowledge about many behaviors and disorders including the kainic acid model of status epilepticus and the 6-OHDA model of Parkinson's disease (Schultz, 1982; Jacob, 1999; Cenci et al., 2002; Williams et al., 2007). Unfortunately, rat models are restricted by limited methods for interrogating the activity of numerous cells simultaneously, especially glia. Traditional electrophysiological techniques for recording neuronal activity are inadequate for less electrically active glial cells. However, glial cells, as well as neurons, exhibit substantial intracellular calcium concentration transients which can be measured as a proxy for cellular activity. Fluorescent synthetic dyes, derived from the EGTA homolog BAPTA, such as Fluo-4, Oregon Green BAPTA, and Indo-1 are frequently used for calcium imaging (Tsien, 1980; Uematsu et al., 1991; Kreitzer et al., 2000; McDonough et al., 2000; Stosiek et al., 2003; Kuga et al., 2011; Lillis et al., 2012), but have several drawbacks. Synthetic dye loading techniques are particularly difficult to employ in mature or pathological tissue, limiting their use to a subset of experimental preparations—those in healthy young tissue (Peterlin et al., 2000; Reeves et al., 2011). Additionally, synthetic dyes cannot be targeted to specific cell types or intracellular regions (Mank and Griesbeck, 2008; Mao et al., 2008) except in special cases (Ding, 2012). Over the past decade, genetic approaches have evolved to ameliorate these issues.

Genetically encoded calcium indicators (GECIs), such as the GFP-based GCaMP family, are a powerful tool for investigation of cellular activity (Nakai et al., 2001; Tian et al., 2009; Chen et al., 2013). Viral vectors are often used to deliver GCaMP to target tissues, but there exist several reasons why use of this approach may not be desirable. Viruses require invasive injections, often times near the location and time of imaging. Adeno-associated virus, while extremely useful for transgene delivery and relatively non-immunogenic, is hampered by a low carrying capacity of less than 5 kb (Grieger and Samulski, 2005). Alternatively, rat transgenic tools are quickly improving but are limited in number and require significant time and labor to develop. *In utero* electroporation (*IUE*) offers a valuable substitute for both of these approaches (Saito and Nakatsuji, 2001; Tabata and Nakajima, 2001; Bai et al., 2003; Borrell et al., 2005; Nakahira and Yuasa, 2005). After injecting DNA into the lateral ventricles of the embryonic brain, an electric field is applied across the uterine walls to facilitate transfection of glia and neuron progenitors which eventually divide and migrate throughout the brain. Unfortunately, transfected plasmid DNA tends to remain episomal and becomes diluted in persistently dividing cells, such as astrocytes, the predominant glial cell. To circumvent this problem, several different transposon systems, including *Tol2* from the Japanese rice fish *Oryzias latipes* or *piggyBac* from the cabbage looper moth *Trichoplusia ni*, can be applied to mediate stable genomic integration of inverted terminal repeat (ITR)-flanked DNA (Cary et al., 1989; Fraser et al., 1995, 1996; Ding et al., 2005; Yoshida et al., 2010; Chen and LoTurco, 2012). *piggyBac* can transpose transgenes of up to 100 kb between plasmid DNA and genomic DNA and has been adapted for use in mammalian systems (Lorenzen et al., 2003; Ding et al., 2005; Wu et al., 2007; VandenDriessche et al., 2009; Li et al., 2011b). When combined with *IUE*, *piggyBac*-mediated transposition results in propagation of the transgene to the entire cell lineage of transfected progenitors (Wu et al., 2007; Chen and LoTurco, 2012).

In this report, we describe a toolset of plasmid constructs, carrying cytosol- or plasma membrane-targeted ITR-flanked GCaMP3 or versions of GCaMP6, designed specifically for calcium imaging of the rat brain following *IUE*. We demonstrate that these constructs are stably expressed well into adulthood and are functional in astrocytes and neurons in acute cortical slices or hippocampal organotypic slice cultures (OSCs). We present data collected with the *piggyBac* ITR-flanked CAG-Lck-GCaMP6f (pPBC-LG6f) plasmid as an example of the utility of these tools. This toolset offers an attractive approach for future studies investigating astrocytic-neuronal network behavior in various rat brain preparations.

Abbreviations: ABS, acute brain slice; Aldh1L1, aldehyde dehydrogenase 1 family, member L1; CAG, cytomegalovirus early enhancer/chicken beta actin; FWHM, full-width at half-maximum; GFAP, glial fibrillary acidic protein; GFP, green fluorescent protein; IRES, internal ribosomal entry site; ITR, inverted terminal repeat; *IUE, in utero* electroporation; KS, Kolmogorov–Smirnov; KW-ANOVA, Kruskal-Wallis One-Way analysis of variance; Lck, lymphocyte-specific protein tyrosine kinase; MWU, Mann–Whitney U; OSC, organotypic slice culture; PB, *piggyBac*; ROI, region of interest.

Materials and Methods

Animals

Pregnant Sprague Dawley CD dams were obtained from Charles River Laboratories, Inc. (Wilmington, MA) and maintained at the University of Utah animal facility. Both male and female animals were used. All experimental protocols were approved by the University of Utah Institutional Animal Care and Use Committee (IACUC).

Plasmid Generation

The GECIs GCaMP3 or GCaMP6 (Tian et al., 2009; Chen et al., 2013) and the red fluorescent reporter protein tdTomato (Shaner et al., 2004) were expressed from circular plasmid DNA that was prepared by standard DNA cloning methods. A binary plasmid mix was used in a 3:1 ratio. The donor plasmid harbors GCaMP and tdTomato connected via an internal ribosomal entry site (IRES; **Figure 1B**) and is driven by the strong ubiquitous promoter cytomegalovirus early enhancer/chicken beta actin (CAG; Niwa et al., 1991). IRES is a bicistronic sequence that allows for simultaneous expression of two proteins separately but from the same RNA transcript. The CAG-GCaMP-IRES-tdTomato construct was flanked with *piggyBac* ITRs obtained from the pZG-s plasmid (**Figure 1B**; Wu et al., 2007). To target GCaMP to the plasma membrane, we spliced the Lck N-terminal sequence to the N-terminus of GCaMP (**Figure 1A**; Shigetomi et al., 2010b).

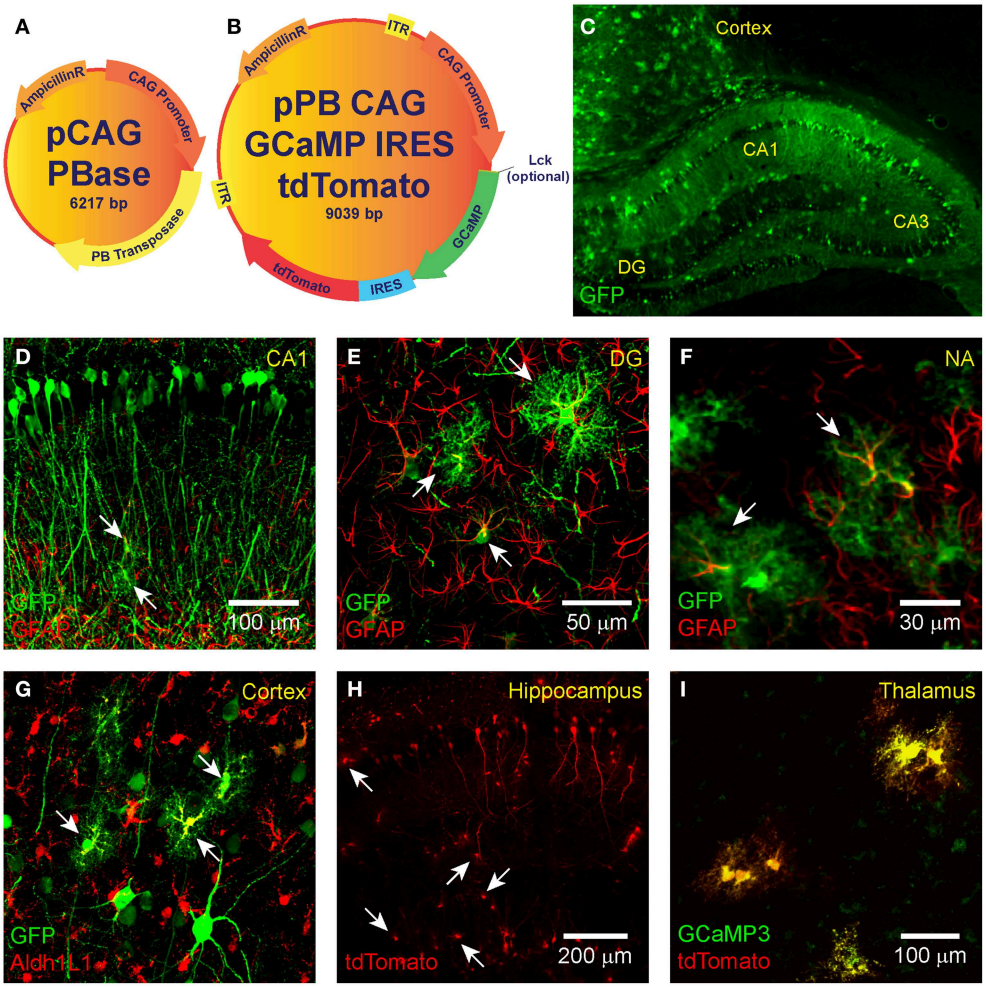

FIGURE 1 | *IUE*-mediated transgene delivery to astrocytes and neurons in various regions of the brain. The binary co-transfection system consists of a **(A)** helper plasmid carrying the *piggyBac* transposase enzyme and a **(B)** donor plasmid carrying the GCaMP (3, 6s, or 6f)-IRES-tdTomato construct flanked with *piggyBac* inverted terminal repeats. A subset of donor plasmids include an N-terminal Lck-tagged GCaMP for plasma membrane targeting. All transgenes are expressed under the control of CAG. **(C–G)** *IUE* of CAG-GFP-IRES-Neo transfected astrocytes and neurons in the **(C,D)** hippocampus, **(C,G)** cortex, the **(E)** dentate gyrus, and **(F)** nucleus accumbens. Fluorophore-conjugated anti-GFP antibody enhanced GFP is shown in green. In **(D–F)** astrocyte-labeling anti-GFAP antibody is shown in red and overlap (transfected astrocytes) in yellow. **(G)** GFAP overlap with GFP was sometimes difficult to detect, so we also stained astrocyte-specific Aldh1L1 which is shown in red with transfected astrocytes in yellow. **(H)** Hippocampal expression pattern of tdTomato expression (naïve fluorescence) and **(I)** co-expression (yellow) of GCaMP3 (green) and tdTomato (red) in putative thalamic neurons following *IUE* transfection of CAG-GCaMP3-IRES-tdTomato (naïve fluorescence). White arrows denote putative astrocytes.

The helper plasmid (pPBase) encodes for the *piggyBac* transposase enzyme (**Figure 1A**; Wu et al., 2007) and is likewise driven by CAG. For some experiments we used the pPB-CAG-GFP-IRES-Neo plasmid (pPBC-GFP; a gift from Sen Wu in the Capecchi lab).

Immunohistochemistry and Confocal Imaging

For confirmation of targeting experiments (**Figures 1C–I**), seven rats were electroporated with pPBC-GFP. Postnatal day (P) 20 rats were anesthetized with Nembutal (50 mg/kg i.p.; Ovation Pharm, Deerfield, IL, USA) and transcardially perfused with 1 × PBS followed by 4% paraformaldehyde (PFA) diluted with 1 × PBS (pH 7.6). Brains were removed and post-fixed for 24 h in 4% PFA at 4°C. Brain sections (40 µm) were then prepared on a vibratome and mounted on glass slides. Slices were blocked with BSA (A2153 Sigma-Aldrich, St. Louis, MO, USA) for 1 h and then incubated with either the primary antibody chicken anti-GFP IgY (1:500 overnight; A10262 Life Technologies, Carlsbad, CA, USA) and secondary antibody DyLight 488-conjugated AffiniPure donkey anti-chicken IgY (1:750 2 h) for GFP-staining or with the Cy3-conjugated mouse anti-glial fibrillary acidic protein (GFAP; 1:1000 overnight; C9205 Sigma-Aldrich, St. Louis, MO, USA) for GFAP-staining. Aldh1L1 was labeled by rabbit anti-Aldh1L1 (ab87117, Abcam, Cambridge, MA, USA). Following antibody

labeling, slides were incubated in 1 × DAPI for 30 min and mounted with ProLong Gold Antifade Mountant (P36930 Invitrogen, Carlsbad, CA, USA).

To test for a possible immune response following *IUE* (**Figure 2**), four rats electroporated with pPBC-GFP and three unmanipulated age-matched controls were sacrificed at P18. The brains were removed and post-fixed for 24 h in 4% PFA solution at 4°C. They were then transferred to a sucrose solution gradient (15 and 30% for 24 h each) at 4°C or until brains sank in solution. Brains were embedded with OCT compound in a "brain box," then frozen and stored at −20°C. Coronal sections (20 μm) were prepared using a cryostat and mounted onto charged glass slides (Superfrost Plus Micro Slide, VWR, Batavia, IL, USA). The sections were permeabilized at room temperature for 40 min with 0.1% Triton-X diluted in 1 × PBS. For GFAP labeling, the same CY3-conjugated anti-GFAP antibody described above was diluted in CytoQ (1:800) and applied for 1.5 h at room temperature. For Iba-1 labeling, primary goat polyclonal anti-Iba1 antibody diluted in CytoQ (1:600, ab5076, Abcam, Cambridge, MA, USA) was applied for 24 h at 4°C, followed by secondary rabbit anti-goat Alexa Fluor 555 antibody (1:500, ab150146, Abcam, Cambridge, MA, USA) for 2 h at room temperature. Finally, ProLong Gold Antifade Mountant with DAPI was applied to the sections as the mounting medium. All imaging was performed using an Olympus Fluoview FV1000 confocal microscope with either 20 × 0.75 NA or 40 × 0.80 NA water immersion objectives (Olympus, Tokyo, Japan). Images were processed using ImageJ.

In Utero Electroporation

Transfection of the embryonic rat brain was accomplished via an established *IUE* protocol (Bai et al., 2003). After induction of a deep anesthetic state with ketamine/xylazine (70/30 mixture, 0.1 mg/g body weight, i.p.), the abdomen of a multiparous pregnant rat was shaved and swabbed with betadine. A laparotomy was performed and embryos (gestational day 13.5–14.5) within the uterine horn were exposed and gently placed on a sterile and irrigated gauze pad. Because the embryos at this age stretch the uterus, they can be clearly visualized with only the aid of a bright fiber optic lamp. A glass capillary tube was pulled (Sutter Instrument, Novato, CA, USA) to a fine point by high heat and filled with a mixture of fast green (1%; Sigma-Aldrich, St. Louis, MO, USA) and DNA plasmid solution (1 μg/μl final). The pipette tip was inserted through the uterus into one of the lateral ventricles of the embryo brain and a small volume (1–3 μl) of the mixture was pressure injected by a picospritzer (Picospritzer III; Parker, Mayfield Heights, OH, USA) or by applying positive pressure through a mouth pipette. Successful injection was confirmed visually by observing fast green filling of the ventricle. For electroporation, a pair of sterilized gold copper alloy plate electrodes (1 × 0.5 cm) were positioned across the head of the embryo on the uterus exterior, and a very brief (1 ms) voltage pulse (65 V) was discharged across the electrodes. In order to specifically target the developing hippocampus and cortex, the paddles were rotated across the top of the head with the positive electrode placed opposite the injected side, as previously described (Navarro-Quiroga et al., 2007; Pacary et al., 2012). The

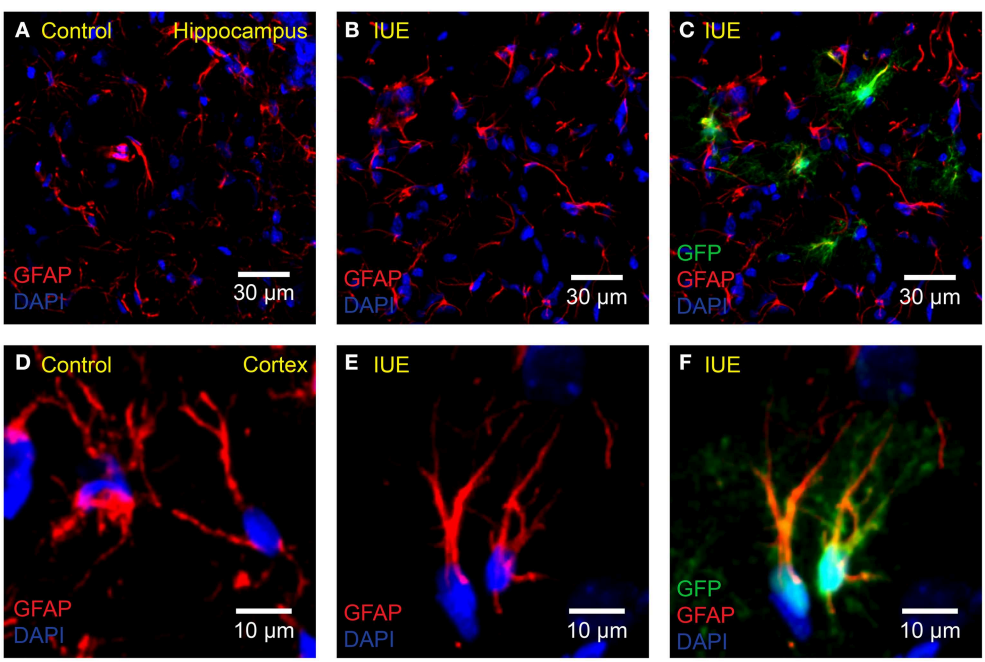

FIGURE 2 | No apparent astrogliosis following *IUE*. Confocal imaging of astrocyte GFAP in the **(A–C)** hippocampus or **(D–F)** cortex of **(A,D)** unelectroporated controls or **(B,C,E,F)** following *IUE* of CAG-GFP-IRES-Neo (green). For better comparison with **(A)**, **(B)** displays only the red (anti-GFAP) and blue (DAPI) channels of **(C)**. Likewise, for comparison with **(D)**, **(E)** displays the anti-GFAP and DAPI channels of **(F)**. Transfected astrocytes are partially yellow/orange. There were no striking qualitative differences in GFAP expression and morphology between age-matched (P18) control and *IUE* groups, even in transfected astrocytes.

embryos within the uterus were returned to the body cavity and the incision closed with sterile Ethicon silk suture 4.0 (Ethicon, Somerville, NJ, USA). Animals were weaned from the mother on P21 and males and females housed separately until used for experiments.

Acute Brain Slice Preparation

Brain slices were prepared using established techniques (Netoff et al., 2005; Kispersky et al., 2012; Smeal et al., 2012). Briefly, electroporated rats of either sex were deeply anesthetized using isoflurane and decapitated at various time points spanning P34 through P127. Brains were rapidly dissected and placed in ice-cold (4°C) oxygenated sucrose Ringer's solution containing (in mM): 200 sucrose, 26 $NaHCO_3$, 10 D-glucose, 3 KCl, 3 MgCl, 1.4 NaH_2PO_4, and 1 $CaCl_2$. The pH was maintained at 7.4 by saturation with 95% O_2–5% CO_2. A vibrating microtome, (VT1200; Leica, Wetzlar, Germany) with the bath chilled to 1.5°C (Minichiller; Huber, Offenburg, Germany), was used to prepare 400 μm thick coronal slices in oxygenated sucrose Ringer's solution (4°C). Following sectioning, slices were transferred to a holding chamber filled with oxygenated artificial cerebrospinal fluid (ACSF; room temperature) containing (in mM): 126 NaCl, 26 $NaHCO_3$, 10 D-glucose, 3 KCl, 2 MgCl, 2 $CaCl_2$, and 1.4 NaH_2PO_4 for at least 1 h. During imaging, slices were placed in a heated (32°C) immersion style recording chamber (Warner Instruments, Hamden, CT, USA) mounted on a microscope stage and perfused with ACSF.

Organotypic Slice Cultures

Hippocampal OSCs were prepared from P10 rats as previously described (Alex et al., 2011). Slices (400 μm) were maintained on membrane inserts (Millicell CM, Millipore, Bedford, MA, USA) in a 6 well plate (4 slices per insert/well), containing 1 ml of culture medium, until imaging experiments were conducted 7–10 days later. Slices were imaged in oxygenated ACSF containing (in mM): 126 NaCl, 26 $NaHCO_3$, 10 D-glucose, 3 KCl, 2 $CaCl_2$, 2 MgCl, and 1.4 NaH_2PO_4.

Two-Photon Imaging

Two-photon imaging was performed using a custom-built two-photon microscope (Lillis et al., 2008; Smeal et al., 2012) assembled around a mode-locked Ti:Sapphire laser source emitting 140 fs pulses at an 80 MHz repetition rate with a wavelength adjustable from 690 to 1040 nm (Chameleon Ultra I; Coherent, Santa Clara, CA, USA). Laser emission wavelengths of 940–950 nm were used to excite GCaMP (Tian et al., 2009; Chen et al., 2013) or 1040 nm to excite tdTomato (Drobizhev et al., 2009, 2011). In this setup, laser power is attenuated using an electro-optic modulator (ConOptics, Danbury, CT, USA) and scanning is accomplished using x-y galvanometer-mounted mirrors (GSI Lumonics, Billerica, MA, USA) controlled by custom LabVIEW software (Lillis et al., 2008) and a PCI-6221 data acquisition board (National Instruments, Austin, TX, USA). Full field of view images were acquired with an x-y raster scan. We used 20 × 0.95 NA or 60 × 0.9 NA objectives (Olympus, Tokyo, Japan). Emitted photons were bandpass filtered (Semrock, Rochester, NY, USA) at (peak/bandwidth): 525/50 nm (GCaMP), 593/46 nm (tdTomato) and collected by a wide band (300-650 nm) and low noise photomultiplier tube (H7360-01; Hamamatsu, Hamamatsu City, Japan). To avoid the "dead zone" on the surface of brain slices, only cells in focal planes at least 30 μm beneath the surface of the slice were monitored.

Event Selection and Data Analysis

Image analysis and automatic time-series event detection were accomplished with custom-written MATLAB (MathWorks, Natick, MA, USA) scripts. Regions of interest (ROIs) were manually selected from movies displaying the change in fluorescence of each pixel at each time point normalized by the mean fluorescence of the noise floor ($\Delta F/F_0$). The noise floor was defined for each pixel as all fluorescence intensity values within two standard deviations of the mean signal. All observable transfected cell somas were analyzed regardless of the presence of spontaneous events. Cell process ROIs were defined as larger than 1 μm^2 with a maximum peak $\Delta F/F_0$ greater than double the standard deviation of the noise floor of the pooled data ($2^*\sigma = 45\%\ \Delta F/F_0$). Each ROI was modified to include only highly correlated pixels ($r > 0.7$). There were no overlapping ROIs. $\Delta F/F_0$ time-series plots were generated for each ROI by averaging $\Delta F/F_0$ values of each pixel at each time point. The event threshold was set to $2^*\sigma$. Events that occurred closely in time were treated as a single event. Events were merged if the minimum $\Delta F/F_0$ value between the event peaks was greater than half of the minimum peak $\Delta F/F_0$ of the two events. The full-width at half-maximum (FWHM) was calculated by measuring the width of the peak at half of the value of the peak $\Delta F/F_0$. FWHM is expressed in seconds (s).

Statistics

Statistical analyses were performed with GraphPad Prism 6 (GraphPad Software, La Jolla, CA, USA). We used Student's *t*-test to compare means of normally distributed data, as determined by the Shapiro–Wilk normality test. Otherwise, the following non-parametric tests were used: the Kolmogorov–Smirnov test (KS-test) to compare cumulative distributions, the Mann–Whitney U test (MWU-test) to compare means; and the Kruskal-Wallis One-Way analysis of variance (KW-ANOVA) with Dunn's *post-hoc* test (Dunn's test) to compare medians between several groups. Statistics are presented as mean ± standard deviation unless otherwise noted. A significance level of $p < 0.05$ was used.

Results

A Plasmid Toolkit for Recording Calcium Transients in the Rat Brain

Following *IUE*, transfected radial glia precursor cells in the subventricular wall of the lateral ventricle migrate, divide and differentiate into neurons, astrocytes, and oligodendrocytes throughout the cortex, hippocampus, and/or other brain regions (Tabata and Nakajima, 2001; Bai et al., 2003; Nakahira and Yuasa, 2005). Mammalian cells lack the ability to replicate plasmid DNA. Therefore, cells that continue to divide at a high rate throughout development, including astrocytes, eventually dilute the transfected plasmid and fail to express the delivered transgene. Transposon systems, such as *piggyBac*, have been exploited

for effective transgene-integration into genomic DNA, resulting in high expression in astrocytes (Yoshida et al., 2010; Chen and LoTurco, 2012; Chen et al., 2014). In the presence of *piggyBac* transposase, single copies of ITR-flanked DNA are cut out of transfected plasmid DNA and inserted into random "TTAA" sites in diverse locations throughout genomic DNA (Fraser et al., 1995, 1996; Lorenzen et al., 2003) preferring transcriptionally active regions (Ding et al., 2005). Transgene-integration mediated by *piggyBac* has adopted the form of a paired plasmid co-transfection scheme consisting of a donor plasmid carrying an ITR-flanked transgene and a helper plasmid carrying *piggyBac* transposase which is not flanked by ITRs, and therefore does not integrate into genomic DNA (Lorenzen et al., 2003; Ding et al., 2005; Chen and LoTurco, 2012; Chen et al., 2014). A cell must receive both the donor plasmid and helper plasmid in order for the ITR-flanked transgene to integrate with high efficiency. We used *piggyBac* to stably express GCaMP (3, 6s, or 6f) throughout each transfected progenitor lineage including astrocyte and neuron populations.

GCaMP expression following *IUE* can be sparse and baseline fluorescence is dim due to low concentrations of unchelated calcium in resting cells. In order to facilitate detection of transfected cells at baseline activity levels, we incorporated tdTomato, a bright red fluorescent protein that localizes to cytosol and is readily detectable regardless of cell activity state. GCaMP and tdTomato were co-expressed in the same cells via IRES. We assembled a set of donor plasmids of the form ITR-CAG-GCaMP-IRES-tdTomato-ITR (**Figure 1B**; **Table 1**). Expression of *piggyBac* transposase was provided by the helper plasmid pPBase (**Figure 1A**; Wu et al., 2007).

Standard GCaMP localizes to cytosol and may not be present in cellular processes where much of the synaptic activity-related calcium transients occur in astrocytes and neurons. The N-terminus of Lck, a lymphocyte-specific, membrane-spanning tyrosine kinase, has been shown to successfully target GCaMP2 and GCaMP3 to the plasma membrane and processes of astrocytes in culture and *in vivo* using viral transfection (Shigetomi et al., 2010a,b, 2013). We created a plasma-membrane targeted version of each plasmid (**Figure 1B**; **Table 1**). The N-terminus of GCaMP, and not tdTomato, was tagged with the N-terminus of Lck (**Figure 1B**). Therefore, most of the cytosolic compartment becomes filled with tdTomato and the borders of the cell can be readily detected. Each plasmid was independently co-electroporated with pPBase. All of the plasmid versions that we have constructed and submitted to Addgene are shown in **Table 1**.

TABLE 1 | A full toolset of plasmid variants for *IUE*.

Plasmid name	ITR-flanked cassette	Subcellular target	Addgene #
pPBC-LG6f	Lck-GCaMP6f	Plasma membrane	62808
pPBC-LG6s	Lck-GCaMP6s	Plasma membrane	62809
pPBC-LG6f-tdT	Lck-GCaMP6f-IRES-tdTomato	Plasma membrane	62807
pPBC-LG3-tdT	Lck-GCaMP3-IRES-tdTomato	Plasma membrane	62810
pPBC-G6f	GCaMP6f	Cytosol	62811
pPBC-G6s	GCaMP6s	Cytosol	62812
pPBC-G6f-tdT	GCaMP6f-IRES-tdTomato	Cytosol	62813
pPBC-G3-tdT	GCaMP3-IRES-tdTomato	Cytosol	62814

All piggyBac ITR-flanked cassettes are driven by the CAG promoter. Plasmids are co-electroporated with a piggyBac transposase-expressing plasmid (Wu et al., 2007).

In Utero Electroporation Robustly Labels Many Brain Regions

IUE can be used to express transgenes in astrocytes and neurons in various regions of the brain. Fluorescent proteins, such as GFP and RFP, have previously been expressed in the cortex and hippocampus of mice (Nakahira and Yuasa, 2005; Navarro-Quiroga et al., 2007; Yoshida et al., 2010; Pacary et al., 2012) and rats (Nakamura et al., 2006; Rosen et al., 2007) following *IUE*, allowing for lineage tracing of transfected cells. We electroporated pPBC-GFP and pPBase between gestational days 13.5–14.5 and used immunohistochemistry and confocal imaging to detect brain region and cell-type expression of GFP. It was sometimes difficult to identify electroporated astrocytes by overlap of the thin intermediate filament GFAP with cytosolic GFP. Therefore, in a subset of slices, we also labeled astrocyte-specific cytosol-localized (similar to GFP) Aldh1L1 to confirm astrocyte transfection (Lovatt et al., 2007; Cahoy et al., 2008; Yang et al., 2011). Electroporated neurons were identified by morphology. We successfully targeted pPBC-GFP to astrocytes and neurons throughout the brain including the hippocampus, dentate gyrus, nucleus accumbens, cortex, thalamus (**Figures 1C–I**), or striatum (not shown). Using the specific electroporation approach described in the Materials and Methods Section, the same patterns of astrocytic and neuronal transfection in the hippocampus and cortex could be reproduced between animals (**Figure 1C**). As expected, because they do not derive from lateral ventricle precursor cells, we did not observe any microglial transfection. We, likewise, electroporated the pPB-CAG-GCaMP3-IRES-tdTomato plasmid (**Supplementary Movie 1**). Transfected cells were readily identified with tdTomato (**Figure 1H**). Co-expression of GCaMP and tdTomato was confirmed in all transfected cells observed (**Figure 1I**). After optimizing the *IUE* technique for our laboratory, we can reliably electroporate the cortex and hippocampus of 80–100% of animals per litter.

No Overt Immune Response in the Brain Following *IUE*

Astrocytes respond to damage and immune activity by switching to a reactive state. This state, termed "reactive astrogliosis" is defined by increased GFAP expression, extended processes, and overlapping of astrocyte domains (Bushong et al., 2002; Oberheim et al., 2008). To test the possibility that *IUE* induces reactive astrogliosis, we compared GFAP expression in the cortex and hippocampus of pPBC-GFP-electroporated rats with unmanipulated age-matched controls (P18). We did not observe any signs of damage or reactive astrogliosis in either group. Astrocytes in both groups appeared normal, only had a few thin GFAP positive processes and did not overlap with neighboring astrocyte domains (Bushong et al., 2002). In addition, it is important to note that astrocytes located near transfected cells did not display a reactive morphology (**Figures 2A–F**).

In the healthy brain, resting microglia exhibit a "ramified" morphology defined by long thin dynamic processes that scan the local area around the stationary soma (Davalos et al., 2005; Nimmerjahn et al., 2005). Following activation, microglia convert to a reactive state, delineated by retraction of processes, and adoption of an "amoeboid" shape. We did not detect overt signs of microglial activation with Iba1 staining (**Figures 3A–I**) of cortical and hippocampal tissue obtained from GFP-transfected P18 rats ($n = 4$ *IUE* animals and $n = 3$ controls). Microglia in the *IUE* brain and age-matched controls retained a resting ramified morphology suggesting that there was no major neuroimmune response to the *IUE* procedure.

Robust Spontaneous Calcium Activity in Organotypic Slice Cultures

Hippocampal OSCs provide an *in vitro* preparation which can be used for chronic studies of intact neural circuits (Khalilov et al., 1997), albeit in the relatively immature brain. OSCs have been used as an *in vitro* model of epileptogenesis (Dyhrfjeld-Johnsen et al., 2010). Following slicing-induced deafferentiation, neuronal networks rearrange, and exhibit spontaneous epileptiform-like activity which can be visualized with calcium indicators (Sabolek et al., 2012). In order to test our plasmids in this system, we prepared OSCs from electroporated P10 rats and imaged astrocytic and neuronal calcium activity with Lck-GCaMP6f (pPBC-LG6f plasmid) 7–10 days later ($n = 3$ slice cultures).

Unlike the normal healthy morphology that was observed in GFP-transfected astrocytes in slices obtained from the mature rat brain (**Figures 1**, **2**), OSC astrocytes exhibited a reactive morphology and organization (**Figure 4A**; **Supplementary Movie 2**). We observed significant astrocytic domain overlap between adjacent astrocytes to the point where it was difficult to assign processes to a specific cell. The example in **Figure 4A** shows

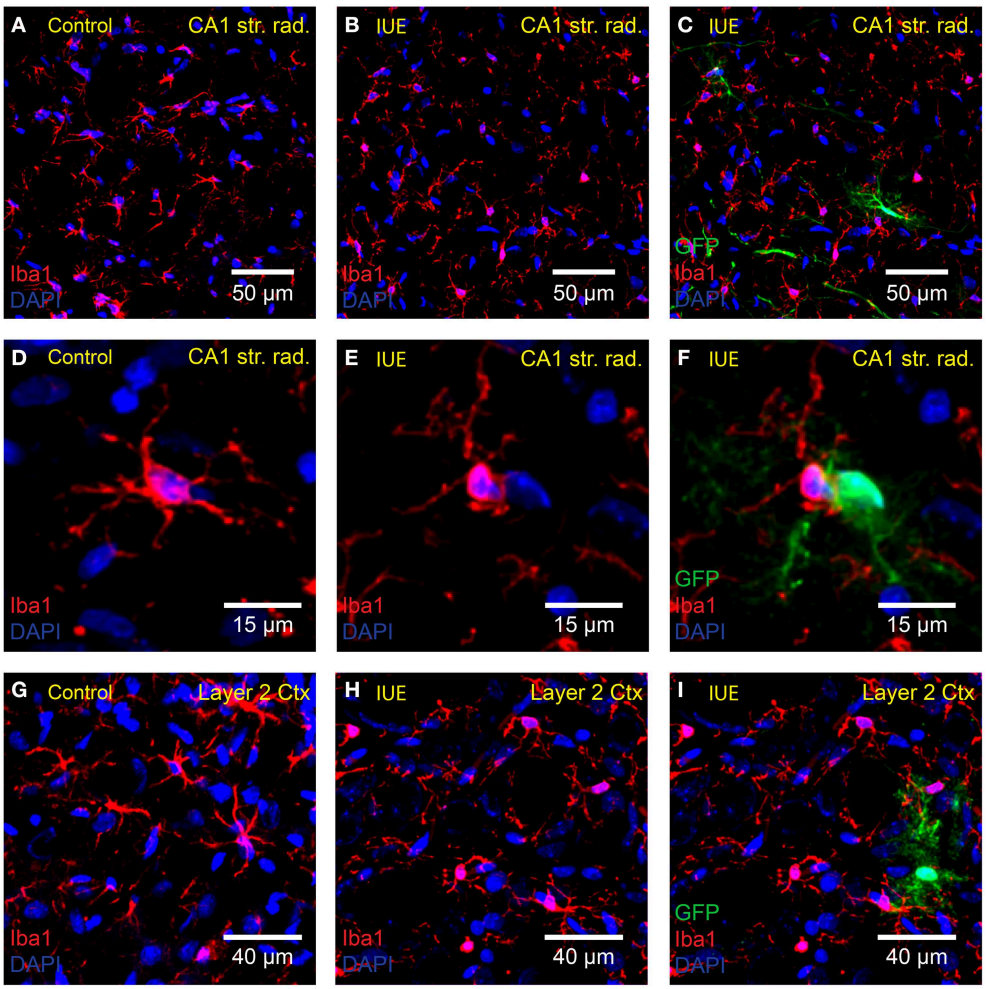

FIGURE 3 | Microglia are not transfected or overtly activated following *IUE*. Confocal imaging of anti-Iba1 (red) stained microglia in the **(A–F)** hippocampal CA1 stratum radiatum and **(G–I)** cortex layer 2 of **(A,D,G)** unelectroporated brains and **(B,C,E,F,H,I)** following *IUE* of CAG-GFP-IRES-Neo. The right-hand column displays images in the middle column overlaid with the green channel (GFP-transfected cells). **(C,F,I)** As expected, anti-Iba1 did not overlap with GFP. Iba1-positive cells near GFP-transfected cells did not appear to be activated. DAPI staining is shown in blue.

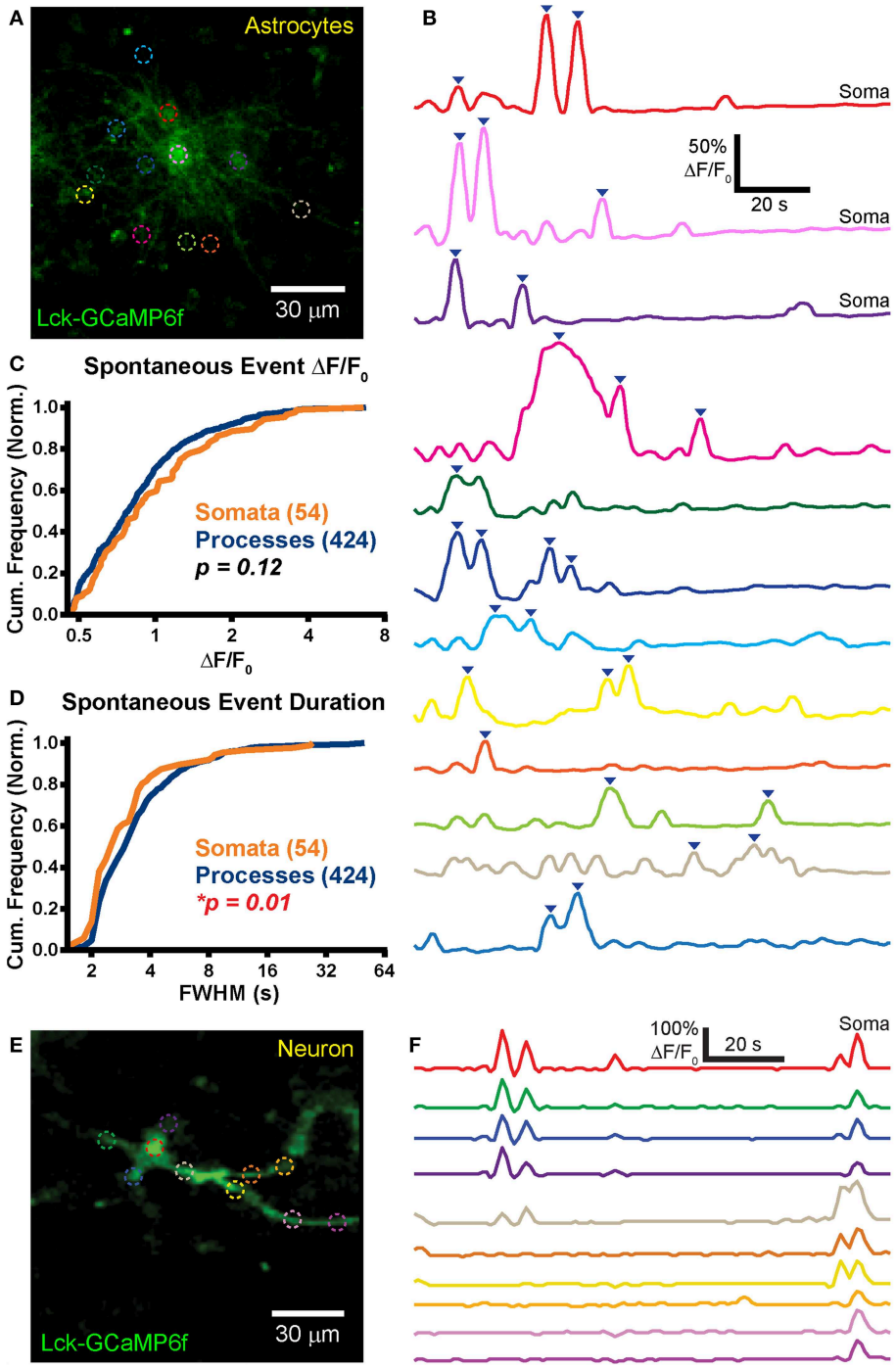

FIGURE 4 | Robust spontaneous transients are observed in astrocytic somas and processes in hippocampal organotypic slice cultures. (A) Example mean calcium activity projection image of astrocytes expressing Lck-GCaMP6f in a hippocampal organotypic slice culture. ROIs are denoted by dashed circles including three adjacent somas. **(B)** $\Delta F/F_0$ traces of ROIs shown in **(A)**. Line colors in **(B)** correspond to ROI colors in **(A)**. Inverted blue arrows mark peaks that reached threshold and were included as events for analysis. "Merged" events, which encompass two proximate peaks, were counted as a single long event (see dark pink and dark green ROIs). **(C)** A cumulative histogram displaying the relative frequency (event counts normalized by total events in each structure) of spontaneous event peak $\Delta F/F_0$ values. The number of total events in each structure is shown in parentheses next to the structure name. **(D)** A cumulative histogram displaying spontaneous event duration. Soma data is shown in orange and process data in blue. The distribution of each measurement was compared between somas and processes. The calculated *p-value* from a Kolmogorov–Smirnov test is shown in the plot. Red text denotes significance and black text denotes no significance detected at a level of $p < 0.05$. **(E)** Example mean calcium activity projection of a neuron expressing Lck-GCaMP6f. **(F)** $\Delta F/F_0$ traces corresponding to ROIs shown in **(E)**.

three putative astrocytes sharing the same domain. Astrocytic processes were also noticeably extended at these time points (**Supplementary Movie 2**). Morphology indicative of astrocyte reactivity in the hippocampus of OSCs was apparent.

Frequent spontaneous calcium activity was observed in both astrocytic somas ($f = 1.9 \pm 1.5$ events/ROI/min; $n = 54$ events in 20 somas; f, event frequency; ROI, region of interest) and processes ($f = 1.2 \pm 1.3$ events/ROI/min; $n = 424$ events in 168 ROIs). In stark contrast to our previously reported acute brain slice (ABS) data obtained from the GFAP-CreER; PC::G5-tdT mouse (Gee et al., 2014), spontaneous OSC somatic events were significantly more frequent than process events ($p = 0.002$; Student's t-test). In fact, we detected above-threshold calcium activity in all 20 OSC astrocytic somas selected for imaging [mean duration of an imaging session (T_{mean}) = 114 s/cell].

Large spontaneous astrocyte event peak $\Delta F/F_0$ values were measured for both somas ($\Delta F/F_0$ = 117 ± 102%) and processes ($\Delta F/F_0$ = 100 ± 73%). The distributions of OSC event peak $\Delta F/F_0$ did not differ significantly between the cellular compartments (**Figure 4C**; $p = 0.12$, $D = 0.14$, KS-test) nor did the means ($p = 0.26$, MWU-test). Event duration was also measured for all spontaneous events in somas (FWHM = 3.2 ± 2 s) and in processes (FWHM = 4.3 ± 4.8 s). The event duration distribution of somas was left-shifted relative to that of processes (**Figure 4D**; $p = 0.01$, $D = 0.23$, KS-test) and the mean event duration was larger in processes than in somas ($p = 0.001$, MWU-test).

Spontaneous events were also observed in OSC neurons (**Figure 4E**; $n = 5$). Activity in different ROIs within a single cell appeared to be highly correlated (**Figure 4F**), reflecting action potential-induced intracellular calcium signaling. We detected no difference in spontaneous neuronal soma ($f = 1.4 \pm 0.6$ events/soma/min; $n = 5$ somas) and process ($f = 2 \pm 2.1$ events/ROI/min; $n = 16$ ROIs) event frequency ($p = 0.53$, Student's t-test).

Frequent Spontaneous Events in Cortical Astrocytic Processes of Young Animals

ABS preparations are relatively quiet with regard to spontaneous neuronal activity. This is likely due to the acute removal of synaptic input to neurons within the slice. Although spontaneous neuronal activity is infrequent in ABS, astrocytes display frequent spontaneous calcium events. We, therefore, employed the pPBC-LG6f plasmid for detecting spontaneous cortical astrocytic activity in ABS ($n = 6$ slices) obtained from young mature rat brains (P34-P70; "young" group). ABS astrocytes did not exhibit the reactive characteristics observed in OSCs. Cortical astrocytic processes were relatively short and did not overlap with adjacent astrocytic processes. It was usually straightforward to correctly assign a process to the correct soma in ABS (**Figure 5A**; **Supplementary Movie 3**).

In line with our previous reported data collected in mouse ABS (Gee et al., 2014) and in contrast to the OSC data reported above, we observed very few spontaneous calcium events in astrocytic somas ($f = 0.8 \pm 1.2$ events/soma/min; $n = 11$ events in 9 somas). Only 4 of 9 imaged somas displayed spontaneous events (T_{mean} = 123 s). The pooled data soma event frequency, which takes into account the imaging duration of soma ROIs with no events, was 0.5 events/soma/min. Spontaneous process event frequency (**Figure 5B**; $f = 3 \pm 1.8$ events/ROI/min, $n = 2058$ events in 287 ROIs) was significantly higher than in somas ($p < 0.0001$; Student's t-test).

The infrequent somatic events that we did detect tended to be small ($\Delta F/F_0$ = 71 ± 18%) whereas process events appeared much larger ($\Delta F/F_0 = 120 \pm 88\%$). The $\Delta F/F_0$ distribution of somatic events was left shifted relative to process events (**Figure 5C**; $p = 0.04$, $D = 0.42$, KS-test) but the difference in means failed to reach significance ($p = 0.07$, MWU-test).

Somatic (FWHM = 2.6 ± 1.1 s) and process event duration (FWHM = 2 ± 1.3 s) were also measured. The event duration distribution of somas was right-shifted relative to that of processes (**Figure 5D**; $p = 0.01$, $D = 0.50$, KS-test) and mean somatic event duration was longer than in processes ($p = 0.01$, MWU-test). We did not observe supra-threshold spontaneous activity in neurons.

Stable and Functional Expression of GCaMP6f in the Adult Rat Cortex

For technical reasons, most published calcium imaging data have been collected from perinatal or adolescent animals. Because of the vast differences in cellular function, connectivity and gene expression between the young and adult brain (Sun et al., 2013), it is important to develop methods for recording activity in tissue obtained from animals of a wide range of ages (Yuste and Katz, 1991; Schwartz et al., 1998; Peterlin et al., 2000; Reeves et al., 2011). To test GCaMP6f function and expression stability in the rat brain following *IUE*, we prepared ABS from older animals (P125-P127; "old" group) electroporated with the pPBC-LG6f plasmid during gestation.

We observed expression and strong Lck-GCaMP6f signal in the adult rat brain ($n = 2$ animals; **Figures 6A,B**). Similar to ABS obtained from younger animals, spontaneous somatic calcium events in astrocytes were infrequent in ABS prepared from older animals ($f = 0.8 \pm 3.3$ events/soma/min; $n = 12$ events in 17 somas; T_{mean} = 141 s/cell) but significantly higher in processes ($f = 2.5 \pm 2.8$ events/ROI/min; $n = 1090$ events in 293 ROIs; $p = 0.04$, Student's t-test). Interestingly, only 2 of 17 imaged somas displayed activity above the $\Delta F/F_0$ threshold and 11 of the 12 total events were observed in a single soma. The peak $\Delta F/F_0$ values were 88 ± 42% in somas and 94 ± 52% in processes. We detected no difference between the peak $\Delta F/F_0$ distributions (**Figure 6C**; $p = 0.92$, $D = 0.16$, KS-test) or means ($p = 0.90$, MWU-test) in somas and processes. We also did not detect any statistical differences between the distributions (**Figure 6D**; $p = 0.13$, $D = 0.34$, KS-test) or means of event FWHM ($p = 0.06$, MWU-test) in somas (FWHM = 2.1 ± 2 s/event) and processes (FWHM = 4.1 ± 6.2 s/event). Similar to the younger ABS group, we also did not observe supra-threshold spontaneous activity in neurons.

Differences in Astrocyte Spontaneous Event Frequency across Preparations

The spontaneous astrocyte event rate for each ROI (events/ROI/min) in the three groups (young, old and OSC) was compared. A significant difference in the median somatic event

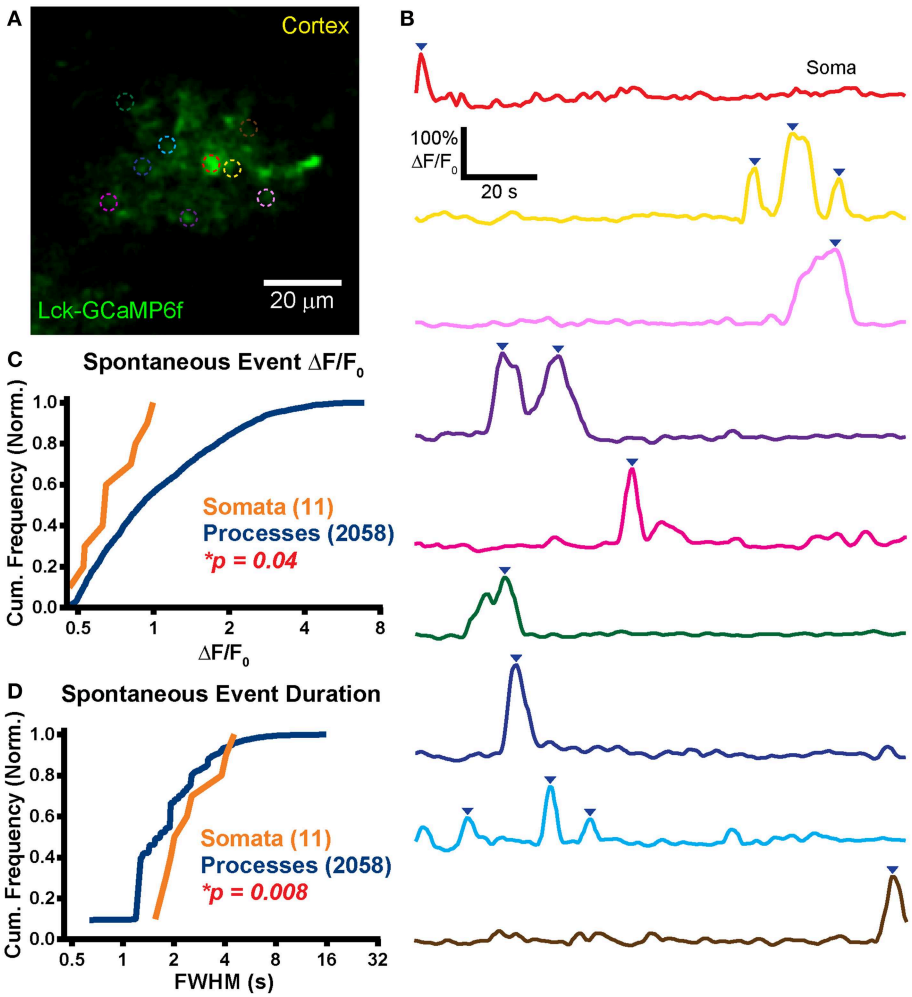

FIGURE 5 | Large spontaneous events in astrocytic processes but not somas. (A) Example mean calcium activity projection image of a cortical astrocyte expressing Lck-GCaMP6f in an acute brain slice obtained from a P34 rat. As in **Figure 4**, ROIs are denoted by dashed circles. **(B)** $\Delta F/F_0$ traces of ROIs shown in **(A)**. Line colors in **(B)** correspond to dashed circle colors in **(A)**. Inverted blue arrows mark peaks that reached threshold and were included as events for analysis. "Merged" events were counted as a single long event (see green ROI). **(C)** A cumulative histogram displaying the relative frequency (event counts normalized by total events in each structure) of spontaneous event peak $\Delta F/F_0$ values. The total events in each structure is shown in parentheses next to the structure name. **(D)** A cumulative histogram displaying spontaneous event duration. Soma data is shown in orange and process data in blue. The distribution of each measurement was compared between somas and processes. The calculated *p-value* from a Kolmogorov–Smirnov test is shown in each plot. Red text denotes significance and black text denotes no significance detected at a level of $p < 0.05$.

rate was detected between groups (reported as median (minimum: maximum) events/soma/min; young: 0 (0: 3.7), $n = 11$ events in 9 somas; old: 0 (0: 13.6), $n = 12$ events in 17 somas; OSC: 1.19 (0.5: 5.2), $n = 54$ events in 20 somas; $p < 0.0001$, KW-ANOVA). OSC somas exhibited a higher spontaneous event frequency than either of the two ABS groups (**Figure 7A**, left; OSC > young, $p = 0.03$; OSC > old, $p < 0.0001$; Dunn's post-test) but no difference was detected between the two ABS groups (young vs. old, $p = 0.55$; Dunn's post-test). Differences in the median process event rate were detected between the groups [young: 2.8 (0.1: 12.1) events/ROI/min, $n = 2058$ events in 287 ROIs; old: 1.5 (0.3: 18.5), $n = 1090$ events in 288 ROIs; OSC: 0.6 (0.2: 7.2), $n = 424$ events in 167 ROIs; $p < 0.0001$, KW-ANOVA]. Inter-group comparisons revealed significant differences in the medians between all groups (**Figure 7A**, right; young > OSC, $p < 0.0001$; old > OSC, $p < 0.0001$; young > old, $p < 0.0001$; Dunn's post-test).

The spontaneous event rate per cell in each group was also compared. All cells which could be distinguished as independent cells were included whether or not we could visualize the soma. A significant difference was detected in the whole astrocyte (soma and processes) event rate between groups [**Figure 7B**; young: 67.4 (9.6: 303.3) events/cell/min, $n = 2069$ events in 9 cells; old: 14.6 (0.8: 260.5), $n = 1102$ events in 26 cells; OSC: 3.1 (0.5: 57), $n = 478$ events in 45 cells; $p < 0.0001$, KW-ANOVA]. The young group astrocytes displayed much higher spontaneous

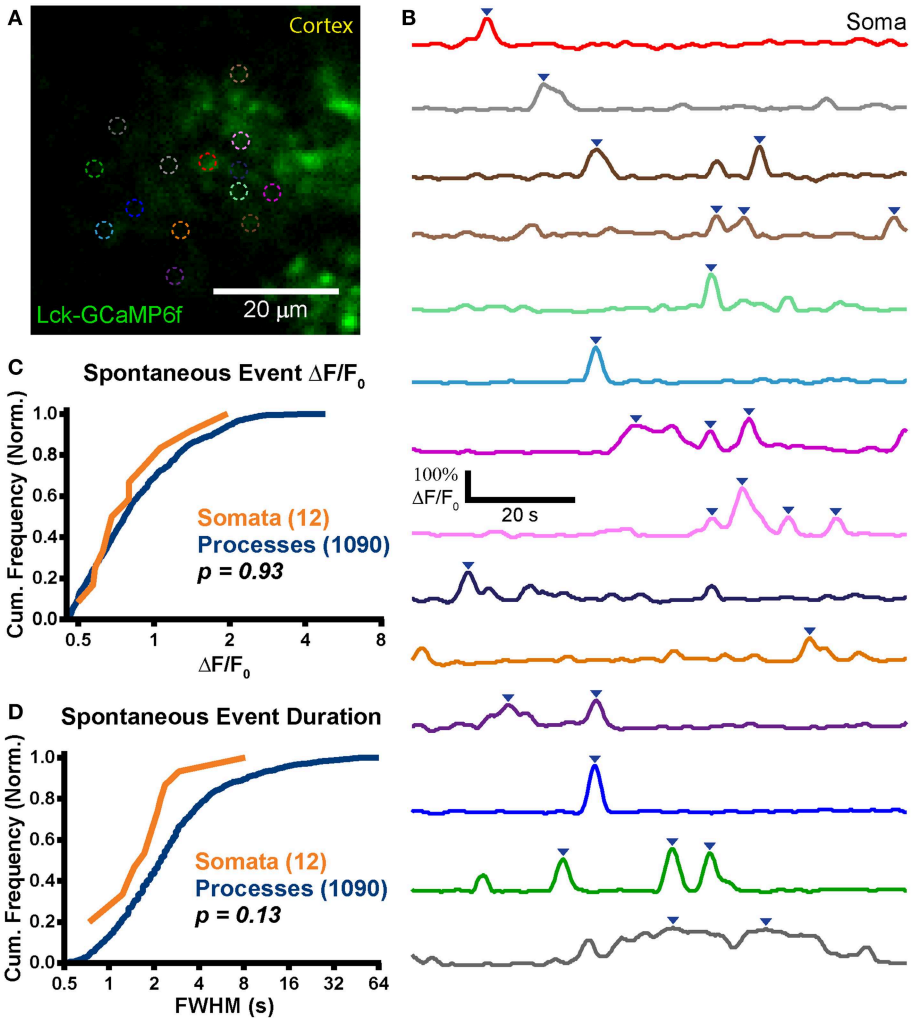

FIGURE 6 | Stable expression in adult animals. (A) Example mean calcium activity projection image of a cortical astrocyte expressing Lck-GCaMP6f in an acute brain slice obtained from a P125 rat. As in **Figures 4**, **5**, ROIs are denoted by dashed circles. **(B)** $\Delta F/F_0$ traces of ROIs shown in **(A)**. Line colors in **(B)** correspond to dashed circle colors in **(A)**. Inverted blue arrows mark peaks that reached threshold and were included as events for analysis. "Merged" events were counted as a single long event (see dark gray ROI). **(C)** A cumulative histogram displaying the relative frequency (event counts normalized by total events in each structure) of spontaneous event peak $\Delta F/F_0$ values. The total events in each structure is shown in parentheses next to the structure name. **(D)** A cumulative histogram displaying spontaneous event duration. Soma data is shown in orange and process data in blue. The distribution of each measurement was compared between somas and processes. The calculated *p-value* from a Kolmogorov–Smirnov test is shown in the plot. Red text denotes significance and black text denotes no significance detected at a level of $p < 0.05$.

event frequency than either the old or OSC groups while the OSC group displayed lower spontaneous event frequency than the ABS groups (young > OSC, $p < 0.0001$; old > OSC, $p = 0.005$; young vs. old, $p = 0.03$; Dunn's post-test).

Discussion

We have demonstrated the suitability of our plasmid toolset for stable and functional expression of GECIs in the rat brain at various ages, in different brain regions, in different cell types, and in different preparations for imaging without the use of viral vectors. Our toolset of novel genetic constructs provides flexibility for the user, who can choose among three different versions of GCaMP (3, 6s, or 6f), with or without tdTomato co-expression and targeting to either the cytosol or plasma membrane (**Table 1**). *IUE* has previously been described as a method of tracking migration of neuron progenitors from the lateral ventricles to cortex (Bai et al., 2003) or to hippocampus (Navarro-Quiroga et al., 2007) and has also been used for GECI delivery (Tian et al., 2009). Transposon systems have previously been combined with *IUE* to stably express transgenes in astrocytes, as well as neurons, until at least P27 (Yoshida et al., 2010; Chen and LoTurco, 2012). We have, on the other hand, demonstrated that the combination of *IUE* with *piggyBac* results in stable astrocytic transgene expression well into adulthood (at least P127), comparable to what has been reported in neurons (Navarro-Quiroga et al., 2007).

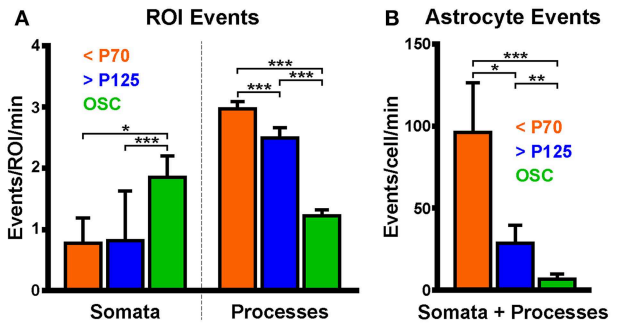

FIGURE 7 | Astrocytic process event frequency varies between preparations. (A) Spontaneous astrocyte event frequency per ROI in somas and processes. Data were separated into three groups according to which preparation or age of rat was used. **(B)** Spontaneous astrocyte event frequency per cell. Colored bars correspond to data collected from acute brain slices obtained from young (orange; <P70) or old (blue, >P125) animals or from hippocampal organotypic slice cultures (green; OSC). Plots display mean ± SEM. Kruskal-Wallis ANOVA using Dunn's *post-hoc* test was used to detect differences in the medians of each group. Significant differences between groups are denoted by $^{*}p < 0.05$, $^{**}p < 0.01$, and $^{***}p < 0.0001$.

Our toolset adds to the existing available tools via inclusion of updated versions of GCaMP and the option of the fluorescent protein, tdTomato. In order to characterize the plasmids and to provide an example of their utility, we measured astrocytic and neuronal spontaneous calcium activity in two different preparations including in brain slices prepared from either young or old adult animals.

The role of spontaneous astrocytic activity is not well-understood but likely reflects changes in the local environment with respect to pH, temperature, oxygenation, immunological processes, and neuronal activity in addition to many other parameters (Wang et al., 2006a,b; Schipke et al., 2008; Haustein et al., 2014). Our results, while only preliminary, are nonetheless intriguing. Interestingly, we observed frequent somatic activity in OSCs and only rare events in both ABS groups. Similarly, we observed supra-threshold neuronal events in OSCs and not in ABS, indicating a possible relationship between spontaneous astrocytic somatic events and local neuronal-network activity. In contrast, astrocytic process events were much more frequent than somatic events in the ABS groups in which we did not observe significant neuronal activity, suggesting that process events may be relatively neuronal-activity independent. Qualitatively, OSC events encompassed a larger cellular volume than events in ABS, which were temporally shorter. Activity within and between cells in OSCs appeared to be more highly correlated than in ABS, possibly reflecting oscillating activity of OSC neuronal networks (**Supplementary Movie 2**). These results will need to be explored in more depth in future studies of spontaneous calcium activity in astrocytic-neuronal networks. However, they demonstrate the types of information which can be gleaned from combining our plasmids with *IUE* for imaging activity in the rat brain.

IUE is a practical and flexible method for delivering GECIs to the rat brain. By altering any of several parameters, such as timing of the *IUE* procedure with respect to embryonic development and spatial paddle placement with respect to the developing brain, different regions and cell types can be targeted (LoTurco et al., 2009; Yoshida et al., 2010). Once mastered, *IUE* can be performed expeditiously and provide a continuous supply of rats, in a timely manner, expressing GECIs or other genetically encoded tools for experiments in specific regions of the brain. In our hands, the cortex and hippocampus can be reliably targeted in 80–100% of animals in each litter.

Delivery of GECIs via *IUE* exhibits several advantages over viral-based methods. First, and perhaps most importantly, the plasmids we describe here are too large to be delivered via adeno-associated viruses. For comparison, it has been demonstrated that *piggyBac* can transpose elements up to 100 kb (Li et al., 2011b). Second, although both *IUE* and viral-based methods require invasive injections, the timing of these injections is likely important with regard to consequential inflammation and tissue damage. *IUE* injections are performed when the lateral ventricles are located superficially in the brain. Thus, only a minimal amount of tissue is disturbed by the injection. Third, the embryonic brain is much more plastic than the mature brain and so healing potential is presumably more favorable with *IUE*. Therefore, *IUE* injections likely cause less tissue damage than post-natal AAV injections. Fourth, whereas expression levels via *IUE* remain stable for months, transfection with viruses can lead to expression that is so high as to be toxic (Howard et al., 2008). Fifth, cloning for *IUE* is faster than for viruses and involves minimal biosafety concerns. Finally, in experiments of animal models of neurological disorders such as epilepsy, wherein inflammation is a critical component of the pathophysiology, repeated injections into adult tissue of viral vectors may confound interpretations, as the very act of physical injections can induce local inflammatory responses. Thus, performing *IUE* weeks to months prior to the experiments in question may be advantageous, especially as work presented here has demonstrated that there are no overt signs of inflammation in or near transfected cells.

However, there are also several drawbacks to the *IUE* technique. First, targeting and expression of plasmids is very sensitive to the injected plasmid concentration, timing of electroporation, and the position of paddles with respect to the brain (Navarro-Quiroga et al., 2007; Yoshida et al., 2010). Second, while astrocytes and neurons are readily transfected via this approach, *IUE* of lateral ventricular precursors will not transfect microglia, which are derived from hematopoietic stem cells. Third, it is difficult to confirm successful transfection following *IUE* which emphasizes the importance of empirically determining precise plasmid concentration, timing of *IUE* and paddle placement in order to replicate expression patterns.

The ability to target GECIs to genetically defined cells and subcellular compartments grants the *IUE* technique an advantage over bulk loading of synthetic dyes into brain tissue. Cre-lox technology has been integrated into plasmid systems and cell-type specific promoters have been used to drive transgene expression (Matsuda and Cepko, 2007). As has been demonstrated with Lck, GECIs can be targeted to specific subcellular compartments for recording of calcium activity in precisely defined regions of a cell (Shigetomi et al., 2010a). This allows for measurement of many

different types of calcium activity which may not be accessible with synthetic dyes. Other N-terminal tags already exist that could conceivably be incorporated into these constructs as well (Li et al., 2011a).

Because integration of new reporters of cellular activity following *IUE* is only limited by the time required for cloning plasmid DNA, many reporter plasmids can be generated and expressed expeditiously. Other types of genetically encoded indicators, such as red-shifted calcium indicators, sypHTomato, and voltage sensitive fluorophores could readily be incorporated to expand the *IUE* toolset (Kralj et al., 2012; Li and Tsien, 2012; Wu et al., 2013). However, this toolset, as described, should contribute to the advancement of our understanding of astrocytic and neuronal activity at many spatial scales in the young or adult rat brain.

Author Contributions

JG, PT, KW, and JW planned and oversaw the project; JG and PT designed the plasmids; JG, SM, SP, and CC built the plasmids; MG and KF performed surgeries; MT, JG, and KF performed immunohistochemistry and confocal imaging; JG, MG, RS, and ME performed two-photon imaging; JG performed data analysis and wrote the manuscript with editing and additional writing from JW, KW, PT, SP, MT, and MG; JW, KW, PT, and MC provided resources; All authors proofread the manuscript.

Acknowledgments

We would like to thank the following people: Joseph LoTurco and Fuyi Chen for invaluable discussions about *in utero* electroporation; Lara Carroll for sharing the IRES-tdTomato construct; Sen Wu, Simon Titen, Eric Peden, Ben Xu, Hyung-song Nam, Matt Hockin, and Joan Shuhua for advice on cloning; E. Jill Dahle, Nathan A. Smith, Jay R. Vargas, Zhenmei Lu, and Kyle P. Lillis for technical assistance. This work was funded by the Epilepsy Foundation Predoctoral Research Training Fellowship (JG), NIH Training Grant T32 NS076067 (MG), the University of Utah Seed Grant Program (PT, KW, JW, and MC), NIH R21 OD016562 (PT) and the Ben B and Iris M Margolis Foundation Award, NIH RC1 NS069033 and NIH R01 NS078331 (KW and JW).

Supplementary Material

The Supplementary Material for this article can be found online at: http://www.frontiersin.org/journal/10.3389/fnmol.2015.00010/abstract

Supplementary Movie 1 | Spontaneous activity in an astrocyte expressing Lck-GCaMP3 and tdTomato in an acute brain slice. Frequent localized spontaneous calcium events can be observed in both the thick proximal and small distal processes. This image was captured using a 60× objective.

Supplementary Movie 2 | Spontaneous calcium activity in hippocampal astrocytes expressing Lck-GCaMP6f in an organotypic slice culture. OSCs were prepared from a P10 animal and imaged 1 week later. Calcium activity within and between astrocytes appeared to be highly correlated. Astrocytic domains were highly overlapped and astrocytic processes were extended, suggesting that these organotypic slice culture astrocytes were reactive. In this movie, several putative neuronal events can be observed. The highly active astrocytes in the center of the field are analyzed further in **Figures 4A,B**.

Supplementary Movie 3 | Spontaneous activity in a cortical astrocyte expressing Lck-GCaMP6f in an acute brain slice. Slices were obtained from a P34 animal. Astrocyte calcium events appeared more random and much smaller than those seen in organotypic slice cultures. Localized events with large fluorescence changes were frequently observed throughout astrocyte processes with only sparse somatic activity. We did not observe astrocytes with overlapping domains or extended processes, consistent with a non-reactive phenotype. Neuronal events (not shown in this movie) were very sparse with and small in amplitude. The upper right astrocyte in this movie is used as the example cell in **Figures 5A,B**.

References

Alex, A. B., Saunders, G. W., Dalpé-Charron, A., Reilly, C. A., and Wilcox, K. S. (2011). CGX-1007 prevents excitotoxic cell death via actions at multiple types of NMDA receptors. *Neurotoxicology* 32, 392–399. doi: 10.1016/j.neuro.2011.03.002

Bai, J., Ramos, R. L., Ackman, J. B., Thomas, A. M., Lee, R. V., and LoTurco, J. J. (2003). RNAi reveals doublecortin is required for radial migration in rat neocortex. *Nat. Neurosci.* 6, 1277–1283. doi: 10.1038/nn1153

Borrell, V., Yoshimura, Y., and Callaway, E. M. (2005). Targeted gene delivery to telencephalic inhibitory neurons by directional *in utero* electroporation. *J. Neurosci. Methods* 143, 151–158. doi: 10.1016/j.jneumeth.2004.09.027

Bushong, E. A., Martone, M. E., Jones, Y. Z., and Ellisman, M. H. (2002). Protoplasmic astrocytes in CA1 stratum radiatum occupy separate anatomical domains. *J. Neurosci.* 22, 183–192.

Cahoy, J. D., Emery, B., Kaushal, A., Foo, L. C., Zamanian, J. L., Christopherson, K. S., et al. (2008). A transcriptome database for astrocytes, neurons, and oligodendrocytes: a new resource for understanding brain development and function. *J. Neurosci.* 28, 264–278. doi: 10.1523/JNEUROSCI.4178-07.2008

Cary, L. C., Goebel, M., Corsaro, B. G., Wang, H. G., Rosen, E., and Fraser, M. J. (1989). Transposon mutagenesis of baculoviruses: analysis of *Trichoplusia ni* transposon IFP2 insertions within the FP-locus of nuclear polyhedrosis viruses. *Virology* 172, 156–169. doi: 10.1016/0042-6822(89)90117-7

Cenci, M. A., Whishaw, I. Q., and Schallert, T. (2002). Animal models of neurological deficits: how relevant is the rat? *Nat. Rev. Neurosci.* 3, 574–579. doi: 10.1038/nrn877

Chen, F., and LoTurco, J. (2012). A method for stable transgenesis of radial glia lineage in rat neocortex by piggyBac mediated transposition. *J. Neurosci. Methods* 207, 172–180. doi: 10.1016/j.jneumeth.2012.03.016

Chen, F., Maher, B. J., and LoTurco, J. J. (2014). PiggyBac transposon-mediated cellular transgenesis in mammalian forebrain by *in utero* electroporation. *Cold Spring Harb. Protoc.* 2014, pdb.prot073650. doi: 10.1101/pdb.prot073650

Chen, T.-W., Wardill, T. J., Sun, Y., Pulver, S. R., Renninger, S. L., Baohan, A., et al. (2013). Ultrasensitive fluorescent proteins for imaging neuronal activity. *Nature* 499, 295–300. doi: 10.1038/nature12354

Davalos, D., Grutzendler, J., Yang, G., Kim, J. V., Zuo, Y., Jung, S., et al. (2005). ATP mediates rapid microglial response to local brain injury *in vivo*. *Nat. Neurosci.* 8, 752–758. doi: 10.1038/nn1472

Ding, S. (2012). *In vivo* imaging of Ca2+ signaling in astrocytes using two-photon laser scanning fluorescent microscopy. *Methods Mol. Biol.* 814, 545–554. doi: 10.1007/978-1-61779-452-0_36

Ding, S., Wu, X., Li, G., Han, M., Zhuang, Y., and Xu, T. (2005). Efficient transposition of the piggyBac (PB) transposon in mammalian cells and mice. *Cell* 122, 473–483. doi: 10.1016/j.cell.2005.07.013

Drobizhev, M., Makarov, N. S., Tillo, S. E., Hughes, T. E., and Rebane, A. (2011). Two-photon absorption properties of fluorescent proteins. *Nat. Methods* 8, 393–399. doi: 10.1038/nmeth.1596

Drobizhev, M., Tillo, S., Makarov, N. S., Hughes, T. E., and Rebane, A. (2009). Absolute two-photon absorption spectra and two-photon brightness of orange and red fluorescent proteins. *J. Phys. Chem. B* 113, 855–859. doi: 10.1021/jp8087379

Dyhrfjeld-Johnsen, J., Berdichevsky, Y., Swiercz, W., Sabolek, H., and Staley, K. J. (2010). Interictal spikes precede ictal discharges in an organotypic hippocampal slice culture model of epileptogenesis. *J. Clin. Neurophysiol.* 27, 418–424. doi: 10.1097/WNP.0b013e3181fe0709

Fraser, M. J., Cary, L., Boonvisudhi, K., and Wang, H. G. (1995). Assay for movement of Lepidopteran transposon IFP2 in insect cells using a baculovirus genome as a target DNA. *Virology* 211, 397–407. doi: 10.1006/viro.1995.1422

Fraser, M. J., Ciszczon, T., Elick, T., and Bauser, C. (1996). Precise excision of TTAA-specific lepidopteran transposons piggyBac (IFP2) and tagalong (TFP3) from the baculovirus genome in cell lines from two species of Lepidoptera. *Insect Mol. Biol.* 5, 141–151. doi: 10.1111/j.1365-2583.1996.tb00048.x

Gee, J. M., Smith, N. A., Fernandez, F. R., Economo, M. N., Brunert, D., Rothermel, M., et al. (2014). Imaging activity in neurons and glia with a Polr2a-based and cre-dependent GCaMP5G-IRES-tdTomato reporter mouse. *Neuron* 83, 1058–1072. doi: 10.1016/j.neuron.2014.07.024

Grieger, J. C., and Samulski, R. J. (2005). Packaging capacity of adeno-associated virus serotypes: impact of larger genomes on infectivity and postentry steps. *J. Virol.* 79, 9933–9944. doi: 10.1128/JVI.79.15.9933-9944.2005

Haustein, M. D., Kracun, S., Lu, X.-H., Shih, T., Jackson-Weaver, O., Tong, X., et al. (2014). Conditions and constraints for astrocyte calcium signaling in the hippocampal mossy fiber pathway. *Neuron* 82, 413–429. doi: 10.1016/j.neuron.2014.02.041

Howard, D. B., Powers, K., Wang, Y., and Harvey, B. K. (2008). Tropism and toxicity of adeno-associated viral vector serotypes 1,2,5,6,7,8,9 in rat neurons and glia *in vitro*. *Virology* 372, 24–34. doi: 10.1016/j.virol.2007.10.007

Jacob, H. J. (1999). Functional genomics and rat models. *Genome Res.* 9, 1013–1016. doi: 10.1101/gr.9.11.1013

Khalilov, I., Esclapez, M., Medina, I., Aggoun, D., Lamsa, K., Leinekugel, X., et al. (1997). A novel *in vitro* preparation: the intact hippocampal formation. *Neuron* 19, 743–749. doi: 10.1016/S0896-6273(00)80956-3

Kispersky, T. J., Fernandez, F. R., Economo, M. N., and White, J. A. (2012). Spike resonance properties in hippocampal O-LM cells are dependent on refractory dynamics. *J. Neurosci.* 32, 3637–3651. doi: 10.1523/JNEUROSCI.1361-11.2012

Kralj, J. M., Douglass, A. D., Hochbaum, D. R., Maclaurin, D., and Cohen, A. E. (2012). Optical recording of action potentials in mammalian neurons using a microbial rhodopsin. *Nat. Methods* 9, 90–95. doi: 10.1038/nmeth.1782

Kreitzer, A. C., Gee, K. R., Archer, E. A., and Regehr, W. G. (2000). Monitoring presynaptic calcium dynamics in projection fibers by *in vivo* loading of a novel calcium indicator. *Neuron* 27, 25–32. doi: 10.1016/S0896-6273(00)00006-4

Kuga, N., Sasaki, T., Takahara, Y., Matsuki, N., and Ikegaya, Y. (2011). Large-scale calcium waves traveling through astrocytic networks *in vivo*. *J. Neurosci.* 31, 2607–2614. doi: 10.1523/JNEUROSCI.5319-10.2011

Li, H., Foss, S. M., Dobryy, Y. L., Park, C. K., Hires, S. A., Shaner, N. C., et al. (2011a). Concurrent imaging of synaptic vesicle recycling and calcium dynamics. *Front. Mol. Neurosci.* 4:34. doi: 10.3389/fnmol.2011.00034

Li, M. A., Turner, D. J., Ning, Z., Yusa, K., Liang, Q., Eckert, S., et al. (2011b). Mobilization of giant piggyBac transposons in the mouse genome. *Nucleic Acids Res.* 39, e148. doi: 10.1093/nar/gkr764

Li, Y., and Tsien, R. W. (2012). pHTomato, a red, genetically encoded indicator that enables multiplex interrogation of synaptic activity. *Nat. Neurosci.* 15, 1047–1053. doi: 10.1038/nn.3126

Lillis, K. P., Eng, A., White, J. A., and Mertz, J. (2008). Two-photon imaging of spatially extended neuronal network dynamics with high temporal resolution. *J. Neurosci. Methods* 172, 178–184. doi: 10.1016/j.jneumeth.2008.04.024

Lillis, K. P., Kramer, M. A., Mertz, J., Staley, K. J., and White, J. A. (2012). Pyramidal cells accumulate chloride at seizure onset. *Neurobiol. Dis.* 47, 358–366. doi: 10.1016/j.nbd.2012.05.016

Lorenzen, M. D., Berghammer, A. J., Brown, S. J., Denell, R. E., Klingler, M., and Beeman, R. W. (2003). piggyBac-mediated germline transformation in the beetle *Tribolium castaneum*. *Insect Mol. Biol.* 12, 433–440. doi: 10.1046/j.1365-2583.2003.00427.x

LoTurco, J., Manent, J.-B., and Sidiqi, F. (2009). New and improved tools for *in utero* electroporation studies of developing cerebral cortex. *Cereb. Cortex* 19(Suppl. 1), i120–i125. doi: 10.1093/cercor/bhp033

Lovatt, D., Sonnewald, U., Waagepetersen, H. S., Schousboe, A., He, W., Lin, J. H.-C., et al. (2007). The transcriptome and metabolic gene signature of protoplasmic astrocytes in the adult murine cortex. *J. Neurosci.* 27, 12255–12266. doi: 10.1523/JNEUROSCI.3404-07.2007

Mank, M., and Griesbeck, O. (2008). Genetically encoded calcium indicators. *Chem. Rev.* 108, 1550–1564. doi: 10.1021/cr078213v

Mao, T., O'Connor, D. H., Scheuss, V., Nakai, J., and Svoboda, K. (2008). Characterization and subcellular targeting of GCaMP-type genetically-encoded calcium indicators. *PLoS ONE* 3:e1796. doi: 10.1371/journal.pone.0001796

Matsuda, T., and Cepko, C. L. (2007). Controlled expression of transgenes introduced by *in vivo* electroporation. *Proc. Natl. Acad. Sci. U.S.A.* 104, 1027–1032. doi: 10.1073/pnas.0610155104

McDonough, S. I., Cseresnyés, Z., and Schneider, M. F. (2000). Origin sites of calcium release and calcium oscillations in frog sympathetic neurons. *J. Neurosci.* 20, 9059–9070.

Nakahira, E., and Yuasa, S. (2005). Neuronal generation, migration, and differentiation in the mouse hippocampal primoridium as revealed by enhanced green fluorescent protein gene transfer by means of *in utero* electroporation. *J. Comp. Neurol.* 483, 329–340. doi: 10.1002/cne.20441

Nakai, J., Ohkura, M., and Imoto, K. (2001). A high signal-to-noise Ca(2+) probe composed of a single green fluorescent protein. *Nat. Biotechnol.* 19, 137–141. doi: 10.1038/84397

Nakamura, K., Yamashita, Y., Tamamaki, N., Katoh, H., Kaneko, T., and Negishi, M. (2006). *In vivo* function of Rnd2 in the development of neocortical pyramidal neurons. *Neurosci. Res.* 54, 149–153. doi: 10.1016/j.neures.2005.10.008

Navarro-Quiroga, I., Chittajallu, R., Gallo, V., and Haydar, T. F. (2007). Long-term, selective gene expression in developing and adult hippocampal pyramidal neurons using focal *in utero* electroporation. *J. Neurosci.* 27, 5007–5011. doi: 10.1523/JNEUROSCI.0867-07.2007

Netoff, T. I., Banks, M. I., Dorval, A. D., Acker, C. D., Haas, J. S., Kopell, N., et al. (2005). Synchronization in hybrid neuronal networks of the hippocampal formation. *J. Neurophysiol.* 93, 1197–1208. doi: 10.1152/jn.00982.2004

Nimmerjahn, A., Kirchhoff, F., and Helmchen, F. (2005). Resting microglial cells are highly dynamic surveillants of brain parenchyma *in vivo*. *Science* 308, 1314–1318. doi: 10.1126/science.1110647

Niwa, H., Yamamura, K., and Miyazaki, J. (1991). Efficient selection for high-expression transfectants with a novel eukaryotic vector. *Gene* 108, 193–199. doi: 10.1016/0378-1119(91)90434-D

Oberheim, N. A., Tian, G.-F., Han, X., Peng, W., Takano, T., Ransom, B., et al. (2008). Loss of astrocytic domain organization in the epileptic brain. *J. Neurosci.* 28, 3264–3276. doi: 10.1523/JNEUROSCI.4980-07.2008

Pacary, E., Haas, M. A., Wildner, H., Azzarelli, R., Bell, D. M., Abrous, D. N., et al. (2012). Visualization and genetic manipulation of dendrites and spines in the mouse cerebral cortex and hippocampus using *in utero* electroporation. *J. Vis. Exp.* e4163. doi: 10.3791/4163

Peterlin, Z. A., Kozloski, J., Mao, B. Q., Tsiola, A., and Yuste, R. (2000). Optical probing of neuronal circuits with calcium indicators. *Proc. Natl. Acad. Sci. U.S.A.* 97, 3619–3624. 65, e4163. doi: 10.1073/pnas.97.7.3619

Reeves, A. M. B., Shigetomi, E., and Khakh, B. S. (2011). Bulk loading of calcium indicator dyes to study astrocyte physiology: key limitations and improvements using morphological maps. *J. Neurosci.* 31, 9353–9358. doi: 10.1523/JNEUROSCI.0127-11.2011

Rosen, G. D., Bai, J., Wang, Y., Fiondella, C. G., Threlkeld, S. W., LoTurco, J. J., et al. (2007). Disruption of neuronal migration by RNAi of Dyx1c1 results in neocortical and hippocampal malformations. *Cereb. Cortex* 17, 2562–2572. doi: 10.1093/cercor/bhl162

Sabolek, H. R., Swiercz, W. B., Lillis, K. P., Cash, S. S., Huberfeld, G., Zhao, G., et al. (2012). A candidate mechanism underlying the variance of interictal spike propagation. *J. Neurosci.* 32, 3009–3021. doi: 10.1523/JNEUROSCI.5853-11.2012

Saito, T., and Nakatsuji, N. (2001). Efficient gene transfer into the embryonic mouse brain using *in vivo* electroporation. *Dev. Biol.* 240, 237–246. doi: 10.1006/dbio.2001.0439

Schipke, C. G., Heidemann, A., Skupin, A., Peters, O., Falcke, M., and Kettenmann, H. (2008). Temperature and nitric oxide control spontaneous calcium transients in astrocytes. *Cell Calcium* 43, 285–295. doi: 10.1016/j.ceca.2007.06.002

Schultz, W. (1982). Depletion of dopamine in the striatum as an experimental model of Parkinsonism: direct effects and adaptive mechanisms. *Prog. Neurobiol.* 18, 121–166. doi: 10.1016/0301-0082(82)90015-6

Schwartz, T. H., Rabinowitz, D., Unni, V., Kumar, V. S., Smetters, D. K., Tsiola, A., et al. (1998). Networks of coactive neurons in developing layer 1. *Neuron* 20, 541–552. doi: 10.1016/S0896-6273(00)80993-9

Shaner, N. C., Campbell, R. E., Steinbach, P. A., Giepmans, B. N. G., Palmer, A. E., and Tsien, R. Y. (2004). Improved monomeric red, orange and yellow fluorescent proteins derived from Discosoma sp. red fluorescent protein. *Nat. Biotechnol.* 22, 1567–1572. doi: 10.1038/nbt1037

Shigetomi, E., Bushong, E. A., Haustein, M. D., Tong, X., Jackson-Weaver, O., Kracun, S., et al. (2013). Imaging calcium microdomains within entire astrocyte territories and endfeet with GCaMPs expressed using adeno-associated viruses. *J. Gen. Physiol.* 141, 633–647. doi: 10.1085/jgp.201210949

Shigetomi, E., Kracun, S., and Khakh, B. S. (2010a). Monitoring astrocyte calcium microdomains with improved membrane targeted GCaMP reporters. *Neuron Glia Biol.* 6, 183–191. doi: 10.1017/S1740925X10000219

Shigetomi, E., Kracun, S., Sofroniew, M. V., and Khakh, B. S. (2010b). A genetically targeted optical sensor to monitor calcium signals in astrocyte processes. *Nat. Neurosci.* 13, 759–766. doi: 10.1038/nn.2557

Smeal, R. M., Economo, M. N., Lillis, K. P., Wilcox, K. S., and White, J. A. (2012). Targeted path scanning: an emerging method for recording fast changing network dynamics across large distances. *J. Bioeng. Biomed. Sci.* S5:002. doi: 10.4172/2155-9538.S5-002

Stosiek, C., Garaschuk, O., Holthoff, K., and Konnerth, A. (2003). *In vivo* two-photon calcium imaging of neuronal networks. *Proc. Natl. Acad. Sci. U.S.A.* 100, 7319–7324. doi: 10.1073/pnas.1232232100

Sun, W., McConnell, E., Pare, J.-F., Xu, Q., Chen, M., Peng, W., et al. (2013). Glutamate-dependent neuroglial calcium signaling differs between young and adult brain. *Science* 339, 197–200. doi: 10.1126/science.1226740

Tabata, H., and Nakajima, K. (2001). Efficient *in utero* gene transfer system to the developing mouse brain using electroporation: visualization of neuronal migration in the developing cortex. *Neuroscience* 103, 865–872. doi: 10.1016/S0306-4522(01)00016-1

Tian, L., Hires, S. A., Mao, T., Huber, D., Chiappe, M. E., Chalasani, S. H., et al. (2009). Imaging neural activity in worms, flies and mice with improved GCaMP calcium indicators. *Nat. Methods* 6, 875–881. doi: 10.1038/nmeth.1398

Tsien, R. Y. (1980). New calcium indicators and buffers with high selectivity against magnesium and protons: design, synthesis, and properties of prototype structures. *Biochemistry (Mosc.)* 19, 2396–2404. doi: 10.1021/bi00552a018

Uematsu, D., Greenberg, J. H., Araki, N., and Reivich, M. (1991). Mechanism underlying protective effect of MK-801 against NMDA-induced neuronal injury *in vivo*. *J. Cereb. Blood Flow Metab.* 11, 779–785. doi: 10.1038/jcbfm.1991.135

VandenDriessche, T., Ivics, Z., Izsvák, Z., and Chuah, M. K. L. (2009). Emerging potential of transposons for gene therapy and generation of induced pluripotent stem cells. *Blood* 114, 1461–1468. doi: 10.1182/blood-2009-04-210427

Wang, T., Zhou, C., Tang, A., Wang, S., and Chai, Z. (2006a). Cellular mechanism for spontaneous calcium oscillations in astrocytes. *Acta Pharmacol. Sin.* 27, 861–868. doi: 10.1111/j.1745-7254.2006.00397.x

Wang, X., Lou, N., Xu, Q., Tian, G.-F., Peng, W. G., Han, X., et al. (2006b). Astrocytic Ca2+ signaling evoked by sensory stimulation *in vivo*. *Nat. Neurosci.* 9, 816–823. doi: 10.1038/nn1703

Williams, P. A., Hellier, J. L., White, A. M., Staley, K. J., and Dudek, F. E. (2007). Development of spontaneous seizures after experimental status epilepticus: implications for understanding epileptogenesis. *Epilepsia* 48(Suppl. 5), 157–163. doi: 10.1111/j.1528-1167.2007.01304.x

Wu, J., Liu, L., Matsuda, T., Zhao, Y., Rebane, A., Drobizhev, M., et al. (2013). Improved orange and red Ca2+ indicators and photophysical considerations for optogenetic applications. *ACS Chem. Neurosci.* 4, 963–972. doi: 10.1021/cn400012b

Wu, S., Ying, G., Wu, Q., and Capecchi, M. R. (2007). Toward simpler and faster genome-wide mutagenesis in mice. *Nat. Genet.* 39, 922–930. doi: 10.1038/ng2060

Yang, Y., Vidensky, S., Jin, L., Jie, C., Lorenzini, I., Frankl, M., et al. (2011). Molecular comparison of GLT1+ and ALDH1L1+ astrocytes *in vivo* in astroglial reporter mice. *Glia* 59, 200–207. doi: 10.1002/glia.21089

Yoshida, A., Yamaguchi, Y., Nonomura, K., Kawakami, K., Takahashi, Y., and Miura, M. (2010). Simultaneous expression of different transgenes in neurons and glia by combining *in utero* electroporation with the Tol2 transposon-mediated gene transfer system. *Genes Cells* 15, 501–512. doi: 10.1111/j.1365-2443.2010.01397.x

Yuste, R., and Katz, L. C. (1991). Control of postsynaptic Ca2+ influx in developing neocortex by excitatory and inhibitory neurotransmitters. *Neuron* 6, 333–344. doi: 10.1016/0896-6273(91)90243-S

Conflict of Interest Statement: The authors declare that the research was conducted in the absence of any commercial or financial relationships that could be construed as a potential conflict of interest.

frontiers in Molecular Neuroscience

ORIGINAL RESEARCH
published: 08 May 2015
doi: 10.3389/fnmol.2015.00012

Intracellular calcium dynamics in cortical microglia responding to focal laser injury in the PC::G5-tdT reporter mouse

Amir Pozner[1,2], *Ben Xu*[1,3], *Sierra Palumbos*[1], *J. Michael Gee*[4], *Petr Tvrdik*[1]* and *Mario R. Capecchi*[1,3]

[1] Department of Human Genetics, University of Utah, Salt Lake City, UT, USA, [2] Department of Chemistry, University of Utah, Salt Lake City, UT, USA, [3] Howard Hughes Medical Institute, Chevy Chase, MD, USA, [4] Department of Bioengineering, University of Utah, Salt Lake City, UT, USA

Microglia, the resident immune cells of the brain parenchyma, are highly responsive to tissue injury. Following cell damage, microglial processes redirect their motility from randomly scouting the extracellular space to specifically reaching toward the compromised tissue. While the cell morphology aspects of this defense mechanism have been characterized, the intracellular events underlying these responses remain largely unknown. Specifically, the role of intracellular Ca^{2+} dynamics has not been systematically investigated in acutely activated microglia due to technical difficulty. Here we used live two-photon imaging of the mouse cortex ubiquitously expressing the genetically encoded Ca^{2+} indicator GCaMP5G and fluorescent marker tdTomato in central nervous system microglia. We found that spontaneous Ca^{2+} transients in microglial somas and processes were generally low (only 4% of all microglia showing transients within 20 min), but baseline activity increased about 8-fold when the animals were treated with LPS 12 h before imaging. When challenged with focal laser injury, an additional surge in Ca^{2+} activity was observed in the somas and protruding processes. Notably, coherent and simultaneous Ca^{2+} rises in multiple microglial cells were occasionally detected in LPS-treated animals. We show that Ca^{2+} transients were pre-dominantly mediated via purinergic receptors. This work demonstrates the usefulness of genetically encoded Ca^{2+} indicators for investigation of microglial physiology.

Keywords: calcium imaging, GECI, GCaMP5G, PC::G5-tdT, microglia, purinergic receptors

OPEN ACCESS

Edited by:
Yoshiyuki Yamada, University of Geneva, Switzerland

Reviewed by:
Inbal Goshen, The Hebrew University, Israel
Axel Nimmerjahn, Salk Institute for Biological Studies, USA

***Correspondence:**
Petr Tvrdik, Department of Human Genetics, University of Utah, 15 N 2030 E, Salt Lake City, UT 84112, USA
petr.tvrdik@genetics.utah.edu

Received: *01 February 2015*
Accepted: *16 April 2015*
Published: *08 May 2015*

Citation:
Pozner A, Xu B, Palumbos S, Gee JM, Tvrdik P and Capecchi MR (2015) Intracellular calcium dynamics in cortical microglia responding to focal laser injury in the PC::G5-tdT reporter mouse. Front. Mol. Neurosci. 8:12. doi: 10.3389/fnmol.2015.00012

Introduction

Microglia are the principal immune cells in the brain. In their ramified, non-activated state, microglia exhibit small somas and elaborate, highly motile processes (Nimmerjahn et al., 2005). This high degree of motility facilitates the interaction of microglial bulbous endings with numerous physiological processes in the central nervous system, ranging from response to cellular damage (Davalos et al., 2005; Wake et al., 2009) to a role in synaptic pruning and response to neuronal activity (Paolicelli et al., 2011; Schafer et al., 2012; Dissing-Olesen et al., 2014; Eyo et al., 2014). The normal ramified morphology of microglia is dependent on the immune-privileged environment of the brain parenchyma and is difficult to reproduce *in vitro*, as serum and other factors present in

the culture media cause immunological activation and subsequent changes in cell morphology and activity. Therefore, intravital imaging approaches that would limit tissue damage such as live two-photon microscopy are necessary for accurate investigations of cellular and physiological responses of microglia in the brain. Although synthetic dyes have been used widely for some applications, genetically encoded fluorescence markers afford significant advantages for intravital imaging experiments (Jung et al., 2000). To enable more detailed studies, we have recently developed a mouse reporter of cellular activity (PC::G5-tdT), which combines the use of a constitutively fluorescent protein (tdTomato) with the GCaMP5G intracellular Ca^{2+} indicator and displays high activity in microglia (Gee et al., 2014).

Ca^{2+} transients reveal underlying intracellular responses to extracellular signals in virtually all cell types of the nervous system (Berridge et al., 2003; Nedergaard et al., 2010; Grienberger and Konnerth, 2012). The information derived from Ca^{2+} signaling *in vivo* is particularly valuable in the studies of microglia, which are not electrically excitable and exceptionally difficult to load with synthetic dyes (Eichhoff et al., 2011; Garaschuk, 2013). As a consequence of limited technology, very little is known about the intracellular activity in microglia responding to physiological and pathophysiological brain processes. One striking example is the well-established paradigm of microglial processes responding to focal laser injury (Davalos et al., 2005; Haynes et al., 2006), which is well-characterized regarding the cell morphology of protruding processes, but poorly understood in terms of intracellular Ca^{2+} dynamics. To overcome this deficiency, we have used a newly generated *Aif1(Iba1)*-IRES-Cre mouse driver to express the PC::G5-tdT reporter in microglia and study the laser ablation paradigm with two-photon microscopy in anesthetized mice. Our results reveal new insights about the relationship between process motility, Ca^{2+} signaling and involvement of purinergic receptors.

Materials and Methods

Animals

Generation of the PC::G5-tdT mouse line was described previously (Gee et al., 2014). The *Aif1(Iba1)*-IRES-Cre strain was generated by inserting the IRES-Cre-FRT-neo-FRT cassette into the 3′ untranslated region of the *Aif1* gene and will be described elsewhere. Additional details are available upon request. The *neo* selection marker was removed by breeding to FLP deleter and bred to homozygosity. All experimental animals were obtained by crossing homozygous PC::G5-tdT reporters with homozygous *Aif1*-IRES-Cre mice. All experiments were reviewed and approved by the University of Utah IACUC committee.

Immunohistochemistry and Confocal Imaging

Adult mice used for immunohistochemistry were deeply anesthetized with Avertin (250 mg/kg body weight) then transcardially perfused with 4% paraformaldehyde (PFA) (EMS 15713) in 1 × PBS (pH 7.6). Following transfusion, brains were dissected, post-fixed in 4% PFA at room temperature, then processed through 10% sucrose in 1 × PBS at 4°C overnight followed by 30% sucrose in 1 × PBS until the brains sank. These brains were embedded in 2% gelatin (Sigma G2500) and 0.9% NaCl in a metal mold, flash frozen on a metal block cooled with liquid nitrogen. Brains were sectioned with a Leica CM1900 at 20 μm thickness, and mounted on SuperFrost Gold Plus microscopy slides (Fisher Scientific). The sections were incubated with primary antibodies, chicken anti-GFP (Aves GFP-1020) and rabbit anti-Iba1 (Wako 019-19741), diluted in Cyto-Q Immuno Diluent and Block (Innovex Biosciences). The sections were then incubated with secondary antibodies, goat anti-chicken AF488 (Life Technologies A11039) and goat anti-rabbit AF647 (Life Technologies A21244) diluted in Cyto-Q immune Diluent. The slides were washed with 1 × PBS and then mounted with Fluoromount-G (Southern Biotech). Slides were imaged with a Leica TCS SP5 confocal microscope. The images were analyzed and processed with Imaris 7.7.2 (Bitplane).

Cranial Window Surgery and Two-Photon Imaging

GCaMP5G-tdTomato labeled cells in cortical layers 1–3 were imaged by two-photon microscopy through a small craniotomy. Surgery was performed as previously described (Mostany and Portera-Cailliau, 2008). Briefly, 2–4 month old mice were anesthetized by inhalation of isoflurane (Vetone) (4% for induction, 1.5% for surgery and imaging). The anesthetized mice were placed on a 37°C heating pad (FHC, Bowdoin, ME) and the depth of anesthesia was evaluated by examination of pinch withdrawal, eyelid reflex, vibrissae movements, and respiration rate. After hair removal and disinfection with 10% povidone-iodine (Vetone), the scalp skin was removed and the skull membrane was scraped using a razor blade. The skull was thoroughly dried with a sterile cotton swab and a circle (∼4 mm in diameter) over the visual or somatosensory cortex was thinned using a high-speed dental drill under a dissecting scope. To prevent damage of the underlying cortex by friction-induced heat, drilling was periodically interrupted to allow heat dissipation while saline was applied to the skull. A window in the skull was carefully opened with forceps keeping the dura intact, and a drop of sterile saline (Teknova) was applied to the exposed region. If needed, a GELFOAM (Pfizer) was applied to control bleeding. A thin 8 mm #0 coverslip was then glued to the skull with Cyanoacrylate (Superglue). One end of a flattened steel nail was cemented (A–M Systems) to the skull behind the window and the other end was inserted into a custom made holder to immobilize the head during imaging. Two-photon imaging was performed with a Prairie Technologies Ultima Multiphoton Microscopy System with a Chameleon Ti:Sapphire laser tuned to 920 nm and a 16× water-immersion objective (0.8 NA; Nikon) at a zoom of 4.3×. The maximal output of the laser power at the sample was kept low (<20 mW) to avoid unintended photo damage. Signal was acquired with GaAsP detectors, using a 490–560 nm bandpass filter for GCaMP5G (Ch3) and a 570–620 nm bandpass filter for tdTomato (Ch2). The maximum imaging depth was < 100 μm below the pial surface and sampling rate was 0.125 frames/s at 1024 × 1024 pixel resolution. Several recordings were acquired at 512 × 512 pixel resolution and

2 s per frame (0.5 Hz) rate (see Supplementary Figures 3E,F). PrairieView 5.2 software was used for image acquisition.

Two-Photon Laser Ablation

Focal laser injury was inflicted by focusing the two-photon laser beam onto a small area in the superficial cortex. The wavelength was set to 920 nm and laser power increased by 400–500%. A small area of 8×8 pixels was scanned at a frequency of 1 Hz for 90 s. The site of injury was visible as a bright auto-fluorescent sphere with a diameter of 10–15 μm.

Drug Administration

Lipopolysaccharide (LPS), from *Escherichia coli* strain 0111:B4 (Sigma, L4391) was dissolved in sterile saline and injected subcutaneously (50 μl, 1 mg/kg body weight) close to the midline of the lower lip. At 12 h, 24 h or 1 month following a single LPS injection, a craniotomy was performed in preparation for *in vivo* imaging. Pharmacological compounds were applied directly to the cortex on the intact dura prior to mounting the cranial window. Imaging was initiated 30 min after application and drugs were maintained in the preparation during the entire session. BAPTA-AM, PPADS (pyridoxal-5-phosphate-6-azophenyl-2′4-disulfonic acid) and bicuculline were purchased from Tocris. Stock solutions were diluted with sterile saline to a final concentration of 5 μg/ml, 5 mM, and 250 μM, respectively.

Image Processing and Analysis

Image processing was performed with NIH ImageJ and Imaris (Bitplane) software. Focal drift was corrected using Imaris 7.7.2 prior to measurements of process motility or Ca^{2+} amplitudes. Process movement was analyzed with the filament-tracking algorithm included in the Imaris package. The distal end of a process was tracked as long as tdTomato was detectable through the 20 min imaging session. Care was taken to include only process ends that displayed directionality toward the injury site. Parameter settings were determined empirically and kept constant for all analyses of process motility, including: Filament Quality > 40, Max Distance $= 3$, Max Gap Size $= 5$, Track Duration > 5 min and Track Displacement Length > 5 min. Process motility was quantified for each cell by averaging the velocity of each process belonging to that cell. Image animations were generated with iMovie. For calcium transient detection in laser injury experiments, the data was first carefully examined in Imaris in slow motion. The spatial location of each potential transient was manually delineated as a region of interest (ROI) including all pixels perceived to be associated with the event. The mean fluorescence intensity F_j of all pixels belonging to an ROI was computed for each frame j. The resulting J-frame time series $F_1 \ldots F_J$ was then plotted and analyzed in Microsoft Excel and Igor Pro (WaveMetrics), using the MultiPeak Fitting 2 Package and Wave Stats. The lowest mean intensity value in each time series was set to 0, baseline was fitted with a cubic polynomial function and potential peaks were detected with the multi-peak fitting algorithm. The baseline was then subtracted and only the transients with amplitudes greater than 2 standard deviations above the mean baseline fluorescence were used in analysis. The temporal boundaries of each transient were determined as the frames containing the first (F_j*) and the last (F_{j*+K-1}) values above the local baseline F_0 (defined for each transient as F_{j*-1}). The highest F_k was designated as the maximum value for that transient (F_{max}). The amplitude of a transient (ΔF) was measured in the original trace as $F_{max}-F_0$. The instance of a transient was defined as the elapsed time between the initiation of imaging and the frame containing F_j*. Please refer to Supplementary Figure 3 for additional information.

Statistical Analysis

Unless otherwise stated, all results are reported as mean ± SEM and statistical tests were considered significant when $p < 0.05$. Statistical calculations (Student's *t*-test, ANOVA) were performed with Microsoft Excel.

Results

Genetic Labeling of Cortical Microglia with GCaMP5G-IRES-tdTomato

Allograft inflammatory factor 1 (*Aif1*), also known as ionized Ca^{2+}-binding adapter molecule 1 (*Iba1*), is specifically expressed in microglia in the adult brain. In order to express the GCaMP5G Ca^{2+} indicator (Akerboom et al., 2012) and the tdTomato fluorescence marker in cortical microglia, we crossed a newly generated *Aif1*-IRES-Cre driver to the PC::G5-tdT reporter (Gee et al., 2014) (**Figure 1A**). When we stained the brains of the progeny with anti-GFP antibody (cross-reacting with GCaMP5G) and anti-Iba1 antibody, virtually all cortical microglia were co-labeled (**Figures 1D,G**). Reproducibly, the *Aif1*-IRES-Cre driver also labeled a number of cortical neurons in layer 6, few hippocampal pyramidal neurons in CA1 and very sparsely in other regions of the brain (**Figures 1B–D**) suggesting a brief transcriptional activation of the *Aif1* gene during early corticogenesis. Nonetheless, in the superficial cortical layers 1–3, which are relevant for *in vivo* imaging through cranial windows, the vast majority of labeled cells are microglia (**Figures 1E–G**). Out of 644 GCaMP5G-positive cells counted, 627 were also co-labeled with anti-Iba1 antibody and 17 were GCaMP5G positive only (2.6%).

in vivo Imaging and Focal Laser Stimulation of Genetically Labeled Microglia

Previously, Ca^{2+} dynamics in adult cortical microglia were studied using single cell electroporation of synthetic Ca^{2+} indicators, such as OGB-1 (Eichhoff et al., 2011). The electroporation procedure was not considered to affect microglia physiology, since OGB-1-labeled cells maintained their ramified morphology for at least 1 h and retained their ATP chemotactic response. Using this method, it was demonstrated that 22% of resting microglia exhibited spontaneous Ca^{2+} transients in the course of a 15 min imaging period.

Here we adapted two-photon laser scanning microscopy through a cranial window (**Figure 2A** and Materials and Methods) to record tdTomato and GCaMP5G signals in Iba1-positive cells in the mouse cortex (Supplementary Figures 1–3 and **Figure 2**). In this model, only 4% of resting microglia exhibited at least one spontaneous Ca^{2+} transient during

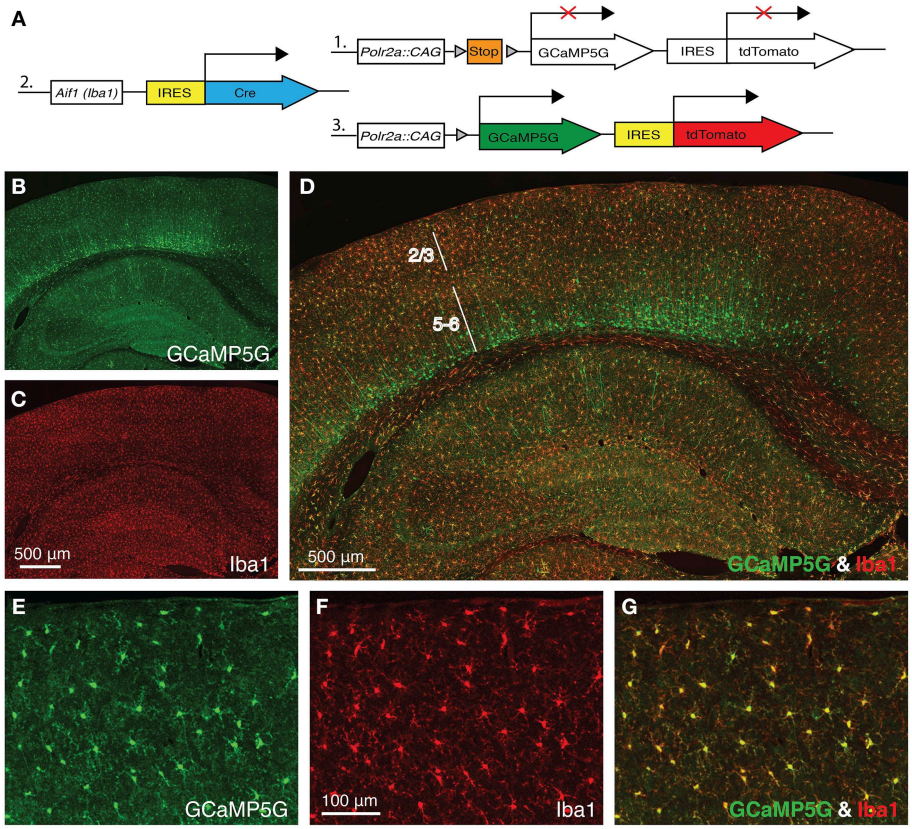

FIGURE 1 | *Aif1*-IRES-Cre driver labels Iba1-positive microglia. (A) A schematic diagram of the PC::G5-tdT allele (1) crossed with *Aif1*-IRES-Cre (2). Expression of IRES-Cre at the *Aif1* locus results in the expression of GCaMP5G and tdTomato following Cre-mediated excision of the STOP cassette (3). **(B–D)** A coronal section of *Aif1*-IRES-Cre; PC::G5-tdT brain stained with anti-GFP (GCaMP5G) and anti-Iba1 antibodies. **(B)** The section was imaged specifically in the green channel (GCaMP5G expression), **(C)** red channel (Iba1 expression) and **(D)** overlay of green and red channels. The PC::G5-tdT allele is expressed in all *Aif1* lineage cells, including layer 5/6 cortical neurons. Layers 2/3 and 5–6 are indicated. **(E–G)** Coronal sections of somatosensory cortex layer 2/3 region of *Aif1*-IRES-Cre; PC::G5-tdT brains stained with anti-GFP and anti-Iba1 antibodies. **(E)** GCaMP5G expression, **(F)** endogenous Iba1 staining and **(G)** Overlay. PC::G5-tdT was co-expressed in all Iba1-positive cells studied in these experiments. Adult animals (6–8 weeks) were used for immunohistochemistry in **(B-G)**.

a 20 min recording session (Supplementary Figure 1 and **Figure 3A**) (5/116, $n = 3$ mice), suggesting that OGB-1 electroporation does affect physiological properties of resting microglia within the 1 h experimental time frame. The use of genetically encoded Ca^{2+} indicators suggests that resting microglia exhibit even fewer spontaneous Ca^{2+} transients than formerly thought.

Next, we tested the Ca^{2+} response to focal injury by inflicting a small laser ablation. In accordance with previously published data (Davalos et al., 2005), microglial processes close to the site of injury thickened their bulbous endings and spread toward the injured site (Supplementary Movie 1). The cortical damage evoked Ca^{2+} transients in 42% of the responding GCaMP5G-expressing microglia (in the first perimeter around the injury, 51/123, $n = 3$ mice) during 20-min long imaging session (**Figure 3A**). Again, in a comparable experiment probing synthetic dye-loaded microglia with micropipette-provoked neuronal damage, 100% of the cells displayed Ca^{2+} transients within 15 min after stimulus (Eichhoff et al., 2011), which is an apparent exaggeration compared to the genetically encoded reporter.

In our experiments, the cells located farther away from the ablation (2nd perimeter) did not demonstrate a directional response toward the injury and did not exhibit significantly increased incidence of Ca^{2+} transients (**Figure 3A** and Supplementary Movies 2, 3). The majority of injury-induced Ca^{2+} transients (>80%) arose in the microglia processes only, while the remainder occurred both in the processes and cell bodies (**Figures 2B,C** and Supplementary Movies 2–3).

Systemic Peripheral Inflammation Increases the Frequency of Calcium Transients in Brain Microglia

Peripheral administration of gram-negative bacterial cell-wall component LPS initiates peripheral inflammation effects. The interaction of LPS with macrophage Toll-like receptors provokes production of proinflammatory cytokines including TNFα, IL-1β, and IL-6 (Jaffer et al., 2010). Subsequently, the

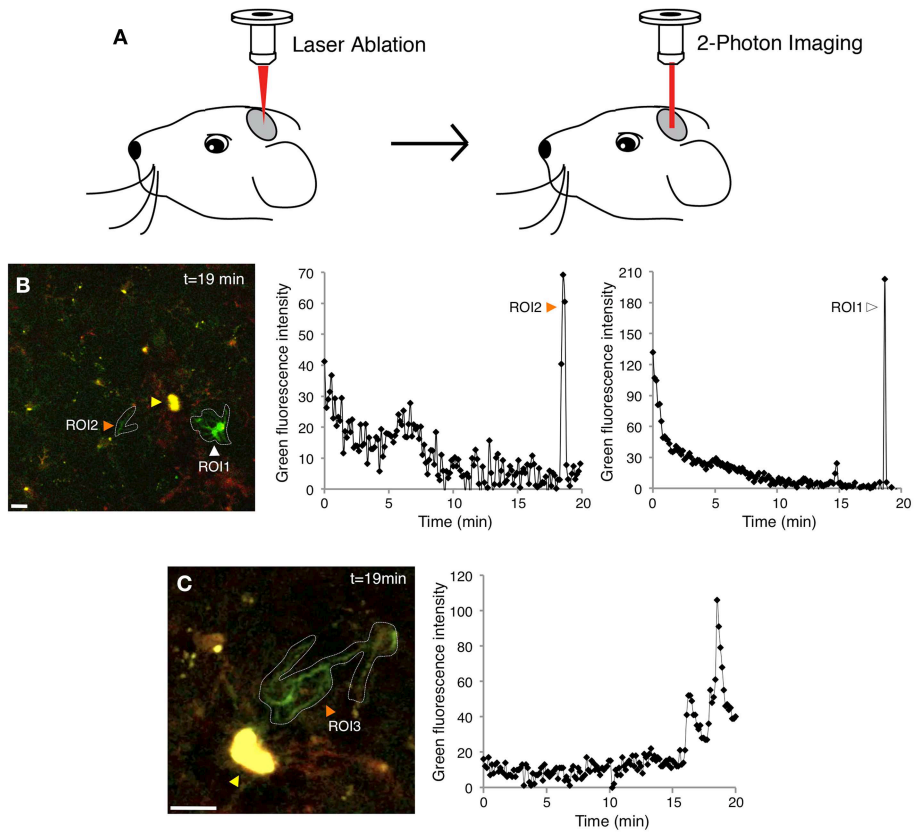

FIGURE 2 | Simultaneous two-photon imaging of tdTomato and GCaMP5G signals in cortical microglia. (A) Cartoon demonstrating the two-photon microscopy approach used to image microglial Ca^{2+} responses after laser inflicted focal injury in layer 2/3 of the somatosensory or visual cortex. **(B)** GCaMP5G fluorescence remains stable, allowing long imaging sessions (Supplementary Movie 2). A recording of green fluorescence intensity in ROI1 (white arrowhead) shows a large Ca^{2+} transient in the soma and processes 19 min after the laser injury. Another recording in ROI2 (orange arrowhead) shows a Ca2+ transient localized mainly to the microglial processes. The corresponding tdTomato fluorescence time series for this experiment is shown in Supplementary Figure 2B and Supplementary Movie 1. **(C)** A different example of a process-restricted Ca^{2+} transient. Variability in branch spiking was often observed in the same cell (Supplementary Movie 3). ROI; Region of Interest. Yellow arrowheads indicate the laser injury sites. Scale bars: 10 μm.

cytokines cross the blood brain barrier via an endocrine-like mechanism and activate microglia (Maier et al., 1998; Lee et al., 2010; Ousman and Kubes, 2012). We sought to evaluate the microglial Ca^{2+} response in the brains of mice that were subjected to peripheral inflammation. In agreement with previous observations (Gyoneva et al., 2014), imaging 24 h after subcutaneous LPS administration to the lower lip revealed that all microglia altered their morphology and phenotype, adopting an activated state. Cells transformed into an amoeboid morphology by retracting their processes, which become fewer and much thicker, and by increasing the size of their soma (**Figure 3B**). Accordingly, microglia displayed an amoeboid-like movement in the vicinity of the site of insult (Supplementary Movie 4). Moreover, activated microglia did not show Ca^{2+} transients during the 20 min long imaging sessions.

Interestingly, when we performed imaging experiments 1 month after a single LPS injection to the lower lip, microglia returned to their resting ramified structure and resumed a typical response to focal brain injury spreading their processes toward the site of insult. In contrast, these formerly activated cells did not resume normal frequency of Ca^{2+} transients in the first perimeter of the injury (4.9%, 4/82, $n = 2$ mice) (Supplementary Movie 5). Hence, the long-term inhibitory effect of a single peripheral immune challenge on microglial Ca^{2+} signaling is in line with the previously shown long-lasting microglial "memory" marked by persistent increase of Iba1 immunoreactivity (Kondo et al., 2011).

When we imaged microglia 12 h after subcutaneous LPS administration, we found that the cells had not yet acquired an amoeboid-like activated appearance (**Figure 3C**). Moreover, these cells displayed an unusually high frequency of spontaneous Ca^{2+} transients (34%, 45/131, $n = 3$ mice) (**Figure 3A**). We termed these cells LPS-primed microglia. Significantly more primed microglia responding to focal laser injury displayed Ca^{2+} transients (67%, 77/115, $n = 3$ mice) (**Figure 3A**). The number of Ca^{2+} transients in more distal primed microglia was similar to resting primed cells (37%, 68/182, $n = 3$ mice) (**Figure 3A**). Most non-primed microglia exhibited only one Ca^{2+} transient in the

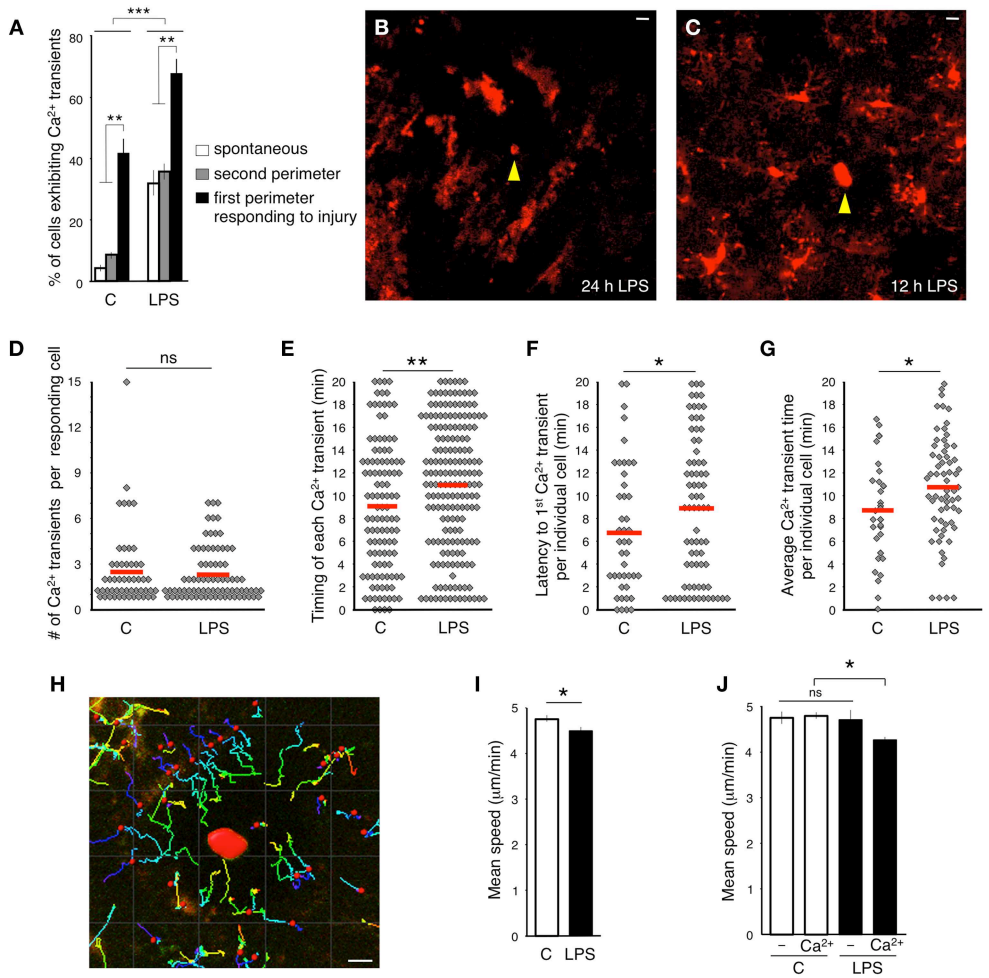

FIGURE 3 | Effect of systemic peripheral inflammation on intracellular calcium dynamics in microglia. (A) Percentage of microglia exhibiting Ca^{2+} transients in response to focal laser injury and LPS induced peripheral inflammation. White bars show the percentage of cells exhibiting spontaneous Ca^{2+} transients. Gray bars specify the percentage of 2nd perimeter microglia positive for Ca^{2+} transients. Black bars illustrate the percentage of Ca^{2+} positive 1st perimeter microglia. We define 1st perimeter microglia as the circle of microglial cells that are most proximal to the laser ablation site. Their processes always spread toward the injury. 2nd perimeter microglia have their cell bodies located farther away, behind the 1st perimeter microglia. 2nd perimeter microglial processes do not spread toward the injury in our experiments. **(B)** A representative image of inflammation-activated microglia with amoeboid-like appearance. Focal laser injury (yellow arrowhead) was induced 24 h after subcutaneous LPS administration and imaged immediately after the ablation. **(C)** Twelve hour after the injection, LPS-primed microglia maintained normal ramified morphology. Focal laser injury (yellow arrowhead) was induced 12 h after LPS administration. **(D)** A graph illustrating the distribution of the number of Ca^{2+} transients in responding cells during the entire imaging session. No significant (ns) differences were detected between control and LPS-primed cells. The red lines indicate the means. **(E)** Time between injury and each individual Ca^{2+} transient emerging in responding cells. **(F)** Latency between the time of injury and the first Ca^{2+} transient observed in a specific responding cell. **(G)** Latency from the time of injury to the average emergence time of all Ca^{2+} transients detected per one responding cell. **(H)** An example of tracking the microglial process movement with Imaris software. The injury site is marked in red. **(I)** Average speed of process protrusion was significantly reduced in LPS-primed microglia. **(J)** No process speed difference was found between LPS-primed microglia not exhibiting Ca^{2+} transients and control cells. In contrast, the mean process speed was significantly reduced in LPS-primed Ca^{2+}-positive microglia. Bar graphs are mean ± SEM from $n = 3$ mice (>10 cells per mouse), (>18 cells per mouse in **I–J**). $^{*}p < 0.05$, $^{**}p < 0.005$ by Student's t-test, $^{***}p < 0.02$ by a 2 × 3 factor ANOVA (treatments × groups). Scale bars: 10 μm.

processes in close apposition to the injury site (110 of 182; 60.4%), suggesting that in naïve microglia, Ca^{2+} activity is triggered in the vicinity of the lesion, either due to the high concentration of a diffusible factor or by the direct physical contact with the lesion. However, the distribution of Ca^{2+} transients in primed microglia was different and displayed an approximate 1:1 ratio (85, or 47.5%, showed transients before the contact and 94, or 52.5%, after the contact), suggesting that primed-microglia in the state of systemic peripheral inflammation are either more sensitized, or subjected to increased concentrations of diffusible factors, or both. There were no significant differences in number of Ca^{2+} transients per injury-evoked cell between LPS-primed and non-primed microglia, within 20 min after injury (**Figure 3D**). However, the latency between injury induction and

the emergence of the Ca^2 transients was significantly delayed in LPS-primed injury-evoked microglia (**Figures 3E–G**).

The amplitude of Ca^{2+} transients (ΔF) in LPS-primed microglia was not significantly different from control (LPS: 153.3 ± 19.2 vs. control: 128.9 ± 18.4; $p = 0.193$, Student's *t*-test; $n = 22$ transients in each group) nor was the difference in transient duration (LPS; 26.9 ± 1.9 s, vs. control: 25.0 ± 1.7 s; $p = 0.237$, Student's *t*-test; $n = 22$ transients per group).

Next, we measured the velocity of the processes protruding toward the focal injury. The tdTomato signal allowed for continuous monitoring of the bulbous endings, despite gradual photo bleaching (Supplementary Figures 1C,D), using the Imaris tracking algorithm (see the Materials and Methods, **Figure 3H**). In line with previous findings (Gyoneva et al., 2014), we determined that the average peak velocity of process extension was decreased in the LPS-primed microglia compared to controls (LPS; 4.53 ± 0.12 μm/min, vs. control; 4.80 ± 0.08 μm/min; $p = 0.038$, Student's *t*-test; $n > 58$ cells) (**Figure 3I**). Of note, this decrease was primarily accounted for by the LPS-primed microglia that exhibited Ca^{2+} transients (**Figure 3J**). In subsequent studies, we used LPS-primed microglia as an experimental baseline for additional pharmacological analyses.

PPADS and BAPTA-AM Have Differential Effects on Microglial Calcium Transients and Process Motility

The relationship between microglial Ca^{2+} transients and process motility in not well-understood. Therefore, we examined the dependence of process extension velocity on intracellular Ca^{2+} by clamping intracellular Ca^{2+} with cell-permeable BAPTA-AM. BAPTA-AM is converted in the cytoplasm to BAPTA, an intracellular Ca^{2+} chelator (Negulescu et al., 1989). As expected, topical application of BAPTA-AM through the craniotomy in LPS-primed mice gradually reduced the frequency of microglial Ca^{2+} transients (**Figure 4A**). Hence, Consistent with previous observations (Eichhoff et al., 2011), microglial Ca^{2+} transients are dependent on the availability of intracellular Ca^{2+}. Moreover, BAPTA-AM application significantly slowed down the process velocity at multiple time points post-administration (e.g., at 60 min, LPS; 4.41 ± 0.09 μm/min, vs. BAPTA-AM; 4.01 ± 0.07 μm/min; $p = 0.0214$, Student's *t*-test; $n = 3$ mice) (**Figure 4B**). However, after 2.5 h the differences were no longer significant. Our data imply that the velocity of microglial process protrusion toward the site of insult is dependent on permissive basal Ca^{2+} levels.

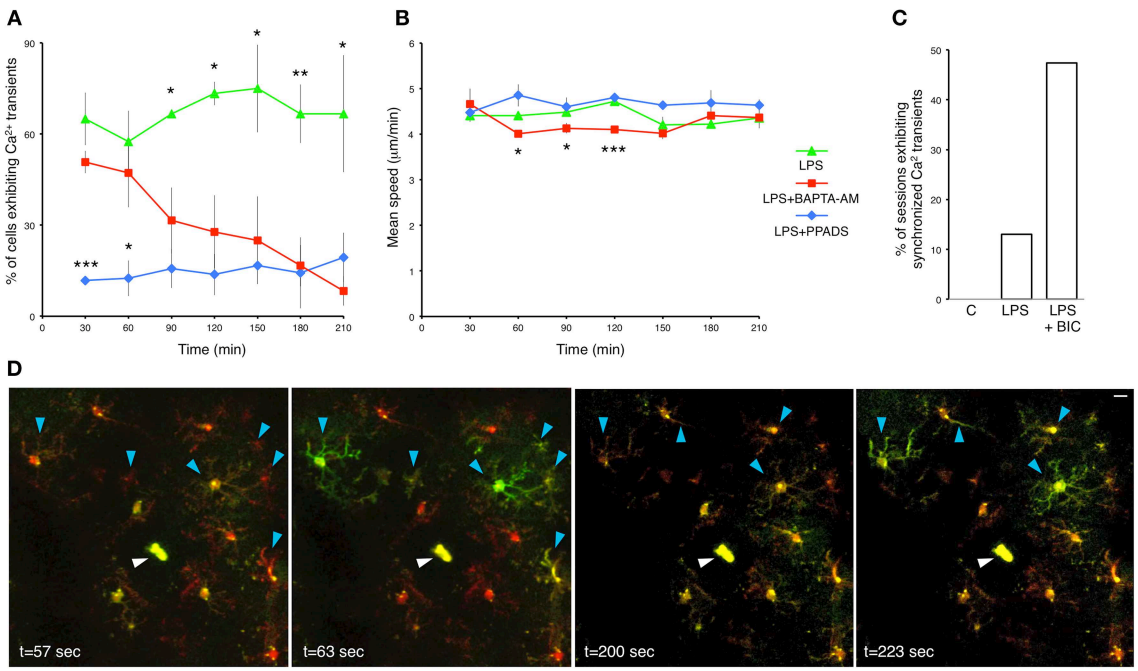

FIGURE 4 | Pharmacological interrogation of calcium responses in LPS-primed microglia. (A) Percentage of LPS-primed microglia exhibiting Ca^{2+} transients in response to focal laser injury as a function of time. BAPTA-AM (5 μg/ml) and PPADS (5 mM) were topically applied through the craniotomy 12 h after subcutaneous LPS administration. Two focal laser injuries were induced half an hour later, and were immediately followed by a 20 min long imaging session. Successive injury/imaging sessions were taken in 30 min intervals. Upper asterisks refer to statistical significance between LPS and LPS+BAPTA-AM treatments. Lower asterisks refer to statistical significance between LPS+BAPTA-AM and LPS+PPADS treatments. **(B)** Average speed of microglial processes as a function of time after BAPTA-AM and PPADS application. **(C)** A bar graph illustrating the fraction of imaging sessions which include synchronized microglial Ca^{2+} transients during 20 min recordings after focal laser injury. C-control: untreated mice. LPS: primed mice 12 h post-subcutaneous LPS administration. LPS+BIC: 12 h LPS-primed mice treated with topical application of bicuculline (250 μM). **(D)** Time lapse images from a representative 20 min recording session showing synchronized microglial Ca^{2+} transients traversing across the entire imaging field. This particular example shows two distinct waves at $t = 63$ s and $t = 223$ s. Blue arrowheads indicate cell bodies and processes of the microglia demonstrating synchronized Ca^{2+} waves. White arrowheads indicate the laser injury sites. Data are mean ± SEM ($n = 3$ mice, 4–10 cells for each time point per mouse). $^*p < 0.05$, $^{**}p < 0.01$, $^{***}p < 0.005$ by Student's *t*-test. Scale bar: 10 μm.

We cannot exclude the possibility that our experiments encompass various interactions between microglia and astrocytes. It has been shown that BAPTA-AM impedes microglia reaction to injury by blocking the astrocyte polarization response (Kim and Dustin, 2006). Injury induced Ca^{2+} increase in astrocytes has been shown to induce ATP secretion, which, in turn, activates purinergic receptors in microglia (Verderio and Matteoli, 2001). When we applied the P2X and P2Y antagonist PPADS, it reduced the frequency of Ca^{2+} transients in LPS-primed microglia with high efficiency (**Figure 4A**). In fact, PPADS down-regulated Ca^{2+} transients more rapidly than BAPTA-AM. Conversely, PPADS did not significantly affect the microglial process movement (**Figure 4B**). Hence, our results do not strongly support the role of purinergic receptors in process motility, but identify them as major mediators of intracellular Ca^{2+} transients.

Synchronous Wave-Like Calcium Activity in LPS-Primed Microglia

Coordinated Ca^{2+} activity in cortical astrocytic networks has been documented (Hirase et al., 2004b), but as yet there has been no evidence of synchronized Ca^{2+} activity in microglia *in vivo*. In our spontaneous, LPS-untreated preparations, synchronized Ca^{2+} activity was never detected (**Figure 4C**). However, we occasionally recorded synchronized Ca^{2+} transients in LPS-primed injury-responding microglia (**Figures 4C,D** and Supplementary Movie 6). About 13% (3 of 23) of 20 min recording sessions post-focal laser injury conducted on LPS-primed mice exhibited synchronized Ca^{2+} transients (**Figure 4C**). Bicuculline, a $GABA_A$ antagonist, attenuates inhibitory synaptic input onto neurons, tipping the excitation/inhibition balance in favor of excitation. As a result, bicuculline has been used to study neuronal hyperactivity in models of epilepsy and Alzheimer's disease (Schwartz and Bonhoeffer, 2001; Busche et al., 2008). In previous studies, microglial Ca^{2+} waves have not been detected *in vivo* after bicuculline administration (Eichhoff et al., 2011; Brawek and Garaschuk, 2013). In contrast, we observed frequent synchronized Ca^{2+} transients in microglia following bicuculline application (47%, 9 of 19, $n = 3$ mice) (**Figure 4C**). Some of the waves spread across the entire imaging field (**Figure 4D** and Supplementary Movie 6), while others were more confined (Supplementary Movie 7). Interestingly, these microglial waves often occurred concomitantly with transient brain motion (Supplementary Movies 7–8). We also observed an increase in cerebral blood flow after bicuculline administration as previously described (Hirase et al., 2004a), which typically manifested as brief expansions of blood capillaries (Supplementary Movie 8). Synchronized microglial Ca^{2+} activity following bicuculline-administration likely reflects epileptiform activity in local neuronal networks. Neuronal release of diffusible factors, such as ATP, activate purinergic receptors expressed by microglia and result in increased Ca^{2+} wave frequency and process motility (Sieger et al., 2012).

Discussion

Recording of intracellular signaling in microglia has been complicated by technical difficulties with dye loading and subsequent amplification of these distortions due to high immune reactivity of these cells. Although the use of cell culture systems and invasive cell labeling techniques provided important initial insights, these findings need to be validated under *in vivo* imaging conditions with endogenous indicators. Here, we targeted the endogenously encoded Ca^{2+} indicator GCaMP5G to all Iba1-positive microglia *in vivo* and used this novel mouse model to study intracellular Ca^{2+} signaling in both control and LPS-challenged microglia. We demonstrate that the PC::G5-tdT reporter mouse provides useful readout for both cell motility and intracellular Ca^{2+} activity in minimally invasive preparations.

In contrast with high motility of the processes, spontaneous intracellular Ca^{2+} transients in unchallenged, resting microglia are very infrequent in the anesthetized brain. In our model, only 4% of recorded microglia showed transients during the imaging period of 20 min, which is in conflict with similar experiments performed with electroporated dyes published by Eichhoff et al. In fact, the percentage of active microglia published by them (22%) is more akin to the situation we observe in LPS-primed microglia (34%), and implies that cell electroporation brings about microglial cell activation. Although our sampling frequency was limited to 0.125 Hz, it is unlikely that any transients went undetected since the average event duration was >20 s, and higher frame rate recordings did not reveal any short-duration events (Supplementary Figures 3E,F).

P2ry12 is the principal purinergic receptor expressed by microglia, along with P2ry13 (Hickman et al., 2013). Microglial response to focal injury in *P2ry12* mutants is attenuated (Haynes et al., 2006) and purinergic antagonists such as PPADS have been claimed to affect the motility of microglial processes responding to injury (Davalos et al., 2005). In our hands, PPADS application dramatically and rapidly decreased the percentage of cells displaying Ca^{2+} rises (**Figure 4A**), unlike the studies performed with synthetic dyes (Eichhoff et al., 2011). However, this PPADS-induced suppression of Ca^{2+} activity did not affect the velocity of bulbous end protrusion (**Figure 4B**). Thus, our data does not support the view that transient Ca^{2+} rises elicited via P2ry12 receptors contribute to process motility. When we applied BAPTA-AM, however, both the frequency of Ca^{2+} transients and velocity of protrusions were significantly decreased, implying that basal intracellular Ca^{2+} levels are still required for full motility in responding microglia.

The role for Ca^{2+} rises in microglia *in vivo* remains to be fully clarified. Studies performed on microglial cells *in vitro* strongly suggest that transient rises in Ca^{2+} concentration mediate the release of nitric oxide, certain cytokines, and chemokines, which are important for the recruitment and activation of various cell types (Hoffmann et al., 2003). It is of high importance to establish the neurological correlates of intracellular Ca^{2+} dynamics in these cells *in vivo*, with potential

implications for conditions where microglia are thought to play a role, such as epilepsy (Devinsky et al., 2013), Alzheimer's disease (Aguzzi et al., 2013) or schizophrenia (Mizoguchi et al., 2014). Development of more powerful genetic tools is therefore highly desirable and will facilitate progress in this field.

Author Contributions

PT conceived the study, PT and AP designed the experiments, AP performed *in vivo* imaging and data analysis, BX generated the *Aif1*-IRES-Cre driver, JG created the PC::G5-tdT mouse line, SP performed immunohistochemistry and confocal imaging, PT and AP wrote the manuscript with editing by JG, MC provided resources and proofread the manuscript.

Acknowledgments

We thank Matthew Hockin for critical reading of the manuscript, Nathan Smith for advice on two-photon imaging and Karl Lustig and June Wangerin for assistance with mouse husbandry. We gratefully acknowledge Arvonn Tully (Bitplane) for excellent Imaris software support and advice on data analysis. This work was funded by NIH R21 OD016562 (to PT) and NIH R01 MH093595 (to MRC).

Supplementary Material

The Supplementary Material for this article can be found online at: http://journal.frontiersin.org/article/10.3389/fnmol.2015.00012/abstract

References

Aguzzi, A., Barres, B. A., and Bennett, M. L. (2013). Microglia: scapegoat, saboteur, or something else? *Science* 339, 156–161. doi: 10.1126/science.1227901

Akerboom, J., Chen, T. W., Wardill, T. J., Tian, L., Marvin, J. S., Mutlu, S., et al. (2012). Optimization of a GCaMP calcium indicator for neural activity imaging. *J. Neurosci.* 32, 13819–13840. doi: 10.1523/JNEUROSCI.2601-12.2012

Berridge, M. J., Bootman, M. D., and Roderick, H. L. (2003). Calcium signalling: dynamics, homeostasis and remodelling. *Nat. Rev. Mol. Cell Biol.* 4, 517–529. doi: 10.1038/nrm1155

Brawek, B., and Garaschuk, O. (2013). Microglial calcium signaling in the adult, aged and diseased brain. *Cell Calcium* 53, 159–169. doi: 10.1016/j.ceca.2012.12.003

Busche, M. A., Eichhoff, G., Adelsberger, H., Abramowski, D., Wiederhold, K. H., Haass, C., et al. (2008). Clusters of hyperactive neurons near amyloid plaques in a mouse model of Alzheimer's disease. *Science* 321, 1686–1689. doi: 10.1126/science.1162844

Davalos, D., Grutzendler, J., Yang, G., Kim, J. V., Zuo, Y., Jung, S., et al. (2005). ATP mediates rapid microglial response to local brain injury *in vivo*. *Nat. Neurosci.* 8, 752–758. doi: 10.1038/nn1472

Devinsky, O., Vezzani, A., Najjar, S., De Lanerolle, N. C., and Rogawski, M. A. (2013). Glia and epilepsy: excitability and inflammation. *Trends Neurosci.* 36, 174–184. doi: 10.1016/j.tins.2012.11.008

Dissing-Olesen, L., Ledue, J. M., Rungta, R. L., Hefendehl, J. K., Choi, H. B., and MacVicar, B. A. (2014). Activation of neuronal NMDA receptors triggers transient ATP-mediated microglial process outgrowth. *J. Neurosci.* 34, 10511–10527. doi: 10.1523/JNEUROSCI.0405-14.2014

Eichhoff, G., Brawek, B., and Garaschuk, O. (2011). Microglial calcium signal acts as a rapid sensor of single neuron damage *in vivo*. *Biochim. Biophys. Acta* 1813, 1014–1024. doi: 10.1016/j.bbamcr.2010.10.018

Eyo, U. B., Peng, J., Swiatkowski, P., Mukherjee, A., Bispo, A., and Wu, L.-J. (2014). Neuronal hyperactivity recruits microglial processes via neuronal NMDA receptors and microglial P2Y12 receptors after status epilepticus. *J. Neurosci.* 34, 10528–10540. doi: 10.1523/JNEUROSCI.0416-14.2014

Garaschuk, O. (2013). Imaging microcircuit function in healthy and diseased brain. *Exp. Neurol.* 242, 41–49. doi: 10.1016/j.expneurol.2012.02.009

Gee, J. M., Smith, N. A., Fernandez, F. R., Economo, M. N., Brunert, D., Rothermel, M., et al. (2014). Imaging activity in neurons and glia with a Polr2a-based and cre-dependent GCaMP5G-IRES-tdTomato reporter mouse. *Neuron* 83, 1058–1072. doi: 10.1016/j.neuron.2014.07.024

Grienberger, C., and Konnerth, A. (2012). Imaging calcium in neurons. *Neuron* 73, 862–885. doi: 10.1016/j.neuron.2012.02.011

Gyoneva, S., Davalos, D., Biswas, D., Swanger, S. A., Garnier-Amblard, E., Loth, F., et al. (2014). Systemic inflammation regulates microglial responses to tissue damage *in vivo*. *Glia* 62, 1345–1360. doi: 10.1002/glia.22686

Haynes, S. E., Hollopeter, G., Yang, G., Kurpius, D., Dailey, M. E., Gan, W.-B., et al. (2006). The P2Y12 receptor regulates microglial activation by extracellular nucleotides. *Nat. Neurosci.* 9, 1512–1519. doi: 10.1038/nn1805

Hickman, S. E., Kingery, N. D., Ohsumi, T. K., Borowsky, M. L., Wang, L.-C., Means, T. K., et al. (2013). The microglial sensome revealed by direct RNA sequencing. *Nat. Neurosci.* 16, 1896–1905. doi: 10.1038/nn.3554

Hirase, H., Creso, J., and Buzsaki, G. (2004a). Capillary level imaging of local cerebral blood flow in bicuculline-induced epileptic foci. *Neuroscience* 128, 209–216. doi: 10.1016/j.neuroscience.2004.07.002

Hirase, H., Qian, L., Barthó, P., and Buzsáki, G. (2004b). Calcium dynamics of cortical astrocytic networks *in vivo*. *PLoS Biol.* 2:E96. doi: 10.1371/journal.pbio.0020096

Hoffmann, A., Kann, O., Ohlemeyer, C., Hanisch, U.-K., and Kettenmann, H. (2003). Elevation of basal intracellular calcium as a central element in the activation of brain macrophages (microglia): suppression of receptor-evoked calcium signaling and control of release function. *J. Neurosci.* 23, 4410–4419.

Jaffer, U., Wade, R. G., and Gourlay, T. (2010). Cytokines in the systemic inflammatory response syndrome: a review. *HSR Proc. Intensive Care Cardiovasc. Anesth.* 2, 161–175.

Jung, S., Aliberti, J., Graemmel, P., Sunshine, M. J., Kreutzberg, G. W., Sher, A., et al. (2000). Analysis of fractalkine receptor CX(3)CR1 function by targeted deletion and green fluorescent protein reporter gene insertion. *Mol. Cell. Biol.* 20, 4106–4114. doi: 10.1128/MCB.20.11.4106-4114.2000

Kim, J. V., and Dustin, M. L. (2006). Innate response to focal necrotic injury inside the blood-brain barrier. *J. Immunol.* 177, 5269–5277. doi: 10.4049/jimmunol.177.8.5269

Kondo, S., Kohsaka, S., and Okabe, S. (2011). Long-term changes of spine dynamics and microglia after transient peripheral immune response triggered by LPS *in vivo*. *Mol. Brain* 4:27. doi: 10.1186/1756-6606-4-27

Lee, S., Zhao, Y. Q., Ribeiro-Da-Silva, A., and Zhang, J. (2010). Distinctive response of CNS glial cells in oro-facial pain associated with injury, infection and inflammation. *Mol. Pain* 6:79. doi: 10.1186/1744-8069-6-79

Maier, S. F., Goehler, L. E., Fleshner, M., and Watkins, L. R. (1998). The role of the vagus nerve in cytokine-to-brain communication. *Ann. N. Y. Acad. Sci.* 840, 289–300. doi: 10.1111/j.1749-6632.1998.tb09569.x

Mizoguchi, Y., Kato, T. A., Horikawa, H., and Monji, A. (2014). Microglial intracellular Ca(2+) signaling as a target of antipsychotic actions for the treatment of schizophrenia. *Front. Cell. Neurosci.* 8:370. doi: 10.3389/fncel.2014.00370

Mostany, R., and Portera-Cailliau, C. (2008). A craniotomy surgery procedure for chronic brain imaging. *J. Vis. Exp.* 12:e680. doi: 10.3791/680

Nedergaard, M., Rodríguez, J. J., and Verkhratsky, A. (2010). Glial calcium and diseases of the nervous system. *Cell Calcium* 47, 140–149. doi: 10.1016/j.ceca.2009.11.010

Negulescu, P. A., Reenstra, W. W., and Machen, T. E. (1989). Intracellular Ca requirements for stimulus-secretion coupling in parietal cell. *Am. J. Physiol.* 256, C241–C251.

Nimmerjahn, A., Kirchhoff, F., and Helmchen, F. (2005). Resting microglial cells are highly dynamic surveillants of brain parenchyma *in vivo*. *Science* 308, 1314–1318. doi: 10.1126/science.1110647

Ousman, S. S., and Kubes, P. (2012). Immune surveillance in the central nervous system. *Nat. Neurosci.* 15, 1096–1101. doi: 10.1038/nn.3161

Paolicelli, R. C., Bolasco, G., Pagani, F., Maggi, L., Scianni, M., Panzanelli, P., et al. (2011). Synaptic pruning by microglia is necessary for normal brain development. *Science* 333, 1456–1458. doi: 10.1126/science.1202529

Schafer, D. P., Lehrman, E. K., Kautzman, A. G., Koyama, R., Mardinly, A. R., Yamasaki, R., et al. (2012). Microglia sculpt postnatal neural circuits in an activity and complement-dependent manner. *Neuron* 74, 691–705. doi: 10.1016/j.neuron.2012.03.026

Schwartz, T. H., and Bonhoeffer, T. (2001). *In vivo* optical mapping of epileptic foci and surround inhibition in ferret cerebral cortex. *Nat. Med.* 7, 1063–1067. doi: 10.1038/nm0901-1063

Sieger, D., Moritz, C., Ziegenhals, T., Prykhozhij, S., and Peri, F. (2012). Long-range Ca2+ waves transmit brain-damage signals to microglia. *Dev. Cell* 22, 1138–1148. doi: 10.1016/j.devcel.2012.04.012

Verderio, C., and Matteoli, M. (2001). ATP mediates calcium signaling between astrocytes and microglial cells: modulation by IFN-gamma. *J. Immunol.* 166, 6383–6391. doi: 10.4049/jimmunol.166.10.6383

Wake, H., Moorhouse, A. J., Jinno, S., Kohsaka, S., and Nabekura, J. (2009). Resting microglia directly monitor the functional state of synapses *in vivo* and determine the fate of ischemic terminals. *J. Neurosci.* 29, 3974–3980. doi: 10.1523/JNEUROSCI.4363-08.2009

Conflict of Interest Statement: The authors declare that the research was conducted in the absence of any commercial or financial relationships that could be construed as a potential conflict of interest.

frontiers in Molecular Neuroscience

METHODS
published: 08 June 2015
doi: 10.3389/fnmol.2015.00020

Wide-field Ca^{2+} imaging reveals visually evoked activity in the retrosplenial area

Tomonari Murakami[1]†, Takashi Yoshida[1,2†], Teppei Matsui[1] and Kenichi Ohki[1,2]**

[1] Department of Molecular Physiology, Graduate School of Medical Sciences, Kyushu University, Fukuoka, Japan, [2] CREST, Japan Science and Technology Agency, Tokyo, Japan

Due to recent advances of genetic manipulation, mouse brain has become a useful model for studying brain function, which demands whole brain functional mapping techniques in the mouse brain. In the present study, to finely map visual responsive areas in the mouse brain, we combined high-resolution wide-field optical imaging with transgenic mice containing the genetically encoded Ca^{2+} indicator, GCaMP3. With the high signal amplitude of GCaMP3 expressing in excitatory neurons, this system allowed neural activity to be observed with relatively fine spatial resolution and cell-type specificity. To evaluate this system, we examined whether non-visual areas exhibited a visual response over the entire surface of the mouse hemisphere. We found that two association areas, the retrosplenial area (RS) and secondary motor/anterior cingulate area (M2/AC), were significantly responsive to drifting gratings. Examination using gratings with distinct spatiotemporal frequency parameters revealed that the RS strongly responded to high-spatial and low-temporal frequency gratings. The M2/AC exhibited a response property similar to that of the RS, though it was not statistically significant. Finally, we performed cellular imaging using two-photon microscopy to examine orientation and direction selectivity of individual neurons, and found that a minority of neurons in the RS clearly showed visual responses sharply selective for orientation and direction. These results suggest that neurons in RS encode visual information of fine spatial details in images. Thus, the present study shows the usefulness of the functional mapping method using a combination of wide-field and two-photon Ca^{2+} imaging, which allows for whole brain mapping with high spatiotemporal resolution and cell-type specificity.

Keywords: wide-field Ca^{2+} imaging, transgenic mouse, GCaMP3, visual response, retrosplenial area

OPEN ACCESS

Edited by:
Katsuhiko Mikoshiba, RIKEN Brain Science Institute, Japan

Reviewed by:
Gabor Petzold, German Center for Neurodegenerative Diseases, Germany
Katsuei Shibuki, Brain Research Institute, Niigata University, Japan

****Correspondence:***
Kenichi Ohki and Tomonari Murakami, Department of Molecular Physiology, Graduate School of Medical Sciences, Kyushu University, Building A of Basic Science, 3-1-1 Maidashi, Higashi-ku, Fukuoka 812-8582, Japan
kohki@med.kyushu-u.ac.jp; t-mura@med.kyushu-u.ac.jp

† These authors have contributed equally to this work.

Received: *02 April 2015*
Accepted: *22 May 2015*
Published: *08 June 2015*

Citation:
Murakami T, Yoshida T, Matsui T and Ohki K (2015) Wide-field Ca^{2+} imaging reveals visually evoked activity in the retrosplenial area. Front. Mol. Neurosci. 8:20. doi: 10.3389/fnmol.2015.00020

Introduction

Whole brain functional mapping, which measures brain activity using techniques such as functional magnetic resonance imaging (fMRI), is useful to exhaustively explore and define areas related to particular information processing in humans and non-human primates (Belliveau et al., 1991; Stoewer et al., 2010; Mantini et al., 2012; Park and Friston, 2013). Although these techniques can be applied to smaller animals like mice (Desai et al., 2011; Jonckers et al., 2011; Guilfoyle et al., 2013), it is difficult to finely map responsive areas in the mouse brain because the spatial resolution

is insufficient to dissociate neural activity in small areas. Moreover, fMRI measures hemodynamic signal derived from neural populations including various cell-types, which makes it difficult to extract activity information from the particular cell-type.

Recently, owing to the development of imaging technique and genetic manipulation, mouse vision has been widely used as a model system to investigate detailed neural function for visual information processing. For example, previous studies using two-photon Ca^{2+} imaging have revealed spatial and functional organization of orientation selectivity in primary visual areas (V1; Ohki et al., 2005) and that neurons in higher visual areas surrounding V1 are specialized to process characteristic spatiotemporal frequency information (Andermann et al., 2011; Marshel et al., 2011; Roth et al., 2012). These visual areas send projection to many areas outside of the visual areas (Wang et al., 2011, 2012; Zingg et al., 2014). In primates, visually responsive areas, including sensory association areas such as parietal and frontal areas, has been defined (Stein and Stanford, 2008). In mice, however, it remains unclear which cortical area outside of visual areas exhibits visual response and it is important to define visual responsive areas for comprehensive understanding of mouse visual system.

In the present study, we performed wide-field Ca^{2+} imaging with transgenic mice expressing genetically encoded Ca^{2+} indicator (GECI), GCaMP3 in excitatory neurons (Zariwala et al., 2012) to map cortical areas responsive to drifting gratings over an entire surface of hemisphere. We found that two sensory association areas, retrosplenial area (RS) and secondary motor/anterior cingulate area (M2/AC), were significantly responsive to drifting gratings. RS more strongly responded to gratings with high-spatial and low-temporal frequencies (HSF–LTF) than gratings with low-spatial and high-temporal frequencies (LSF–HTF). Moreover, cellular imaging using two-photon microscopy revealed that the neurons in RS had orientation and direction selectivity. These results suggest that neurons in RS encode information about the orientation of edges and are specialized to process fine details of visual images. Thus, through these examinations, we show usefulness of functional mapping using a combination of wide-field and two-photon Ca^{2+} imaging.

Materials and Methods

Animal Preparation and Surgery for *In Vivo* Wide-Field Ca^{2+} Imaging

Emx1-IRES-cre (Gorski et al., 2002, Jax stock # 005628) and Ai38 (Zariwala et al., 2012, Jax stock # 014538) mice were obtained from the Jackson Laboratory. These mice were crossed to obtain transgenic mice in which all of the cortical excitatory neurons expressed GCaMP3. The transgenic mice (P60–90) were prepared for *in vivo* wide-field Ca^{2+} imaging. Anesthesia was induced and maintained during surgery with 3 and 1–2% isoflurane, respectively. During recording, mice were sedated with chlorprothixene (0.3–0.8 mg/kg, Sigma–Aldrich, St. Louis, MO, USA) and isoflurane was reduced to 0.5% (Smith and Häusser, 2010; Marshel et al., 2011; Akerboom et al., 2012). A custom-made metal head plate was attached to the skull using dental cement (Sun Medical Company, Ltd, Shiga, Japan). The skull over the cortex were kept moist for transparency, and sealed with artificial cerebrospinal fluid [ACSF; 150 mM NaCl, 2.5 mM KCl, and 10 mM HEPES (pH 7.4)] and a glass coverslip. Body temperature was maintained at 37°C using a heating pad. All experiments were carried out in accordance with the institutional animal welfare guidelines laid down by the Animal Care and Use Committee of Kyushu University, and approved by the Ethical Committee of Kyushu University.

In Vivo Wide-Field Ca^{2+} Imaging

Wide-field imaging of Ca^{2+} signals *in vivo* was performed using a macro zoom fluorescence microscope (MVX-10, Olympus, Tokyo, Japan), equipped with a 1× objective (1× MVX Plan Apochromat Lens, NA 0.25, Olympus). GCaMP3 was excited by a 100 W mercury lamp through a GFP mirror unit (U-MGFPHQ/XL, Olympus; excitation peak: 488 nm, emission peak: 507 nm). Ca^{2+} signals were collected at a frame rate of 10–20 Hz using a cooled CCD camera (DS-Qi1Mc, Nikon, Tokyo, Japan) controlled by NIS-elements BR (Nikon). For recording of the entire hemisphere, a rectangular region (12 mm × 9 mm) was imaged at 320 × 240 pixels, at a focus set at 0.75 mm in depth from the top of cortical surface which firstly comes into focus.

Animal Preparation and Surgery for *In Vivo* Two-Photon Ca^{2+} Imaging

Wild type mice (C57BL/6) were prepared for *in vivo* Ca^{2+} imaging as described previously (Ohki et al., 2005; Ohtsuki et al., 2012; Hagihara and Ohki, 2013). In brief, a custom-made metal plate was mounted on the skull, and a craniotomy was carefully performed above V1 or the RS region using stereotaxic coordinates. We dissolved 0.8 mM Oregon Green 488 BAPTA-1 AM (OGB1-AM, Life Technologies, Grand Island, NY, USA) in dimethyl sulfoxide with 20% pluronic acid and mixed it with ACSF containing 0.05 mM Alexa594 (Life Technologies) or 0.025 mM sulforhodamine 101 (SR101, Sigma–Aldrich). A glass pipette (3–5 μm tip diameter) was filled with this solution and inserted into the cortex at a depth of approximately 250 μm from the surface. The solution was pressure-ejected from the pipette (about 0.5 psi for 1 s, 10–20 times). After confirming OGB1-AM loading, the craniotomy was sealed with a coverslip. After surgery, the isoflurane concentration was reduced to 0.5% and chlorprothixene (0.3–0.5 mg/kg) was administered intramuscularly before recording experiments (Smith and Häusser, 2010; Marshel et al., 2011; Akerboom et al., 2012).

In Vivo Two-Photon Ca^{2+} Imaging

Changes in Ca^{2+} fluorescence in cortical neurons were monitored using a two-photon microscope (Nikon A1MP) equipped with a mode-locked Ti:sapphire laser (MaiTai Deep See, Spectra Physics, Santa Clara, CA, USA). The excitation light was focused with a 25× objective (Nikon PlanApo, NA: 1.10). The average laser power delivered to the brain was <20 mW, depending on the depth of focus. OGB1-AM was excited at

920 nm and the emission was filtered at 517–567 nm. Images were obtained using Nikon NIS Elements software. A square region of the cortex (512 × 512 pixels, approximately 250 or 330 μm on a side) was imaged at 30 Hz frame rate. Images were obtained from depths of 200–300 μm for experiments in layers 2/3. Stereotaxic coordinates of recording sites were 1–1.5 mm anterior from lambda, 2.5–3.0 mm lateral from the midline for V1, 2.0–2.5 mm anterior from lambda and approximately 0.5 mm lateral from midline for the RS which corresponded to the dysgranular area of the RS (Franklin and Paxinos, 2008).

Visual Stimulation

The visual stimulus sets were generated using custom-written programs running on PsychoPy (Peirce, 2007). Stimulus presentation was synchronized with frame acquisition of images using a counter board (NI USB-6501, National instruments, Austin, TX, USA). We positioned a 32-inch LCD monitor 18 cm from the mouse's right eye and the monitor was adjusted to be parallel to the mouse's right eye. In wide-field imaging, drifting sinusoidal-wave gratings (100% contrast) were presented in an aperture (40° diameter). The three parameter sets of SF and TF were used ([SF, TF] = [0.08, 1.0], [0.04, 2.0], [0.01, 4.0], [cycles per degree (cpd), Hz]). Each stimulus started with a blank period of uniform gray (6 s), which was followed by 2 s visual stimulation. The stimuli were presented in random order and repeated 50 times. In two-photon imaging, drifting square-wave gratings (100% contrast) were presented in full screen. The TF was set at 1.0–4.0 Hz and the SF was set at 0.01–0.16 cpd for the RS recording. The SF and TF were set at 2.0 Hz and 0.04 cpd for V1 recording. Each stimulus started with a blank period of uniform gray (4 s), which was followed by 4 s visual stimulation. The eight direction stimuli were presented in random order and repeated 10–15 times.

Data Analysis

Images were analyzed with Matlab (Mathworks, Natick, MA, USA) and ImageJ (National Institutes of Health, USA). In wide-field imaging experiments, images were realigned by maximizing the correlation between frames. The baseline signal (F) of each trial was average of Ca^{2+} signals during 1 s before each stimulus onset. Visual response signal (dF) of each trial was average of Ca^{2+} signals during each stimulus period. To obtain response map, we calculated the fluorescence ratio change (dF/F) map of each trial, and averaged them across trials. The T-value map was calculated across the dF/F maps of 50 trials. These maps were spatially smoothed with a Gaussian filter (size: 25 × 25 pixels; sigma: 5 pixels). To define regions of interest (ROIs), six cortical regions [V1, RS, M2/AC, primary auditory area (A1), primary somatosensory area (S1), and primary motor area (M1)] were selected by reference to stereotaxic coordinates in the Mouse Brain Atlas (Franklin and Paxinos, 2008). ROI size was a 7 × 7 pixel square (about 260 μm × 260μm). Time courses of individual ROIs were extracted by summing pixel values within ROIs. Time course of each trial was normalized by F of each trial. We defined the initial rise of response to visual stimuli as the time point when calcium signal exceeded the threshold (three SD of the baseline signal).

For pixel-based analysis in two-photon imaging experiments, images were averaged over stimulus repetitions and stimulus period. dF maps were obtained by subtracting the averaged image of the blank period from that of each stimulus (total eight directions). Color-coded direction and orientation maps were obtained from these eight direction dF maps and four orientation dF maps which were average of the two opposite direction dF maps. The hue of each pixel was determined by the preferred direction and orientation defined by vector averaging, the color saturation was proportional to [1–circular variance (CV)] of the direction and orientation, and the brightness was proportional to the F to the best direction and orientation. Color-coded maps were spatially smoothed with a Gaussian filter (size: 5 × 5 pixels; sigma: 1 pixel).

For cell-based analysis in two-photon imaging experiments, ROIs of individual neurons were automatically identified by template matching with a circular template about the size of the soma. Automatically identified neurons were visually inspected, and errors were corrected manually. Time courses of individual neurons were extracted by summing pixel values within cell contours. Slow drift of the baseline signal over minutes was removed by a low-cut filter (Gaussian, cut-off, 2 minutes). High frequency noise was removed by a high-cut filter [third order Savitzky–Golay filter with 31 time points (∼1 second)] only for time course presentation. To minimize neuropil signal contamination, the time course of the neuropil signal obtained from surrounding part of a cell body was subtracted from each neuron's time course after multiplying by a scaling factor (Kerlin et al., 2010). The scaling factor was determined in each field of view (FOV) by computing the ratio of the fluorescent signal of the blood vessel to that of the surrounding background signal averaged across several blood vessels. After removing the neuropil signal, the time course was used to obtain the signal change (mean fluorescence change normalized by baseline, dF/F) in response to each stimulus direction/orientation. Visually responsive neurons were defined by the following criteria; $p < 0.01$ by analysis of variance (ANOVA) applied to dF/F across blank and eight direction periods and dF/F > 2% in response to the best direction. Of all responsive neurons, direction-selective neurons were defined by ANOVA ($p < 0.01$) across eight directions and direction selectivity index (DSI > 0.33, see below). Orientation-selective neurons were defined by ANOVA ($p < 0.01$) across four orientations and orientation selectivity index (OSI > 0.33, see below). In the analysis of the RS, in each FOV, we chose a single spatial and temporal frequency parameter set in which the largest number of responsive neurons was obtained, and used data of this parameter for further analyses.

For responsive neurons, DSI and OSI were defined as follows: DSI, (response to preferred direction − response to null direction)/(response to preferred direction + response to null direction); OSI, (response to preferred orientation − response to orthogonal orientation)/(response to preferred orientation + response to orthogonal orientation). Direction and orientation selectivities were also assessed by (1−CV) of direction and orientation, respectively.

Detection of GCaMP3 Expression of Neurons and Astrocytes

GCaMP3 expression of neurons and astrocytes of a Emx1-GCaMP3 mouse was recorded using two-photon microscope. To label astrocytes, SR101 was injected to layer 2/3. We imaged three planes at the depth of 180–260 μm. ROIs of individual neurons and astrocytes were manually identified by cropping around SR101 negative and positive cells, respectively ($n = 15$ cells each from three planes). GCaMP3 localized at cytosol with excluding nucleus. Therefore, the GCaMP3 intensities of individual cells were determined as the top 10% intensities of all pixels in each ROI. ROIs of blood vessels running horizontally were manually identified, and the background intensity in each plane was defined as GCaMP3 intensity averaged across vessel ROIs. The background intensity was subtracted from the GCaMP3 intensities of cells in the same plane. The subtracted intensities of cells were normalized by averaged intensities of SR101 negative cells (neurons) in each plane.

Statistical Analyses

All data are presented as the mean ± SEM, unless stated otherwise. Visually responsive ROIs of wide-field imaging were defined by Student's *t*-test ($p < 0.05$). An ANOVA was performed when more than two groups were compared, which was followed by Tukey's honestly significant difference (HSD) test. Throughout the study, $p < 0.05$ was considered statistically significant, other than the definitions of visually responsive ROIs and selective neurons. In wide-field imaging experiments, the sample size n was defined as the number of animals. In two-photon imaging experiments, the sample size *n* was defined as the number of neurons.

Results

RS and M2/AC were Responsive to Drifting Gratings

To evaluate the ability of functional mapping by wide-field Ca^{2+} imaging in GECI transgenic mice, we explored visually responsive areas over the entire hemisphere including areas outside of the visual cortices. We recorded transcranial Ca^{2+} signals from Emx1-GCaMP3 mice (Zariwala et al., 2012) to monitor the visual response to drifting gratings (0.02 cpd, 1.0 Hz) under light anesthesia (**Figure 1A**). Because cre expression is observed in both glial cells and excitatory neurons in the Emx1-IRES-cre line (Gorski et al., 2002), we checked the GCaMP expression in astrocytes with injection of SR101 into Emx1-GCaMP3 mice (Supplementary Figure S1). Compared to GCaMP3 expression of neurons at the cytosol, we observed significantly weaker GCaMP3 expression in SR101 positive astrocytes (Supplementary Figure S1F). Moreover, recent studies reported that astrocytes do not respond to grating stimuli in mouse visual cortex (Bonder and McCarthy, 2014; Paukert et al., 2014). Therefore, we considered that the GCaMP3 signals of astrocytes were negligibly small. **Figures 1B–D** show an example of recorded transcranial visual response. Apparent visual responses were observed in the V1 and lateral and medial higher visual areas (**Figures 1B,C**). Outside of the visual areas, we found that the RS and M2/AC responded to the gratings. Visual responses in these areas were significant (**Figures 1B–D**, V1: $p < 10^{-26}$, RS: $p < 10^{-5}$, M2/AC: $p < 0.01$; Student's *t*-test), though the response amplitudes in the RS and M2/AC were smaller than those in visual areas. A significant response was not observed in other areas (**Figure 1D**, A1: $p = 0.155$, S1: $p = 0.253$, M1: $p = 0.733$; Student's *t*-test). Population analysis of the response amplitudes across six mice confirmed that the V1, RS and M2/AC were significantly responsive to gratings (**Figure 1E**, V1: $p < 10^{-4}$, RS: $p < 0.007$, M2/AC: $p < 0.047$), but other areas were not (A1: $p = 0.893$, S1: $p = 0.166$, M1: $p = 0.859$; Student's *t*-test). Because the response in V1 seemed to begin earlier than those in the RS and M2/AC in the representative animal (**Figure 1B**), we compared the initial rise of the visual responses among these three areas. The initial rise of response in the RS and M2/AC were delayed compared with V1, and the difference between V1 and M2/AC was statistically significant across animals (**Figures 1F,G**, $p < 0.05$; ANOVA and *post hoc* Tukey's HSD test). Taken together, these results reveal that the RS and M2/AC respond to drifting gratings with latency comparable to that in V1.

Visual Response Properties of the RS and M2/AC

We next investigated the visual response properties of the RS and M2/AC. Previous studies in mice have reported that low speed gratings (12.5 °/s) with high spatial and low temporal frequency [HSF–LTF; (0.08 cpd, 1.0 Hz)] evoke visual responses in a set of visual areas belonging to the ventral stream, and high speed gratings (200 °/s) with low spatial and high temporal frequency [LSF-HTF; (0.02 cpd, 4.0 Hz)] evoke visual responses in another set of areas belonging to the dorsal stream (Andermann et al., 2011; Marshel et al., 2011). Thus, we used three grating stimuli with distinct SF and TF ([cpd, Hz] = [0.08, 1.0], [0.04, 2.0] and [0.02, 4.0]; Speeds of these gratings were 12.5, 50 and 200 °/s, respectively; **Figure 2A**) to examine whether the RS and M2/AC exhibit response properties similar to those of the visual areas belonging to the ventral or dorsal streams.

This analysis revealed distinct response properties between V1 and the two association areas. V1 strongly responded to gratings of all three sets of parameters with slight preference to low speed (**Figure 2C**; averaged time courses of representative animal). The RS exhibited a stronger response to low speed gratings than the others (**Figure 2E**). The M2/AC also showed slightly higher response to low speed gratings; however, the response amplitude was small (**Figure 2F**). As an example of dorsal stream in mouse extrastriate cortex, we examined visual response in rostrolateral area (RL), which was identified as a discrete region separated from V1 based on visual response during stimulus period (**Figures 1B** and **2B**). As with a previous report (Marshel et al., 2011), the RL showed higher response to high speed gratings (**Figure 2D**).

Population analysis across six animals showed that the visual response in the RS was significantly stronger following low speed grating when compared with other gratings (**Figure 2I**, $p < 0.05$; ANOVA and *post hoc* Tukey's HSD test). The M2/AC

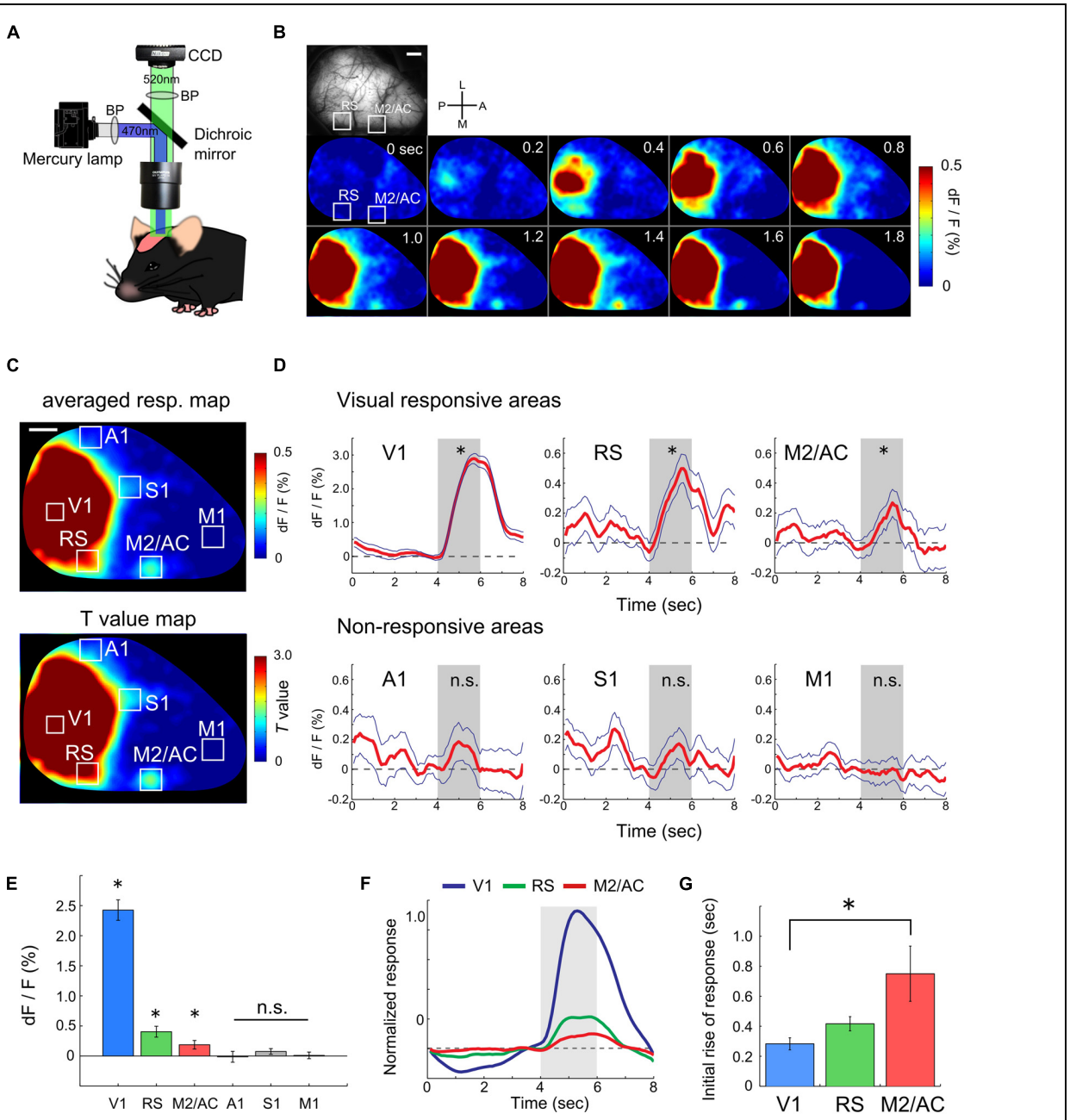

FIGURE 1 | Functional mapping of visual responsive areas.
(A) Experimental setup of wide-field Ca^{2+} imaging. **(B)** An example of a visual response in an entire hemisphere. (Top-left) Shows field of view (FOV). White two squares indicate regions of the RS and M2/AC. From upper left to lower right, sequential Ca^{2+} imaging snapshots from stimulus onset are presented (frame rate at 200 ms). **(C)** Representative response map averaged across 50 trials (top) and corresponding *T*-value map (bottom). Same animal as in **(B)**. **(D)** Representative average time courses of visually responsive (upper) and non-responsive areas (bottom). Each time course was obtained from regions of interests (ROIs) located in each area. ROI size was 260 μm × 260 μm which smaller than the white squares in **(B)** and **(C)**. Blue line: SE. Dashed line: baseline of Ca^{2+} signal. Gray shade: stimulus period. **(E)** Averaged signal change (dF/F) across animals (n = 6 mice). **(F)** Averaged time courses of the visual response in V1, RS, and M2/AC across animals (n = 6 mice). **(G)** Timing of the initial rises of the visual response. Error bar: SE, $*p < 0.05$, n.s.: non-significant, by Student's *t*-test in **(D)** and **(E)**, and by ANOVA and *post hoc* Tukey's HSD test in **(G)**. Scale bars in **(B)** and **(C)**: 1 mm.

also showed a stronger response as the speed of gratings became slower, but the effect was not significant (**Figure 2J**, $p = 0.309$; ANOVA). The RL showed a stronger response as the speed of gratings became higher, but the effect was not significant (**Figure 2H**, $p = 0.196$; ANOVA). In V1, there was no significant difference between the responses to three gratings (**Figure 2G**, $p = 0.139$; ANOVA), although V1 had a slight tendency to respond strongly to low speed gratings, similar to

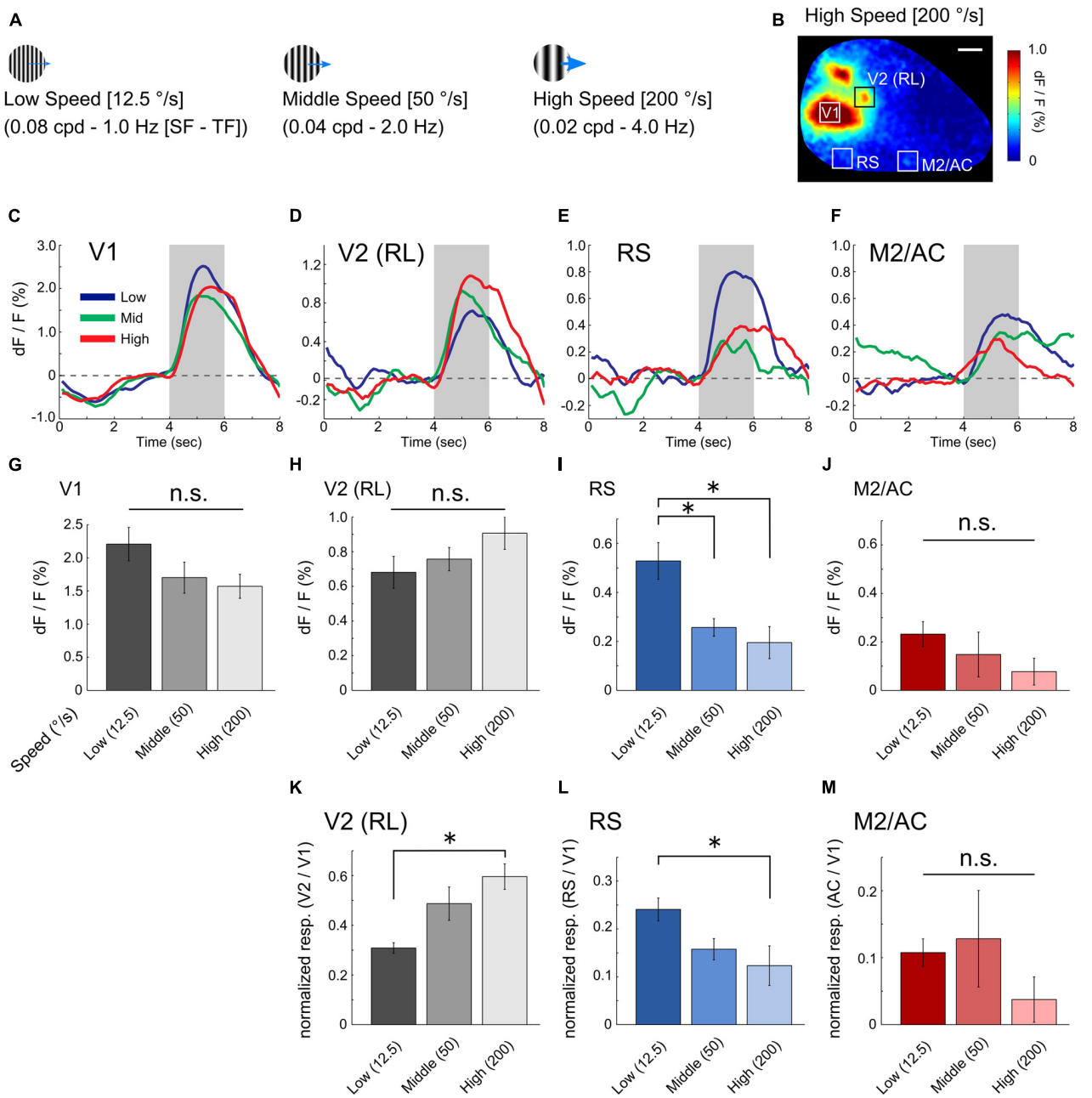

FIGURE 2 | Visual response properties in V1, RS, and M2/AC. **(A)** Schematics of drifting gratings with three spatiotemporal frequency parameters. **(B)** An example of the visual response to high speed gratings. **(C–F)** Averaged time courses of V1, V2 (RL), RS, and M2/AC in the representative animal. **(G–J)** Averaged signal changes in visual response to three gratings in V1 (**G**, from left to right, 2.208 ± 0.251%, 1.701 ± 0.234%, 1.570 ± 0.181%), RL (**H**, 0.680 ± 0.092%, 0.757 ± 0.067%, 0.906 ± 0.093%), RS (**I**, 0.528 ± 0.075%, 0.257 ± 0.036%, 0.195 ± 0.066%), and M2/AC (**J**, 0.232 ± 0.051%, 0.148 ± 0.092%, 0.077 ± 0.055%). **(K–M)** Normalized response in the RL (**K**, 0.308 ± 0.022, 0.487 ± 0.067, 0.596 ± 0.051), RS (**L**, 0.241 ± 0.023, 0.158 ± 0.022, 0.123 ± 0.041), and M2/AC (**M**, 0.108 ± 0.020, 0.128 ± 0.072, 0.03 ± 0.034). Averaged across animals ($n = 6$ mice). Error bar: SE, $^*p < 0.05$, n.s.: non-significant by ANOVA and *post hoc* Tukey's HSD test. Scale bar in **(B)**: 1 mm.

the RS and M2/AC. To examine whether the preference for low speed gratings in the RS and M2/AC was stronger than that in V1, we normalized the responses in the RS and M2/AC by that in V1 for each stimulus condition (**Figures 2L,M**). In the RS, the normalized visual response to low speed gratings remained stronger than the response to high speed gratings ($p < 0.05$; ANOVA and *post hoc* Tukey's HSD test). In M2/AC, the normalized visual response to low speed and middle speed gratings seemed stronger than the response to high speed gratings, but the effect was not significant ($p = 0.38$; ANOVA). In

RL, the normalized response to high speed gratings was stronger than that to low speed gratings (**Figure 2K**, $p < 0.05$; ANOVA and *post hoc* Tukey's HSD test). Taken together, these results suggest that the RS contains characteristic functional features, distinct from V1, and similar to visual areas belonging to the ventral stream (Marshel et al., 2011).

Orientation and Direction Selectivity of Neurons in the RS

We found that the RS was responsive to visual stimulation, but it was still unknown whether information associated with the direction and orientation of the drifting gratings was transmitted to the RS. Because wide-field Ca^{2+} imaging lacks cellular resolution, we could not examine orientation and direction selectivity of individual neurons. Thus, we recorded neural activity at the cellular level using two-photon Ca^{2+} imaging to examine orientation and direction selectivity of neurons in the RS. Unfortunately, fluorescent signals from Emx1-GCaMP3 mice were not bright enough for cellular imaging, thus the synthetic Ca^{2+} indicator (OGB1-AM) was injected in the RS (**Figure 3A**; 2.0–2.5 mm anterior from lambda and 0.5–1.0 mm left from the central suture) of wild-type mice and the visual response of neurons loaded with the indicator was monitored. **Figure 3B** shows examples of orientation and direction maps. Ca^{2+} signal time courses of two representative neurons clearly showed a selective response to gratings drifting in a particular direction (**Figure 3C**).

Next, we compared the response properties of neurons in the RS with those in V1 (RS: $n = 645$ neurons from three mice; V1: $n = 708$ neurons from two mice). Compared with neurons in V1, the proportion of visually responsive neurons in the RS was very low (**Figure 4A**, V1: 73.1%, 518/708 neurons; RS: 12.7%, 82/645 neurons). However, many of the responsive neurons in the RS were orientation and direction selective, (**Figures 4B,C**; Direction selective neurons: 56.1%; Orientation selective neurons: 67.1%), at a proportion comparable to those in V1 (Direction selective neurons: 65.8%; Orientation selective neurons: 74.3%). OSI, DSI and 1–CV (direction) in the RS were higher than those in V1[**Figures 4D,F,G**; OSI, V1: 0.66 ± 0.01, RS: 0.83 ± 0.03, $p < 10^{-7}$; DSI, V1: 0.49 ± 0.01, RS: 0.65 ± 0.04,$p = 10^{-4}$; 1–CV (direction), V1: 0.38 ± 0.01, RS: 0.52 ± 0.03, $p < 0.001$; Wilcoxon's rank-sum test]. However, there was no significant difference in 1–CV (orientation) between the RS and V1 (**Figure 4E**, V1: 0.50 ± 0.01, RS: 0.55 ± 0.03; $p = 0.103$). These results suggest that neurons in the RS encode information associated with the orientation and direction of the edges.

Discussion

In the present study, we performed whole brain functional mapping of visual responsive areas using high-resolution wide-field optical imaging with transgenic mice expressing GCaMP3. We found that two association areas, the RS and M2/AC, were significantly responsive to drifting gratings. Moreover, the RS preferred low speed gratings with HSF–LTF. Finally, we performed cellular imaging using two-photon microscopy to examine whether neurons in RS were selective for direction and orientation of the gratings. These results indicate that neurons in the RS encode information associated with the orientation of edges and are specialized to process fine details in images rather than fast movement. Thus, the present study reveals the usefulness of wide-field Ca^{2+} imaging in GECI transgenic mice for whole brain functional mapping.

Advantages of Wide-Field Ca^{2+} Imaging in GECI Transgenic Mice

Wide-field Ca^{2+} imaging in GCaMP transgenic mice is a useful method owing to some advantages for functional mapping. One of the advantages is the ability to monitor cell-type specific activity. For example, expression of GCaMP3 in Ai38 mice can be controlled by the cell type-specific Cre-driver mouse lines (Madisen et al., 2010; Gerfen et al., 2013). In our study, we monitored activity of excitatory neurons, using Emx1-GCaMP3 mice. Unlike fMRI, intrinsic signal optical imaging and voltage sensitive dye (VSD) imaging, which record hemodynamic or VSD signals reflecting population activity, most likely derived from all cell-types, wide-field Ca^{2+} imaging in the cell-type specific transgenic mouse lines is a convenient way to overcome this point.

Another advantage is that the Ca^{2+} signal amplitude of GCaMP is stronger than the intrinsic signals of hemodynamics and flavoproteins (Vanni and Murphy, 2014). Although intrinsic optical imaging of both hemodynamics and flavoprotein signals are widely used for functional mapping (Kalatsky and Stryker, 2003; Tohmi et al., 2006), the strong signal amplitude of GCaMP should be useful for reliable mapping. Indeed, we noticed that wide-field Ca^{2+} imaging in GCaMP3 transgenic mice is more efficient for retinotopy mapping across visual areas than intrinsic optical imaging (unpublished observation). Moreover, in the present study, we could detect weak activity of the RS and M2/AC to grating, most likely because of the strong signal amplitude of GCaMP3 (**Figure 1**). Indeed, we could not detect visual response in RS or M2/AC using intrinsic signal imaging with wild-type mice under the same anesthetic condition.

Moreover, wide-field imaging in GCaMP transgenic mice can be followed by two-photon imaging for cellular activity observation in the same animal. In a previous study, combination of wide-field and two-photon imaging revealed cellular-scale spatial distributions of auditory stimulus tuning in an area-scale functional map in A1 of GCaMP3 transgenic mice (Issa et al., 2014). Unfortunately, in the present study, imaging of the RS in Emx1-GCaMP3 mice with two-photon microscopy showed visual responses only in a small number of neurons, which was insufficient for population analysis (Supplementary Figure S2). In V1, we detected more responsive neurons by two-photon imaging in Emx1-GCaMP3 mice than in the RS. The reason why we could record more responsive neurons using OGB1-AM than GCaMP3 is probably because OGB1-AM is more sensitive to few action potentials than GCaMP3 (Akerboom et al., 2012). Recently reported improved GCaMP subtypes and their transgenic lines (Chen et al., 2013; Madisen et al., 2015) could be applicable to multi-scale imaging even in higher association areas. Taken

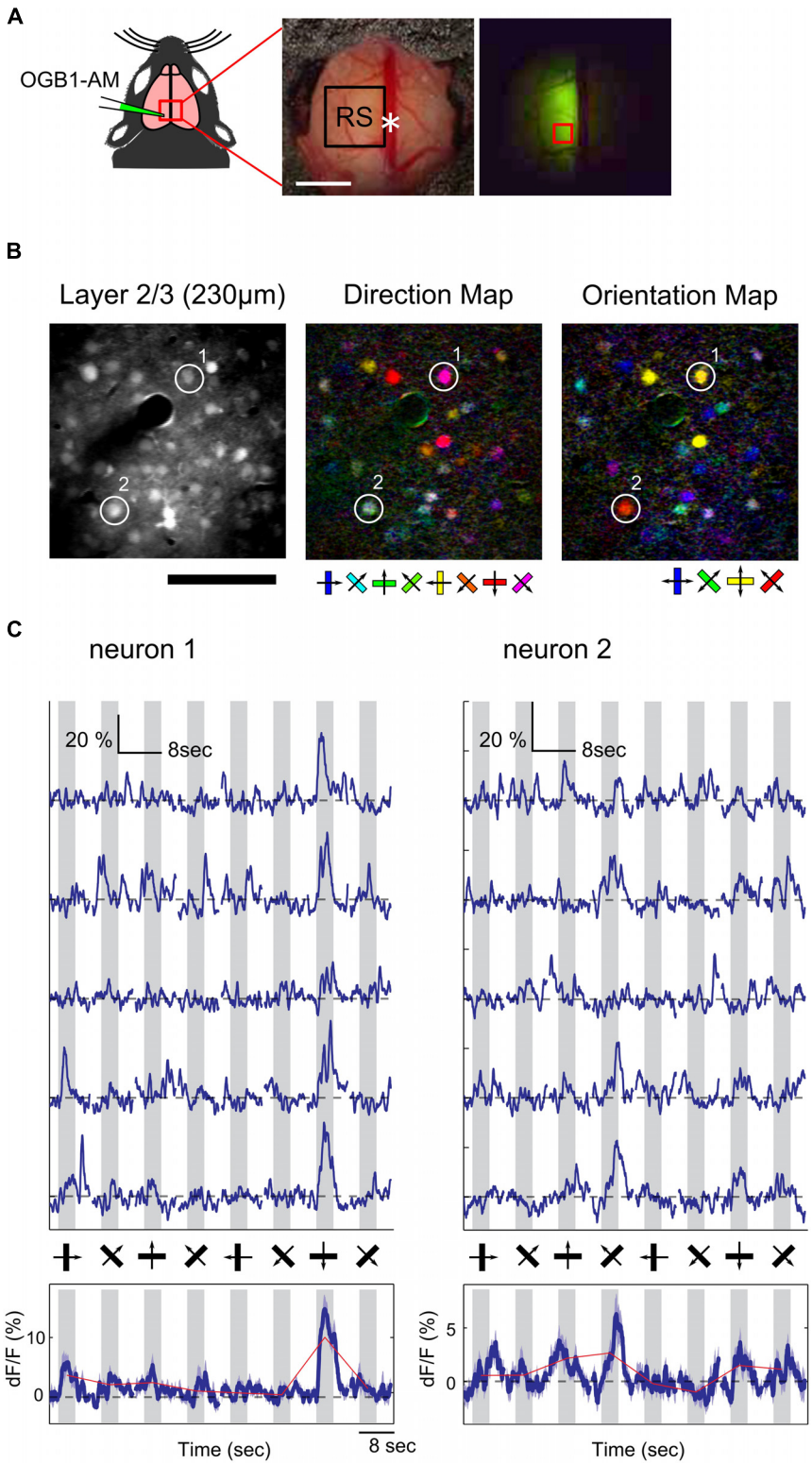

FIGURE 3 | Two-photon Ca^{2+} imaging in the RS. (A) Schematic of OGB1-AM injection in the RS. White asterisk: landmark position of the RS (2.5 mm anterior from lambda). Scale bar, 1 mm. (Right) An example of an OGB1-AM injected region. Red square: imaging FOV shown in **(B)**. **(B)** Representative FOV (left) and color-coded maps of preferred direction (center) and orientation (right) of neurons in the RS. Scale bar: 100 μm. **(C)** Representative time courses of two neurons shown in **(B)**. (Upper) Examples of five trials. (Bottom) Averaged time courses from 15 trials. Dashed line: baseline of Ca^{2+} signal. Gray shade: stimulus period.

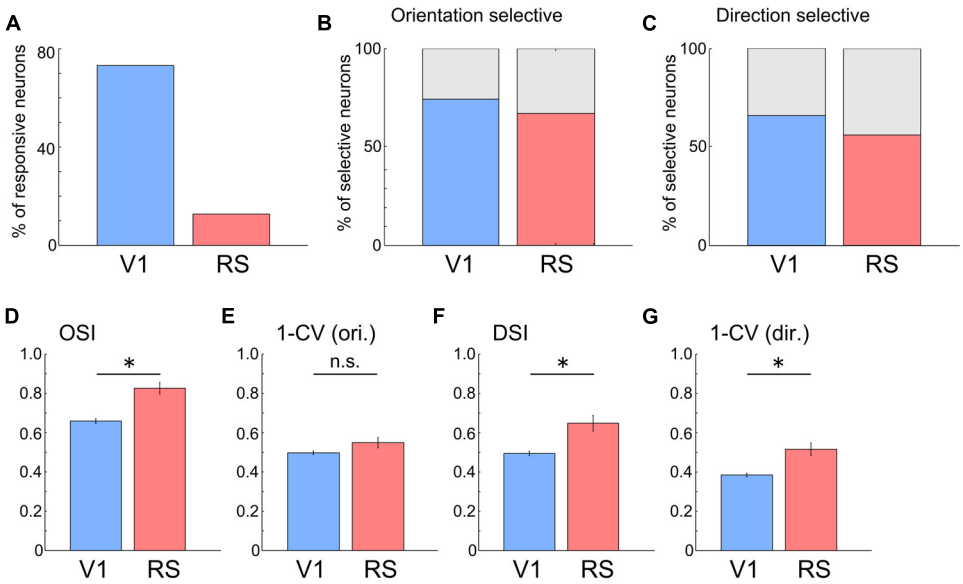

FIGURE 4 | Orientation and direction selectivity in the RS.
(A) Proportion of responsive neurons to all recorded neurons. V1: 73.1%, 518/708 neurons; RS: 12.7%, 82/645 neurons. **(B)** Proportion of orientation selective neurons to all responsive neurons. V1: 74.3%. RS: 67.1%. **(C)** Proportion of direction selective neurons to all responsive neurons. V1: 65.8%. RS: 56.1%. **(D–G)** Comparison of OSI (**D**, V1: 0.66 ± 0.01, RS: 0.83 ± 0.03), 1−CV (orientation) (**E**, V1: 0.50 ± 0.01, RS: 0.55 ± 0.03), DSI (**F**, V1: 0.49 ± 0.01, RS: 0.65 ± 0.04) and 1−CV (direction) (**G**, V1: 0.38 ± 0.01, RS: 0.52 ± 0.03) between neurons in V1 and RS. *$p < 0.05$, n.s.: non-significant by Wilcoxon's rank-sum test.

together, wide-field Ca^{2+} imaging in GECI transgenic mice is a promising new tool for functional mapping of cortical areas.

Visual Response in the RS and M2/AC

In mouse, several higher visual areas surrounding V1 are specialized to process characteristic spatiotemporal frequency information (Andermann et al., 2011; Marshel et al., 2011; Roth et al., 2012). These areas are considered to constitute two visual pathways corresponding to the dorsal and ventral pathways in primates (Ungerleider and Mishkin, 1982; Felleman and Van Essen, 1991). The RS and M2/AC receive projections from these higher visual areas (Wang et al., 2011, 2012; Zingg et al., 2014), and there are reciprocal connections between the RS and M2/AC (Oh et al., 2014; Zingg et al., 2014). Optogenetic and electrical stimulations of V1 and higher visual areas support the connections from the visual areas to the RS and M2/AC (Lim et al., 2012; Hishida et al., 2014). A previous study (Mohajerani et al., 2013) using VSD imaging has shown that VSD signal is restricted within the RS, M2/AC and visual areas only during short time window after flashed LED stimulation (around 55 ms after stimulation), and then quickly spreads over the entire cortex (>60 ms after stimulation). This is probably because VSD signal reflects both sub- and supra-threshold activity, while Ca^{2+} signal reported by GCaMP3 detects mostly supra-threshold activity, suitable for detecting the visually responsive areas which show supra-threshold response to visual stimulation. Further, visual response properties of the RS such as orientation, direction, spatial frequency, and temporal frequency selectivity remained unknown. To the best of our knowledge, the present study is the first to examine and characterize the visual response properties of the RS.

The RS of mice receives projection mainly from three visual areas, the posteromedial area (PM), anteromedial area (AM), and anterior higher visual area (A; Wang et al., 2012). These three areas exhibit distinct visual response properties. The previous three studies using two-photon imaging have reported that neurons in the PM prefer low speed gratings with HSF-LTF (Andermann et al., 2011; Marshel et al., 2011; Roth et al., 2012). In contrast, the majority of neurons in the AM are specialized to process high speed gratings with LSF–HTF, whereas the minority of neurons are selective to HSF–LTF (Marshel et al., 2011). Similarly, it was reported that neurons in area A were selective to high speed gratings (Gao et al., 2007). These studies suggest that AM and A belong to dorsal stream. Thus, among the three areas, the selectivity of the PM is similar to that of the RS, which suggests that visual responses of the RS are derived mostly from the PM, rather than the other two areas. Another possibility is that neurons in the AM and A projecting to the RS may be the minority of neurons that have selectivity to HSF–LTF (Glickfeld et al., 2013; Matsui and Ohki, 2013).

As for the functional properties, PM (Andermann et al., 2011; Marshel et al., 2011; Roth et al., 2012) and RS (present study) prefers low speed gratings, as other V2 areas belonging to ventral stream. These studies may suggest that RS and PM have a similar property of the ventral stream. However, PM and RS are thought to belong to dorsal stream from their areal location and inter-areal connections (Wang et al., 2012). Moreover, psychophysical and lesion studies of PM suggest that PM is important for optomotor learning (Prusky et al., 2008; Umino et al., 2008), and

RS is also considered important for spatial navigation and spatial working memory (Vann et al., 2009; Kravitz et al., 2011; Yoder et al., 2011). These studies suggest that RS and PM are part of the dorsal stream (Glickfeld et al., 2014). Thus, it is more likely that the dorsal stream may contain two distinct pathways to process both inputs of high and low speed gratings.

Visual information processing in the RS is considered important for spatial navigation and spatial working memory (Vann et al., 2009; Kravitz et al., 2011; Yoder et al., 2011). The RS has head direction neurons, which become active when the mouse turns in a particular direction (Cho and Sharp, 2001). These studies also suggest that RS belong to the dorsal stream. Moreover, the RS encodes and stores memory of the landmark in the water maze task (Czajkowski et al., 2014). It is interesting to know whether and how the direction/orientation tunings observed here interact with information processing involving head direction selectivity and spatial navigation. Recently, the virtual reality system has been used to investigate the neural function of spatial navigation (Dombeck et al., 2010). A combination of virtual reality and wide-field and two-photon Ca^{2+} imaging may be a strong approach to address this question.

The M2/AC exhibited a visual response, although its visual response property was ambiguous in contrast with the RS, which was most likely due to low signal amplitude of the M2/AC (**Figures 2F,J**). Anatomically, the M2/AC receives strong projections from the RS (Oh et al., 2014; Zingg et al., 2014). It was also reported that the M2/AC is activated by electrical stimulation of the RS more strongly than that of higher visual areas (Hishida et al., 2014). These reports suggest that the M2/AC is a downstream area of the RS. Previous studies in mice suggest that the M2/AC may be important for modulating visual information processing. It was reported that neurons in the M2/AC send feedback projection to GABAergic neurons in V1 to improve visual discrimination (Zhang et al., 2014). Moreover, feedback projection from the M2/AC to higher visual areas is stronger than that to V1 (Zhang et al., 2014; Zingg et al., 2014). Thus, though these studies suggest that M2/AC is important for modulation of visual processing, details of the functional properties of the M2/AC neurons remain unknown. A combination of behavioral tasks that require feedback projection and wide-field and two-photon Ca^{2+} imaging may enable us to investigate how the M2/AC modulates neural activities in visual areas.

Author Contributions

T. Murakami, TY, and KO designed the research. T. Murakami performed wide-field Ca^{2+} imaging experiments and analyzed the data. TY performed two-photon imaging experiments and analyzed the data. T. Murakami, TY, T. Matsui, and KO wrote the manuscript. All authors discussed the results and commented on the manuscript.

Acknowledgments

We thank A. Honda and Y. Sono for animal care and genotyping. This work was supported by JSPS KAKENHI (Grant number 25221001 to KO), grants from CREST-JST (to KO), Grant-in-Aid for Scientific Research on Innovative Areas (25117004 to KO), Strategic International Research Cooperative Program, SCIP, JST (to KO), Ichiro Kanehara Foundation for the Promotion of Medical Sciences and Medical Care (to TY), and the Uehara Memorial Foundation (to TY). T. Matsui (201204982) and T. Murakami (201503597) were supported by JSPS Research Fellowship for Young Scientists. A part of this work was carried out under the Brain/MINDS by the MEXT. We appreciate the technical support of the Research Support Center, Graduate School of Medical Sciences, Kyushu University.

Supplementary Material

The Supplementary Material for this article can be found online at: http://journal.frontiersin.org/article/10.3389/fnmol.2015.00020/abstract

References

Akerboom, J., Chen, T. W., Wardill, T. J., Tian, L., Marvin, J. S., Mutlu, S., et al. (2012). Optimization of a GCaMP calcium indicator for neural activity imaging. *J. Neurosci.* 32, 13819–13840. doi: 10.1523/JNEUROSCI.2601-12.2012

Andermann, M. L., Kerlin, A. M., Roumis, D. K., Glickfeld, L. L., and Reid, R. C. (2011). Functional specialization of mouse higher visual cortical areas. *Neuron* 72, 1025–1039. doi: 10.1016/j.neuron.2011.11.013

Belliveau, J. W., Kennedy, D. N. Jr., McKinstry, R. C., Buchbinder, B. R., Weisskoff, R. M., Cohen, M. S., et al. (1991). Functional mapping of the human visual cortex by magnetic resonance imaging. *Science* 254, 716–719. doi: 10.1126/science.1948051

Bonder, D. E., and McCarthy, K. D. (2014). Astrocytic Gq-GPCR-linked IP3R-dependent Ca^{2+} signaling does not mediate neurovascular coupling in mouse visual cortex in vivo. *J. Neurosci.* 34, 13139–13150. doi: 10.1523/JNEUROSCI.2591-14.2014

Chen, T. W., Wardill, T. J., Sun, Y., Pulver, S. R., Renninger, S. L., Baohan, A., et al. (2013). Ultrasensitive fluorescent proteins for imaging neuronal activity. *Nature* 499, 295–300. doi: 10.1038/nature12354

Cho, J., and Sharp, P. E. (2001). Head direction, place, and movement correlates for cells in the rat retrosplenial cortex. *Behav. Neurosci.* 115, 3–25. doi: 10.1037/0735-7044.115.1.3

Czajkowski, R., Jayaprakash, B., Wiltgen, B., Rogerson, T., Guzman-Karlsson, M. C., Barth, A. L., et al. (2014). Encoding and storage of spatial information in the retrosplenial cortex. *Proc. Natl. Acad. Sci. U.S.A.* 111, 8661–8666. doi: 10.1073/pnas.1313222111

Desai, M., Kahn, I., Knoblich, U., Bernstein, J., Atallah, H., Yang, A., et al. (2011). Mapping brain networks in awake mice using combined optical neural control and fMRI. *J. Neurophysiol.* 105, 1393–1405. doi: 10.1152/jn.00828.2010

Dombeck, D. A., Harvey, C. D., Tian, L., Looger, L. L., and Tank, D. W. (2010). Functional imaging of hippocampal place cells at cellular resolution during virtual navigation. *Nat. Neurosci.* 13, 1433–1440. doi: 10.1038/nn.2648

Felleman, D. J., and Van Essen, D. C. (1991). Distributed hierarchical processing in the primate cerebral cortex. *Cereb. Cortex* 1, 1–47. doi: 10.1093/cercor/1.1.1

Franklin, K. B. J., and Paxinos, G. (2008). *The Mouse Brain in Stereotaxic Coordinates*, 3rd Edn. San Diego, CA: Academic Press.

Gao, E., Deangelis, G. C., and Burkhalter, A. H. (2007). Functionally specialized areas in mouse extrastriate visual cortex. *Abstract in 2007 Neuroscience Meeting Planner of the 37th Annual Meeting of Society for Neuroscience*, San Diego, CA. Program No. 280.12/FF25.

Gerfen, C. R., Paletzki, R., and Heintz, N. (2013). GENSAT BAC cre-recombinase driver lines to study the functional organization of cerebral cortical and basal ganglia circuits. *Neuron* 80, 1368–1383. doi: 10.1016/j.neuron.2013.10.016

Glickfeld, L. L., Andermann, M. L., Bonin, V., and Reid, R. C. (2013). Cortico-cortical projections in mouse visual cortex are functionally target specific. *Nat. Neurosci.* 16, 219–226. doi: 10.1038/nn.3300

Glickfeld, L. L., Reid, R. C., and Andermann, M. L. (2014). A mouse model of higher visual cortical function. *Curr. Opin. Neurobiol.* 24, 28–33. doi: 10.1016/j.conb.2013.08.009

Gorski, J. A., Talley, T., Qiu, M., Puelles, L., Rubenstein, J. L., and Jones, K. R. (2002). Cortical excitatory neurons and glia, but not GABAergic neurons, are produced in the Emx1-expressing lineage. *J. Neurosci.* 22, 6309–6314.

Guilfoyle, D. N., Gerum, S. V., Sanchez, J. L., Balla, A., Sershen, H., Javitt, D. C., et al. (2013). Functional connectivity fMRI in mouse brain at 7T using isoflurane. *J. Neurosci. Methods* 214, 144–148. doi: 10.1016/j.jneumeth.2013.01.019

Hagihara, K. M., and Ohki, K. (2013). Long-term down-regulation of GABA decreases orientation selectivity without affecting direction selectivity in mouse primary visual cortex. *Front. Neural Circuits* 7:28. doi: 10.3389/fncir.2013.00028

Hishida, R., Kudoh, M., and Shibuki, K. (2014). Multimodal cortical sensory pathways revealed by sequential transcranial electrical stimulation in mice. *Neurosci. Res.* 87, 49–55. doi: 10.1016/j.neures.2014.07.004

Issa, J. B., Haeffele, B. D., Agarwal, A., Bergles, D. E., Young, E. D., and Yue, D. T. (2014). Multiscale optical Ca^{2+} imaging of tonal organization in mouse auditory cortex. *Neuron* 83, 944–959. doi: 10.1016/j.neuron.2014.07.009

Jonckers, E., Van Audekerke, J., De Visscher, G., Van der Linden, A., and Verhoye, M. (2011). Functional connectivity fMRI of the rodent brain: comparison of functional connectivity networks in rat and mouse. *PLoS ONE* 6:e18876. doi: 10.1371/journal.pone.0018876

Kalatsky, V. A., and Stryker, M. P. (2003). New paradigm for optical imaging: temporally encoded maps of intrinsic signal. *Neuron* 38, 529–545. doi: 10.1016/S0896-6273(03)00286-1

Kerlin, A. M., Andermann, M. L., Berezovskii, V. K., and Reid, R. C. (2010). Broadly tuned response properties of diverse inhibitory neuron subtypes in mouse visual cortex. *Neuron* 67, 858–871. doi: 10.1016/j.neuron.2010.08.002

Kravitz, D. J., Saleem, K. S., Baker, C. I., and Mishkin, M. (2011). A new neural framework for visuospatial processing. *Nat. Rev. Neurosci.* 12, 217–230. doi: 10.1038/nrn3008

Lim, D. H., Mohajerani, M. H., Ledue, J., Boyd, J., Chen, S., and Murphy, T. H. (2012). In vivo large-scale cortical mapping using channelrhodopsin-2 stimulation in transgenic mice reveals asymmetric and reciprocal relationships between cortical areas. *Front. Neural Circuits* 6:11. doi: 10.3389/fncir.2012.00011

Madisen, L., Garner, A. R., Shimaoka, D., Chuong, A. S., Klapoetke, N. C., Li, L., et al. (2015). Transgenic mice for intersectional targeting of neural sensors and effectors with high specificity and performance. *Neuron* 85, 942–958. doi: 10.1016/j.neuron.2015.02.022

Madisen, L., Zwingman, T. A., Sunkin, S. M., Oh, S. W., Zariwala, H. A., Gu, H., et al. (2010). A robust and high-throughput Cre reporting and characterization system for the whole mouse brain. *Nat. Neurosci.* 13, 133–140. doi: 10.1038/nn.2467

Mantini, D., Hasson, U., Betti, V., Perrucci, M. G., Romani, G. L., Corbetta, M., et al. (2012). Interspecies activity correlations reveal functional correspondence between monkey and human brain areas. *Nat. Methods* 9, 277–282. doi: 10.1038/nmeth.1868

Marshel, J. H., Garrett, M. E., Nauhaus, I., and Callaway, E. M. (2011). Functional specialization of seven mouse visual cortical areas. *Neuron* 72, 1040–1054. doi: 10.1016/j.neuron.2011.12.004

Matsui, T., and Ohki, K. (2013). Target dependence of orientation and direction selectivity of corticocortical projection neurons in the mouse V1. *Front. Neural Circuits* 7:143. doi: 10.3389/fncir.2013.00143

Mohajerani, M. H., Chan, A. W., Mohsenvand, M., LeDue, J., Liu, R., McVea, D. A., et al. (2013). Spontaneous cortical activity alternates between motifs defined by regional axonal projections. *Nat. Neurosci.* 16, 1426–1435. doi: 10.1038/nn.3499

Oh, S. W., Harris, J. A., Ng, L., Winslow, B., Cain, N., Mihalas, S., et al. (2014). A mesoscale connectome of the mouse brain. *Nature* 508, 207–214. doi: 10.1038/nature13186

Ohki, K., Chung, S., Ch'ng, Y. H., Kara, P., and Reid, R. C. (2005). Functional imaging with cellular resolution reveals precise micro-architecture in visual cortex. *Nature* 433, 597–603. doi: 10.1038/nature03274

Ohtsuki, G., Nishiyama, M., Yoshida, T., Murakami, T., Histed, M., Lois, C., et al. (2012). Similarity of visual selectivity among clonally related neurons in visual cortex. *Neuron* 75, 65–72. doi: 10.1016/j.neuron.2012.05.023

Park, H. J., and Friston, K. (2013). Structural and functional brain networks: from connections to cognition. *Science* 342, 1238411. doi: 10.1126/science.1238411

Paukert, M., Agarwal, A., Cha, J., Doze, V. A., Kang, J. U., and Bergles, D. E. (2014). Norepinephrine controls astroglial responsiveness to local circuit activity. *Neuron* 82, 1263–1270. doi: 10.1016/j.neuron.2014.04.038

Peirce, J. W. (2007). PsychoPy–Psychophysics software in Python. *J. Neurosci. Methods* 162, 8–13. doi: 10.1016/j.jneumeth.2006.11.017

Prusky, G. T., Silver, B. D., Tschetter, W. W., Alam, N. M., and Douglas, R. M. (2008). Experience-dependent plasticity from eye opening enables lasting, visual cortex-dependent enhancement of motion vision. *J. Neurosci.* 28, 9817–9827. doi: 10.1523/JNEUROSCI.1940-08.2008

Roth, M. M., Helmchen, F., and Kampa, B. M. (2012). Distinct functional properties of primary and posteromedial visual area of mouse neocortex. *J. Neurosci.* 32, 9716–9726. doi: 10.1523/JNEUROSCI.0110-12.2012

Smith, S. L., and Häusser, M. (2010). Parallel processing of visual space by neighboring neurons in mouse visual cortex. *Nat. Neurosci.* 13, 1144–1149. doi: 10.1038/nn.2620

Stein, B. E., and Stanford, T. R. (2008). Multisensory integration: current issues from the perspective of the single neuron. *Nat. Rev. Neurosci.* 9, 255–266. doi: 10.1038/nrn2331

Stoewer, S., Ku, S. P., Goense, J., Steudel, T., Logothetis, N. K., Duncan, J., et al. (2010). Frontoparietal activity with minimal decision and control in the awake macaque at 7 T. *Magn. Reson. Imaging* 28, 1120–1128. doi: 10.1016/j.mri.2009.12.024

Tohmi, M., Kitaura, H., Komagata, S., Kudoh, M., and Shibuki, K. (2006). Enduring critical period plasticity visualized by transcranial flavoprotein imaging in mouse primary visual cortex. *J. Neurosci.* 26, 11775–11785. doi: 10.1523/JNEUROSCI.1643-06.2006

Umino, Y., Solessio, E., and Barlow, R. B. (2008). Speed, spatial, and temporal tuning of rod and cone vision in mouse. *J. Neurosci.* 28, 189–198. doi: 10.1523/JNEUROSCI.3551-07.2008

Ungerleider, L. G., and Mishkin, M. (1982). "Two cortical visual systems," in *Analysis of Visual Behavior*, eds D. J. Ingel, M. A. Goodale, and R. J. W. Mansfield (Cambridge, MA: Massachusetts Institute of Technology), 549–586.

Vann, S. D., Aggleton, J. P., and Maguire, E. A. (2009). What does the retrosplenial cortex do? *Nat. Rev. Neurosci.* 10, 792–802. doi: 10.1038/nrn2733

Vanni, M. P., and Murphy, T. H. (2014). Mesoscale transcranial spontaneous activity mapping in GCaMP3 transgenic mice reveals extensive reciprocal connections between areas of somatomotor cortex. *J. Neurosci.* 34, 15931–15946. doi: 10.1523/JNEUROSCI.1818-14.2014

Wang, Q., Gao, E., and Burkhalter, A. (2011). Gateways of ventral and dorsal streams in mouse visual cortex. *J. Neurosci.* 31, 1905–1918. doi: 10.1523/JNEUROSCI.3488-10.2011

Wang, Q., Sporns, O., and Burkhalter, A. (2012). Network analysis of corticocortical connections reveals ventral and dorsal processing streams in mouse visual cortex. *J. Neurosci.* 32, 4386–4399. doi: 10.1523/JNEUROSCI.6063-11.2012

Yoder, R. M., Clark, B. J., and Taube, J. S. (2011). Origins of landmark encoding in the brain. *Trends Neurosci.* 34, 561–571. doi: 10.1016/j.tins.2011.08.004

Zariwala, H. A., Borghuis, B. G., Hoogland, T. M., Madisen, L., Tian, L., De Zeeuw, C. I., et al. (2012). A Cre-dependent GCaMP3 reporter mouse for neuronal imaging in vivo. *J. Neurosci.* 32, 3131–3141. doi: 10.1523/JNEUROSCI.4469-11.2012

Zhang, S., Xu, M., Kamigaki, T., Hoang Do, J. P., Chang, W. C., Jenvay, S., et al. (2014). Selective attention. Long-range and local circuits for top-down modulation of visual cortex processing. *Science* 345, 660–665. doi: 10.1126/science.1254126

Zingg, B., Hintiryan, H., Gou, L., Song, M. Y., Bay, M., Bienkowski, M. S., et al. (2014). Neural networks of the mouse neocortex. *Cell* 156, 1096–1111. doi: 10.1016/j.cell.2014.02.023

Conflict of Interest Statement: The authors declare that the research was conducted in the absence of any commercial or financial relationships that could be construed as a potential conflict of interest.

frontiers in Molecular Neuroscience

ORIGINAL RESEARCH
published: 23 September 2015
doi: 10.3389/fnmol.2015.00053

Habituation of glomerular responses in the olfactory bulb following prolonged odor stimulation reflects reduced peripheral input

M. Cameron Ogg, Mounir Bendahamane and Max L. Fletcher**

Department of Anatomy and Neurobiology, University of Tennessee Health Science Center, Memphis, TN, USA

Following prolonged odor stimulation, output from olfactory bulb (OB) mitral/tufted (M/T) cells is decreased in response to subsequent olfactory stimulation. Currently, it is unclear if this decrease is a function of adaptation of peripheral olfactory sensory neuron (OSN) responses or reflects depression of bulb circuits. We used wide-field calcium imaging in anesthetized transgenic GCaMP2 mice to compare excitatory glomerular layer odor responses before and after a 30-s odor stimulation. Significant habituation of subsequent glomerular odor responses to both the same and structurally similar odorants was detected with our protocol. To test whether depression of OSN terminals contributed to this habituation, olfactory nerve layer (ON) stimulation was used to drive glomerular layer responses in the absence of peripheral odor activation of the OSNs. Following odor habituation, in contrast to odor-evoked glomerular responses, ON stimulation-evoked glomerular responses were not habituated. The difference in response between odor and electrical stimulation following odor habituation provides evidence that odor response reductions measured in the glomerular layer of the OB are most likely the result of OSN adaptation processes taking place in the periphery.

Keywords: calcium imaging, GCaMP2, olfactory bulb, glomerular layer, habituation

OPEN ACCESS

Edited by:
Yoshiyuki Yamada, University of Geneva, Switzerland

Reviewed by:
Fábio Marques Simões de Souza, Federal University of ABC (UFABC), Brazil
Johannes Reisert, Monell Chemical Senses Center, USA

****Correspondence:***
M. Cameron Ogg and Max L. Fletcher, Department of Anatomy and Neurobiology, University of Tennessee Health Science Center, 855 Monroe Avenue, Memphis, TN 38163, USA
mogg@uthsc.edu; mfletch4@uthsc.edu

Received: *01 June 2015*
Accepted: *29 August 2015*
Published: *23 September 2015*

Citation:
Ogg MC, Bendahamane M and Fletcher ML (2015) Habituation of glomerular responses in the olfactory bulb following prolonged odor stimulation reflects reduced peripheral input. Front. Mol. Neurosci. 8:53. doi: 10.3389/fnmol.2015.00053

Introduction

Olfactory sensory neurons (OSNs) in the nasal epithelium expressing the same type of olfactory receptor project to glomeruli in the olfactory bulb (OB; Mori et al., 1999; Feinstein and Mombaerts, 2004), a dense cluster of dendrites from interneurons and output mitral/tufted (M/T) cells. Because odors bind differentially to the olfactory receptors, each odor generates a unique pattern of glomerular activation in the bulb (Mori et al., 1999, 2006). These patterns can be visualized at either the presynaptic OSN input level or at the postsynaptic M/T cell level *in vivo* using various imaging methods (Pain et al., 2011; Fletcher and Bendahmane, 2014) and in some cases can reflect real time changes in responsivity following changes in odor input.

One such change, habituation, is the process by which animals decrease their responses to repeated or continually present stimuli (Wilson and Linster, 2008; Rankin et al., 2009). In the olfactory system, short-term habituation is likely primarily driven by a reduction of neuronal responsivity at several stages along the olfactory pathway from the periphery to the cortex (Dalton, 2000; Zufall and Leinders-Zufall, 2000; Wilson and Linster, 2008; Reisert and Zhao, 2011).

Numerous studies have probed adaptation of OSN responses (Zufall and Leinders-Zufall, 2000; Reisert and Zhao, 2011) and M/T cell OB output (Wilson, 2000; Best and Wilson, 2004; Chaudhury et al., 2010). However, olfactory information is processed throughout the layers of the OB, including via inhibitory networks within the glomerular layer (Wachowiak and Shipley, 2006; Nagayama et al., 2014). Yet, few studies have addressed the impact of habituating odor stimulation on odor responses in the glomerular layer of the OB (Schafer et al., 2005; Lecoq et al., 2009).

Similarly to OSN and M/T cell output responses, these studies found glomerular layer response decreases with prolonged odor exposure or brief, very strong odor stimulations (Schafer et al., 2005; Lecoq et al., 2009). However, these studies both relied on recording methods that reflect the total activity of the glomerular circuit [functional magnetic resonance imaging (fMRI; Schafer et al., 2005) and local field potential recordings (Lecoq et al., 2009)] that cannot differentiate excitatory output responses from inhibitory interneuronal responses. Further, the extent to which this reduction reflects decreased input from OSNs, as suggested by a recent study (Lecoq et al., 2009), or a reduction in responsiveness of OB neurons is still unclear.

To address these questions about olfactory habituation in the glomerular layer, we measured glomerular responses before and after prolonged odor exposure in anesthetized transgenic mice expressing the fluorescent calcium indicator GCaMP2 in M/T and excitatory juxtaglomerular (JG) cells (Díez-García et al., 2005; Fletcher et al., 2009). We assessed glomerular responses to the same odorant (self-habituation) and to structurally similar, representationally overlapping odorants (cross-habituation) and compared them to that of M/T cell output responses reported previously (Wilson, 2000). To dissect the role of OSN adaptation in post-synaptic glomerular habituation, we also compared post-habituated odor-driven responses to responses driven by olfactory nerve layer (ON) electrical stimulation (Fletcher et al., 2009).

We found that glomerular odor responses to both the habituating odor (self-habituation) and to an odor that is structurally similar to the habituating odor (cross-habituation) decreased following a 30 s continuous odor pulse. At the moderate odor concentrations used in this study, neural response changes following self-habituation were relatively uniform across glomeruli regardless of initial response intensity. Therefore, the glomerular representation (spatial map and relative intensity) of the habituated odor was unchanged. In contrast, post habituation ON stimulation-evoked glomerular responses displayed little habituation. The difference in glomerular habituation between odor and electrical stimulation provides evidence that the odor response reductions measured in the OB are most likely the result of OSN adaptation processes taking place in the periphery and not a consequence of adaptation of the OSN-M/T synapse.

Materials and Methods

Animals and Surgery

Experiments were performed using 20 adult transgenic male and female mice expressing the green fluorescent Ca^{2+} indicator GCaMP2 under the Kv3.1 potassium channel promoter (Díez-García et al., 2005). Under this promoter, GCaMP2 is expressed in M/T cells and a subpopulation of JG cells (Fletcher et al., 2009). Mice were anesthetized with urethane (2 mg/kg, i.p.) and given an injection of methyl scopolamine (0.05 mg/kg, i.p) to prevent nasal congestion. Mice were secured in a custom stereotaxic apparatus (Narishige) with a heating pad underneath to maintain body temperature. To create an imaging window, a skin incision was made over the dorsal surface of the mouse head and the bone overlying the OBs was thinned with a dental drill. In cases in which electrical stimulation was used, part of the bone was removed after thinning. In some cases lidocaine was applied to the bulb through a small incision in the dura. A dental-cement well was built around the olfactory bulbs and filled with Ringer's solution. During imaging sessions, animals were freely breathing and the respiratory rate was monitored from the respiratory oscillation observed in the odor-evoked GCaMP2 odor-evoked signal. All animal care protocols were approved by the University of Tennessee Institutional Animal Care and Use Committee.

Odorant Presentation

Odors [2-hexanone, 2-heptanone, and ethyl butyrate (Sigma-Aldrich)] were delivered using a flow-dilution olfactometer previously described (Fletcher et al., 2009). Separate flow controllers for the clean air and the pure odorant vapor were used to mix the flow streams at the end of the odor delivery system to achieve an approximate concentration of 0.25, 0.5, or 0.75% saturated vapor (s.v.) at a flow rate of 0.7 L/min. The odor concentration used for each animal was a concentration that activated discrete, stable glomeruli.

Olfactory Nerve Stimulation

For olfactory nerve layer electrical stimulation (ONS), a single current pulse (2 ms, 45–100 μA) was delivered to the OB dorsal surface using a bipolar tungsten electrode (World Precision Instruments). This method has been shown previously to evoke increased glomerular GCaMP signals via synaptically driven activity and is not a result of direct electric current stimulating glomerular postsynaptic dendrites (Fletcher et al., 2009). Further, topical application of the Na^{+} channel blocker lidocaine onto the OB completely blocked all ONS driven glomerular activity (see "Results" Section).

Experimental Protocol

Experiment 1: Habituation Timeline

For control trials, odor pulse duration was 1 s with an inter-stimulus interval of at least 2 min. For the habituation trial, odor pulse duration was 30 s. For post-habituation trials, odor pulse duration was 1 s and the inter-stimulus interval varied.

Experiment 2: Cross-Habituation

For control trials, odor pulse duration was 1 s with an inter-stimulus interval of at least 2 min. Two-hexanone (C6) was presented during the 30-s habituation trial. Two-heptanone (C7)

was given 30 s post-habituation and C6 was given 1 min post-habituation. We waited at least 10 min for the animals to recover from the first habituation, established new baseline responses for the two odors, and repeated the experiment with C7 as the habituating odor.

Experiment 3: ON-Stimulation

For control trials, odor pulse duration was 1 s and ONS duration was 2 ms with an inter-stimulus interval of at least 2 min. For the habituation trial, odor pulse duration was 30 s. For post-habituation trials, odor pulse duration was 1 s, ONS duration was 2 ms, and the inter-stimulus interval varied. Post-habituation trials occurred within 1 min following the odor habituation trial.

Optical Imaging and Analysis

Imaging was performed using a Scientifica Slicescope equipped with a 10 × (0.3 NA) Olympus objective. The dorsal OB was illuminated with a LED light source centered at 480 nm. GCaMP2 signals were band-pass filtered with a Chroma emission filter (HQ535/50) and collected using a CCD camera at 25 Hz (NeuroCCD-SM256, Redshirt Imaging). Maps of stimulus-evoked spatial activity were generated by first correcting for photo-bleaching and then spatially low-pass filtered as described previously (Fletcher et al., 2009). The stimulus-evoked change in fluorescence (ΔF) was calculated by subtracting the average of five frames immediately preceding stimulus onset from the average of five frames centered on the peak of the response generated by the first respiration or electrical stimulation. Glomerular response amplitude (ΔF/F) was calculated by dividing the stimulus-evoked change in fluorescence by the resting fluorescence. For quantitative analysis, discrete glomeruli were visually identified and the response amplitude was measured from a ROI (2 × 2 pixel average) at the center of each (Fletcher et al., 2009). The response of each glomerulus was averaged across control trials. A glomerulus was considered to respond if its mean ΔF/F response to a stimulus was greater than the background ΔF/F signal. Background signal was defined as the mean ± 2 SD ΔF/F value obtained from adjacent regions containing no glomerular activity (Fletcher, 2011). Habituation was measured by dividing the post-habituation response of each glomerulus by its average control response. To identify overlapping glomeruli in both the cross-habituation and ONS experiments (i.e., glomeruli that respond to both odors or to both odor and ONS), ROIs were placed at the center of all glomeruli activated by either odor delivery or ONS for each animal. Glomeruli that responded significantly, as defined above, to both stimuli were defined as shared and were pooled across animals for analysis (Fletcher, 2011).

Statistical Analysis

Statistical analyses were performed using Prism 5.0 software (Graphpad). Values are expressed as mean normalized response ± SEM (unless otherwise indicated). Data were compared using one sample *t*-test, paired *t*-test, one-way ANOVA, and repeated measures ANOVA (Dunnett's test and Tukey's test *post hoc* analyses were performed when appropriate). Statistical significance was defined as $p < 0.05$.

Results

To determine how a 30-s odor exposure impacts subsequent glomerular responses to that odor, we measured glomerular responses to 1-s odor pulses before and after a single prolonged exposure in ten animals (**Figure 1**). Following the habituation trial, the mean normalized glomerular responses changed (ANOVA: $F_{(5,395)} = 37.03$, $p < 0.0001$), and *post hoc* tests showed significant reduction from baseline responses 1 min (70.1 ± 2.1%, $n = 95$), 2 min (73.8 ± 3.3%, $n = 61$), and 4 min (85.2 ± 2.5%, $n = 49$) post exposure (**Figure 1C**). Mean responses at 6 min (94.5 ± 2.5%, $n = 61$) and 11 min (96.6 ± 2.7%, $n = 40$) post-habituation were not significantly different from the baseline, indicating that recovery had occurred by 6 min.

To determine if there was an effect of response intensity on the amount of habituation, we compared the responses of each glomerulus before and 1 min after habituating odor exposure (**Figures 2A,B**). Linear regression analysis yielded a best-fit line with a slope (1.1 ± 0.1, not significant) showing that habituation has a uniform effect regardless of response intensity, and does not disproportionately

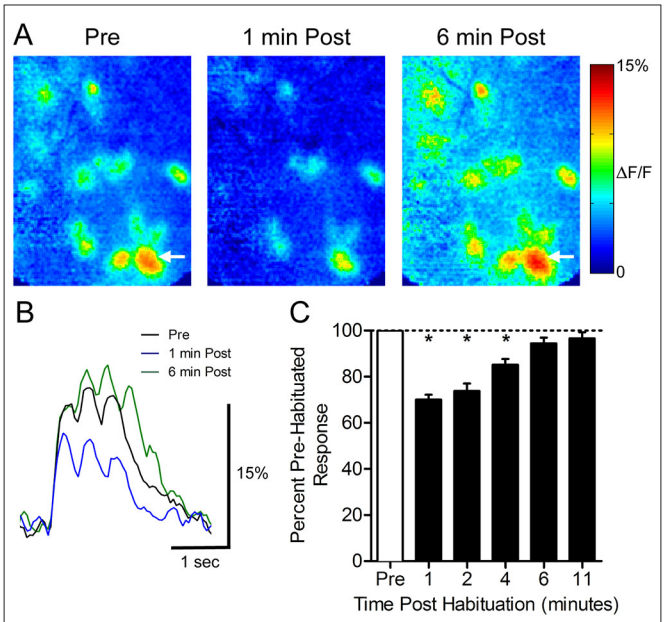

FIGURE 1 | Thirty seconds odor exposure decreases subsequent glomerular responses to that odor for several minutes. (A) Pseudo-color glomerular responses to 2-heptanone (0.5% s.v.) at 10× magnification. One minute after the habituating odor exposure (1 min Post), glomerular responses are decreased from their baseline (Pre). After 6 min, the responses have recovered (6 min Post). **(B)** GCamp2 fluorescence traces from the glomerulus indicated by arrows in **(A)**. **(C)** The timeline of recovery from habituation. Mean normalized glomerular responses for all animals were reduced for several minutes post exposure. Error bars indicate SEM. *$p < 0.05$.

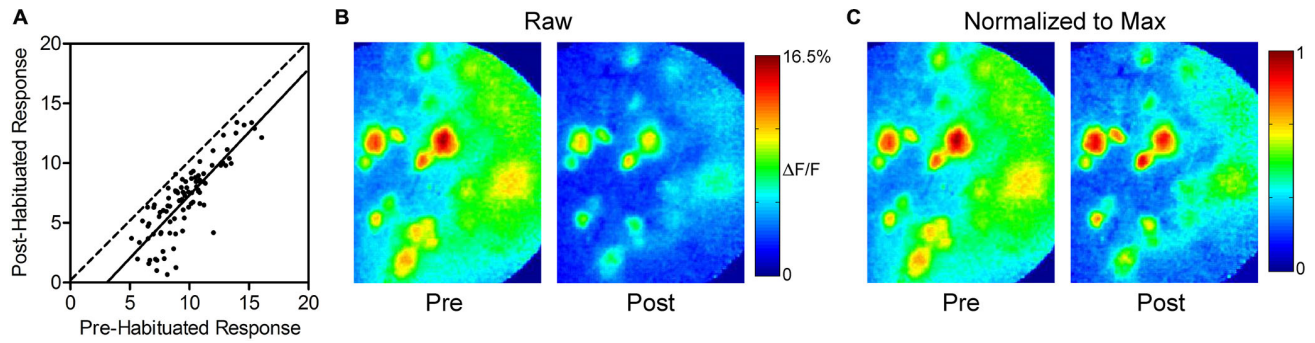

FIGURE 2 | Thirty seconds odor exposure uniformly decreases subsequent glomerular responses, regardless of initial intensity. (A) Responses of each glomerulus before and 1 min after the habituating odor exposure are plotted against each other. The dashed line has a slope of unity. The solid best-fit line is parallel to the line with a slope of unity, indicating that glomeruli maintain their relative odor responses following habituation. The downward shift of the line reflects the effect of habituation across glomeruli. **(B)** Psuedo-color glomerular responses to 2-heptanone (0.5% s.v.) at 10× magnification before (Pre) and after (Post) the habituating odor exposure. **(C)** The glomerular responses shown in **(B)**, normalized to the maximum glomerulus in each representation, illustrating that glomeruli maintain their relative odor responses following habituation, as discussed in **(A)**.

decrease the response of either strongly or weakly responding glomeruli. The uniform reduction leaves relative glomerular response magnitudes of individual odor representations intact following prolonged odor stimulation. This effect is illustrated in **Figure 2C**, which highlights the similarity of pre- and post-habituation odor maps when they are normalized to the maximally responding glomerulus in each odor representation.

We next evaluated whether prolonged exposure to an odor would affect the subsequent glomerular response to a structurally similar odor, an effect known as cross-habituation (Wilson, 2000). In five animals, pre-habituation baseline responses to 2-hexanone (C6) and 2-heptanone (C7) were established (**Figure 3A**). These odors differ by only a single carbon and share some activated glomeruli (**Figure 3B**). We assessed the effects of both self- and cross-habituation in shared glomeruli (**Figure 3C**). Pooling all habituation trials, regardless of habituating odor, shared glomeruli showed reduced mean normalized responses to both the habituated odor (59.1 ± 2.4% of baseline) and to the cross-habituated odor (66.9 ± 1.8% of baseline) with responses to the habituated odor significantly lower than those to the cross-habituated odor (paired *t*-test: $t_{(61)} = 2.53$, $p < 0.05$, $n = 62$ glomeruli; **Figure 3D**). When the longer carbon chain odorant, C7, was used as the habituating odor, the cross-habituation (response to C6: 64.3 ± 2.4% of baseline) was not different from self-habituation (response to C7: 60.1 ± 3.1% of baseline; paired *t*-test: $t_{(40)} = 0.97$, $p = 0.33$, $n = 41$ glomeruli; **Figure 3E**). However, when the shorter carbon chain odorant, C6, was used as the habituating odor, the cross-habituation (response to C7: 72.1 ± 2.7% of baseline) was significantly less than the self-habituation (response to C6: 57.3 ± 3.8% of baseline; paired *t*-test: $t_{(20)} = 4.92$, $p < 0.0001$, $n = 21$ glomeruli; **Figure 3F**).

We used olfactory nerve-stimulation (ONS) to assess whether reduced glomerular responses following prolonged odor stimulation reflect synaptic depression of OSN input. To accomplish this, we stimulated the axons of the OSNs within the OB to generate glomerular responses without odorant activation. In two animals, responses to ONS were compared before and after OB lidocaine application to verify that ONS was not directly activating glomeruli (**Figure 4D**; gray trace). Following bulbar lidocaine application, glomerular responses to ONS were completely blocked (Pre: 7.0 ± 0.3% ΔF/F; Post: 0.3 ± 0.2% ΔF/F; one sample *t*-test: $t_{(21)} = 1.85$, $p = 0.09$, $n = 22$ glomeruli). In four animals, pre-habituation baseline responses to one of the odors and to electrical ONS were established (**Figure 4A**). Analysis was performed on overlapping glomeruli that were activated by both the odor and the ON stimulation ($n = 28$; **Figure 4B**). Glomerular responses changed within 1 min following the odor habituation trial (ANOVA: $F_{(3,81)} = 21.25$, $p < 0.0001$). Post hoc tests showed significant reduction of the mean glomerular response to odor (Pre: 11.4 ± 0.6% ΔF/F; Post: 8.3 ± 0.5% ΔF/F; **Figures 4C–E**). However, in the same glomeruli, the mean glomerular response to ONS was not significantly reduced following odor habituation (Pre: 8.2 ± 0.4% ΔF/F; Post: 7.7 ± 0.4% ΔF/F), demonstrating that postsynaptic responses independent of odor input were not depressed.

Discussion

We imaged excitatory postsynaptic glomerular odor responses and observed reductions in glomerular responsiveness following prolonged odor stimulation. Glomerular responses to an odor were decreased following exposure to both the same odorant (self-habituation) and a structurally similar odorant (cross-habituation). ONS following odor habituation showed that these decreases were not a result of OSN-M/T cell synaptic adaptation and suggests that reduced glomerular responses reflect processes taking place in the periphery.

Decreased OB activity following prolonged odor stimulation has been observed with multiple recording modalities (Potter and Chorover, 1976; Chaput and Panhuber, 1982; Wilson,

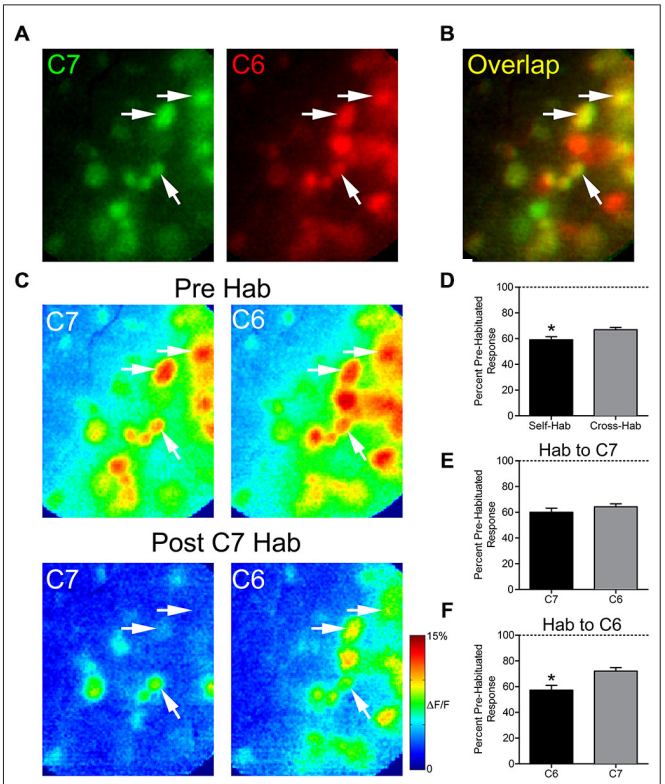

FIGURE 3 | Thirty seconds odor exposure decreases subsequent glomerular responses to a structurally similar odor. (A) Baseline glomerular responses to 2-heptanone (C7) and 2-hexanone (C6) in the same animal displayed in different color channels (C7, 0.5% s.v.: green; C6, 0.5% s.v.: red) at 10× magnification. **(B)** Overlay of the baseline glomerular responses to C7 and C6 shown in **(A)**, highlighting glomeruli (yellow) that respond to both odors. White arrows indicate some examples of these shared glomeruli. **(C)** Pseudo-color glomerular responses to C7 and C6 before (Pre Hab) and after (Post C7 Hab) a 30-s exposure to C7. For both odors, glomerular responses are decreased from their baseline following the habituating odor exposure. **(D)** Mean normalized glomerular responses to both the habituated odor and the cross-habituated odor are reduced. Habituated responses are significantly lower than cross-habituated responses. **(E)** When C7 was used as the habituating odor, self- and cross-habituated responses were not significantly different. **(F)** When C6 was used as the habituating odor, self-habituated responses were significantly lower than cross-habituated responses. Error bars indicate SEM. $*p < 0.05$.

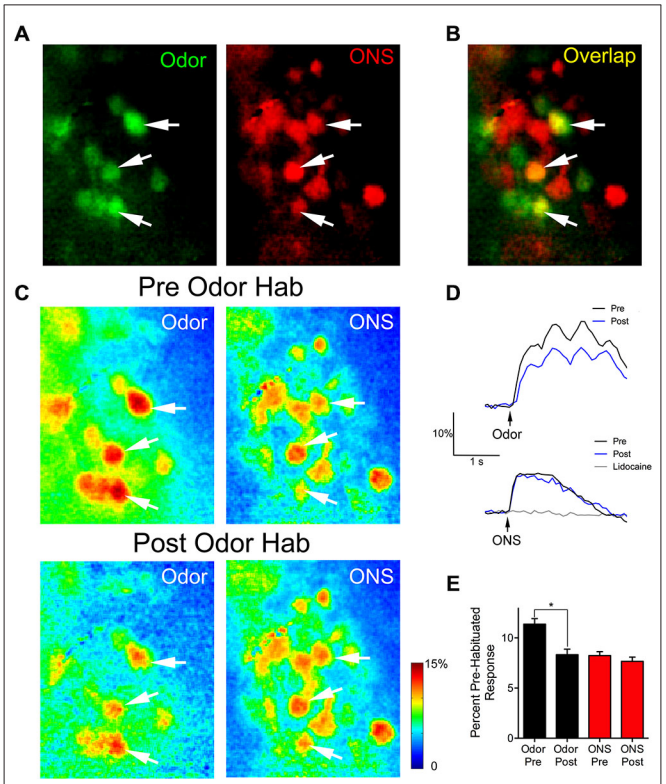

FIGURE 4 | Thirty seconds odor exposure decreases subsequent glomerular responses to odors, but not to ON electrical stimulation. (A) Baseline glomerular responses to an odor presentation and ON electrical stimulation (ONS) in the same animal displayed in different color channels (2-heptanone, 0.5% s.v.: green; ONS, 100 μA: red) at 10× magnification. **(B)** Overlay of the baseline glomerular responses to odor and ONS shown in **(A)**, highlighting glomeruli (yellow) that respond to both stimuli. White arrows indicate some examples of these shared glomeruli. **(C)** Pseudo-color glomerular responses to odor and ONS before (Pre Odor Hab) and after (Post Odor Hab) a 30-s exposure to 2-heptanone. Thirty seconds after a habituating odor exposure (bottom panel), glomerular responses to 2-heptanone are significantly decreased compared to control. However, 1 min after the habituating odor exposure, glomerular responses to ON stimulation are unchanged. **(D)** Example fluorescence traces taken from an overlapping glomerulus (**A–C**: middle white arrow) responding to both 2-heptanone (top panel) and ONS (bottom panel) before (black trace) and after (blue trace) odor habituation. The gray trace in the bottom panel shows the response to ONS following bulbar lidocaine application. Black arrows indicate stimulus onset. **(E)** Population data show glomerular responses to the odor were significantly reduced following odor habituation, while pre and post ONS responses in the same glomeruli were unchanged. Error bars indicate SEM. $*p < 0.05$.

2000; McKeegan and Lippens, 2003; Schafer et al., 2005; Chaudhury et al., 2010). An fMRI study in anesthetized rats found that the glomerular layer showed significantly decreased BOLD signal responses to subsequent odor exposures for up to 5 min following a 32-s odor presentation (Schafer et al., 2005). Electrophysiological recordings of single M/T cell odor responses in anesthetized rats (Wilson, 2000; Fletcher and Wilson, 2003) showed a similar amount of habituation and recovery time of several minutes. Our results fit well with these studies and demonstrate that reduced excitatory odor responses following habituation can be seen at the earliest stages of OB response and are propagated through the OB relatively unchanged.

Our finding of significant cross-habituation at the glomerular population level is similar to previous electrophysiological studies in anesthetized rats that showed single-unit M/T cell responses to other structurally similar odors within their receptive field are also significantly decreased following prolonged exposure to an odor (Wilson, 2000; Fletcher and Wilson, 2003; Chaudhury et al., 2010). Overall, we found that self-habituation results in a larger reduction of the glomerular response than cross-habituation. However, further analysis showed that the effects of cross-habituation are asymmetrical. While the magnitude of self- and cross-habituation are the same after prolonged exposure to the longer carbon chain odorant, after exposure to the shorter chain odorant the

magnitude of cross-habituation is significantly less than that of self-habituation. Asymmetrical effects have been observed in the OB (Wilson, 2000), and even perceptually in humans (Cain, 1970). While still unexplained, the asymmetry could reflect the fact that odorants of increasing carbon chain length activate increasing percentages of OSNs (Malnic et al., 1999). In our case, if C6 is unable to activate as many OSNs as C7, then there is a higher likelihood that there will be un-habituated C7 neurons after an exposure to C6, resulting in less cross-habituation magnitude at the glomerular layer.

ON-stimulation allowed us to test whether glomerular habituation still occurs in the absence of epithelial OSN activation. A similar method was used to explore the effects of odor habituation on synaptic efficiency at the M/T cell-piriform cortex pyramidal neuron synapse (Wilson, 1998). Interestingly, we found that, after prolonged odor exposure, glomeruli had decreased responses to odor, but showed no significant decreases in their response to ON-stimulation. These results indicate that even though their response to odor is decreased following prolonged odor exposure, postsynaptically, the M/T cell dendrites can still be activated and presynaptically, glutamate is available and able to be released effectively from the OSN terminals (i.e., adaptation is likely occurring distal to the ON layer). Lecoq et al. (2009) found evidence that fast adaptation of the glomerular odor response during high-concentration odor stimulation in anesthetized rats is also peripherally mediated. Together, these results suggest that OB glomerular habituation at the timescale of our experiments is mediated by peripheral OSN adaptation and does not heavily rely on synaptic depression of OSN input or further processing via bulbar circuits.

In contrast to our findings, some studies have demonstrated that recovery from adaptation takes place faster in the periphery than in the OB (Potter and Chorover, 1976; Schafer et al., 2005), indicating that additional bulb circuitry was involved. However, in our study M/T glomerular response seems relatively unaffected by bulb processes. This could be due to differences in methodology, since the prior studies used either longer (e.g., 10 min) or repeated (e.g., 10 × 30 s) odor presentations. Because they utilized more intensive odor stimulation, these studies might reflect bulbar depression mechanisms uncovered by studies which used protocols involving repeated (Chaudhury et al., 2010) or much longer (Larkin et al., 2010; Das et al., 2011; Ramaswami, 2014) odor presentations.

Peripheral olfactory adaptation is complex and still not well understood, however, several possible mechanisms have been outlined (Zufall and Leinders-Zufall, 2000; Reisert and Zhao, 2011). Studies have indicated that the gaseous signaling molecules, carbon monoxide and nitric oxide, play a role in OSN adaptation that has been shown to last for several minutes (Zufall and Leinders-Zufall, 1997, 1998; Brunert et al., 2009). It has been postulated that these messengers could be important not only for habituation, but for cross-habituation as well, since they are able to diffuse across the nasal epithelium and potentially affect others OSNs (Brunert et al., 2009). While our experiments did not allow us to probe the specific peripheral adaptation processes underlying the decreased glomerular responses, if the OSNs synapsing onto the glomeruli we observed were adapted in this manner, it could explain the relatively subtle, but longer-lasting decrements we recorded.

In conclusion, the present study found that glomerular responses to odors are decreased following a habituation trial, however, our ON-stimulation experiment showed that this reduction seems to reflect uniform distal adaptation of OSNs, rather than transmitter rundown at the glomerular synapse or depression of bulb circuits. Intriguingly, this indicates that though input to the glomerular layer has been reduced, it can still be activated, should contingencies change. The OB, including the glomerular layer, receives cortical feedback (Brunjes et al., 2005; Boyd et al., 2012; Markopoulos et al., 2012) as well as cholinergic, noradrenergic, and serotonergic input (Fletcher and Chen, 2010), all of which have been shown to modulate OB responsivity (Petzold et al., 2009; Ma and Luo, 2012; Eckmeier and Shea, 2014; Rothermel et al., 2014). Future experiments should probe the potential of these centrifugal inputs to affect OB habituation.

Funding

This research was supported by the Pew Biomedical Science Scholars Program and by the National Institutes of Health Grant DC013779 to MLF.

References

Best, A. R., and Wilson, D. A. (2004). Coordinate synaptic mechanisms contributing to olfactory cortical adaptation. *J. Neurosci.* 24, 652–660. doi: 10.1523/jneurosci.4220-03.2004

Boyd, A. M., Sturgill, J. F., Poo, C., and Isaacson, J. S. (2012). Cortical feedback control of olfactory bulb circuits. *Neuron* 76, 1161–1174. doi: 10.1016/j.neuron.2012.10.020

Brunert, D., Kurtenbach, S., Isik, S., Benecke, H., Gisselmann, G., Schuhmann, W., et al. (2009). Odorant-dependent generation of nitric oxide in mammalian olfactory sensory neurons. *PLoS One* 4:e5499. doi: 10.1371/journal.pone.0005499

Brunjes, P. C., Illig, K. R., and Meyer, E. A. (2005). A field guide to the anterior olfactory nucleus (cortex). *Brain Res. Brain Res. Rev.* 50, 305–335. doi: 10.1016/j.brainresrev.2005.08.005

Cain, W. S. (1970). Odor intensity after self-adaptation and cross-adaptation. *Percept. Psychophys.* 7, 271–275. doi: 10.3758/bf03210163

Chaput, M. A., and Panhuber, H. (1982). Effects of long duration odor exposure on the unit activity of olfactory bulb cells in awake rabbits. *Brain Res.* 250, 41–52. doi: 10.1016/0006-8993(82)90951-9

Chaudhury, D., Manella, L., Arellanos, A., Escanilla, O., Cleland, T. A., and Linster, C. (2010). Olfactory bulb habituation to odor stimuli. *Behav. Neurosci.* 124, 490–499. doi: 10.1037/a0020293

Dalton, P. (2000). Psychophysical and behavioral characteristics of olfactory adaptation. *Chem. Senses* 25, 487–492. doi: 10.1093/chemse/25.4.487

Das, S., Sadanandappa, M. K., Dervan, A., Larkin, A., Lee, J. A., Sudhakaran, I. P., et al. (2011). Plasticity of local GABAergic interneurons drives olfactory habituation. *Proc. Natl. Acad. Sci. U S A* 108, E646–E654. doi: 10.1073/pnas.1106411108

Díez-García, J., Matsushita, S., Mutoh, H., Nakai, J., Ohkura, M., Yokoyama, J., et al. (2005). Activation of cerebellar parallel fibers monitored in transgenic mice expressing a fluorescent Ca2+ indicator protein. *Eur. J. Neurosci.* 22, 627–635. doi: 10.1111/j.1460-9568.2005.04250.x

Eckmeier, D., and Shea, S. D. (2014). Noradrenergic plasticity of olfactory sensory neuron inputs to the main olfactory bulb. *J. Neurosci.* 34, 15234–15243. doi: 10.1523/JNEUROSCI.0551-14.2014

Feinstein, P., and Mombaerts, P. (2004). A contextual model for axonal sorting into glomeruli in the mouse olfactory system. *Cell* 117, 817–831. doi: 10.1016/j.cell.2004.05.011

Fletcher, M. L. (2011). Analytical processing of binary mixture information by olfactory bulb glomeruli. *PLoS One* 6:e29360. doi: 10.1371/journal.pone.0029360

Fletcher, M. L., and Bendahmane, M. (2014). Visualizing olfactory learning functional imaging of experience-induced olfactory bulb changes. *Prog. Brain Res.* 208, 89–113. doi: 10.1016/B978-0-444-63350-7.00004-8

Fletcher, M. L., and Chen, W. R. (2010). Neural correlates of olfactory learning: critical role of centrifugal neuromodulation. *Learn. Mem.* 17, 561–570. doi: 10.1101/lm.941510

Fletcher, M. L., Masurkar, A. V., Xing, J., Imamura, F., Xiong, W., Nagayama, S., et al. (2009). Optical imaging of postsynaptic odor representation in the glomerular layer of the mouse olfactory bulb. *J. Neurophysiol.* 102, 817–830. doi: 10.1152/jn.00020.2009

Fletcher, M. L., and Wilson, D. A. (2003). Olfactory bulb mitral-tufted cell plasticity: odorant-specific tuning reflects previous odorant exposure. *J. Neurosci.* 23, 6946–6955.

Larkin, A., Karak, S., Priya, R., Das, A., Ayyub, C., Ito, K., et al. (2010). Central synaptic mechanisms underlie short-term olfactory habituation in drosophila larvae. *Learn. Mem.* 17, 645–653. doi: 10.1101/lm.1839010

Lecoq, J., Tiret, P., and Charpak, S. (2009). Peripheral adaptation codes for high odor concentration in glomeruli. *J. Neurosci.* 29, 3067–3072. doi: 10.1523/jneurosci.6187-08.2009

Ma, M., and Luo, M. (2012). Optogenetic activation of basal forebrain cholinergic neurons modulates neuronal excitability and sensory responses in the main olfactory bulb. *J. Neurosci.* 32, 10105–10116. doi: 10.1523/JNEUROSCI.0058-12.2012

Malnic, B., Hirono, J., Sato, T., and Buck, L. B. (1999). Combinatorial receptor codes for odors. *Cell* 96, 713–723. doi: 10.1016/s0092-8674(00)80581-4

Markopoulos, F., Rokni, D., Gire, D. H., and Murthy, V. N. (2012). Functional properties of cortical feedback projections to the olfactory bulb. *Neuron* 76, 1175–1188. doi: 10.1016/j.neuron.2012.10.028

McKeegan, D. E. F., and Lippens, N. (2003). Adaptation responses of single avian olfactory bulb neurones. *Neurosci. Lett.* 344, 83–86. doi: 10.1016/s0304-3940(03)00449-x

Mori, K., Nagao, H., and Yoshihara, Y. (1999). The olfactory bulb: coding and processing of odor molecule information. *Science* 286, 711–715. doi: 10.1126/science.286.5440.711

Mori, K., Takahashi, Y. K., Igarashi, K. M., and Yamaguchi, M. (2006). Maps of odorant molecular features in the mammalian olfactory bulb. *Physiol. Rev.* 86, 409–433. doi: 10.1152/physrev.00021.2005

Nagayama, S., Homma, R., and Imamura, F. (2014). Neuronal organization of olfactory bulb circuits. *Front. Neural Circuits* 8:98. doi: 10.3389/fncir.2014.00098

Pain, F., L'Heureux, B., and Gurden, H. (2011). Visualizing odor representation in the brain: a review of imaging techniques for the mapping of sensory activity in the olfactory glomeruli. *Cell. Mol. Life Sci.* 68, 2689–2709. doi: 10.1007/s00018-011-0708-4

Petzold, G. C., Hagiwara, A., and Murthy, V. N. (2009). Serotonergic modulation of odor input to the mammalian olfactory bulb. *Nat. Neurosci.* 12, 784–791. doi: 10.1038/nn.2335

Potter, H., and Chorover, S. L. (1976). Response plasticity in hamster olfactory bulb: peripheral and central processes. *Brain Res.* 116, 417–429. doi: 10.1016/0006-8993(76)90490-x

Ramaswami, M. (2014). Network plasticity in adaptive filtering and behavioral habituation. *Neuron* 82, 1216–1229. doi: 10.1016/j.neuron.2014.04.035

Rankin, C. H., Abrams, T., Barry, R. J., Bhatnagar, S., Clayton, D. F., Colombo, J., et al. (2009). Habituation revisited: an updated and revised description of the behavioral characteristics of habituation. *Neurobiol. Learn. Mem.* 92, 135–138. doi: 10.1016/j.nlm.2008.09.012

Reisert, J., and Zhao, H. (2011). Perspectives on: information and coding in mammalian sensory physiology: response kinetics of olfactory receptor neurons and the implications in olfactory coding. *J. Gen. Physiol.* 138, 303–310. doi: 10.1085/jgp.201110645

Rothermel, M., Carey, R. M., Puche, A., Shipley, M. T., and Wachowiak, M. (2014). Cholinergic inputs from basal forebrain add an excitatory bias to odor coding in the olfactory bulb. *J. Neurosci.* 34, 4654–4664. doi: 10.1523/JNEUROSCI.5026-13.2014

Schafer, J. R., Kida, I., Rothman, D. L., Hyder, F., and Xu, F. (2005). Adaptation in the rodent olfactory bulb measured by fMRI. *Magn. Reson. Med.* 54, 443–448. doi: 10.1002/mrm.20588

Wachowiak, M., and Shipley, M. T. (2006). Coding and synaptic processing of sensory information in the glomerular layer of the olfactory bulb. *Semin. Cell Dev. Biol.* 17, 411–423. doi: 10.1016/j.semcdb.2006.04.007

Wilson, D. A. (1998). Habituation of odor responses in the rat anterior piriform cortex. *J. Neurophysiol.* 79, 1425–1440.

Wilson, D. A. (2000). Comparison of odor receptive field plasticity in the rat olfactory bulb and anterior piriform cortex. *J. Neurophysiol.* 84, 3036–3042.

Wilson, D. A., and Linster, C. (2008). Neurobiology of a simple memory. *J. Neurophysiol.* 100, 2–7. doi: 10.1152/jn.90479.2008

Zufall, F., and Leinders-Zufall, T. (1997). Identification of a long-lasting form of odor adaptation that depends on the carbon Monoxide/cGMP second-messenger system. *J. Neurosci.* 17, 2703–2712.

Zufall, F., and Leinders-Zufall, T. (1998). Role of cyclic GMP in olfactory transduction and adaptation. *Ann. N. Y. Acad. Sci.* 855, 199–204. doi: 10.1111/j.1749-6632.1998.tb10566.x

Zufall, F., and Leinders-Zufall, T. (2000). The cellular and molecular basis of odor adaptation. *Chem. Senses* 25, 473–481. doi: 10.1093/chemse/25.4.473

Conflict of Interest Statement: The authors declare that the research was conducted in the absence of any commercial or financial relationships that could be construed as a potential conflict of interest.